Springer Series in
OPTICAL SCIENCES 162

founded by H.K.V. Lotsch

Editor-in-Chief: W.T. Rhodes, Atlanta

Editorial Board: A. Adibi, Atlanta
T. Asakura, Sapporo
T.W. Hänsch, Garching
T. Kamiya, Tokyo
F. Krausz, Garching
B. Monemar, Linköping
H. Venghaus, Berlin
H. Weber, Berlin
H. Weinfurter, München

Springer Series in

OPTICAL SCIENCES 162

The Springer Series in Optical Sciences, under the leadership of Editor-in-Chief William T. Rhodes, Georgia Institute of Technology, USA, provides an expanding selection of research monographs in all major areas of optics: lasers and quantum optics, ultrafast phenomena, optical spectroscopy techniques, optoelectronics, quantum information, information optics, applied laser technology, industrial applications, and other topics of contemporary interest.

With this broad coverage of topics, the series is of use to all research scientists and engineers who need up-to-date reference books.

The editors encourage prospective authors to correspond with them in advance of submitting a manuscript. Submission of manuscripts should be made to the Editor-in-Chief or one of the Editors. See also www.springer.com/series/624

Editor-in-Chief

William T. Rhodes

Georgia Institute of Technology
School of Electrical and Computer Engineering
Atlanta, GA 30332-0250, USA
E-mail: bill.rhodes@ece.gatech.edu

Editorial Board

Ali Adibi

Georgia Institute of Technology
School of Electrical and Computer Engineering
Atlanta, GA 30332-0250, USA
E-mail: adibi@ee.gatech.edu

Toshimitsu Asakura

Hokkai-Gakuen University
Faculty of Engineering
1-1, Minami-26, Nishi 11, Chuo-ku
Sapporo, Hokkaido 064-0926, Japan
E-mail: asakura@eli.hokkai-s-u.ac.jp

Theodor W. Hänsch

Max-Planck-Institut für Quantenoptik
Hans-Kopfermann-Straße 1
85748 Garching, Germany
E-mail: t.w.haensch@physik.uni-muenchen.de

Takeshi Kamiya

Ministry of Education, Culture, Sports
Science and Technology
National Institution for Academic Degrees
3-29-1 Otsuka, Bunkyo-ku
Tokyo 112-0012, Japan
E-mail: kamiyatk@niad.ac.jp

Ferenc Krausz

Ludwig-Maximilians-Universität München
Lehrstuhl für Experimentelle Physik
Am Coulombwall 1
85748 Garching, Germany *and*
Max-Planck-Institut für Quantenoptik
Hans-Kopfermann-Straße 1
85748 Garching, Germany
E-mail: ferenc.krausz@mpq.mpg.de

Bo Monemar

Department of Physics
and Measurement Technology
Materials Science Division
Linköping University
58183 Linköping, Sweden
E-mail: bom@ifm.liu.se

Herbert Venghaus

Fraunhofer Institut für Nachrichtentechnik
Heinrich-Hertz-Institut
Einsteinufer 37
10587 Berlin, Germany
E-mail: venghaus@hhi.de

Horst Weber

Technische Universität Berlin
Optisches Institut
Straße des 17. Juni 135
10623 Berlin, Germany
E-mail: weber@physik.tu-berlin.de

Harald Weinfurter

Ludwig-Maximilians-Universität München
Sektion Physik
Schellingstraße 4/III
80799 München, Germany
E-mail: harald.weinfurter@physik.uni-muenchen.de

For further volumes:
http://www.springer.com/series/624

Myung K. Kim

Digital Holographic Microscopy

Principles, Techniques, and Applications

Springer

Myung K. Kim
Department of Physics
University of South Florida
4202 E. Fowler Avenue
Tampa, FL 33620
USA
mkkim@usf.edu

Springer Series in Optical Sciences ISSN 0342-4111 e-ISSN 1556-1534
ISBN 978-1-4419-7792-2 e-ISBN 978-1-4419-7793-9
DOI 10.1007/978-1-4419-7793-9
Springer New York Dordrecht Heidelberg London

Library of Congress Control Number: 2011931894

© Springer Science+Business Media, LLC 2011
All rights reserved. This work may not be translated or copied in whole or in part without the written permission of the publisher (Springer Science+Business Media, LLC, 233 Spring Street, New York, NY 10013, USA), except for brief excerpts in connection with reviews or scholarly analysis. Use in connection with any form of information storage and retrieval, electronic adaptation, computer software, or by similar or dissimilar methodology now known or hereafter developed is forbidden.
The use in this publication of trade names, trademarks, service marks, and similar terms, even if they are not identified as such, is not to be taken as an expression of opinion as to whether or not they are subject to proprietary rights.

Printed on acid-free paper

Springer is part of Springer Science+Business Media (www.springer.com)

In memory of my father

Preface

Digital holography is an emergent new imaging technology that inherits many of the unique capabilities of conventional holography but provides novel solutions to some of the key problems that have been limiting its applications and further development. By replacing the photochemical procedures with electronic imaging and having a direct numerical access to the complex optical field, a wide range of new imaging capabilities become available, many of them difficult or infeasible in conventional holography. In recent years, research activities in digital holography have seen exponential growth and application areas have been expanding especially in microbiology and medical imaging. Increasing number of researchers in traditional physics and electrical engineering departments as well as all other areas of engineering, biology, and medicine are interested in exploring the potential capabilities of digital holography. This book is intended to provide a brief but consistent introduction to the principles of digital holography as well as giving an organized overview of the large number of techniques and applications being developed. This will also shed some light on the range of possibilities for further developments. As such, the intended audience is the students and new researchers interested in developing new techniques and exploring new applications of digital holography.

First chapters, 1–5, describe the basic principles of digital holography. A brief history of holography, both conventional (or analog) and digital, is given in Chap. 1, followed by a brief summary of scalar diffraction theory and Fourier optics in Chap. 2 and a general description of the holography processes in Chap. 3. Chapter 4 describes basic numerical methods of calculating optical diffraction. Simulation examples are used to clarify the procedures as well as compare between different methods as clearly as possible. Chapter 5 describes general behavior of the digital holographic images as well as a small number of basic optical configurations that are used in, or are the starting points of, most digital holography experiments.

Chapters 6–10 describe specific techniques of digital holography in some detail. Chapter 6 highlights some of the theoretical developments that enhance the capabilities of digital holography and applications. The zero-order (or dc) and

twin-image terms are important issues in holography, and digital holography provides novel approaches, as described in Chap. 7. In particular, the phase-shifting techniques of Chap. 8 provide highly effective methods for removing the dc and twin terms. The concept of phase shifting is also applied to a number of other special techniques that lead to some quite remarkable capabilities, as will be seen in later chapters. Chapters 9 and 10 collect a number of techniques developed for special capabilities of digital holography imaging, grouped according to whether they involve reconfiguration of hardware or involve numerical processing only.

Final two chapters survey the techniques and applications of microscopy and low-coherence imaging. In Chap. 11, the digital holographic microscopy, and especially its applications in quantitative phase microscopy, are described. Special techniques of digital holographic microscopy, as well as related techniques for quantitative phase microscopy, are surveyed. Digital holographic imaging with low-coherence sources, described in Chap. 12, may hold particularly significant potential for novel imaging methods that have been very difficult or unfeasible in conventional holography.

It is to be noted that the biological microscopy applications of digital holography is emphasized here. This is one of the many areas one can expect significant amount of new development from. But it leaves some of the other major areas such as interferometric metrology and optical information processing outside the main scope of this book. Certainly the book has many deficiencies, both in content and presentations, but it is hoped that this will provide helpful starting materials and stimulus for entering the exciting and rapidly developing field of digital holography. Feedback of comments and corrections from readers addressed to *mkkim@usf.edu* would be most appreciated.

My sincere thanks go to all the students of our Digital Holography and Microscopy Laboratory at the University of South Florida, who have worked hard to produce many of the nice images that are touted here. Appreciation also goes to several colleagues who have given me insights and encouragements at important points of various phases of research represented here, including especially Profs. C.M. Lo and D. Richards. Special thanks to Ms. J. Burke of Springer for her unlimited patience and help with this book project. Financial support of the National Science Foundation during much of the research presented here is gratefully acknowledged. Finally, gratitude and affection to my family for putting up with my absurd work habit. Now I will go take the dogs out for a walk. . .

Tampa, FL Myung K. Kim
March 2011

Contents

1 Introduction 1
1.1 Conventional (Analog) Holography 1
1.2 Digital Holography 5
References 9

2 Diffraction and Fourier Optics 11
2.1 Fourier Transform and Mathematical Background 11
2.1.1 One-Dimensional Definition 11
2.1.2 Two-Dimensional Definition 12
2.1.3 Cartesian Geometry 14
2.1.4 Cylindrical Geometry 15
2.1.5 Basic Properties of Fourier Transforms 15
2.1.6 Convolution and Correlation 16
2.1.7 Some Useful Formulas 18
2.2 Scalar Diffraction Theory 19
2.3 Diffraction from a 2D Aperture 20
2.3.1 Paraxial (Fresnel) Approximation 21
2.3.2 Fraunhofer Diffraction 22
2.4 Propagation of Angular Spectrum 22
2.5 Propagation Through a Lens 25
2.5.1 Fourier Transform by a Lens 27
2.5.2 Imaging by a Lens 27
2.5.3 Lens of Finite Aperture 28
References 28

3 Principles of Holography 29
3.1 Introduction 29
3.2 Basic Concept 29
3.2.1 Holographic Terms 31
3.3 Holography of Plane Waves 32
3.4 Holography of Point Sources 34

3.4.1 Magnifications 36
3.4.2 Collimated References 36
3.5 Holographic Processes 37
3.5.1 Amplitude and Phase Holograms 37
3.5.2 Transmission and Reflection Holograms 38
3.5.3 Thin and Thick Holograms 38
3.5.4 Hologram Materials 39
3.5.5 Phase Conjugation by Photorefractive Crystals 40
3.5.6 Four-Wave Mixing 40
3.5.7 Spectral Hole Burning 40
3.5.8 Stimulated Photon Echo 41
References 42

4 Basic Methods of Numerical Diffraction 43
4.1 Discrete Fourier Transform 43
4.1.1 Programming Implementation of Fourier Transform 46
4.2 Fresnel Transform Method 47
4.3 Huygens Convolution Method 49
4.4 Angular Spectrum Method 50
4.5 Comparison of Methods 51
References 53

5 Digital Holography Configurations 55
5.1 General Behavior of Digital Holographic Images 55
5.2 Digital Gabor Holography 60
5.3 Digital In-line Holography 61
5.4 Digital Image Plane Holography 63
5.5 Digital Fourier Holography 64
5.6 Digital Fresnel Holography 66
References 68

6 Theoretical Studies of Digital Holography 71
6.1 Digital Sampling of Hologram 71
6.2 Wigner Distribution Function 74
6.2.1 Basic Properties of WDF 74
6.2.2 Fourier Transform by a Lens 75
6.2.3 Fourier Holography 76
6.2.4 Fresnel Holography 77
6.2.5 Space–Bandwidth Product 77
6.3 Fractional-Order Fourier Transform 78
6.4 Wavelets 80
References 82

7 Suppression of DC and Twin-Image Terms 85
7.1 Suppression of DC Terms 85
7.2 Phase-Shifting Methods 88

7.3 Speckle Methods 90
7.4 Filtering of Angular Spectrum 91
References 93

8 Phase-Shifting Digital Holography 95
8.1 Basic Principles of PSDH 95
8.2 Reduced Number of Steps 97
8.2.1 Three-Step Method 97
8.2.2 Two-Step Methods 98
8.3 Unknown Phase Steps 99
8.4 Techniques of PSDH 101
8.4.1 Phase-Shifting Methods 101
8.4.2 Heterodyne Digital Holography 101
8.4.3 Asynchronous Digital Holography 103
8.4.4 Parallel Phase-Shifting 103
8.4.5 Fractional Talbot Effect 103
8.4.6 Spatial Phase-Shifting 104
8.5 Errors and Noise in PSDH 105
References 105

9 Numerical Techniques of Digital Holography 109
9.1 Numerical Focusing 109
9.1.1 Extended Focus 111
9.2 Pixel Resolution Control 112
9.2.1 Zero-Padding Method 112
9.2.2 Two-Step Propagation Method 113
9.3 Optical Phase Unwrapping 114
9.4 Diffraction Between Tilted Planes 119
9.5 Aberration Compensation 122
References 123

10 Special Techniques of Digital Holography 129
10.1 Synthetic Aperture Methods 129
10.2 Multiplane Phase Retrieval 131
10.2.1 Noniterative Methods 131
10.2.2 Iterative Methods 134
10.2.3 Other Methods of Phase Retrieval 135
10.3 Dynamic Systems 135
10.4 Noise Reduction 137
10.5 Nonlinear Optics 137
10.5.1 Imaging of NLO Materials 137
10.5.2 Digital Holography by NLO Light 138
10.6 Optical Parameters of Digital Holography 139
10.6.1 Color Digital Holography 139
10.6.2 Polarization Digital Holography 141
10.6.3 Other Wavelengths and Particles 141
References 142

11 Digital Holographic Microscopy 149
11.1 Optical Microscope Basics 149
11.1.1 Optical Configuration 149
11.1.2 Magnification 151
11.1.3 Resolution 151
11.1.4 Objective Lenses 152
11.1.5 Eye 152
11.1.6 Camera 153
11.2 Optical Microscopy Techniques 153
11.2.1 Bright Field Microscopy 153
11.2.2 Dark-Field Microscopy 154
11.2.3 Zernike Phase-Contrast Microscopy 154
11.2.4 Differential Interference Contrast 155
11.2.5 Interference Microscopy 156
11.2.6 Polarization Microscopy 157
11.2.7 Fluorescence Microscopy 157
11.2.8 Confocal Laser Scanning Microscopy 158
11.2.9 Multiphoton Excitation and Nonlinear Optical Microscopy 159
11.3 Digital Holographic Microscopy 159
11.3.1 Light Source 160
11.3.2 Interferometers 160
11.3.3 Camera 163
11.3.4 Computer 163
11.3.5 Examples 165
11.3.6 Comparisons of Analog and Digital Holographic Microscopy 166
11.4 Quantitative Phase Microscopy by DHM 168
11.5 Cell Microscopy and Other Applications 169
11.6 Special Techniques of DHM 174
11.6.1 Total Internal Reflection Digital Holographic Microscopy 174
11.6.2 Multimode Microscopy from a Single Hologram 177
11.6.3 Dark-Field DHM 179
11.6.4 DH Interferometer with a Beam-Splitter Cube 179
11.6.5 Lens-Free On-Chip Holographic Microscopy 180
11.7 Other Methods of Quantitative Phase Microscopy 181
11.7.1 Fourier Phase Microscopy 181
11.7.2 Hilbert Phase Microscopy 181
11.7.3 Diffraction Phase Microscopy 182
11.7.4 Quantitative DIC 183
11.7.5 Spiral Phase-Contrast Microscopy 184
11.7.6 Low-Coherence Interference Microscopy 185
References 187

12 Low-Coherence and Tomographic Techniques 191
12.1 Techniques of Low-Coherence Digital Holographic Microscopy 191
12.1.1 Low-Coherence Sources 192
12.1.2 Rotating Ground Glass 193
12.1.3 Fresnel Incoherent Correlation Holography 195
12.1.4 Achromatic Fringe System 197
12.1.5 Triangular Interferometer 198
12.1.6 Conoscopic Holography 199
12.2 Optical Scanning Holography 200
12.2.1 Basic Principles of OSH 200
12.2.2 Imaging Characteristics of OSH 201
12.2.3 Related Techniques and Applications 203
12.3 Optical Coherence Tomography 204
12.3.1 Time-Domain OCT 204
12.3.2 Fourier-Domain OCT 205
12.3.3 Doppler OCT 206
12.3.4 Optical Coherence Microscopy 206
12.3.5 Phase-Sensitive OCT 208
12.3.6 Differential Phase-Contrast OCT 208
12.3.7 Phase-Dispersion Microscopy 208
12.3.8 Phase-Referenced Interferometry 209
12.4 Full-Field Optical Coherence Tomography 209
12.4.1 Principles of FFOCT 209
12.4.2 Techniques and Applications of FFOCT 212
12.4.3 Light-in-Flight Digital Holography 215
12.5 Digital Interference Holography 215
12.5.1 Principles of DIH 215
12.5.2 Related Techniques and Applications of DIH 220
12.6 Tomography 221
12.6.1 Optical Projection Tomography 221
12.6.2 Optical Diffraction Tomography 222
12.6.3 Holographic Optical Coherence Imaging 223
12.6.4 Turbid Imaging 223
References 225

Index 231

Table of Acronyms

AH	Analog holography
AOM	Acousto-optic modulator
ASM	Angular spectrum method
CGH	Computer-generated holography
DGH	Digital Gabor holography
DH	Digital holography
DHM	Digital holographic microscopy
DIC	Differential interference contrast
DIH	Digital interference holography
DPC	Differential phase contrast
DPM	Diffraction phase microscopy
ESPI	Electronic speckle pattern interferometry
FDOCT	Fourier (frequency) domain OCT
FFOCT	Full-field OCT
FFT	Fast fourier transform
FINCH	Fresnel incoherent correlation holography
FOV	Field of view
FPM	Fourier phase microscopy
FRFT	Fractional-order fourier transform
FTM	Fresnel transform method
FZP	Fresnel zone pattern
HCM	Huygens convolution method
HOCI	Holographic optical coherence imaging
HPM	Hilbert phase microscopy
LCDH	Low-coherence digital holography
LD	Laser diode
LED	Light-emitting diode
LIF	Light in flight

NLO	Nonlinear optics
OCM	Optical coherence microscopy
OCT	Optical coherence tomography
ODT	Optical diffraction tomography
OPT	Optical projection tomography
OPU	Optical phase unwrapping
OSH	Optical scanning holography
PDM	Phase dispersion microscopy
PRI	Phase referenced interferometry
PSDH	Phase-shifting digital holography
PSF	Point spread function
PSI	Phase-shifting interferometry
PZT	Lead zirconate titanate
QPM	Quantitative phase microscopy
SBP	Space–bandwidth product
SDOCT	Spectral domain OCT
SHG	Second harmonic generation
SLD	Superluminescent diode
SLM	Spatial light modulator
SSOCT	Swept source OCT
TDOCT	Time-domain OCT
TIR	Total internal reflection
TIRFM	TIR fluorescence microscopy
TIRHM	TIR holographic microscopy
WDF	Wigner distribution function
ZPC	Zernike phase contrast

Chapter 1
Introduction

Digital holography (DH) is an emerging technology of new paradigm in general imaging applications. By replacing the photochemical procedures of conventional holography with electronic imaging, a door opens to a wide range of new capabilities. Although many of the remarkable properties of holography have been known for decades, their practical applications have been constrained because of the cumbersome procedures and stringent requirements on equipment. A real-time process is not feasible except for special materials and effects, such as the photorefractives. In digital holography, the holographic interference pattern is optically generated by superposition of object and reference beams, which is digitally sampled by a CCD camera and transferred to a computer as an array of numbers. The propagation of optical field is completely and accurately described by diffraction theory, which allows numerical reconstruction of the image as an array of complex numbers representing the amplitude and phase of the optical field. Digital holography offers a number of significant advantages such as the ability to acquire holograms rapidly, availability of complete amplitude and phase information of the optical field, and versatility of the interferometric and image processing techniques. Indeed, digital holography by numerical diffraction of optical fields allows imaging and image processing techniques that are difficult or not feasible in real space holography. We begin by giving a brief overview of the historical development of holography, both the conventional or analog holography and the digital holography.

1.1 Conventional (Analog) Holography

Holography was invented in 1948 by Dennis Gabor (British Thomson-Houston, UK), in an effort to improve the resolution of the electron microscope, where the correction of the electron lens aberrations posed increasing technical difficulty. Instead of attempting to perfect the electron imaging lens, Gabor dispensed it altogether and realized that the diffraction pattern of the electron beam contained

M.K. Kim, *Digital Holographic Microscopy: Principles, Techniques, and Applications*, Springer Series in Optical Sciences 162,
DOI 10.1007/978-1-4419-7793-9_1, © Springer Science+Business Media, LLC 2011

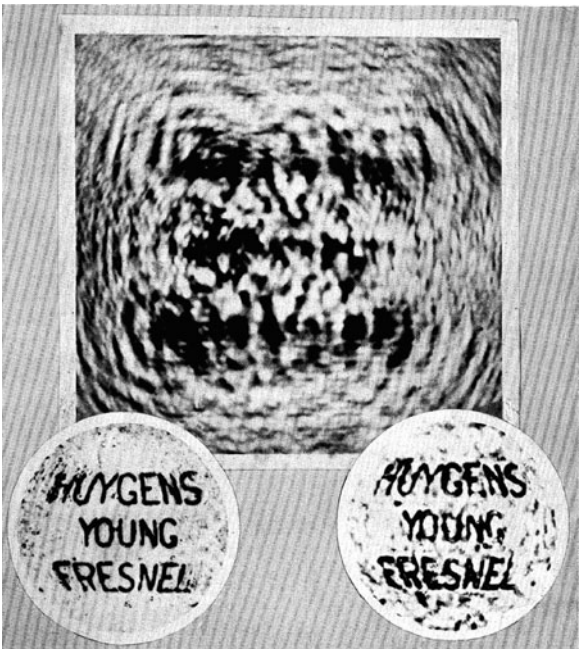

Fig. 1.1 One of the first holograms of D. Gabor. *Top*: the hologram; *lower left*: the object; *lower right*: reconstructed image. (Reprinted from [2] by permission of the Royal Society, London)

complete information regarding the amplitude and phase of the electron wave. The record of the electron wave diffraction is then used to optically synthesize the object field. This allowed the use of optics of visible light for image formation, which is much easier and developed task compared to electron optics. He named the new imaging principle as holography, for its ability to record the whole optical field [1–3].

Gabor's work was inspired by the X-ray microscope of W.L. Bragg (Cavendish Laboratory, Cambridge, UK), who drilled numerous tiny holes at the positions of the X-ray diffraction spots, the hole sizes being proportional to the diffraction intensity. "When a parallel monochromatic beam passes through these holes, and then through a lens, the Fraunhofer fringes build up an image of the crystal structure" [4]. In a sense this was a precursor of binary-coded Fourier hologram. He later used photographic plates in place of the manually drilled hole patterns [5]. On the other hand, the "diffraction diagrams" contain information on the intensities only, but not on the phases. Gabor realized that "if a diffraction diagram of an object is taken with coherent illumination, and a coherent background is added to the diffracted wave, the photograph will contain the full information on the modifications which the illuminating wave has suffered in traversing the object" [2]. In these papers, Gabor laid down theoretical foundations and anticipated novel and important features of the new imaging methods, such as aberration compensation by replicating the aberrations of the recording optics in the reconstruction optics.

Although Gabor's demonstration experiments (Fig. 1.1) were by optical means both for recording and reconstruction, lack of light sources of sufficiently high

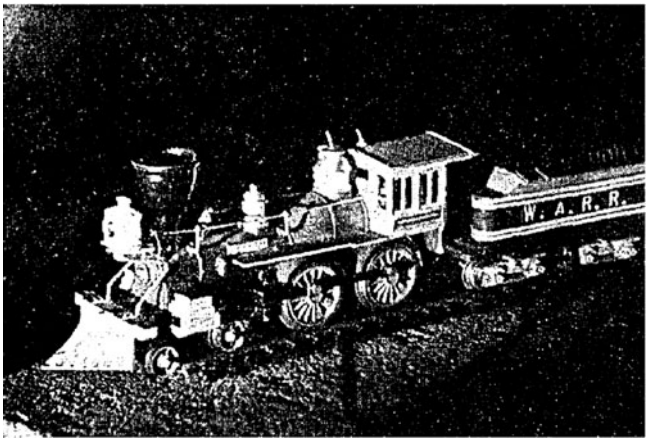

Fig. 1.2 One of the first holograms of a three-dimensional object by Leith & Upatnieks. (Reprinted from [11] by permission of OSA)

coherence and intensity prevented much progress in optical holography [6, 7]. During the 1950s, the holography principle was mostly applied to electron and X-ray microscopy, under the name of diffraction microscopy [8]. Two critical inventions provided the trigger for a truly explosive growth of optical holography techniques and applications. One was the powerful coherent source of light in laser to provide high quality interference contrast. The other, due to Emmett Leith and Juris Upatnieks (University of Michigan, Ann Arbor) [9–12], was the off-axis illumination with a separate reference wave, thus eliminating the problem of the zero-order and twin images of the Gabor's on-axis configuration. In [9], the holography process is described from a communication theory viewpoint, consisting of modulation, frequency dispersion, and square-law detection. They note that "a complex signal of bandwidth W can be represented by a real signal of bandwidth $2W$, in which the real signal is derived from the complex one by placing the signal on a carrier and using only the real part," which immediately suggests the off-axis configuration. They have demonstrated reconstruction of two types of objects, which are not suitable for Gabor process: objects which do not transmit a strong background wave (e.g., transparent lettering against a dark background) and continuous-tone objects. In 1964, they demonstrated holographic reconstruction of three-dimensional solid objects (Fig. 1.2), which resemble to a high degree the original objects, for example, they are three dimensional and exhibit a parallax between near and more distant objects [11].

Soon many new techniques and applications of holography began to develop. The holography is now a mature field, and an excellent survey is given, for example, in [13]. All different types of lasers have been used for generation and viewing of holograms, from diode lasers to high power gas lasers, covering not only the visible wavelengths but also the infrared, ultraviolet, and X-ray [14, 15]. The white-light reflection holography developed by Yuri N. Denisyuk (USSR) [16, 17]

and by Stephen Benton (Polaroid Corp.) [18] made many practical display applications possible and now are ubiquitous such as on credit cards. Many different types of recording materials have been developed, including silver halide photographic emulsion, dichromated gelatin, photoresists, and photopolymers. In photorefractive crystals, such as $LiNbO_3$, exposure of light causes reversible changes in index of refraction, and can be used for creating holograms. Volume holograms have distinct properties compared to the usual planar holograms, such as the requirement of phase matching for Bragg diffraction. Similarly, a number of nonlinear optical effects also give rise to reversible or real-time holographic diffraction and phase conjugate image formation processes, including four-wave mixing, spectral hole burning, and photon echoes [19]. In fact, the holography provides a unifying principle for understanding a wide range of nonlinear optical phenomena.

A most important engineering application of holography is in interferometry. Because the phase as well as the intensity information is reconstructed, wavefronts which were originally separated in time or space or even wavefronts of different wavelengths can be compared by holographic interferometry [20]. Changes in the shape of objects with rough surfaces can be studied with interferometric precision and allows nondestructive testing of deformation, vibration, and surface contours, as well as variations in refractive indices due to thermal, chemical, and biological processes. A large number of holographic interferometry techniques have been developed, including double exposure holography, time average holography, heterodyne holography, phase-shifting interferometry, multiwavelength interferometry, and speckle interferometry. In fact, digital holography evolved naturally from the effort to utilize electronic imaging in interferometry, such as in electronic speckle pattern interferometry (ESPI) [21].

Holograms can store not only three-dimensional images of objects, but also any types of properly encoded data. Holographic data storage provides a number of advantages including high capacity and high speed parallel processing. Volume hologram materials such as photorefractives, photopolymers, and nonlinear crystals are potential candidates for such applications. Holographic data storage can also be tightly integrated with various powerful techniques of holographic image processing, such as encryption, pattern recognition, associative memory, and neural network [22].

We also note two specific holographic imaging applications, namely holographic microscopy and particle analysis. In conventional microscopy, the depth of field is very narrow and decreases as the square of the magnification. At a given focal position of the microscope, the observed field consists of the focal plane sharply in focus together with the blurred background of the out-of-focus planes of the extended object. A photomicrograph or a single frame of video microscopy records the single focal plane, and the information on the rest of the object volume is lost. With holographic microscopy, the entire volume of an object can be recorded on a single hologram [23, 24]. Although these are obvious advantages for recording dynamic scenes of microbes and particles in a volume, holographic microscopy has thus far found limited practical applications. The holographic

image magnification can be achieved by using different wavelengths or curvatures for recording and reconstruction of hologram, but the range of wavelengths of available coherent sources is very limited and curvature mismatch leads to aberrations. In a more successful approach, microscopically recorded holograms are examined using a conventional microscope, which is very useful for phase and interference microscopy [25].

1.2 Digital Holography

The propagation of optical field is completely and accurately described by diffraction theory and therefore amenable to numerical computation. The first demonstration of feasibility of numerical reconstruction of hologram was by Joseph Goodman (Stanford University) et al. in 1967 [26]. Summarizing their description, the pattern of interference between the reference and object waves is directly detected on the photosensitive surface of the vidicon (lens assembly removed). The output of the vidicon is sampled in a 256 × 256 array, and quantized to eight gray levels. The PDP-6 computer is programmed to perform a two-dimensional Fourier transform of the array, and to take the squared modulus of the result. A Cooley–Tukey algorithm (i.e., fast Fourier transform, FFT) is employed, allowing the image to be obtained with 5 min of computation time. The computer output is presented optically on an oscilloscope display (Fig. 1.3). Another precursor to digital holography was a Fourier-transform holographic microscope by Haddad et al. (Los Alamos National Laboratory) in 1992 [27]. They used a tiny drop of glycerol as a lens to create the spherically diverging reference illumination necessary for Fourier-transform holography. They have used a customized CCD with a sensitive area of 2,048 × 2,048 square pixels with 9 μm pixel pitch. FFT calculations on a PC produced microholographic images of an ascaris section. Processing with a numerical lens demonstrated numerical focusing to different focal distances.

Starting in 1994, Ulf Schnars and Werner Jueptner (University of Bremen, Germany), published a number of experiments on CCD recording and numerical reconstruction of holograms in Fresnel off-axis configurations (Fig. 1.4), and demonstrated the feasibility of its use in metrology of macroscopic objects [28–30]. By this time, the CCD cameras and computing technologies have developed to a sufficient level for practical implementation of digital holography, and increasing number of researchers began developing new techniques and applications, as will be described in the rest of this book. In 1999, Christian Depeursinge's group (École Polytechnique Fédérale de Lausanne, Switzerland) demonstrated quantitative phase microscopy by digital holography, that directly produces a surface profile with less than a few nanometer effective noise (Fig. 1.5) [31, 32]. Conventional, that is, analog, holography also reconstructs the phase

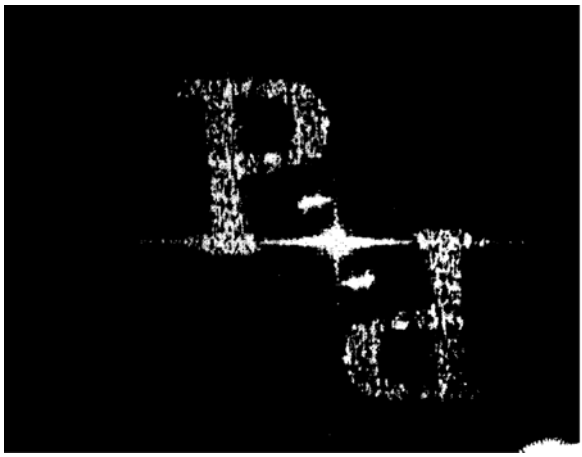

Fig. 1.3 Digitally computed image from electronically detected hologram, by J. Goodman. (Reprinted from [26] by permission of AIP)

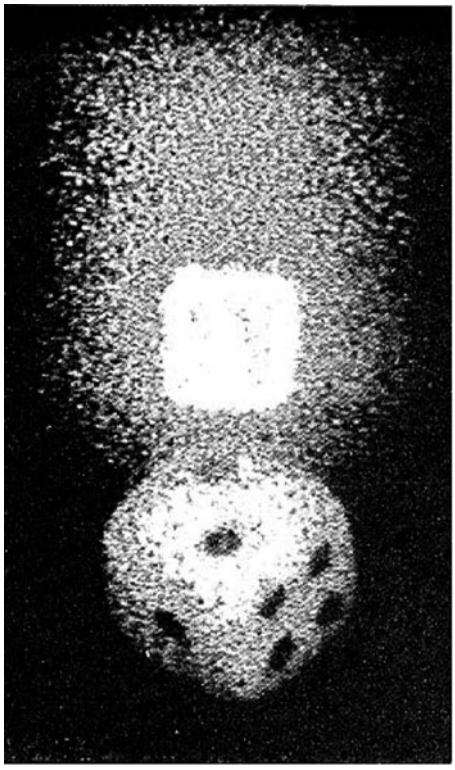

Fig. 1.4 One of the first digital holograms of W. Jueptner and U. Schnars. (Reprinted from [29] by permission of OSA)

information, but in order to extract the phase information one has to perform another interference experiment, whereas in digital holography, the phase information is directly available as soon as the optical field is calculated as a set of complex numbers. The quantitative phase microscopy is an important aspect of digital

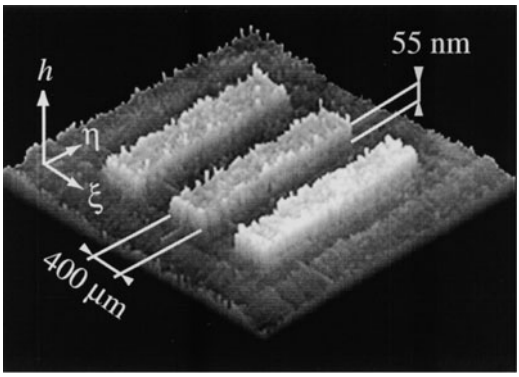

Fig. 1.5 Phase-contrast image obtained with a pure phase object, by C. Depeursinge et al. (Reprinted from [31] by permission of OSA)

holography, allowing many imaging and processing capabilities that are difficult or infeasible in real space holography [33].

Various useful and special techniques have been developed to enhance the capabilities and to extend the range of applications. In digital holographic microscopy, a single hologram is used to numerically focus on the holographic image at any distance [34, 35]. Direct access to the phase information leads to quantitative phase microscopy with nanometer sensitivity of transparent or reflective phase objects [31, 36, 37], and allows further manipulations such as aberration correction [38]. Multiwavelength optical phase unwrapping is a fast and robust method for removing 2π-discontinuities compared to software algorithm-based methods [39]. A significant constraint of digital holography is the pixel count and resolution of the imaging devices. Suppression of the zero-order and the twin images by phase-shifting digital holography allows efficient use of the pixel array [40]. Digital Gabor holography, without separate reference beam, is useful for particle imaging applications by providing four-dimensional space–time record of particle fields [41]. Having a close root in electronic speckle pattern interferometry (ESPI) [21], metrology of deformations and vibrations is a major application area of digital holography [42, 43]. Optical processing, such as pattern recognition and encryption, by digital holography also offers new capabilities [44].

The accelerating development of digital holography is in no small part due to the advances in computational power. Using a modest personal computer, a 2D FFT of 1,024 $\times$ 1,024 array, for example, takes a fraction of a second, compared to many minutes of photochemical processing in conventional holography. A typical sensitivity of a photographic plate is ~10^5 photons per μm^2, whereas a CCD sensitivity can be ~10^0 photons per μm^2 without much effort. This translates to a large reduction in the exposure time as well as substantially simpler requirements on the apparatus stability against vibrations and other disturbances. With these parameters, it is easy to foresee that the strength and versatility of digital holography techniques will only continue to increase at a robust rate.

The term digital holography (DH) is used in a few different contexts. One is a narrow meaning as used in this book, namely, the optical generation of a hologram

followed by electronic acquisition and numerical reconstruction of the image. Another is the opposite process of calculating the holographic interference numerically, followed by printing or other output to real space so that the reconstruction can be carried out by optical means. This is now more commonly referred to as the computer-generated hologram (CGH). The CGH has a somewhat longer history, and earlier in its development, DH and CGH were basically synonymous [45–47]. In 1967, A.W. Lohmann and D.P. Paris (IBM) showed that "when a hologram is desired from an object which does not exist physically but is known in mathematical terms, one can compute the hologram" [48]. A plotter was used to make a drawing at a larger scale, which is then reduced photographically. In order to represent the phase using a black-and-white plotter, they introduced a technique called binary detour-phase hologram, where the position of a plotted pixel is shifted according to the phase. The resulting optically reconstructed images were completely analogous to ones produced with gray-scale holograms. CGH can be used to produce holograms of fictitious objects with prescribed intensity and phase structure. Many computation techniques have been developed as well as the means of optical reconstruction.

The following is a short list of some of the recent books, feature issues and review papers that may be of general interest.

- J. Goodman, *Introduction to Fourier optics* (Roberts & Co., 2005).
- P. Hariharan, Optical Holography: Principles, Techniques, and Applications, 2 ed. (Cambridge University Press, 1996).
- L. Yaroslavsky, Digital holography and digital image processing: principles, methods, algorithms (Kluwer Academic, 2004).
- W. Jueptner, and U. Schnars, Digital Holography: Digital Hologram Recording, Numerical Reconstruction, and Related Techniques (Springer-Verlag, Berlin Heidelberg, 2005).
- T. Kreis, Handbook of holographic interferometry: Optical and digital methods (Wiley-VCH, 2005).
- T. Poon, ed. Digital holography and three-dimensional display: principles and applications (Springer, 2006).
- T. C. Poon, T. Yatagai, and W. Juptner, "Digital holography – coherent optics of the 21st century: introduction," Applied Optics 45, 821–821 (2006).
- T. C. Poon, B. Lee, H. Yoshikawa, and W. Osten, "Digital holography and 3D imaging: introduction to the feature issue," Applied Optics 47, DH1-DH1 (2008).
- T. C. Poon, B. Lee, H. Yoshikawa, and J. Rosen, "Digital Holography and 3-D Imaging: feature introduction," Applied Optics 48, DH2-DH2 (2009).
- P. Banerjee, G. Barbastathis, M. K. Kim, and N. Kukhtarev, "Digital holography and 3-D imaging," Appl. Opt. 50, DH1-DH2 (2011).
- U. Schnars, and W. P. O. Juptner, "Digital recording and numerical reconstruction of holograms," Measurement Science & Technology 13, R85-R101 (2002).
- M. K. Kim, "Principles and techniques of digital holographic microscopy," SPIE Reviews 1, 1–50 (2010).

References

1. D. Gabor, "A new microscope principle," Nature **161**, 777–778 (1948).
2. D. Gabor, "Microscopy by reconstructed wavefronts," Proc. Roy. Soc. **A197**, 454–487 (1949).
3. D. Gabor, "Microscopy by reconstructed wavefronts: II," Proc. Phys. Soc. **B64**, 449–469 (1951).
4. W. L. Bragg, "A new type of x-ray microscope," Nature **143**, 678 (1939).
5. W. L. Bragg, "The x-ray microscope," Nature **149**, 470–471 (1942).
6. G. L. Rogers, "Experiments in diffraction microscopy," Proc. Roy. Soc. Edinburgh **63A**, 193–221 (1952).
7. H. M. A. El-Sum, and P. Kirkpatrick, "Microscopy by reconstructed wavefronts," Phys. Rev. **85**, 763 (1952).
8. M. E. Haine, and T. Mulvey, "Diffraction Microscopy with X-Rays," Nature **170**, 202–203 (1952).
9. E. N. Leith, and J. Upatniek, "Reconstructed wavefronts and communication theory," J. Opt. Soc. Am. **52**, 1123–1130 (1962).
10. E. N. Leith, and J. Upatnieks, "Wavefront reconstruction with continuous-tone objects," J. Opt. Soc. Am. **53**, 1377–1381 (1963).
11. E. N. Leith, and J. Upatnieks, "Wavefront reconstruction with diffused illumination and three-dimensional objects," J. Opt. Soc. Am. **54**, 1295–1301 (1964).
12. H. J. Caulfield, "Emmett Leith: a personal perspective," Applied Optics **47**, A119-A122 (2008).
13. P. Hariharan, *Optical Holography: Principles, Techniques, and Applications, 2 ed.* (Cambridge University Press, 1996).
14. G. Faigel, and M. Tegze, "X-ray holography," Reports on Progress in Physics **62**, 355–393 (1999).
15. J. C. Solem, and G. C. Baldwin, "Micro-Holography of Living Organisms," Science **218**, 229–235 (1982).
16. Y. N. Denisyuk, "On the reproduction of the optical properties of an object by the wave field of its scattered radiation," Opt. & Spectr. **15**, 279–284 (1963).
17. Y. N. Denisyuk, "On the reproduction of the optical properties of an object by the wave field of its scattered radiation," Opt. & Spectr. **18**, 152–157 (1965).
18. S. A. Benton, "Hologram Reconstructions with Extended Incoherent Sources," Journal of the Optical Society of America **59**, 1545–1546 (1969).
19. R. A. Fisher, *Optical Phase Conjugation* (Elsevier, 1983).
20. T. Kreis, *Handbook of holographic interferometry: Optical and digital methods* (Wiley-VCH, 2005).
21. A. F. Doval, "A systematic approach to TV holography," Measurement Science & Technology **11**, R1-R36 (2000).
22. N. Collings, *Optical pattern recognition using holographic techniques* (Addison-Wesley, 1988).
23. D. Gabor, and W. P. Goss, "Interference Microscope with Total Wavefront Reconstruction," J. Opt. Soc. Am. **56**, 849–858 (1966).
24. C. Knox, "Holographic microscopy as a technique for recording dynamic microscopic subjects," Science **153**, 989–990 (1966).
25. K. Snow, and Vandewar.R, "An Application of Holography to Interference Microscopy," Applied Optics **7**, 549–554 (1968).
26. J. W. Goodman, and R. W. Lawrence, "Digital Image Formation from Electronically Detected Holograms," Applied Physics Letters **11**, 77–79 (1967).
27. W. S. Haddad, D. Cullen, J. C. Solem, J. W. Longworth, A. McPherson, K. Boyer, and C. K. Rhodes, "Fourier-Transform Holographic Microscope," Applied Optics **31**, 4973–4978 (1992).

28. U. Schnars, and W. P. O. Juptner, "Digital Recording and Reconstruction of Holograms in Hologram Interferometry and Shearography," Applied Optics **33**, 4373–4377 (1994).
29. U. Schnars, and W. Juptner, "Direct Recording of Holograms by a Ccd Target and Numerical Reconstruction," Applied Optics **33**, 179–181 (1994).
30. U. Schnars, "Direct Phase Determination in Hologram Interferometry with Use of Digitally Recorded Holograms," Journal of the Optical Society of America a-Optics Image Science and Vision **11,** 2011–2015 (1994).
31. E. Cuche, F. Bevilacqua, and C. Depeursinge, "Digital holography for quantitative phase-contrast imaging," Optics Letters **24**, 291–293 (1999).
32. E. Cuche, P. Marquet, and C. Depeursinge, "Simultaneous amplitude-contrast and quantitative phase-contrast microscopy by numerical reconstruction of Fresnel off-axis holograms," Applied Optics **38**, 6994–7001 (1999).
33. W. Jueptner, and U. Schnars, *Digital Holography: Digital Hologram Recording, Numerical Reconstruction, and Related Techniques* (Springer-Verlag, Berlin Heidelberg, 2005).
34. S. Grilli, P. Ferraro, S. De Nicola, A. Finizio, G. Pierattini, and R. Meucci, "Whole optical wavefields reconstruction by digital holography," Optics Express **9**, 294–302 (2001).
35. C. J. Mann, L. F. Yu, and M. K. Kim, "Movies of cellular and sub-cellular motion by digital holographic microscopy," Biomed. Eng. Online **5**, 21 (2006).
36. C. J. Mann, L. F. Yu, C. M. Lo, and M. K. Kim, "High-resolution quantitative phase-contrast microscopy by digital holography," Optics Express **13**, 8693–8698 (2005).
37. J. Kuhn, F. Charriere, T. Colomb, E. Cuche, F. Montfort, Y. Emery, P. Marquet, and C. Depeursinge, "Axial sub-nanometer accuracy in digital holographic microscopy," Measurement Science & Technology **19**, (2008).
38. P. Ferraro, S. De Nicola, A. Finizio, G. Coppola, S. Grilli, C. Magro, and G. Pierattini, "Compensation of the inherent wave front curvature in digital holographic coherent microscopy for quantitative phase-contrast imaging," Applied Optics **42**, 1938–1946 (2003).
39. J. Gass, A. Dakoff, and M. K. Kim, "Phase imaging without 2-pi ambiguity by multiwavelength digital holography," Opt. Lett. **28**, 1141–1143 (2003).
40. I. Yamaguchi, and T. Zhang, "Phase-shifting digital holography," Optics Letters **22**, 1268–1270 (1997).
41. W. B. Xu, M. H. Jericho, I. A. Meinertzhagen, and H. J. Kreuzer, "Digital in-line holography for biological applications," Proceedings of the National Academy of Sciences of the United States of America **98**, 11301–11305 (2001).
42. U. Schnars, and W. P. O. Juptner, "Digital recording and numerical reconstruction of holograms," Measurement Science & Technology **13**, R85-R101 (2002).
43. I. Yamaguchi, "Holography, speckle, and computers," Optics and Lasers in Engineering **39**, 411–429 (2003).
44. O. Matoba, T. Nomura, E. Perez-Cabre, M. S. Millan, and B. Javidi, "Optical Techniques for Information Security," Proc. IEEE **97**, 1128–1148 (2009).
45. B. R. Brown, and A. W. Lohmann, "Complex Spatial Filtering with Binary Masks," Applied Optics **5**, 967–969 (1966).
46. G. Hutton, "Fast-Fourier-transform holography: recent results," Opt. Lett. **3**, 30–32 (1978).
47. L. Yaroslavsky, *Digital holography and digital image processing: principles, methods, algorithms* (Kluwer Academic, 2004).
48. A. W. Lohmann, and D. P. Paris, "Binary Fraunhofer Holograms Generated by Computer," Applied Optics **6**, 1739–1748 (1967).

Chapter 2
Diffraction and Fourier Optics

Diffraction and Fourier optics are at the foundation of the theory of holographic image formation and therefore essential in the description of holographic processes and techniques. In this chapter, we review the scalar diffraction theory, which is used to describe the propagation of the optical field from an input plane to the output plane. The propagation of light through a lens is an essential part of any imaging system, and its mathematical description is relevant to holographic image formation as well.

2.1 Fourier Transform and Mathematical Background

We begin with a brief summary of basic results from Fourier analysis and related mathematical background, mostly without proof, the main purpose being establishing basic notations and collecting in one place useful expressions that are frequently used in Fourier optics [1].

2.1.1 One-Dimensional Definition

In a one-dimensional (1D) system, according to the Fourier theorem, if $f(x)$ is a reasonably well-behaved function, then it can be decomposed into a superposition of sine and cosine functions, or imaginary exponentials, of various frequencies. (Note that in this book, the term frequency will usually refer to the spatial frequencies.) The amplitudes of the decomposition are the Fourier transform of the function, thus

$$f(x) = \frac{1}{\sqrt{2\pi}} \int_{-\infty}^{\infty} \mathrm{d}k F(k) \exp(ikx) = \mathfrak{F}^{-1}\{F(k)\}[x],$$
$$F(k) = \frac{1}{\sqrt{2\pi}} \int_{-\infty}^{\infty} \mathrm{d}x f(x) \exp(-ikx) = \mathfrak{F}\{f(x)\}[k]. \tag{2.1}$$

M.K. Kim, *Digital Holographic Microscopy: Principles, Techniques, and Applications*, Springer Series in Optical Sciences 162,
DOI 10.1007/978-1-4419-7793-9_2, © Springer Science+Business Media, LLC 2011

Table 2.1 Examples of Fourier transform pairs. See Fig. 2.1 for illustrations

$f(x)$	$\mathcal{F}\{f\}[k]$	
$f(x)=\delta(x-x_0)$	$F(k)=\frac{1}{\sqrt{2\pi}}\exp(-ikx_0)$	
$f(x)=\delta(x-x_0)+\delta(x+x_0)$	$F(k)=\sqrt{\frac{2}{\pi}}\cos(kx_0)$	Fig. 2.1a
$f(x)=\exp(ik_0x)$	$F(k)=\sqrt{2\pi}\delta(k-k_0)$	
$f(x)=\cos(k_0x)$	$F(k)=\sqrt{\frac{\pi}{2}}\{\delta(k-k_0)+\delta(k+k_0)\}$	
$f(x)=\mathrm{rect}\left(\frac{x}{a}\right)$ $=\begin{cases}1; x\in[-a,a]\\ 0;\text{otherwise}\end{cases}$	$F(k)=\sqrt{\frac{2}{\pi}}a\,\mathrm{sinc}(ka)$ $=\sqrt{\frac{2}{\pi}}a\frac{\sin(ka)}{ka}$	Fig. 2.1b
$f(x)=\exp\left(-\frac{x^2}{a^2}\right)$	$F(k)=\frac{a}{\sqrt{2}}\exp\left(-\frac{1}{4}a^2k^2\right)$	Fig. 2.1c
$f(x)=\exp\left(\frac{i}{2}\alpha x^2\right)$	$F(k)=\frac{i}{\alpha}\exp\left(-\frac{i}{2}\frac{k^2}{\alpha}\right)$	Fig. 2.1d
$f(x)=\mathrm{comb}\left(\frac{x}{a}\right)$ $=\sum_{n=-\infty}^{\infty}\delta(x-na)$	$F(k)=\frac{\sqrt{2\pi}}{a}\mathrm{comb}\left(\frac{k}{2\pi/a}\right)$ $=\frac{\sqrt{2\pi}}{a}\sum_{n=-\infty}^{\infty}\delta\left(k-n\frac{2\pi}{a}\right)$	Fig. 2.1e

The particular notation with square brackets is used to explicitly display the variable of transform. Examples of the Fourier transform pairs are listed in Table 2.1 and illustrated in Fig. 2.1. Thus, an even (odd) pair of delta functions transforms to cosine (sine) function. A rectangle function transforms to a sinc function. The transforms of Gaussian, chirp, or comb functions transform respectively to the same type of functions.

2.1.2 Two-Dimensional Definition

For a two-dimensional (2D) system, the Fourier transform is written as

$$f(x,y)=\frac{1}{2\pi}\iint \mathrm{d}k_x\mathrm{d}k_yF\left(k_x,k_y\right)\exp\left[i\left(k_xx+k_yy\right)\right]=\mathcal{F}^{-1}\left\{F\left(k_x,k_y\right)\right\}[x,y],$$
$$F\left(k_x,k_y\right)=\frac{1}{2\pi}\iint \mathrm{d}x\mathrm{d}yf(x,y)\exp\left[-i\left(k_xx+k_yy\right)\right]=\mathcal{F}\{f(x,y)\}\left[k_x,k_y\right]. \tag{2.2}$$

Generalization to N-dimensional system is straightforward, noting that the factor $\sqrt{2\pi}$ in (2.1) becomes $(2\pi)^{N/2}$.

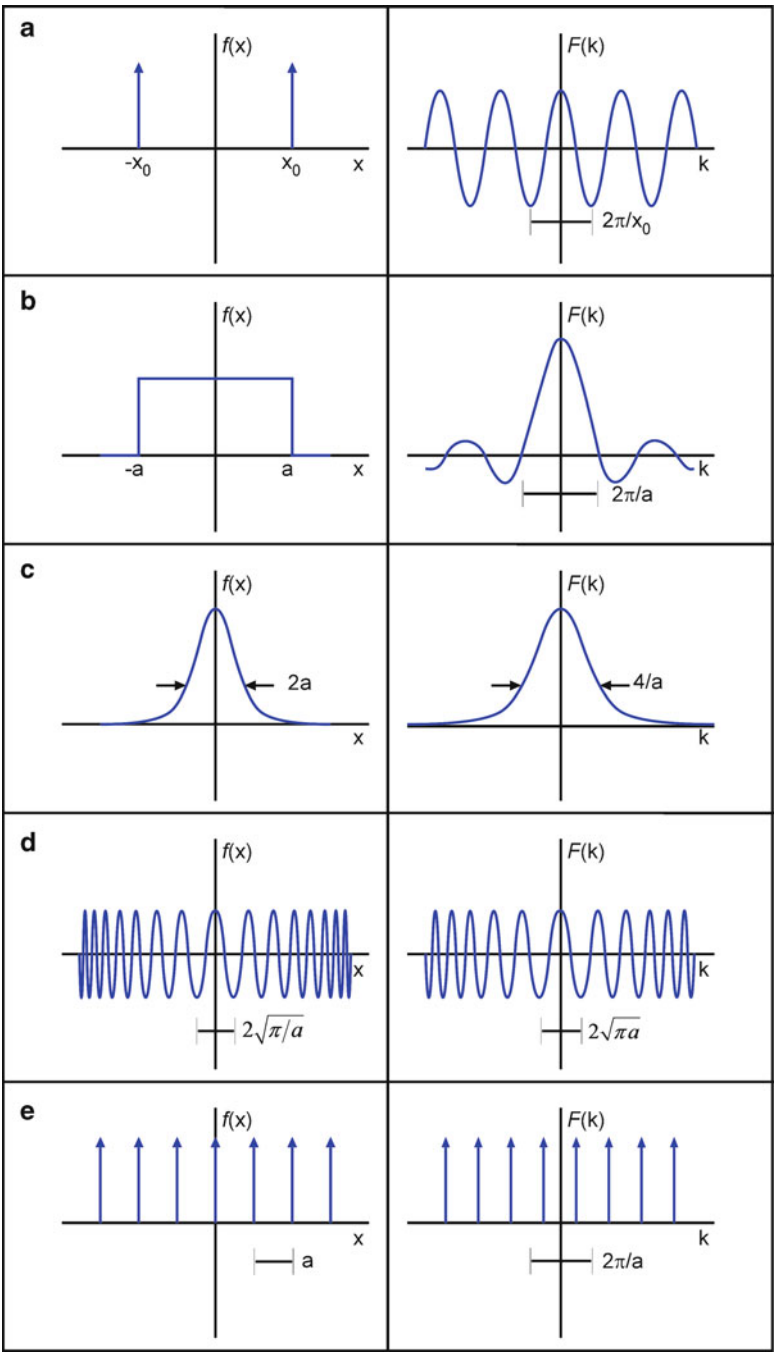

Fig. 2.1 Examples of Fourier transform pairs

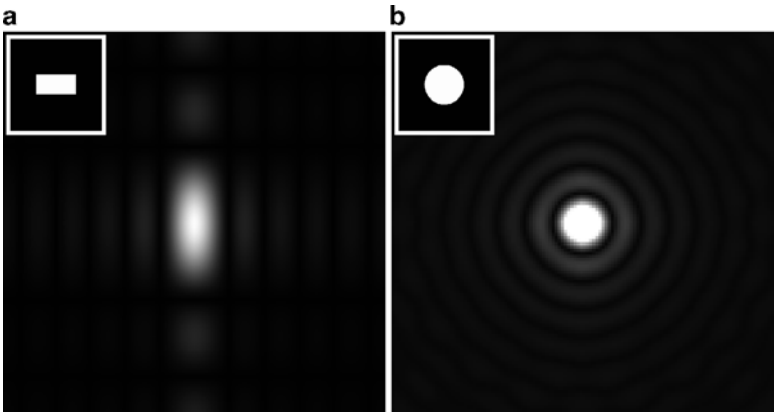

Fig. 2.2 (**a**) *Rectangular aperture* and its Fourier transform. (**b**) *Circular aperture* and its Fourier transform

2.1.3 Cartesian Geometry

If the function is separable in Cartesian coordinates, $f(x,y) = f_x(x)f_y(y)$, then so is the transform:

$$\mathfrak{F}\{f(x,y)\} = \mathfrak{F}\{f_x(x)\}\mathfrak{F}\{f_y(y)\}, \tag{2.3}$$

that is,

$$F(k_x,k_y) = F_x(k_x)F_y(k_y). \tag{2.4}$$

An important example is a rectangular aperture,

$$f(x,y) = \text{rect}\left(\frac{x}{a_x}\right)\text{rect}\left(\frac{y}{a_y}\right), \tag{2.5}$$

whose transform is

$$F(k_x,k_y) = \frac{2}{\pi}a_x\,a_y\text{sinc}\,(k_xa_x)\text{sinc}\,(k_ya_y). \tag{2.6}$$

The function $|F(k_x,k_y)|^2$ is illustrated in Fig. 2.2a with $f(x,y)$ displayed in the inset. Note that the horizontal orientation of the long side of the rectangle results in the vertical orientation of the central bright spot in the transform. This is an example of the uncertainty principle that higher localization in the spatial dimension corresponds to larger spread in the frequency dimension, and vice versa.

2.1.4 Cylindrical Geometry

If the 2D function is given in cylindrical coordinates, with

$$\begin{cases} x = \rho\cos\varphi \\ y = \rho\sin\varphi \end{cases} \quad \text{and} \quad \begin{cases} k_x = k\cos\eta \\ k_y = k\sin\eta \end{cases}, \tag{2.7}$$

then the Fourier transform is

$$F(k,\eta) = \frac{1}{2\pi}\int_0^\infty \rho \mathrm{d}\rho \int_0^{2\pi} \mathrm{d}\varphi f(\rho,\varphi)\exp[-ik\rho\cos(\varphi-\eta)]. \tag{2.8}$$

If the function has cylindrical symmetry, so that $f = f(\rho)$, then

$$F(k,\eta) = \int_0^\infty f(\rho)\rho J_0(k\rho)\mathrm{d}\rho = \Re\{f(\rho)\}[k], \tag{2.9}$$

which is called the Fourier–Bessel transform. An important example is a circular aperture of radius a:

$$f(\rho)\begin{cases} 1 & \rho \leqslant a \\ 0 & \rho > a \end{cases} \tag{2.10}$$

Its Fourier transform is the Airy disk, illustrated in Fig. 2.2b:

$$F(k) = \int_0^a \rho J_0(k\rho)\mathrm{d}\rho = \frac{a}{k}J_1(ka). \tag{2.11}$$

The first zero of the Bessel function $J_1(x)$ is at $x \approx 3.83$, which defines the size of the Airy disk. This is also to be compared with the first zero of sinc function $\mathrm{sinc}(x)$ at $x = \pi \approx 3.14$.

2.1.5 Basic Properties of Fourier Transforms

We list several of the well-known properties of Fourier transform in Table 2.2. The similarity property shows that if the function f is stretched in the x-direction, then its transform is shrunk in corresponding direction k_x. The shift theorem states that a shift of the spatial position of a function amounts to an additional phase oscillation in the frequency domain, which is the basis of the large field of interferometry. In the uncertainty relation, the uncertainties are defined as the root-mean-square deviation.

Table 2.2 Basic theorems of Fourier transform

Linearity:	$\mathcal{F}\{\alpha f + \beta g\} = \alpha F + \beta G$
Similarity:	$\mathcal{F}\{f(ax)\} = \frac{1}{\lvert a\rvert} F\left(\frac{k}{a}\right)$
	$\mathcal{F}\{f(-x)\} = F(-k)$
Shift Property	$\mathcal{F}\{f(x - x_0)\} = F(k)\mathrm{e}^{-ikx_0}$
Parseval's Theorem:	$\int_{-\infty}^{\infty} \lvert f(x)\rvert^2 \mathrm{d}x = \int_{-\infty}^{\infty} \lvert F(k)\rvert^2 \mathrm{d}k$
Uncertainty principle:	$\Delta x \Delta k \geq 1$
Repeated transforms:	$\mathcal{F}\mathcal{F}^{-1}\{f(x)\} = \mathcal{F}^{-1}\mathcal{F}\{f(x)\} = f(x)$
	$\mathcal{F}\mathcal{F}\{f(x)\} = f(-x)$

2.1.6 Convolution and Correlation

Another important result is the convolution theorem,

$$\mathcal{F}\{f \odot g\} = \sqrt{2\pi} F\, G, \tag{2.12}$$

where the convolution of two functions is defined as

$$f \odot g(x) = \int \mathrm{d}x' f(x') g(x - x') = g \odot f(x). \tag{2.13}$$

In particular, the convolution of a function $g(x)$ with a delta function $\delta(x - x_0)$ located at $x = x_0$ copies the function to that location,

$$\delta(x - x_0) \odot g(x) = g(x - x_0). \tag{2.14}$$

Considering that any function $f(x)$ is a superposition of many delta functions with different amplitudes and positions, the convolution of $f(x)$ with a "spread function" $g(x)$ is simply a similar superposition of many copies of $g(x)$ with corresponding amplitudes and positions. This is illustrated in Fig. 2.3, where the function $f(x)$ representing a pattern of point sources in the Big Dipper is convolved with the spread function $g(x)$ to yield the "image" that includes the effect of the spread function.

Relatedly, the cross-correlation of two functions is defined as

$$f \otimes g(x) = \int \mathrm{d}x' f(x') g^*(x' - x) = f(x) \odot g^*(-x) \tag{2.15}$$

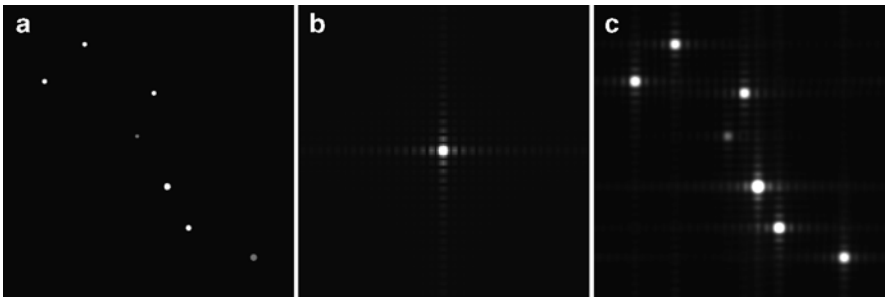

Fig. 2.3 Example of convolution. (**a**) Input image, (**b**) PSF, and (**c**) output image

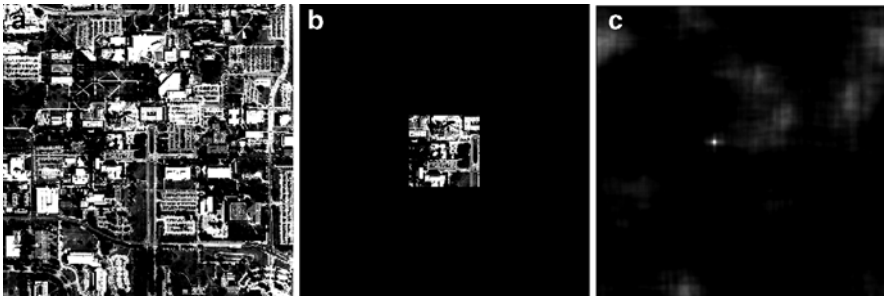

Fig. 2.4 Example of correlation. (**a**) Input image, (**b**) search image, and (**c**) result

and one can also write

$$\mathfrak{F}\{f \otimes g\} = \sqrt{2\pi} F\, G^* \tag{2.16}$$

In particular, the correlation of a function with itself is called the auto-correlation,

$$f \otimes f(x) = \int \mathrm{d}x' f(x') f^*(x' - x). \tag{2.17}$$

It is clear that if the function $f(x)$ is highly random, then $f \otimes f(0) = \int \mathrm{d}x' |f(x')|^2$, while for $x \neq 0, f \otimes f(x) \approx 0$. If $g(x)$ is a shifted copy or partial copy of $f(x)$, then the cross-correlation has a large peak corresponding to the shift, which is the basis of pattern recognition by cross-correlation. In Fig. 2.4, the cross-correlation of the

map of the University of South Florida with a small area from it identifies the location of the Physics building. Roughly speaking, the lateral size of the correlation peak indicates the distance beyond which the randomness sets in.

2.1.7 Some Useful Formulas

Here we list some of the useful formulas that may come in handy throughout the discussions of diffraction and Fourier optics. Delta functions have numerous representations, including

$$\begin{aligned}
\delta(x-x_0) &= \lim_{a\to 0}\frac{1}{\pi}\frac{a}{x^2+a^2},\\
\delta(x-x_0) &= \lim_{a\to 0}\frac{1}{\sqrt{\pi}a}\exp\left[-\frac{(x-x_0)^2}{a^2}\right],\\
\delta(x-x_0) &= \lim_{a\to 0}\frac{1}{\pi a}\mathrm{sinc}\left(\frac{x-x_0}{a}\right),\\
\delta(x-x_0) &= \frac{1}{2\pi}\int \mathrm{d}k\exp[ik(x-x_0)],\\
\delta(\mathbf{r}-\mathbf{r}_0) &= \frac{1}{(2\pi)^3}\int \mathrm{d}^3k\exp[i\mathbf{k}\bullet(\mathbf{r}-\mathbf{r}_0)].
\end{aligned} \tag{2.18}$$

Note that the delta function in N-dimension has the dimensions of $(\text{length})^{-N}$.

The Gaussian integrals are needed frequently:

$$\int_{-\infty}^{\infty}\exp\left(-px^2\right)\mathrm{d}x = \sqrt{\frac{\pi}{p}}, \tag{2.19}$$

$$\int_{-\infty}^{\infty}\exp\left(-px^2+qx\right)\mathrm{d}x = \sqrt{\frac{\pi}{p}}\exp\left(\frac{q^2}{4p}\right), \tag{2.20}$$

which are valid for any complex number p whose real part is nonnegative, $\mathrm{Re}\{p\}\geq 0$. And finally,

$$\int_{-\infty}^{\infty}\mathrm{sinc}(ax)\mathrm{d}x = \frac{\pi}{a}, \tag{2.21}$$

$$\int_{-\infty}^{\infty}\frac{1}{x^2+a^2}\mathrm{d}x = \frac{\pi}{a}. \tag{2.22}$$

2.2 Scalar Diffraction Theory

The theory of propagation and diffraction of electromagnetic fields has a long history of development and has many subtleties that need to be considered carefully in order to arrive at accurate and consistent results [2]. In-depth discussions can be found in a number of authoritative textbooks such as [3, 4]. Here we take a practical approach and take the Fresnel–Kirchoff diffraction formula as the starting point, which is known to yield highly accurate results for a wide range of configurations. Referring to Fig. 2.5, a spherical wave from the point source at S illuminates the aperture Σ:

$$E_\Sigma = E_S \frac{\exp[i(kr' - \omega t)]}{kr'}. \tag{2.23}$$

The field at a point P behind the aperture is then given by

$$E_P = -\frac{i}{4\pi} E_S e^{-i\omega t} \int_\Sigma d\Sigma \frac{\exp[ik(r + r')]}{rr'} \left(\hat{\mathbf{r}} - \hat{\mathbf{r}'}\right) \bullet \hat{\mathbf{n}}, \tag{2.24}$$

where the carets (^) represent unit vectors along the relevant directions. This expression can be interpreted in terms of Huygens principle [2, 5], where the field at a point in the aperture gives rise to a secondary spherical wavelet proportional to

$$-i \frac{\exp(ikr)}{4\pi r} \left(\hat{\mathbf{r}} - \hat{\mathbf{r}'}\right) \bullet \hat{\mathbf{n}}. \tag{2.25}$$

The obliquity factor $\frac{1}{2}\left(\hat{\mathbf{r}} - \hat{\mathbf{r}'}\right) \bullet \hat{\mathbf{n}}$ becomes $\hat{\mathbf{r}} \bullet \hat{\mathbf{n}}$ or $-\hat{\mathbf{r}'} \bullet \hat{\mathbf{n}}$ in Rayleigh–Sommerfeld theory, depending on the boundary conditions imposed on the screen Σ. When the propagation is paraxial, the obliquity factor becomes close to unity in all three cases, which we take to be the case. The field at the observation point P is then

$$E_P = -\frac{i}{2\pi} \int_\Sigma d\Sigma E_\Sigma \frac{\exp(ikr)}{r}. \tag{2.26}$$

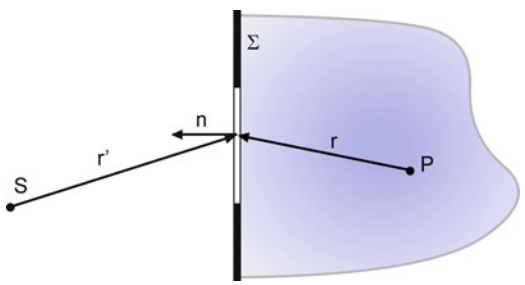

Fig. 2.5 Geometry of Fresnel–Kirchoff diffraction formula. *S* Source point, *P* observation point

2.3 Diffraction from a 2D Aperture

To be more specific, we consider the geometry of Fig. 2.6, where the input field $E_0(x_0, y_0)$ on the input plane Σ_0 propagates along the general z-direction and results in the output field $E(x, y; z)$ on the output plane Σ. Then (2.26) is written as

$$\begin{aligned} E(x, y; z) &= -\frac{ik}{2\pi} \iint_{\Sigma_0} \mathrm{d}x_0 \mathrm{d}y_0 E_0(x_0, y_0) \frac{\exp(ikr)}{r}, \\ &= -\frac{ik}{2\pi z} \iint_{\Sigma_0} \mathrm{d}x_0 \mathrm{d}y_0 E_0(x_0, y_0) \exp\left[ik\sqrt{(x - x_0)^2 + (y - y_0)^2 + z^2}\right], \end{aligned} \tag{2.27}$$

where we made a further approximation of $r \approx z$ in the denominator, but not in the exponent. This integral is a convolution

$$E(x, y; z) = E_0 \odot S_{\mathrm{H}} \tag{2.28}$$

with the kernel

$$S_{\mathrm{H}}(x, y; z) = -\frac{ik}{2\pi z} \exp\left[ik\sqrt{x^2 + y^2 + z^2}\right], \tag{2.29}$$

which is also referred to as the point spread function (PSF). (More precisely, this is a coherent spread function.) We will refer to this as the Huygens PSF, as far as the integral representing the Huygens spherical wavelet propagation.

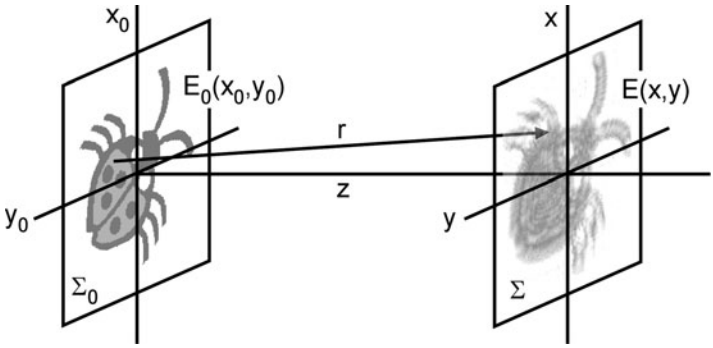

Fig. 2.6 Geometry of diffraction from a 2D aperture

2.3.1 Paraxial (Fresnel) Approximation

For theoretical developments and other purposes, it is often useful to make paraxial, or Fresnel, approximation of the PSF

$$r = \sqrt{(x-x_0)^2 + (y-y_0)^2 + z^2} \approx z + \frac{(x-x_0)^2 + (y-y_0)^2}{2z}, \tag{2.30}$$

which is valid for $z^3 \gg \frac{k}{8}\left[(x-x_0)^2 + (y-y_0)^2\right]^2_{\max}$. Then the Fresnel PSF is

$$S_{\mathrm{F}}(x,y;z) = -\frac{ik}{2\pi z}\exp(ikz)\exp\left[\frac{ik}{2z}\left(x^2+y^2\right)\right], \tag{2.31}$$

where the spherical wavefront is approximated with a parabolic wavefront, or a 2D chirp function. The diffraction field is expressed with a single Fourier transform of spatial frequencies

$$k_x = k\frac{x}{z}; \quad k_y = k\frac{y}{z}. \tag{2.32}$$

Thus

$$\begin{aligned} E(x,y;z) &= -\frac{ik}{2\pi z}\exp(ikz)\iint\limits_{\Sigma_0} \mathrm{d}x_0\mathrm{d}y_0 E_0(x_0,y_0)\exp\left\{\frac{ik}{2z}\left[(x-x_0)^2+(y-y_0)^2\right]\right\}, \\ &= -\frac{ik}{2\pi z}\exp(ikz)\exp\left[\frac{ik}{2z}\left(x^2+y^2\right)\right] \\ &\quad\times\iint\limits_{\Sigma_0}\mathrm{d}x_0\mathrm{d}y_0 E_0(x_0,y_0)\exp\left[\frac{ik}{2z}\left(x_0^2+y_0^2\right)\right]\exp\left[-\frac{ik}{z}(xx_0+yy_0)\right], \\ &= -\frac{ik}{z}\exp(ikz)\exp\left[\frac{ik}{2z}\left(x^2+y^2\right)\right]\mathfrak{F}\left\{E_0(x_0,y_0)\exp\left[\frac{ik}{2z}\left(x_0^2+y_0^2\right)\right]\right\}\left[k_x,k_y\right] \end{aligned} \tag{2.33}$$

or

$$E(x,y;z) = 2\pi\exp\left[\frac{ik}{2z}\left(x^2+y^2\right)\right]\mathfrak{F}\{E_0(x_0,y_0)\,S_{\mathrm{F}}(x_0,y_0;z)\}\left[k_x,k_y\right]. \tag{2.34}$$

This is also referred to as the Fresnel transform.

2.3.2 *Fraunhofer Diffraction*

If we make further approximation and ignore terms of order $\frac{x_0^2+y_0^2}{z^2} \ll 1$ to write

$$r \approx z + \frac{x^2+y^2}{2z} - \frac{xx_0+yy_0}{z}, \tag{2.35}$$

then the output field is proportional to the Fourier transform of the input field:

$$\begin{aligned} E(x,y;z) &= -\frac{ik}{2\pi z}\exp(ikz)\exp\left[\frac{ik}{2z}\left(x^2+y^2\right)\right]\iint\limits_{\Sigma_0} \mathrm{d}x_0\mathrm{d}y_0\, E_0(x_0,y_0)\exp\left[-\frac{ik}{z}(xx_0+yy_0)\right], \\ &= -\frac{ik}{z}\exp(ikz)\exp\left[\frac{ik}{2z}\left(x^2+y^2\right)\right]\mathfrak{F}\{E_0(x_0,y_0)\}\left[k_x,k_y\right]. \end{aligned} \tag{2.36}$$

Therefore, for example, the Fraunhofer diffraction pattern of a rectangular aperture is a sinc function and for a circular aperture it is an Airy disk pattern, as is well known.

2.4 Propagation of Angular Spectrum

An alternative approach to describing the diffraction is given by the angular spectrum or the plane-wave decomposition. Analytically, the angular spectrum approach is shown to be equivalent to the Huygens convolution described above. On the other hand, the angular spectrum picture has the advantage of being more intuitive and free from some of the subtle difficulties of boundary conditions. It also leads to a more robust and trouble-free numerical calculations of diffraction, as we will see in later chapters.

Given an input field $E_0(x_0,y_0)$, its Fourier transform

$$A_0\left(k_x,k_y\right) = \mathfrak{F}\{E_0\} = \frac{1}{2\pi}\iint\limits_{\Sigma_0}\mathrm{d}x_0\mathrm{d}y_0 E_0(x_0,y_0)\exp\left[-i\left(k_xx_0+k_yy_0\right)\right] \tag{2.37}$$

describes the amplitudes of various plane-wave components that comprise the input pattern, according to the basic principle of Fourier transform, depicted in Fig. 2.7. The input field $E_0(x_0,y_0)$ is of course the inverse Fourier transform of the angular spectrum:

$$E_0(x_0,y_0) = \mathfrak{F}^{-1}\{A_0\} = \frac{1}{2\pi}\iint \mathrm{d}k_x\mathrm{d}k_y A_0\left(k_x,k_y\right)\exp\left[i\left(k_xx_0+k_yy_0\right)\right]. \tag{2.38}$$

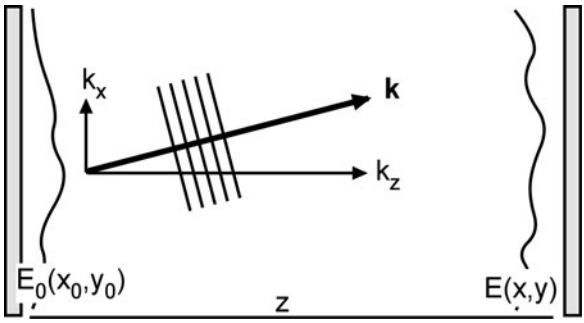

Fig. 2.7 Propagation of a plane-wave component in the angular spectrum

The complex exponential $\exp\left[i\left(k_x x_0 + k_y y_0\right)\right]$ is the projection on the (x_0, y_0)-plane of a plane wave propagating along the wave vector $\mathbf{k} = \left(k_x, k_y, k_z\right)$, where

$$k_z = \sqrt{k^2 - k_x^2 - k_y^2}. \tag{2.39}$$

Thus the input field $E_0(x_0, y_0)$ can be viewed as a projection of many plane-wave components propagating in various directions $\mathbf{k} = \left(k_x, k_y, k_z\right)$, with complex amplitude of each component given by $A_0\left(k_x, k_y\right)$. After propagation over a distance z, each plane-wave component acquires a phase factor $\exp(ik_z z)$, so that the output field is given by

$$E(x, y; z) = \frac{1}{2\pi} \iint\limits_{\Sigma_0} \mathrm{d}k_x \mathrm{d}k_y A_0\left(k_x, k_y\right) \exp\left[i\left(k_x x + k_y y + k_z z\right)\right], \tag{2.40}$$

which is an inverse Fourier transform of $A_0\left(k_x, k_y\right) \exp(ik_z z)$:

$$\begin{aligned} E(x, y; z) &= \mathfrak{F}^{-1}\left\{A_0\left(k_x, k_y\right) \exp\left[i\sqrt{k^2 - {k_x}^2 - {k_y}^2}\, z\right]\right\}[x, y], \\ &= \mathfrak{F}^{-1}\left\{\mathfrak{F}\{E_0\} \exp\left[i\sqrt{k^2 - {k_x}^2 - {k_y}^2}\, z\right]\right\}. \end{aligned} \tag{2.41}$$

One can make several observations here. First, the square root factor in the exponent requires that

$${k_x}^2 + {k_y}^2 \leqslant k^2. \tag{2.42}$$

That is, the diffraction imposes a low-pass filtering of the input spatial frequencies. Input spatial structures finer than the wavelength do not propagate to far field. Only near field probes can access such evanescent field. Second, note that the

description is based only on the fundamental properties of Fourier transform, without having to invoke particular boundary conditions. Third, the physical picture of diffraction is constructed from a set of plane waves, which by definition is well-behaved everywhere in space. On the other hand, the Huygens principle and Rayleigh–Sommerfeld theory are all built up from the behavior of spherical waves of point sources, which inherently involves singularities at the point sources. Note the factor $r \approx z$ in the denominator of (2.34), whereas the angular spectrum result (2.41) does not have such factor. These observations have important consequences when we discretize the integrals for numerical calculation of the diffraction in Chap. 4.

Still, the angular spectrum result is equivalent to the convolution result, as shown in [6]. First, expand the expressions for the Fourier and inverse transforms in (2.41)

$$\begin{aligned} E(x,y;z) &= \frac{1}{(2\pi)^2} \iint_{\Sigma_0} \mathrm{d}x_0 \mathrm{d}y_0 E_0(x_0,y_0) \iint_{\Sigma_0} \mathrm{d}k_x \mathrm{d}k_y \exp i\left[k_x(x-x_0)+k_y(y-y_0)\right] \\ &\qquad \exp\left(i\sqrt{k^2-{k_x}^2-{k_y}^2}z\right), \\ &= \frac{1}{2\pi} \iint_{\Sigma_0} \mathrm{d}x_0 \mathrm{d}y_0 E_0(x_0,y_0) \mathfrak{F}^{-1}\left\{\exp\left[i\sqrt{k^2-{k_x}^2-{k_y}^2}z\right]\right\}[x-x_0, y-y_0]. \end{aligned} \tag{2.43}$$

Noting the following Fourier transform

$$\mathfrak{F}\left\{\exp\left[ik\sqrt{x^2+y^2+z^2}\right]\right\}[k_x,k_y] = \frac{iz}{k}\exp\left[i\sqrt{k^2-{k_x}^2-{k_y}^2}z\right], \tag{2.44}$$

(2.41) is indeed seen to be the Huygens convolution,

$$E(x,y;z) = E_0 \odot S_{\mathrm{H}}. \tag{2.45}$$

If we take the paraxial approximation

$$k_z \approx k - \frac{{k_x}^2+{k_y}^2}{2k}, \tag{2.46}$$

then

$$\begin{aligned} E(x,y;z) &= \exp(ikz)\mathfrak{F}^{-1}\left\{\mathfrak{F}\{E_0\}\exp\left[-i\frac{{k_x}^2+{k_y}^2}{2k}z\right]\right\}, \\ &= E_0 \odot S_{\mathrm{F}}. \end{aligned} \tag{2.47}$$

Obviously, the angular spectrum method under paraxial approximation is equivalent to the Fresnel transform as well.

2.5 Propagation Through a Lens

We now describe the propagation of an optical field through a lens. We use the paraxial approximation and Fresnel transform expression of diffraction, which allow us to describe the process in closed analytical forms. For a thin lens of focal length f, its effect is to introduce a quadratic phase in the transmitted optical field (Fig. 2.8),

$$E'(x,y) = E(x,y)\exp\left[-\frac{ik}{2f}\left(x^2+y^2\right)\right] = E(x,y)\psi_f(x,y). \tag{2.48}$$

Refer to Fig. 2.9 and consider the propagation of light from the input plane, Σ_0, to the output plane, Σ_1, through the lens at Σ'-plane. The three planes Σ_0, Σ', and Σ_1 are positioned at $z = 0$, z_0, and $z_0 + z_1$, respectively. The input field is $E_0(x_0, y_0)$. The field at the entrance pupil of the lens is the Fresnel transform of the input field over a distance z_0

$$E'(x',y') = -\frac{ik}{2\pi z_0}\exp(ikz_0)\iint_{\Sigma_0} \mathrm{d}x_0\mathrm{d}y_0 E_0(x_0,y_0)\exp\left\{\frac{ik}{2z_0}\left[(x'-x_0)^2+(y'-y_0)^2\right]\right\}. \tag{2.49}$$

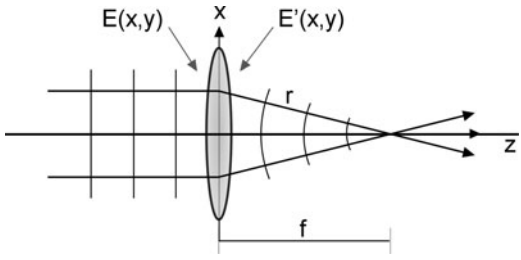

Fig. 2.8 Transmission through a thin lens

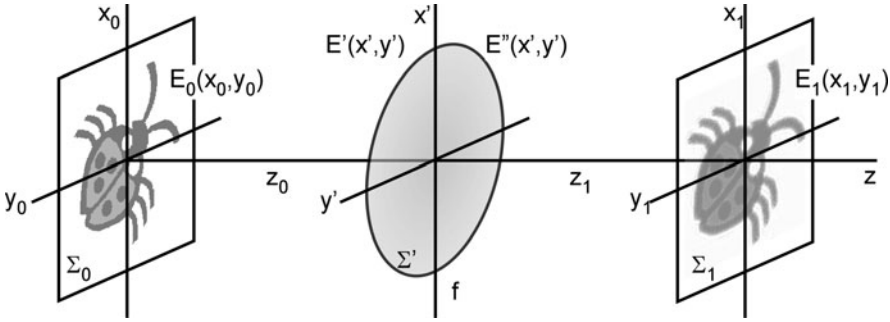

Fig. 2.9 Geometry of imaging by a lens

To save space, here and occasionally elsewhere, we will abbreviate all (x, y) terms with (x) expressions only – the missing (y) terms should be clear from the context. For example, (2.49) is abbreviated as

$$E'(x', y') = -\frac{ik}{2\pi z_0} \exp(ikz_0) \iint_{\Sigma_0} \mathrm{d}x_0 E_0(x_0) \exp\left[\frac{ik}{2z_0}(x' - x_0)^2\right]. \tag{2.50}$$

The field at the exit pupil of the lens becomes

$$E''(x', y') = -\frac{ik}{2\pi z_0} \exp(ikz_0) \exp\left(-\frac{ik}{2f}x'^2\right) \iint_{\Sigma_0} \mathrm{d}x_0 E_0(x_0) \exp\left[\frac{ik}{2z_0}(x' - x_0)^2\right]. \tag{2.51}$$

Further propagation over the distance z_1 yields the output field

$$\begin{aligned}
E_1(x_1, y_1) &= -\frac{k^2}{4\pi^2 z_0 z_1} \exp[ik(z_0 + z_1)] \iint_{\Sigma_0} \mathrm{d}x_0 E_0(x_0) \\
&\quad \times \iint_{\Sigma'} \mathrm{d}x' \exp\left[\frac{ik}{2z_0}(x' - x_0)^2 - \frac{ik}{2f}x'^2 + \frac{ik}{2z_1}(x_1 - x')^2\right], \\
&= -\frac{k^2}{4\pi^2 z_0 z_1} \exp[ik(z_0 + z_1)] \exp\left(\frac{ik}{2z_1}x_1^2\right) \iint_{\Sigma_0} \mathrm{d}x_0 E_0(x_0) \exp\left(\frac{ik}{2z_0}x_0^2\right) \\
&\quad \times \iint_{\Sigma'} \mathrm{d}x' \exp\left[\frac{ik}{2q}x'^2 - ik\left(\frac{x_0}{z_0} + \frac{x_1}{z_1}\right)x'\right], \\
&= -\frac{ik}{2\pi z'} \exp[ik(z_0 + z_1)] \exp\left(\frac{ik}{2z_1}x_1^2\right) \iint_{\Sigma_0} \mathrm{d}x_0 E_0(x_0) \exp\left(\frac{ik}{2z'_0}x_0^2 - \frac{ikx_1}{z'}x_0\right),
\end{aligned} \tag{2.52}$$

where

$$\begin{cases}
\dfrac{1}{q} = \dfrac{1}{z_0} - \dfrac{1}{f} + \dfrac{1}{z_1}, \\
z' = \dfrac{z_0 z_1}{q} = z_0 + z_1 - \dfrac{z_0 z_1}{f}, \\
z'_0 = \dfrac{z_0^2}{z_0 - q}, \\
z'_1 = \dfrac{z_1^2}{z_1 - q}.
\end{cases} \tag{2.53}$$

One may note some similarity and difference with the Fresnel diffraction (2.33). We can use (2.52) to derive some of the familiar properties of the lens.

2.5.1 Fourier Transform by a Lens

Let $z_1 = f$. Then $q = z_0$ and $z_0' \to \infty$, so that

$$E_1(x_1, y_1) = -\frac{ik}{f} \exp[ik(z_0 + f)] \exp\left[\frac{ik}{2z'_1} x_1^2\right] \mathfrak{F}\{E_0(x_0)\}[k_x] \tag{2.54}$$

with $k_x = \dfrac{kx_1}{f}$ and $k_y = \dfrac{ky_1}{f}$. If, further, $z_0 = z_1 = f$, then

$$E_1(x_1, y_1) = -\frac{ik}{f} \exp(2ikf) \mathfrak{F}\{E_0(x_0)\}[k_x] \tag{2.55}$$

and the fields at the two focal planes are Fourier transform of each other.

2.5.2 Imaging by a Lens

If $1/q = (1/z_0) + (1/z_1) - (1/f) = 0$, then re-evaluate the integrals in the second line of (2.51) as

$$\begin{aligned}
E_1(x_1, y_1) &= -\frac{k^2}{4\pi^2 z_0 z_1} \exp[ik(z_0 + z_1)] \exp\left(\frac{ik}{2z_1} x_1^2\right) \iint\limits_{\Sigma_0} \mathrm{d}x_0 E_0(x_0) \exp\left(\frac{ik}{2z_0} x_0^2\right) \\
&\quad \times \iint\limits_{\Sigma'} \mathrm{d}x' \exp\left[-ik\left(\frac{x_0}{z_0} + \frac{x_1}{z_1}\right)x'\right], \\
&= -\frac{z_0}{z_1} \exp[ik(z_0 + z_1)] \exp\left(\frac{ik}{2z_1} x_1^2\right) \\
&\quad \times \iint\limits_{\Sigma_0} \mathrm{d}x_0 E_0(x_0) \exp\left(\frac{ik}{2z_0} x_0^2\right) \delta\left(x_0 + \frac{z_0}{z_1} x_1\right), \\
&= -\frac{z_0}{z_1} \exp[ik(z_0 + z_1)] \exp\left(\frac{ik}{2f} \frac{z_0}{z_1} x_1^2\right) E_0\left(-\frac{z_0}{z_1} x_1\right).
\end{aligned} \tag{2.56}$$

This expression accounts for the amplitude scaling $(-z_0/z_1)$ and the image inversion and magnification $E_0(-(z_0/z_1)x_1)$. The lateral magnification is $M_x \equiv -\frac{z_1}{z_0}$. The quadratic phase term is due to the fact that the object Σ_0 and image Σ_1 planes are not spherical from the center of the lens.

2.5.3 Lens of Finite Aperture

If the finite aperture of the lens or presence of aberrations is represented with an aperture amplitude function $A(x', y')$, so that ψ_f is replaced with $A\psi_f$ in (2.48), then, at the image position where $\frac{1}{q} = 0$,

$$\begin{aligned}
E_1(x_1, y_1) &= -\frac{k^2}{4\pi^2 z_0 z_1}\left\{\exp[ik(z_0+z_1)]\exp\left(\frac{ik}{2z_1}{x_1}^2\right)\right\} \\
&\quad\times \iint\limits_{\Sigma_0} \mathrm{d}x_0 E_0(x_0)\exp\left(\frac{ik}{2z_0}{x_0}^2\right)\iint\limits_{\Sigma'}\mathrm{d}x' A(x')\exp\left[-ik\left(\frac{x_0}{z_0}+\frac{x_1}{z_1}\right)x'\right], \\
&= -\frac{k^2}{2\pi z_0 z_1}\{\cdots\}\iint\limits_{\Sigma_0}\mathrm{d}x_0\, E_0(x_0)\exp\left(\frac{ik}{2z_0}{x_0}^2\right)\mathfrak{F}\{A\}\left[\frac{k}{z_0}(x_0-\tilde{x}_1)\right], \\
&= \frac{k^2}{2\pi z_0 z_1}\{\cdots\}\left\{E_0(\tilde{x}_1)\exp\left(\frac{ik}{2z_0}{\tilde{x}_1}^2\right)\right\}\odot\mathfrak{F}\{A\}\left[-\frac{k}{z_0}\tilde{x}_1\right], \\
&= \frac{k^2}{2\pi z_0 z_1}\exp[ik(z_0+z_1)]\exp\left(\frac{ik}{2z_1}{x_1}^2\right) \\
&\quad\times\left\{E_0\left(-\frac{z_0}{z_1}x_1\right)\exp\left(\frac{ik}{2z_1}\frac{z_0}{z_1}x_1^2\right)\right\}\odot\mathfrak{F}\{A\}\left[\frac{k}{z_1}x_1\right],
\end{aligned} \tag{2.57}$$

where

$$\tilde{x}_0 \equiv -\frac{z_1}{z_0}x_0; \quad \tilde{x}_1 \equiv -\frac{z_0}{z_1}x_1. \tag{2.58}$$

That is, the image is convolved (i.e., smoothed) with the Fourier transform of the aperture function.

References

1. J. Goodman, *Introduction to Fourier optics* (Roberts & Co., 2005).
2. D. A. B. Miller, "Huygens's wave propagation principle corrected," Opt. Lett. **16**, 1370–1372 (1991).
3. M. Born, and E. Wolf, *Principles of Optics* (Cambridge University Press, Cambridge, 1999).
4. J. W. Goodman, *Introduction to Fourier Optics, 2 ed.* (McGraw Hill, Boston, 1996).
5. F. Depasse, M. A. Paesler, D. Courjon, and J. M. Vigoureux, "Huygens-Fresnel principle in the near field," Opt. Lett. **20**, 234–236 (1995).
6. G. C. Sherman, "Application of Convolution Theorem to Rayleighs Integral Formulas," Journal of the Optical Society of America **57**, 546–547 (1967).

Chapter 3
Principles of Holography

3.1 Introduction

The basic principle of holography consists of the recording of the hologram by interference between the object wave and the reference wave followed by the diffraction and propagation of another reference wave resulting in the formation of the holographic image. This is illustrated with two elementary holograms: holography of plane waves and holography of point sources. Holography can be realized through a large range of materials and optical processes. A brief overview of the holographic processes is given below.

3.2 Basic Concept

Figure 3.1 depicts general concepts of conventional and digital holography. Light reflected from, or transmitted through an object arrives at the hologram plane while another light wave, the reference, simultaneously illuminates the hologram plane. The superposition and interference of the two light waves result in fringe or speckle patterns, which are then recorded by an intensity-sensitive medium or device. The system may include other optical elements such as lenses and mirrors to manipulate magnifications and other parameters. The reference light may be a plane wave or spherical wave. Or it may be of more complicated structure, but a requirement is that it be of known or well-controlled structure, so that it may be replicated in the read process. To reconstruct or read the hologram, another reference wave illuminates the hologram, which then diffracts from the fringe or speckle patterns. One of the diffracted waves forms an image which reproduces the original object wave in both the amplitude and the phase. It is the reconstruction of the whole optical field, including the phase, that gives rise to a multitude of unique properties and applications of holography, in contrast to photography which can only reproduce the intensity.

M.K. Kim, *Digital Holographic Microscopy: Principles, Techniques, and Applications*, Springer Series in Optical Sciences 162,
DOI 10.1007/978-1-4419-7793-9_3, © Springer Science+Business Media, LLC 2011

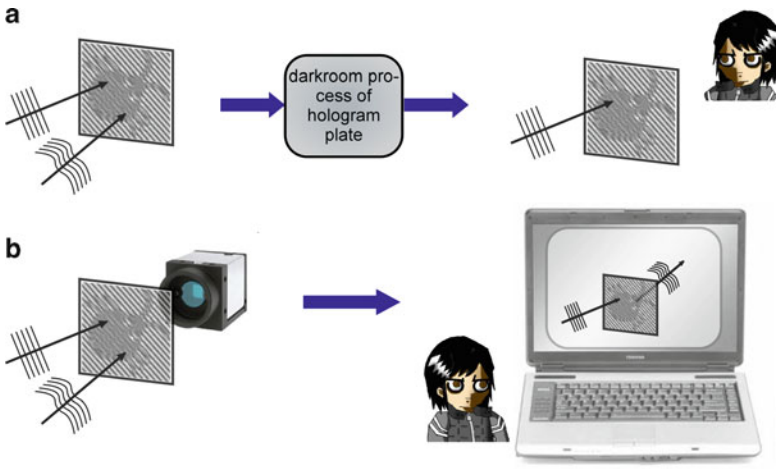

Fig. 3.1 Basic concept of (**a**) the conventional holography and (**b**) the digital holography

In the conventional real space holography (Fig. 3.1a), the hologram is recorded on a photographic plate or any other media whose optical transmission or reflection property changes in response to the light intensity impinging on it. Recording and reconstruction both take place in real space using real light and real optical components. On the other hand, propagation and diffraction of light is completely and accurately described by electromagnetic diffraction theory. Therefore, it is possible to simulate part or all of the holography process by numerical computation. In computer-generated holography (CGH), the hologram is calculated numerically inside a computer and the result is printed photographically or projected on an electronic device such as a spatial light modulator (SLM). Reconstruction then takes place in real space with real light. Conversely, in digital holography (DH) (Fig. 3.1b) the recording process is in real space, but the hologram is captured on an electronic camera, such as CCD or CMOS cameras, and transferred to a computer in a digital form. The reconstruction is carried out numerically inside the computer, whose result is displayed on the monitor or stored or output electronically for further processing and manipulation. Numerical processing of holograms in CGH and DH lead to a wide range of unique properties and capabilities [1, 2].

- In CGH, holograms can be produced of fictitious objects that are unlikely or impossible in real space, such as objects of unusual phase topology.
- Compared to photochemical recording, electronic recording by CCD or CMOS sensors is much faster, more controllable, and closer to linear sensitivity. It is also more economical in the long run by not requiring a dark room, chemical supplies, and the photo-processing labor.
- In DH, holograms can be processed in ways that are difficult or infeasible in real space, such as superposition of multiple holograms illuminated with different wavelengths.

- One of the most important distinctions of DH is the direct access to the phase of the optical field. The real space holography does reproduce the phase of the optical field, but it is not directly available to human observer or intensity-sensitive detectors until another interferometric experiment is carried out. On the other hand, in DH, the calculation of the optical field gives immediate access to an array of complex numbers that includes the phase information.
- An important issue is the resolution. Current electronic camera resolution, at several microns or more, is at least an order of magnitude lower than photographic media, and it will probably be some time before they become comparable. This does place a limitation on certain kinds of applications, such as holographic recording with parallax effect.

3.2.1 Holographic Terms

If the hologram plane is simultaneously illuminated with an object field E_O and reference field E_R, the resulting intensity is

$$I = |E_R + E_O|^2 = |E_R|^2 + |E_O|^2 + E_R{}^* E_O + E_R E_O{}^*. \tag{3.1}$$

The hologram is developed, photochemically or electronically, so that its amplitude transmittance is proportional to the intensity. For reconstruction, another reference field $E_R{}'$ illuminates the hologram, so that the transmitted light is

$$\begin{aligned} E &= E_R{}' I = E_R{}' |E_R + E_O|^2, \\ &= E_R{}' |E_R|^2 + E_R{}' |E_O|^2 + E_R{}' E_R{}^* E_O + E_R{}' E_R E_R{}^*. \end{aligned} \tag{3.2}$$

The first two terms are referred to as the zero-order terms and represent the noninterfering intensity patterns of the reference and object fields, separately. If the reference fields have no spatial structure, then the last two terms are proportional to the complex object field and its conjugate, and they are called the first-order twin-image terms. As shown in Fig. 3.2a, b, when the two reference waves E_R and $E_R{}'$ are from the same side of the hologram, one of the twin terms forms virtual orthoscopic image on the same side as the object, while the other forms real pseudoscopic image on the opposite side of the hologram. With the pseudoscopic image, what would be the front surface of the object appears farther away from the observer. If the two reference fields are opposite to each other (Fig. 3.2a, c) the virtual image behaves as a specular reflection with respect to the original object field, while the real image behaves as a phase conjugate reflection, forming the image at the exact location of the original object.

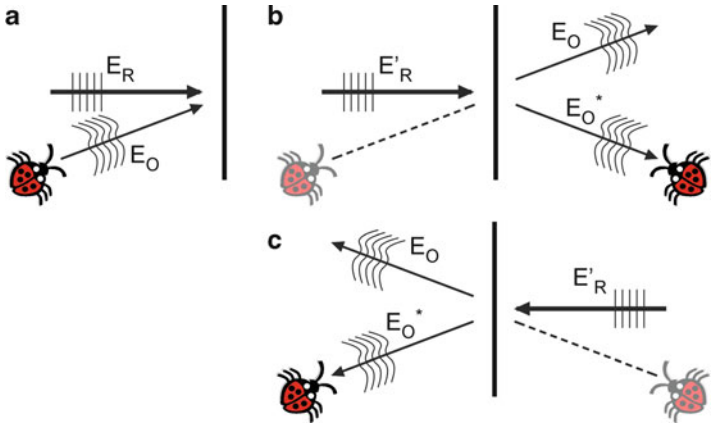

Fig. 3.2 Holographic terms for (**a**) hologram recording and (**b**) hologram reconstruction with the reference in the same direction as the recording or (**c**) in the opposite direction

3.3 Holography of Plane Waves

Now we consider two elementary processes of holographic image formation, namely holography of plane waves and of point sources. According to Fourier theory, an arbitrary wavefront can be analyzed as a superposition of many plane waves. Equally fundamental view of a wavefront is that it consists of many spherical wavefronts from point sources. First, let us consider holography by plane waves (Fig. 3.3). Suppose a plane wave E_1 is normally incident on the hologram plane at $z = 0$ and another plane wave E_2 is incident at an angle φ from the z-axis:

$$E_1 = \mathcal{E}_1 \exp(i\mathbf{k}_1 \bullet \mathbf{r}) = \mathcal{E}_1 \exp(ikz), \tag{3.3}$$

$$E_2 = \mathcal{E}_2 \exp(i\mathbf{k}_2 \bullet \mathbf{r}) = \mathcal{E}_2 \exp[ik(x \sin\varphi + z \cos\varphi)]. \tag{3.4}$$

The intensity distribution is

$$I_{12} = |E_1 + E_2|^2_{z=0} = |\mathcal{E}_1|^2 + |\mathcal{E}_2|^2 + 2\mathcal{E}_1\mathcal{E}_2 \cos(kx \sin\varphi), \tag{3.5}$$

which is a cosine grating pattern with a spatial frequency that depends on the relative direction of the incident plane waves. Assuming, as before, that the amplitude transmittance of the developed hologram is proportional to the intensity I_{12}, the hologram is illuminated with a third plane wave E_3 at an angle φ'

$$E_3 = \mathcal{E}_3 \exp(i\mathbf{k}_3 \bullet \mathbf{r}) = \mathcal{E}_3 \exp[ik'(x \sin\varphi' + z \cos\varphi')], \tag{3.6}$$

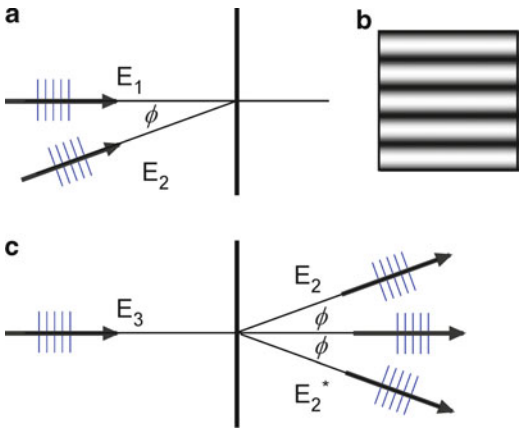

Fig. 3.3 Holography of plane waves. (**a**) Incident plane waves, (**b**) sine grating hologram, and (**c**) diffraction from the sine grating hologram

where we include the possibility of the wavelength being different from the first two waves. The lateral size of the hologram is a, and the Fraunhofer diffraction is calculated as

$$\begin{aligned}
E(\theta) &\propto \int_{-a/2}^{a/2} \mathrm{d}x I_{12} E_3(z=0) \exp(-ikx\sin\theta) \\
&= \int_{-a/2}^{a/2} \mathrm{d}x \Big\{ |\mathcal{E}_1|^2 + |\mathcal{E}_2|^2 + 2\mathcal{E}_1\mathcal{E}_2 \cos[kx\sin\varphi] \Big\} \mathcal{E}_3 \exp[ik'x(\sin\varphi' - \sin\theta)], \\
&= \left[|\mathcal{E}_1|^2 + |\mathcal{E}_2|^2 \right] \mathcal{E}_3 \, a\mathrm{sinc}\left[\frac{k'a}{2} (\sin\varphi' - \sin\theta) \right] \\
&\quad + \mathcal{E}_1\mathcal{E}_2\mathcal{E}_3 \, a\mathrm{sinc}\left[\frac{ka}{2}\sin\varphi - \frac{k'a}{2}(\sin\varphi' - \sin\theta) \right] \\
&\quad + \mathcal{E}_1\mathcal{E}_2\mathcal{E}_3 \, a\mathrm{sinc}\left[\frac{ka}{2}\sin\varphi + \frac{k'a}{2}(\sin\varphi' - \sin\theta) \right].
\end{aligned} \tag{3.7}$$

The characteristic sinc function behavior of finite aperture becomes delta function as the aperture, that is, the hologram size becomes infinite.

$$\begin{aligned}
E(\theta) \xrightarrow[a\to\infty]{} &\left[|\mathcal{E}_1|^2 + |\mathcal{E}_2|^2 \right] \mathcal{E}_3 \delta(\theta - \varphi') \\
&+ \mathcal{E}_1\mathcal{E}_2\mathcal{E}_3 [\delta(\theta + \mu\varphi - \varphi') + \delta(\theta - \mu\varphi - \varphi')],
\end{aligned} \tag{3.8}$$

where

$$\mu \equiv \frac{k}{k'} = \frac{\lambda'}{\lambda}. \tag{3.9}$$

The first term in these equations is the zero-order term, that represents the undiffracted reference wave propagating along the $\theta = \varphi'$ direction. The next two

terms are the first-order "twin-image" terms that propagate along the directions $\theta = \mp\mu\varphi + \varphi'$. For the case of $\varphi' = 0$, the twin images in the directions $\theta = \mp\mu\varphi$ represent the real and virtual images on either side of the hologram. The wavelength mismatch μ leads to rescaling of the image position and size.

3.4 Holography of Point Sources

Another important model of holographic image formation is that of point sources [3–6]. As depicted in Fig. 3.4, suppose two point sources $\mathcal{E}_1\delta(x - x_1, y - y_1, z - z_1)$ and $\mathcal{E}_2\delta(x - x_2, y - y_2, z - z_2)$ emit spherical waves toward the hologram plane $\mathcal{E}_0(x_0, y_0)$ at $z = 0$. Using Fresnel approximation, the fields at $z = 0$ are

$$E_1(x_0, y_0; z = 0) = \mathcal{E}_1 \exp\left\{-ikz_1 - \frac{ik}{2z_1}\left[(x_0 - x_1)^2 + (y_0 - y_1)^2\right]\right\}, \tag{3.10}$$

$$E_2(x_0, y_0; z = 0) = \mathcal{E}_2 \exp\left\{-ikz_2 - \frac{ik}{2z_2}\left[(x_0 - x_2)^2 + (y_0 - y_2)^2\right]\right\}. \tag{3.11}$$

The intensity on the hologram plane is, abbreviating all (x, y)-terms with (x)-terms only,

$$\begin{aligned} I_{12}(x_0, y_0) &= |E_1 + E_2|^2, \\ &= |\mathcal{E}_1|^2 + |\mathcal{E}_2|^2 + 2\mathcal{E}_1\mathcal{E}_2 \cos\left[k(z_1 - z_2) + \frac{k}{2z_1}(x_0 - x_1)^2 - \frac{k}{2z_2}(x_0 - x_2)^2\right], \\ &= |\mathcal{E}_1|^2 + |\mathcal{E}_2|^2 + 2\mathcal{E}_1\mathcal{E}_2 \cos\left[k\zeta_{12} + \frac{k}{2z_{12}}(x_0 - x_{12})^2\right], \end{aligned} \tag{3.12}$$

where

$$\begin{cases} \dfrac{1}{z_{12}} \equiv \dfrac{1}{z_1} - \dfrac{1}{z_2}, \\ x_{12} \equiv \dfrac{\dfrac{x_1}{z_1} + \dfrac{x_2}{z_2}}{\dfrac{1}{z_1} + \dfrac{1}{z_2}}, \\ \zeta_{12} \equiv (z_1 - z_2)\left[1 + \dfrac{1}{2}\dfrac{(x_1 - x_2)^2}{(z_1 + z_2)^2}\right]. \end{cases} \tag{3.13}$$

This is a Newton's ring or Fresnel zone pattern (FZP), which, as is well known, behaves like a lens. Illumination of the pattern with another point source $\mathcal{E}_3\delta(x - x_3, y - y_3, z - z_3)$, with a possibly different wavelength, then forms a

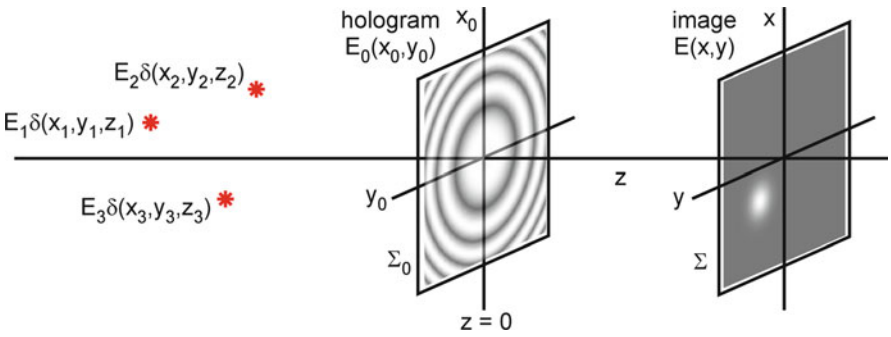

Fig. 3.4 Geometry for holography of point sources

focused image, as follows. The field from the third source arriving at the hologram plane is

$$E_3(x_0, y_0; z = 0) = \mathcal{E}_3 \exp\left\{-ik'z_3 - \frac{ik'}{2z_3}\left[(x_0 - x_3)^2 + (y_0 - y_3)^2\right]\right\}. \tag{3.14}$$

The optical field at another plane $\Sigma(x, y)$ at an arbitrary distance z is calculated using Fresnel diffraction formula. We calculate only the twin-image terms, that arise from

$$I_{12}^{\pm}(x_0, y_0) = \mathcal{E}_1\mathcal{E}_2 \exp\left[\pm ik\zeta_{12} \pm \frac{ik}{2z_{12}}(x_0 - x_{12})^2\right], \tag{3.15}$$

so that

$$\begin{aligned} E^{\pm}(x, y; z) &= -\frac{ik'}{2\pi z}\exp(ik'z)\iint_{\Sigma_0} \mathrm{d}x_0 I_{12}^{\pm}(x_0) E_3 \exp\left[\frac{ik'}{2z}(x - x_0)^2\right], \\ &= -\frac{ik'}{2\pi z}\mathcal{E}_1\mathcal{E}_2\mathcal{E}_3 \exp(\pm ik\zeta_{12} - ik'z_3 + ik'z) \\ &\quad \times \iint_{\Sigma_0} \mathrm{d}x_0 \exp\left[\pm\frac{ik}{2z_{12}}(x_0 - x_{12})^2 - \frac{ik'}{2z_3}(x_0 - x_3)^2 + \frac{ik'}{2z}(x_0 - x)^2\right]. \end{aligned} \tag{3.16}$$

After some algebraic effort, we obtain

$$E^{\pm}(x, y; z) = \alpha^{\pm}\mathcal{E}_1\mathcal{E}_2\mathcal{E}_3 \exp[\pm ik(z_1 - z_2) - ik'(z_3 - z)] \exp\left[\frac{ik'}{2}\frac{(x - X^{\pm})^2}{z - Z^{\pm}} + i\Phi^{\pm}\right], \tag{3.17}$$

where

$$\begin{cases} Z^{\pm} \equiv \dfrac{1}{\pm\mu\left(\dfrac{1}{z_1}-\dfrac{1}{z_2}\right)+\dfrac{1}{z_3}}, \\ X^{\pm} \equiv \left[\pm\mu\left(\dfrac{x_1}{z_1}-\dfrac{x_2}{z_2}\right)+\dfrac{x_3}{z_3}\right]Z^{\pm}, \\ \Phi^{\pm} \equiv \dfrac{k}{2}\left[\pm\mu\dfrac{(x_1-x_2)^2}{z_1z_2}+\dfrac{(x_2-x_3)^2}{z_2z_3}-\dfrac{(x_1-x_3)^2}{z_1z_3}\right]Z^{\pm}, \\ \alpha^{\pm} = \dfrac{1}{1-\dfrac{z}{Z^{\pm}}}. \end{cases} \tag{3.18}$$

The results show that the fields $E^{\pm}(x,y;z)$ are spherical waves centered at $(X^{\pm},Y^{\pm},Z^{\pm})$.

3.4.1 Magnifications

Various magnifications can be easily calculated. The lateral magnification is

$$M_x{}^{\pm} = \frac{\partial X^{\pm}}{\partial x_1} = \pm\mu\frac{Z^{\pm}}{z_1}, \tag{3.19}$$

the axial magnification is

$$M_z{}^{\pm} = \frac{\partial Z^{\pm}}{\partial z_1} = \pm\mu\frac{Z^{\pm 2}}{z_1^2} = \pm\frac{1}{\mu}M_x{}^{\pm 2}, \tag{3.20}$$

and the angular magnification is

$$M_{x/z}{}^{\pm} = \frac{\partial\left(X^{\pm}/Z^{\pm}\right)}{\partial(x_1/z_1)} = \pm\mu. \tag{3.21}$$

3.4.2 Collimated References

For the special case of collimated references, we take $z_2, z_3 \to \infty$, so that

$$\begin{cases} Z^{\pm} \equiv \pm z_1/\mu, \\ X^{\pm} \equiv x_1, \\ \Phi^{\pm} \equiv 0, \end{cases} \tag{3.22}$$

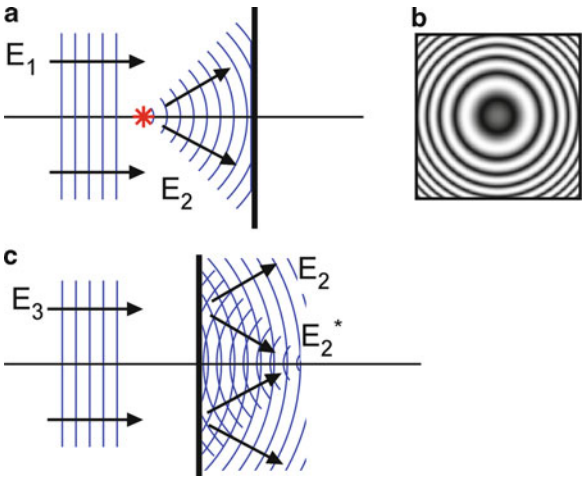

Fig. 3.5 Holography of a point source. (**a**) Incident plane and spherical waves, (**b**) Fresnel zone hologram, and (**c**) diffraction from the Fresnel zone hologram

and the magnifications are

$$\begin{cases} M_x{}^{\pm} = 1, \\ M_z{}^{\pm} = \pm 1/\mu\,, \\ M_{x/z}{}^{\pm} = \pm\mu. \end{cases} \tag{3.23}$$

As depicted in Fig. 3.5, the interference of a plane wave and a spherical wave results in a Fresnel zone pattern, which is a two-dimensional chirp function. As one moves out from the center, the local frequency of the fringes increases, so that the plane wave reference diffracts through increasingly larger angles, just like a lens. And the diffraction has components both toward and away from the center, as well as an undiffracted transmission. This hologram in effect behaves like a superposition of three "lenses" – a converging lens, a diverging lens, and a plane transmission.

3.5 Holographic Processes

There have been developed a wide range of processes and techniques developed for holography[7]. Holography also turns out to be a unifying principle of many different areas of nonlinear optics[8]. Here we list some of the main types and processes of holography.

3.5.1 Amplitude and Phase Holograms

The complex hologram transmission function may have amplitude or phase components, or both. Their behaviors may be illustrated with the Fraunhofer

diffraction from cosine amplitude or phase gratings. For a one-dimensional grating with spatial frequency β and amplitude modulation a, the transmission function is

$$T(x) = 1 + a\cos\beta x \tag{3.24}$$

The Fraunhofer diffraction from the grating is

$$E(k_x) \sim \int \mathrm{d}x T(x)\exp(-ik_x x) \sim \delta(k_x) + \frac{1}{2}\delta(k_x - \beta) + \frac{1}{2}\delta(k_x + \beta). \tag{3.25}$$

That is, the grating produces the zero-order and the twin images, as we have seen before. On the other hand, for a phase grating with the transmission function

$$T(x) = \exp[i\varphi_0 + i\varphi_1\cos(\beta x)] \sim \exp(i\varphi_0)\sum_n J_n(\varphi_1)\exp(in\beta x) \tag{3.26}$$

the Fraunhofer diffraction is

$$E(k_x) \sim \exp(i\varphi_0)\sum_n J_n(\varphi_1)\delta(k_x - n\beta) \tag{3.27}$$

and the phase grating produces many diffraction orders.

3.5.2 Transmission and Reflection Holograms

A hologram made of a photographic transparency is ordinarily a transmission hologram. It is also possible to set up a reflection hologram by arranging the object and reference waves to impinge from opposite sides of the film. The standing wave fringes parallel to the plane of the film surface, after proper treatment, act as reflecting surfaces. More general geometries of transmission and reflection holograms are possible with volume (thick) holograms.

3.5.3 Thin and Thick Holograms

So far we have assumed that the transmission is a two-dimensional function. On the other hand, the absorption, dispersion, and scattering properties may vary in a three-dimensional volume of a material, whose thickness is not negligible. Transmission of light through such a thick hologram, or a volume hologram, needs to take into

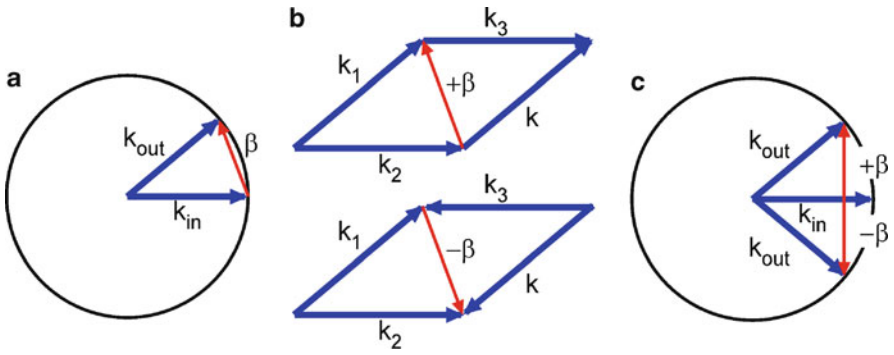

Fig. 3.6 Wave-vector matching. (**a**) Grating vector in volume hologram, and (**b**) diffraction from grating, and (**c**) grating vector in thin hologram

consideration the build-up of diffracted field and depletion of the undiffracted field. A main result of such a coupled wave theory is the requirement of wave-vector matching for Bragg diffraction. Suppose the volume hologram consists of a sinusoidal volume grating with a grating vector $\vec{\beta}$, then an incident plane wave with wave-vector $\mathbf{k}_{in}$ diffracts into the direction $\mathbf{k}_{out} = \mathbf{k}_{in} + \vec{\beta}$, while $|\mathbf{k}_{in}| = |\mathbf{k}_{out}| = k$, as depicted in Fig. 3.7a. Further suppose that the sinusoidal volume grating results from the interference of two plane waves with wave-vectors $\mathbf{k}_1$ and $\mathbf{k}_2$, so that $\vec{\beta} = \pm(\mathbf{k}_1 - \mathbf{k}_2)$. Then relabeling $\mathbf{k}_{in}$ and $\mathbf{k}_{out}$ as $\mathbf{k}_3$ and $\mathbf{k}$, respectively, we have

$$\mathbf{k} = \pm(\mathbf{k}_1 - \mathbf{k}_2) + \mathbf{k}_3, \tag{3.28}$$

with $|\mathbf{k}_1| = |\mathbf{k}_2| = |\mathbf{k}_3| = |\mathbf{k}| = k$. Thus the four-wave-vectors form a rhombus, as shown in Fig. 3.6b. In contrast, the wave-vector geometry of a thin hologram in Fig. 3.6c, shows that the wave-vector matching condition applies only to the component along the hologram plane.

3.5.4 Hologram Materials

A most commonly used material in conventional holography is the silver halide photographic emulsions. Other photochemical materials include dichromated gelatin, photoresists, photopolymers, photochromics, and photothermoplastics, which change absorption or refractive index as a function of local intensity of light. Typical resolution of these materials is better than 1 μm and required exposure is $10^{-2}\mathrm{J}/\mathrm{m}^2$, which corresponds to about 10^4 photons/$\mu\mathrm{m}^2$. Most of these materials require chemical or other processing to reveal the latent images.

3.5.5 Phase Conjugation by Photorefractive Crystals

Real-time hologram formation without processing is possible with photorefractive crystals, such as lithium niobate ($LiNbO_3$) and BSO ($Bi_{12}SiO_{20}$), where local intensity gradient causes charge migration and variation of local index of refraction, thus forming phase gratings. In (3.28), if we take two plane wave reference fields such that $\mathbf{k}_1 + \mathbf{k}_3 = 0$, then $\mathbf{k} = -\mathbf{k}_2$. This means that if $\mathbf{k}_2$ represents one of plane wave components of an object field, then each and every such wave-vector component is reversed, so that a real image forms at the exact position of the object. Furthermore, if the intensity of the reference $\mathbf{k}_3$ is very high, then it is possible that the image is higher in intensity than the object, which can have important and interesting applications [8].

3.5.6 Four-Wave Mixing

The index grating formation can also arise from third-order susceptibility $\chi^{(3)}$ of a material. From the definition of nonlinear susceptibility

$$P = \chi^{(1)}E + \chi^{(2)}E^2 + \chi^{(3)}E^3 + \cdots = \chi E \tag{3.29}$$

and dropping the second-order term for isotropic materials, the effective index of refraction can be written as

$$n' = \sqrt{1 + 4\pi\chi} \approx n\left[1 + \frac{2\pi\chi^{(3)}}{n^2}E^2\right]. \tag{3.30}$$

Intensity variation leads to variation of local refractive index. Propagation of the four-wave mixing signal follows the same wave-vector matching geometry of the thick hologram in (3.28). Four-wave mixing is a nearly instantaneous process for real-time holography [9].

3.5.7 Spectral Hole Burning

Inhomogeneous broadening of absorption spectrum such as in organic dye molecules and use of narrowband tunable laser allows recording of multiple holograms, or any optical information, at the same location. Saturation of a single channel with a narrowband laser results in bleaching and reduced absorption of the channel, as depicted in Fig. 3.7a. Each of such spectral hole represents a channel for storing

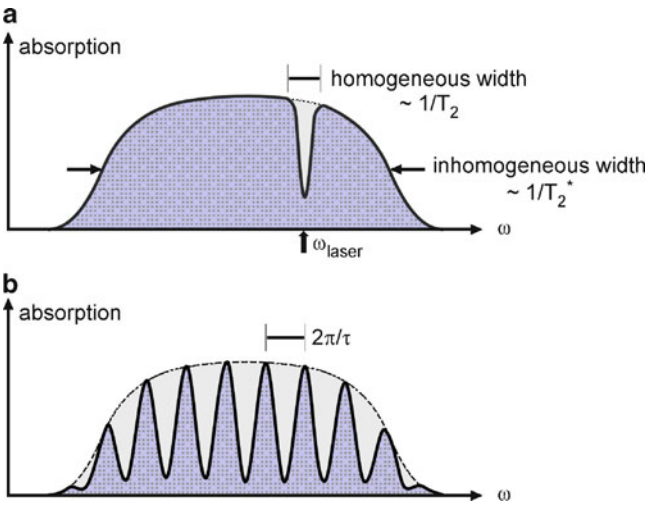

Fig. 3.7 Spectral hole burning by (**a**) a cw monochromatic laser and (**b**) two short pulses with a time delay, τ

information in the spectral domain. The volume of the spectral hole burning material can also be utilized for storing spatial information, such as holographic interference pattern. By repeating holographic image storage while stepping the laser wavelength, some thousands of holograms can be recorded in a single sample volume [10].

3.5.8 Stimulated Photon Echo

If, instead of using a narrowband cw laser, one uses a short-pulse laser, then its Fourier bandwidth may cover a substantial part of the absorption band. Further, if two such pulses are incident with a time delay τ, then it can be shown that the absorption spectrum acquires the shape of a cosine spectral grating with a period $2\pi/\tau$, as shown in Fig. 3.7b. The situation is analogous to the spatial cosine grating by interference of two plane waves, or Fourier transform of two point sources. In general, more complicated pulse shape results in the recording of its Fourier transform on the absorption spectrum. For reconstruction, excitation with another short pulse causes reemission of the original pulse shape, which is called the stimulated photon echo, depicted in Fig. 3.8. The delay time τ and the storage time T are constrained by the phase relaxation time T_2 and population relaxation time T_1, respectively. The spatial holography within the volume of the storage

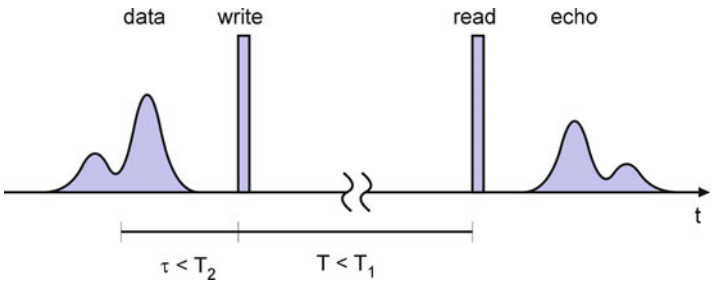

Fig. 3.8 Stimulated photon echo as a time-domain holography process

material proceeds in the same manner as any other holography processes. This completes the holographic processes for all four dimensions – space **k** • **r** and time ωt [11]. True four-dimensional holographic movies can be recorded [12].

References

1. T. Poon, ed. *Digital holography and three-dimensional display: principles and applications* (Springer, 2006).
2. M. K. Kim, "Principles and techniques of digital holographic microscopy," SPIE Reviews **1**, 1–50 (2010).
3. D. Gabor, "Microscopy by reconstructed wavefronts," Proc. Roy. Soc. **A197**, 454–487 (1949).
4. D. Gabor, "Microscopy by reconstructed wavefronts: II," Proc. Phys. Soc. **B64**, 449–469 (1951).
5. E. N. Leith, J. Upatnieks, and K. A. Haines, "Microscopy by wavefront reconstruction," J. Opt. Soc. Am. **55**, 981–986 (1965).
6. R. W. Meier, "Magnification and 3rd-Order Aberrations in Holography," Journal of the Optical Society of America **55**, 987–992 (1965).
7. P. Hariharan, *Optical Holography: Principles, Techniques, and Applications, 2 ed.* (Cambridge University Press, 1996).
8. R. A. Fisher, *Optical Phase Conjugation* (Elsevier, 1983).
9. A. Yariv, "Phase Conjugate Optics and Real-Time Holography," Ieee Journal of Quantum Electronics **14**, 650–660 (1978).
10. R. M. Shelby, J. A. Hoffnagle, G. W. Burr, C. M. Jefferson, M. P. Bernal, H. Coufal, R. K. Grygier, H. Gunther, R. M. Macfarlane, and G. T. Sincerbox, "Pixel-matched holographic data storage with megabit pages," Optics Letters **22**, 1509–1511 (1997).
11. X. A. Shen, A. D. Nguyen, J. W. Perry, D. L. Huestis, and R. Kachru, "Time-domain holographic digital memory," Science **278**, 96–100 (1997).
12. M. K. Kim, and R. Kachru, "Storage and Phase Conjugation of Multiple Images Using Backward-Stimulated Echoes in Pr-3+−Laf3," Optics Letters **12**, 593–595 (1987).

Chapter 4
Basic Methods of Numerical Diffraction

The basic methods of numerical diffraction are based on the Huygens convolution, the Fresnel transform, and the angular spectrum description of diffraction given in Chap. 2. Simulation examples are used to illustrate their general behaviors and to make comparisons regarding the advantages and limitations of these methods. The angular spectrum method is seen to have particular strength in that it yields reasonable results without minimum or maximum distance limits.

4.1 Discrete Fourier Transform

Referring to Fig. 4.1a, the Fourier transform of a function $f(x)$ is defined as

$$F(k) = \mathfrak{F}\{f(x)\}[k] = \frac{1}{\sqrt{2\pi}} \int_{-\infty}^{\infty} \mathrm{d}x f(x) \exp(-ikx). \tag{4.1}$$

The function is sampled by multiplying with a comb function of period δx,

$$\hat{f}(x) = f(x)\mathrm{comb}\left(\frac{x}{\delta x}\right) = f(x) \sum_{m=-\infty}^{\infty} \delta(x - m\delta x). \tag{4.2}$$

The Fourier transform of the sampled function is

$$\begin{aligned} \tilde{F}(k) &= \mathfrak{F}\{\hat{f}(x)\}[k] = \mathfrak{F}\left\{f(x)\mathrm{comb}\left(\frac{x}{\delta x}\right)\right\}[k], \\ &= \frac{1}{\delta x} F(k) \odot \mathrm{comb}\left(\frac{k}{K}\right), \\ &= \frac{1}{\delta x} \sum_{n=-\infty}^{\infty} F(k - nK), \end{aligned} \tag{4.3}$$

M.K. Kim, *Digital Holographic Microscopy: Principles, Techniques, and Applications*, Springer Series in Optical Sciences 162,
DOI 10.1007/978-1-4419-7793-9_4, © Springer Science+Business Media, LLC 2011

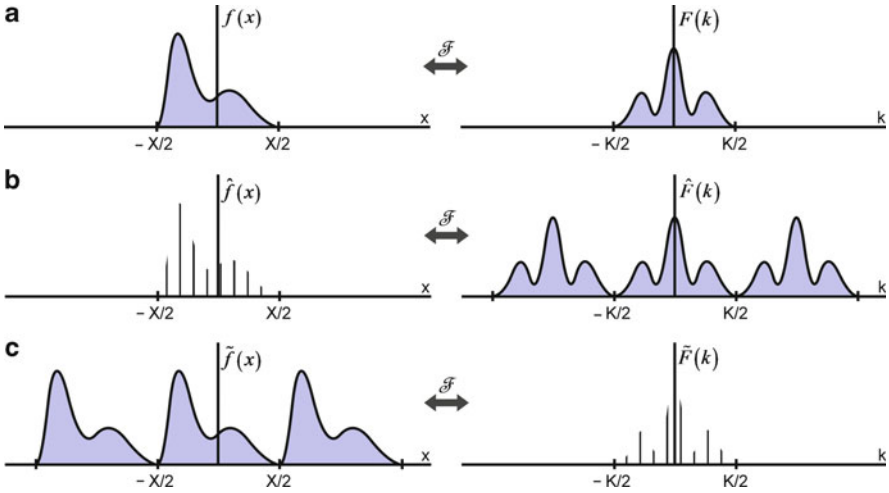

Fig. 4.1 (**a**) A spatial function and its Fourier transform, (**b**) a sampled spatial function and its Fourier transform, and (**c**) a sampled frequency spectrum and its inverse Fourier transform

where

$$K = \frac{2\pi}{\delta x}. \tag{4.4}$$

If $f(x)$ is band-limited, so that $F(k) = 0$ for $k \notin [-(K/2), (K/2)]$, then $\tilde{F}(k) = F(k)$ for $k \in [-(K/2), (K/2)]$. That is, $\tilde{F}(k)$ accurately represents $F(k)$ in that interval, as depicted in Fig. 4.1b.

Conversely, the spectrum $F(k)$ is sampled by multiplying with a comb function of period δk,

$$\hat{F}(k) = F(k)\mathrm{comb}\left(\frac{k}{\delta k}\right) = F(k)\sum_{n=-\infty}^{\infty}\delta(k - n\delta k). \tag{4.5}$$

The inverse Fourier transform of the sampled spectrum is

$$\begin{aligned}\tilde{f}(x) &= \mathfrak{F}^{-1}\{\hat{F}(k)\}[x] = \mathfrak{F}^{-1}\left\{F(k)\mathrm{comb}\left(\frac{k}{\delta k}\right)\right\}[x],\\ &= \frac{1}{\delta k}f(x) \odot \mathrm{comb}\left(\frac{x}{X}\right),\\ &= \frac{1}{\delta k}\sum_{m=-\infty}^{\infty} f(x - mX),\end{aligned} \tag{4.6}$$

where

$$X = \frac{2\pi}{\delta k}. \tag{4.7}$$

If $f(x)$ is space-limited, so that $f(x) = 0$ for $x \notin [-(X/2), (X/2)]$, then $\tilde{f}(x) = f(x)$ for $x \in [-(X/2), (X/2)]$. That is, $\tilde{f}(x)$ accurately represents $f(x)$ in that interval, as depicted in Fig. 4.1c.

If the function $f(x)$ is both space-limited and band-limited, then one can write the Fourier transform as a Fourier series, with $f_m \equiv \tilde{f}(x_m)$ and $F_n \equiv \tilde{F}(k_n)$

$$\begin{aligned}\tilde{F}(k_n) &= \frac{1}{\sqrt{2\pi}} \int_{-X/2}^{X/2} \mathrm{d}x f(x) \mathrm{comb}\left(\frac{x}{\delta x}\right) \exp(-ik_n x), \\ &= \frac{\delta x}{\sqrt{2\pi}} \sum_{m=-M/2}^{M/2} f(x_m) \exp(-ik_n x_m), \\ &= F_n,\end{aligned} \tag{4.8}$$

where

$$\begin{cases} x_m = m\delta x \quad (m = -M/2, -M/2+1, \ldots, M/2-1), \\ \delta x = 2\pi/K \end{cases} \tag{4.9}$$

and

$$\begin{cases} k_n = n\delta k \quad (n = -N/2, -N/2+1, \ldots, N/2-1), \\ \delta k = 2\pi/X. \end{cases} \tag{4.10}$$

Similarly, the inverse Fourier transform is written as

$$\begin{aligned}\tilde{f}(x_m) &= \frac{1}{\sqrt{2\pi}} \int_{-K/2}^{K/2} \mathrm{d}k F(k) \mathrm{comb}\left(\frac{k}{\delta k}\right) \exp(ikx_m), \\ &= \frac{\delta k}{\sqrt{2\pi}} \sum_{n=-N/2}^{N/2} F(k_n) \exp(ik_n x_m), \\ &= f_m.\end{aligned} \tag{4.11}$$

These Fourier series are usually calculated using one of the fast Fourier transform (FFT) algorithms, which leads to $M = N$.

4.1.1 Programming Implementation of Fourier Transform

For the purpose of maintaining the theoretical development as symmetrical as possible between the space and frequency domains, we have defined the discrete Fourier and inverse Fourier transforms as

$$\begin{cases} F_n = \dfrac{\delta x}{\sqrt{2\pi}} \displaystyle\sum_{m=-N/2}^{N/2} f_m \exp(-ik_n x_m), \\ f_m = \dfrac{\delta k}{\sqrt{2\pi}} \displaystyle\sum_{n=-N/2}^{N/2} F_n \exp(ik_n x_m). \end{cases} \tag{4.12}$$

One should note, on the other hand, that most prepackaged FFT routines, such as in MatLab or LabVIEW, define them as

$$\begin{cases} F_n = \displaystyle\sum_{m=0}^{N-1} f_m \exp(-ik_n x_m), \\ f_m = \dfrac{1}{N} \displaystyle\sum_{n=0}^{N-1} F_n \exp(ik_n x_m). \end{cases} \tag{4.13}$$

As a concrete example, consider $f_m = \cos\left(\frac{2\pi}{\lambda} x_m\right)$ with $x_m \in [-(X/2) : \delta x : (X/2))$, $\lambda = 10$, $X = 100$, and $\delta x = 1$, depicted in Fig. 4.2a. Then $K/2\pi = 1$ and $\delta k/2\pi = 0.01$. The result of FFT on f_m using MatLab is shown in Fig. 4.2b, where the horizontal axis is the index n. As output by MatLab, the 0th element is the zero-frequency component, the 1st element is the $1\delta k/2\pi$ frequency component, ..., the mth element is the $m\delta k/2\pi$ frequency component, and so on up to the last element $(N-1)\delta k/2\pi$. Especially for image processing, it is more convenient to place the zero-frequency element in the center, and we take $k_n \in [-(K/2) : \delta k : (K/2))$ instead of $[0 : \delta k : K)$. By way of periodicity of $\tilde{F}$, this is equivalent to taking the right half of F_n and swapping it with the left half. As shown in Fig. 4.2c, this is accomplished by the *FFTSHIFT* operation of MatLab. To maintain a correspondence with (4.12), we also multiply with the factor $\delta x/\sqrt{2\pi}$. The result F_n vs. $k_n/2\pi$ is plotted in Fig. 4.2c. A peak appears at the frequency $k_n/2\pi = 0.1$ as expected, while the other peak at 0.9 that exceeds the Nyquist frequency $K/2$ is now aliased to a negative frequency -0.1. It is also verified that

$$\sum_{m=0}^{N-1} \delta x |f_m|^2 = \sum_{n=0}^{N-1} \delta k |F_n|^2, \tag{4.14}$$

as required by the Parseval's theorem. The Fourier transform is in general complex: the real and imaginary parts of F_n are displayed in Fig. 4.2d, e. For the present

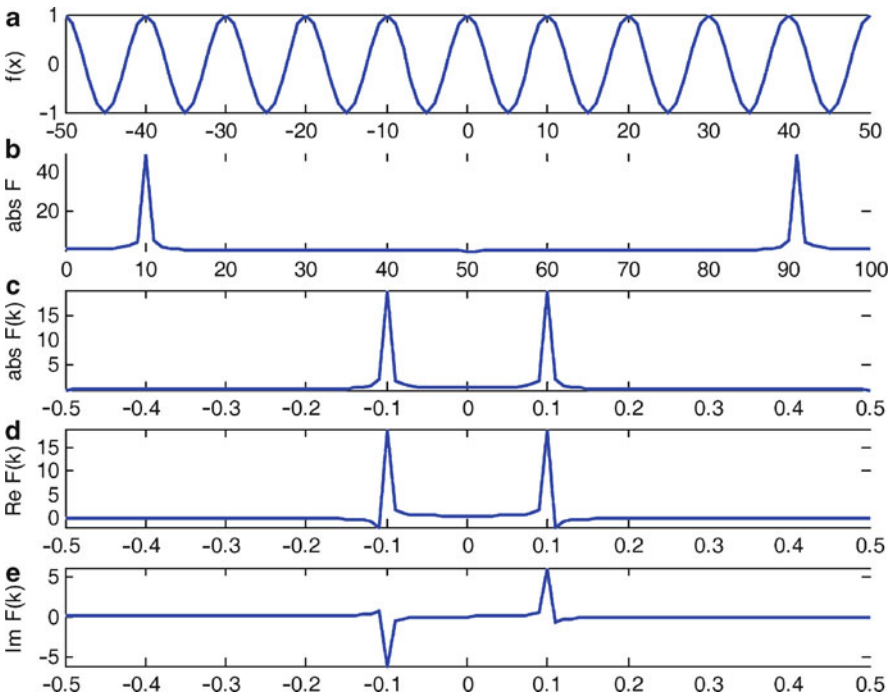

Fig. 4.2 An example of discretized Fourier transform. (**a**) A cosine function, (**b**) the amplitude of FFT as output from Matlab, (**c**) after FFTSHIFT and scaling of the axes, (**d**) the real part, and (**e**) the imaginary part

example of f_m, the imaginary part of the Fourier transform should be zero. The calculated imaginary part is small but nonzero because of the finite step δx, which should be made smaller for more accurate result.

4.2 Fresnel Transform Method

Under Fresnel approximation, the propagation of optical field from a plane Σ_0 at $z = 0$ to another plane Σ along the z-axis is given by the Fresnel transform (2.34), repeated here,

$$E(x, y; z) = 2\pi \exp\left[\frac{ik}{2z}\left(x^2 + y^2\right)\right] \mathfrak{F}\{E_0(x_0, y_0) S_{\mathrm{F}}(x_0, y_0; z)\}\left[k_x, k_y\right], \tag{4.15}$$

where the Fresnel PSF is

$$S_{\mathrm{F}}(x, y; z) = -\frac{ik}{2\pi z} \exp(ikz) \exp\left[\frac{ik}{2z}\left(x^2 + y^2\right)\right] \tag{4.16}$$

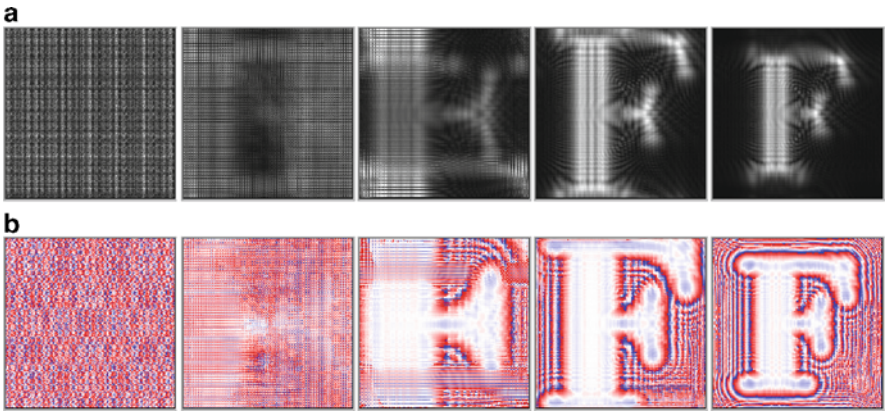

Fig. 4.3 An example of numerical diffraction by Fresnel transform method. (**a**) Amplitude images and (**b**) phase images. The input object is 256 × 256 μm^2 in size and the images are calculated at distances $z = 0$, 125, 250, 375, 500 μm

and the spatial frequencies are

$$k_x = k\frac{x}{z}; \qquad k_y = k\frac{y}{z}. \tag{4.17}$$

The Fresnel transform method (FTM) therefore involves a single Fourier transform, and can be implemented by the use of FFT [1–7]. For numerical calculation, a $X_0 \times Y_0$ area of the input field $E_0(x_0, y_0)$ is sampled on a $N_x \times N_y$ array with the pixel size of $\delta x_0 \times \delta y_0$. The output field $E(x, y)$ is then another $N_x \times N_y$ array of area $X \times Y$ and pixel size $\delta x \times \delta y$. An example of numerical diffraction by Fresnel transform method is shown in Fig. 4.3, where the input pattern at $z = 0$ is the letter "F" in an opaque screen of 256 × 256 μm^{2}area with 256 × 256 pixels and the wavelength is assumed to be $\lambda = 0.633$ μm. (Most of the simulation examples here and in the following chapters will use similar set of parameters, unless otherwise noted.) The top row shows the amplitude of the diffracted field at distances of $z = 0$, 125, 250, 375, 500 μm. The bottom row shows the phase patterns at corresponding distances, where the factor $\exp(-ikz)$ has been multiplied to remove the rapid phase variation due to overall z-propagation.

One pixel in $E(x, y; z)$ corresponds to $\delta k_x = \frac{k}{z}\delta x$, which in the Σ-plane corresponds to

$$\delta x = \frac{z}{k}\delta k_x = \frac{2\pi z}{kX_0} = \frac{\lambda}{X_0}z. \tag{4.18}$$

That is, the pixel size, and the Σ-plane size, grows linearly with the distance, as is evident in Fig. 4.3. In fact, the field of view at the five distances are $X = 0$, 79, 158, 236, 315 μm. There are methods to address the problem of nonconstant pixel resolution, which will be discussed in Sect. 9.2. Also evident is the presence of a minimum distance to obtain valid diffraction pattern. To avoid aliasing [8], the output plane Σ needs to be at least as large as the input plane Σ_0, which leads to

$$z_{\min} = \frac{{X_0}^2}{N\lambda}. \tag{4.19}$$

In Fig. 4.7a is shown a yz-cross section of the propagation over a range of $z = 0$–500 μm along the middle of the vertical line of the letter "F". For the present example, $z_{\min} = 404$ μm and the wrapping or aliasing is evident in Fig. 4.7a at shorter distances. (The apparent $z_{\min}$ is somewhat shorter than 404 μm because the letter "F" does not fill the whole screen.)

4.3 Huygens Convolution Method

The diffraction can be calculated from the Huygens convolution integral (2.27)

$$\begin{aligned} E(x,y;z) &= E_0 \odot S_{\mathrm{H}}, \\ &= \mathfrak{F}^{-1}\left\{\mathfrak{F}\{E_0(x_0,y_0)\}\left[k_x,k_y\right]\mathfrak{F}\{S_{\mathrm{H}}(x_0,y_0)\}\left[k_x,k_y\right]\right\}[x,y], \end{aligned} \tag{4.20}$$

where the Huygens PSF is

$$S_{\mathrm{H}}(x,y;z) = -\frac{ik}{2\pi z}\exp\left[ik\sqrt{x^2+y^2+z^2}\right]. \tag{4.21}$$

Thus, the Huygens convolution method (HCM) requires three Fourier transforms [2, 6, 9–11]. An example of numerical diffraction by HCM, is shown in Fig. 4.4, using the same set of parameters as in Fig. 4.3. Unlike FTM, the pixel resolution in HCM does not depend on the propagation distance because of the combination of $\mathfrak{F}$ and $\mathfrak{F}^{-1}$. Figure 4.7b shows the behavior of the HCM diffraction over the distance $z = 0$–500 μm. Although the short-distance behavior appears to be better than FTM, the minimum distance $z_{\min}$ for HCM is similar to FTM, the improvement being mainly due to the use of spherical PSF instead of parabolic one. Also note that one can use the Fresnel PSF S_{F} as an approximation to S_{H} and obtain result with similar quality, though such approximation is really not necessary.

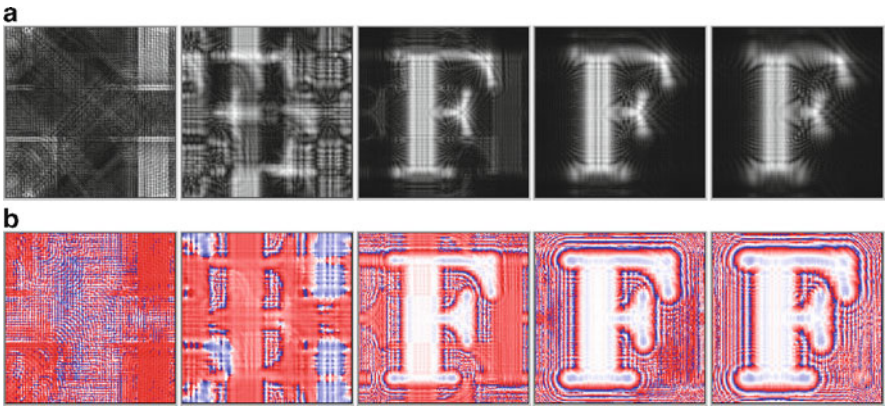

Fig. 4.4 An example of numerical diffraction by Huygens convolution method, using the same parameters as in Fig. 4.3. (**a**) Amplitude images and (**b**) phase images

4.4 Angular Spectrum Method

The diffraction is calculated by angular spectrum method (ASM) according to

$$E(x,y;z) = \mathfrak{F}^{-1}\left\{ \mathfrak{F}\{E_0(x_0,y_0)\}\left[k_x,k_y\right] \exp\left[iz\sqrt{k^2 - {k_x}^2 - {k_y}^2}\right] \right.$$
$$\left. \operatorname{circ}\left(\frac{\sqrt{{k_x}^2 + {k_y}^2}}{k}\right) \right\}[x,y], \tag{4.22}$$

which requires two Fourier transforms [12–18]. In image plane holographic microscopy, for example, where the input field E_0 may be actually a magnified image of a microscopic object, the effective pixel size may be smaller than the wavelength and the argument of the square root in the imaginary exponent in (4.22) may become negative in parts of the spectral domain, and the circle function is then required. An example of numerical diffraction by ASM, is shown in Fig. 4.5, using the same set of parameters as in Fig. 4.3, and Fig. 4.7c shows the behavior of the ASM diffraction over the distance $z = 0$–500 μm. Evidently, the ASM yields valid diffraction image at short distances, including zero. The difference between HCM and ASM in (4.20) and (4.22) is the replacement of $\mathfrak{F}\left\{-\frac{ik}{2\pi z}\exp\left[ik\sqrt{x^2+y^2+z^2}\right]\right\}$ with $\exp\left[iz\sqrt{k^2-k_x^2-k_y^2}\right]$, which are

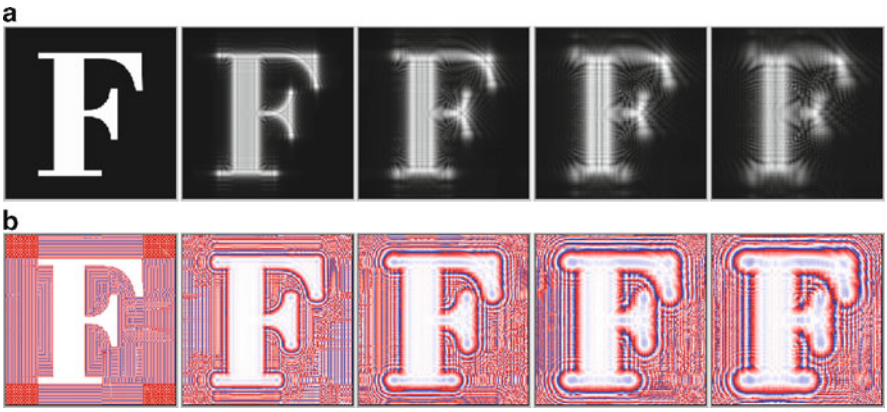

Fig. 4.5 An example of numerical diffraction by angular spectrum method, using the same parameters as in Fig. 4.3. (**a**) Amplitude images and (**b**) phase images

analytically equivalent. But in numerical calculations, the $1/z$-factor in the former creates problems while the latter is well-behaved at all distances. We can also apply the Fresnel approximation

$$\sqrt{k^2 - {k_x}^2 - {k_y}^2} = k - \frac{{k_x}^2 + {k_y}^2}{2k} \tag{4.23}$$

in (4.22) for calculating ASM, which again usually results in insignificant difference.

4.5 Comparison of Methods

These methods, sometimes referred to with ambiguous or inconsistent names, have distinct advantages and disadvantages [2, 11, 19]. Referring to Fig. 4.6, the ASM is based on propagation of plane waves. Sampling of the plane waves by the discrete pixels of CCD does not vary with the distance, and therefore the ASM does not have any distance limitations. On the other hand, the HCM is based on the propagation of spherical wavefronts (or parabolic approximation for FTM). When the center of curvature is too close to the CCD array, local fringe frequency on the CCD plane may be higher than the Nyquist frequency. This occurs when the distance is smaller than $z_{\min} = {X_0}^2/N\lambda$, which in our example is 404 μm. The behavior of diffraction field calculated by the three methods over a range of $z = 0$–500 μm is shown in Fig. 4.7.

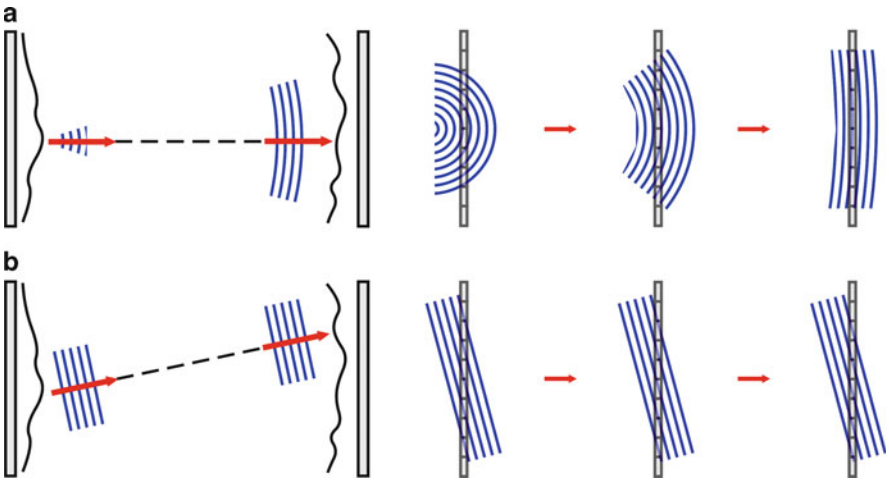

Fig. 4.6 Conceptual comparison of (**a**) Huygens convolution method and (**b**) angular spectrum method. The diagrams on the *right* depict how the wavefronts interact with the CCD array at various distances

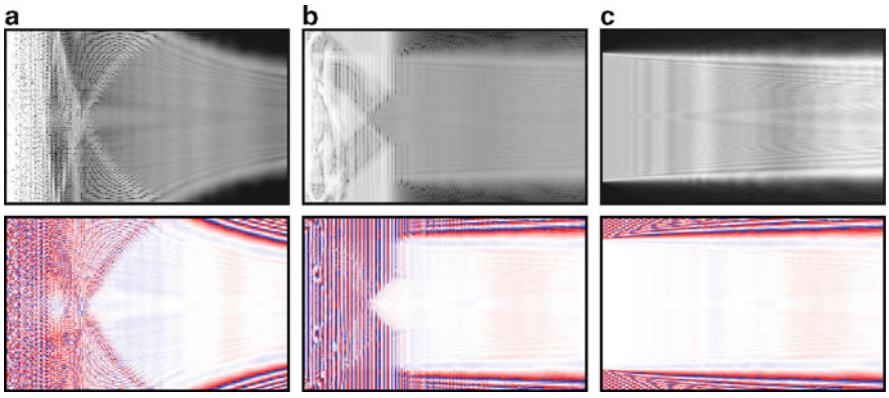

Fig. 4.7 Comparison of numerical diffraction by (**a**) FTM, (**b**) HCM, and (**c**) ASM. Amplitude (*upper row*) and phase (*lower row*) profiles on an x–z plane, over the distance range of $z = 0$–$500\ \mu\text{m}$

Moreover, there also is a maximum distance that yields correct diffraction pattern for HCM. For large enough distances the fringe period of spherical wavefront becomes larger than the entire CCD array, failing to record any diffraction information. This occurs when the distance is larger than

$$z_{\max} = \frac{{X_0}^2}{2\lambda}, \tag{4.24}$$

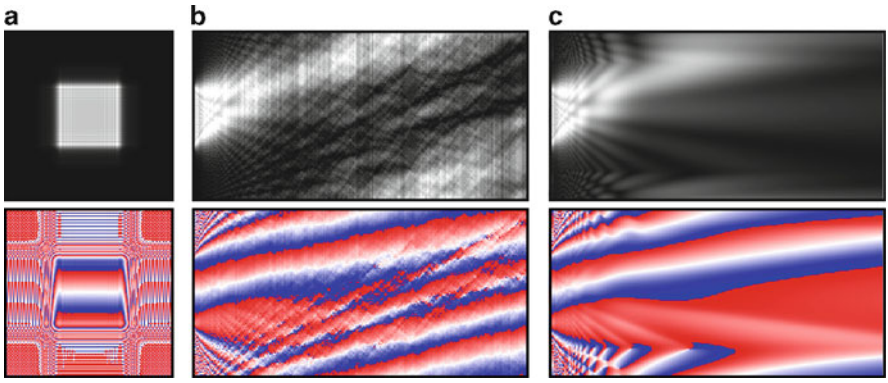

Fig. 4.8 Comparison of numerical diffraction by (**b**) ASM and (**c**) HCM. Amplitude (*upper row*) and phase (*lower row*) profiles on an *x*–*z* plane, over the distance range of $z = 0$–20,000 μm. The input, shown in (**a**), is a square opening illuminated with a slightly tilted plane wave

which for our numerical example, is 51,800 μm. The ASM does not have this limitation either. Behaviors of ASM and HCM diffraction at large distances are illustrated in Fig. 4.8, where the distance range is $z = 0$–20,000 μm and the input pattern is an open square with slightly tilted wavefront – by two wavelengths over the vertical size of the square opening, as may be noticed in the phase image of Fig. 4.8a. In Fig. 4.8b, the ASM correctly depicts the propagation of the transmitted beam of light at a slight angle. When the beam reaches the limit of *x*-frame size, it wraps around to the other side and continues to propagate. Note that a beam of initial width of 128 μm does not spread appreciably after propagation of 20 mm. On the other hand, in Fig. 4.8c, the HCM starts out with a similar pattern as ASM but it progressively loses high-frequency structures eventually becoming structureless as it approaches $z_{\max}$.

References

1. U. Schnars, and W. Juptner, "Direct Recording of Holograms by a Ccd Target and Numerical Reconstruction," Applied Optics **33**, 179–181 (1994).
2. U. Schnars, and W. P. O. Juptner, "Digital recording and numerical reconstruction of holograms," Measurement Science & Technology **13**, R85-R101 (2002).
3. D. Y. Wang, J. Zhao, F. Zhang, G. Pedrini, and W. Osten, "High-fidelity numerical realization of multiple-step Fresnel propagation for the reconstruction of digital holograms," Applied Optics **47**, D12-D20 (2008).
4. I. Yamaguchi, J. Kato, S. Ohta, and J. Mizuno, "Image formation in phase-shifting digital holography and applications to microscopy," Applied Optics **40**, 6177–6186 (2001).
5. E. Cuche, P. Marquet, and C. Depeursinge, "Simultaneous amplitude-contrast and quantitative phase-contrast microscopy by numerical reconstruction of Fresnel off-axis holograms," Applied Optics **38**, 6994–7001 (1999).

6. U. Schnars, T. M. Kreis, and W. P. O. Juptner, "Digital recording and numerical reconstruction of holograms: Reduction of the spatial frequency spectrum," Optical Engineering **35**, 977–982 (1996).
7. T. M. Kreis, and W. P. O. Juptner, "Suppression of the dc term in digital holography," Optical Engineering **36**, 2357–2360 (1997).
8. L. Onural, "Sampling of the diffraction field," Applied Optics **39**, 5929–5935 (2000).
9. S. Grilli, P. Ferraro, S. De Nicola, A. Finizio, G. Pierattini, and R. Meucci, "Whole optical wavefields reconstruction by digital holography," Optics Express **9**, 294–302 (2001).
10. J. C. Li, P. Tankam, Z. J. Peng, and P. Picart, "Digital holographic reconstruction of large objects using a convolution approach and adjustable magnification," Optics Letters **34**, 572–574 (2009).
11. F. Dubois, L. Joannes, and J. C. Legros, "Improved three-dimensional imaging with a digital holography microscope with a source of partial spatial coherence," Applied Optics **38**, 7085–7094 (1999).
12. D. Leseberg, "Computer-Generated 3-Dimensional Image Holograms," Applied Optics **31**, 223–229 (1992).
13. C. J. Mann, L. F. Yu, and M. K. Kim, "Movies of cellular and sub-cellular motion by digital holographic microscopy," Biomed. Eng. Online **5**, 21 (2006).
14. L. F. Yu, and M. K. Kim, "Wavelength-scanning digital interference holography for tomographic three-dimensional imaging by use of the angular spectrum method," Optics Letters **30**, 2092–2094 (2005).
15. G. Sheoran, S. Dubey, A. Anand, D. S. Mehta, and C. Shakher, "Swept-source digital holography to reconstruct tomographic images," Optics Letters **34**, 1879–1881 (2009).
16. J. W. Weng, J. G. Zhong, and C. Y. Hu, "Digital reconstruction based on angular spectrum diffraction with the ridge of wavelet transform in holographic phase-contrast microscopy," Optics Express **16**, 21971–21981 (2008).
17. S. J. Jeong, and C. K. Hong, "Pixel-size-maintained image reconstruction of digital holograms on arbitrarily tilted planes by the angular spectrum method," Applied Optics **47**, 3064–3071 (2008).
18. S. Kim, and S. J. Lee, "Measurement of 3D laminar flow inside a micro tube using micro digital holographic particle tracking velocimetry," J. Micromech. Microeng. **17**, 2157–2162 (2007).
19. M. K. Kim, L. F. Yu, and C. J. Mann, "Digital holography and multi-wavelength interference techniques," in *Digital Holography and Three Dimensional Display: Principles and Applications*, T. C. Poon, ed. (2006), pp. 51–72 (Chap. 52).

Chapter 5
Digital Holography Configurations

Some of the general characteristics of digital holographic images are illustrated using simulated examples. Holographic image location and magnification are dependent on, and therefore can be controlled by, the choice of wavelengths and reference directions and curvatures. Optical configurations frequently used in digital holography experiments are described and compared.

5.1 General Behavior of Digital Holographic Images

We first study, through a few simulated examples, the general behavior of the digital holographic images and compare with some of the results that we have obtained in previous chapters. Numerical diffraction is calculated using the angular spectrum method.

Ex. 1: Formation of Hologram and Reconstruction of Image

The top row of Fig. 5.1 simulates formation of a hologram. The object (Fig. 5.1a), is a letter "F" in an opaque screen of area $256 \times 256\ \mu m^2$ with 256×256 pixels. The object is illuminated with a plane wave, of wavelength $\lambda = 0.633\ \mu m$, which propagates to the hologram plane at a distance 500 μm, at normal incidence. The object field E_O arriving at the hologram plane is shown in Fig. 5.1b. The hologram plane is of the same size and pixel count as the object plane. A plane-wave reference, E_R, of the same wavelength as the object, is also incident on the hologram plane at an angle φ, such that it produces 50 fringes across the x-direction, that is, $k_x/2\pi = (50/256)\ \mu m^{-1}$ and $\varphi = \sin^{-1}(k_x/k) = 0.124$ rad. Intensity of the interference between the object and the reference $|E_O + E_R|^2$ is the hologram (Fig. 5.1c). Propagation of the object field from the object plane at $z = -500\ \mu m$ to the hologram plane at $z = 0$ is shown in Fig. 5.1d, where, for clearer illustration of the z-propagation, we use as the object a square opening of quarter the frame size, instead of the letter "F".

M.K. Kim, *Digital Holographic Microscopy: Principles, Techniques, and Applications*, Springer Series in Optical Sciences 162,
DOI 10.1007/978-1-4419-7793-9_5, © Springer Science+Business Media, LLC 2011

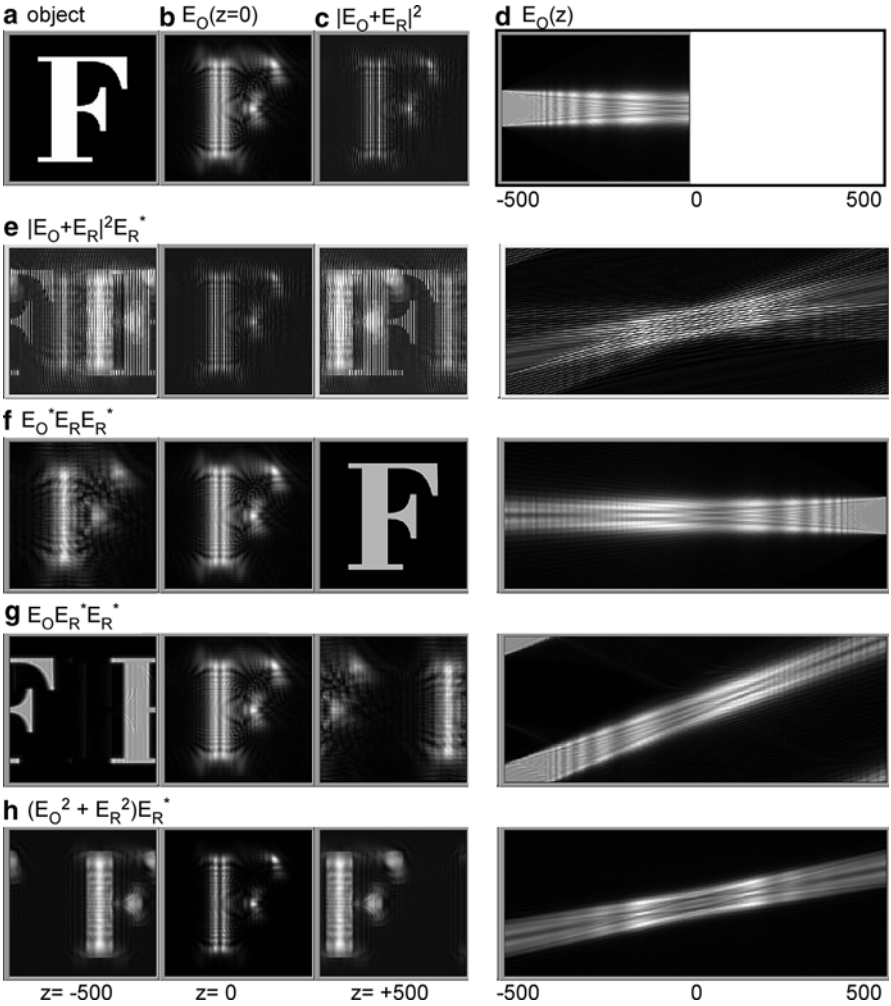

Fig. 5.1 Formation of hologram and reconstruction of image. (**a**–**d**) in the *top row* illustrate formation of the hologram. (**a**) Input object at $z = -500$ μm, 256 × 256 μm; (**b**) object field at the hologram plane, $z = 0$; (**c**) hologram after interference with tilted plane reference; (**d**) propagation of object field from z $= -500$ to 0 μm. (**e**–**h**) Illustrate the image reconstruction by illumination of the hologram with a tilted plane wave, conjugate to the first reference. (**e**) *x*–*y* images at $z = -500$, 0, and +500 μm, and *x*–*z* cross-section of the fields propagating along the *z*-direction from $z = -500$ to +500 μm. All the holographic terms – the zero-order and the twin-image terms – are included in the computation. (**f**) Same as (**e**), but only the real-image term is included in computation. (**g**) Only the virtual image term is included. (**h**) Only the zero-order term is included

Figure 5.1e illustrates the holographic image reconstruction, for which the hologram is illuminated with another plane-wave reference, E_R'. Recall from Chap. 3 the holographic terms are

$$\left(|E_R|^2 + |E_O|^2\right)E_R' + E_O E_R^* E_R' + E_O^* E_R E_R'. \tag{5.1}$$

We take, in this example, $E_R' = E_R^*$, that is, it is incident at the angle $-\varphi$. In digital holography, we are free to calculate the propagation forward or backward with equal ease. The diffraction of the field $|E_O + E_R|^2 E_R^*$ is calculated over the range $z = -500$ to +500 μm, and the x–y images are shown at $z = -500$, 0, and +500 μm. Normally, $z = +500$ μm is where the holographic image is expected. One can indeed recognize a focused image in the center of the x–y image plane at $z = +500$ μm, but it is also superposed with the zero-order and twin images. In the x–z panel of Fig. 5.1e, one can discern the three diffraction orders – 0 and ± 1 – diverging from the hologram plane.

There are many methods to separate out the zero-order and twin-image terms, which will be discussed in this and later chapters. But it is illustrative to separate the holographic terms artificially and observe how each term propagates. Thus in Fig. 5.1f, we take the term $E_O^* E_R E_R^*$ and propagate it over the same range as in Fig. 5.1e. Because this term is proportional to E_O^*, its forward propagation is equivalent to the backward propagation of E_O – i.e., it forms a focused image at $z = +500$ μm. In Fig. 5.1g, we take the twin term $E_O E_R^* E_R^*$ and propagate over the same range. Because this is proportional to E_O, one has to propagate backward to the original object position at $z = -500$ μm to form a focused image. Furthermore, because it also has E_R^{*2} factor, the image is shifted by an angle 2φ. Also notice the wrapping of the image around the boundaries. On the other hand, at $z = +500$ μm, the twin-image term is out of focus. Finally in Fig. 5.1h, we take the zero-order term, or dc term, and propagate similarly. In this case, there is no focusing of the image but straight propagation along the direction φ of the reference wave.

Unless these terms are somehow separated, they all contribute to the field pattern at the image plane, thus causing significant amount of interference, as in Fig. 5.1e, and distorting the focused holographic image. In the following examples, we take only the $E_O^* E_R E_R^*$ term, and observe its behavior in terms of several parameters.

Ex. 2: Wavelength Mismatch

In Fig. 5.2, the effect of using a different wavelength for reconstruction is shown. In Fig. 5.2a, $\lambda = \lambda' = 0.633$ μm and the image forms at $z = +500$ μm, marked with an arrow, as expected. Here we display both the amplitude (upper row) and phase (lower row) of each image. If the wavelength of the second reference wave is changed by $\mu = \lambda'/\lambda = 2/3$ to $\lambda' = 0.422$ μm, then, according to (3.21), the image distance increases by 3/2 to $z = 750$ μm, while the lateral magnification remains the same, as seen in Fig. 5.2b. In addition, according to (3.7), because of the mismatch of the wavelengths, the image propagates at an angle $(\mu - 1)\varphi = -\varphi/3$ and the image is shifted.

Ex. 3: Spherical Reference Waves

Now we use spherical reference waves, with radius of curvature $R = 1{,}000$ μm, instead of plane waves. Then the complex hologram (i.e., without zero-order or twin-image terms) has the phase curvature, but if we use the same spherical wave $R' = 1{,}000$ μm for reconstruction, then the effect of the curvature is compensated. The image forms at $z = 500$ μm with unit magnification, as shown in Fig. 5.3a.

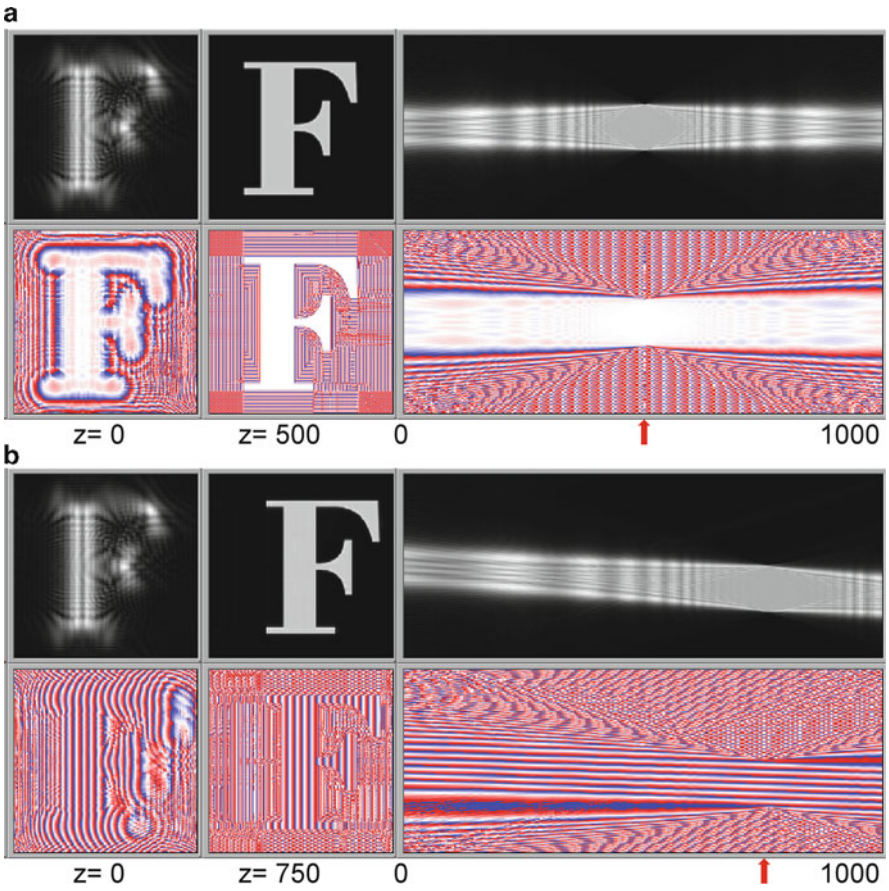

Fig. 5.2 Effect of wavelength mismatch. (**a**) The same wavelength is used for recording and reconstruction, $\lambda = \lambda' = 0.633$ μm. (**b**) A shorter wavelength is used for reconstruction, $\lambda' = 0.422$ μm. For each part, both the amplitude (*upper row*) and phase (*lower row*) of the fields are depicted. The *arrows* indicate the image locations

On the other hand, if the second curvature is different, then the image position is given by

$$\frac{1}{z} = \frac{1}{z_0} - \frac{1}{R} + \frac{1}{R'} \tag{5.2}$$

and the lateral magnification is

$$M_x = \frac{1}{1 - z_0((1/R) - (1/R'))}. \tag{5.3}$$

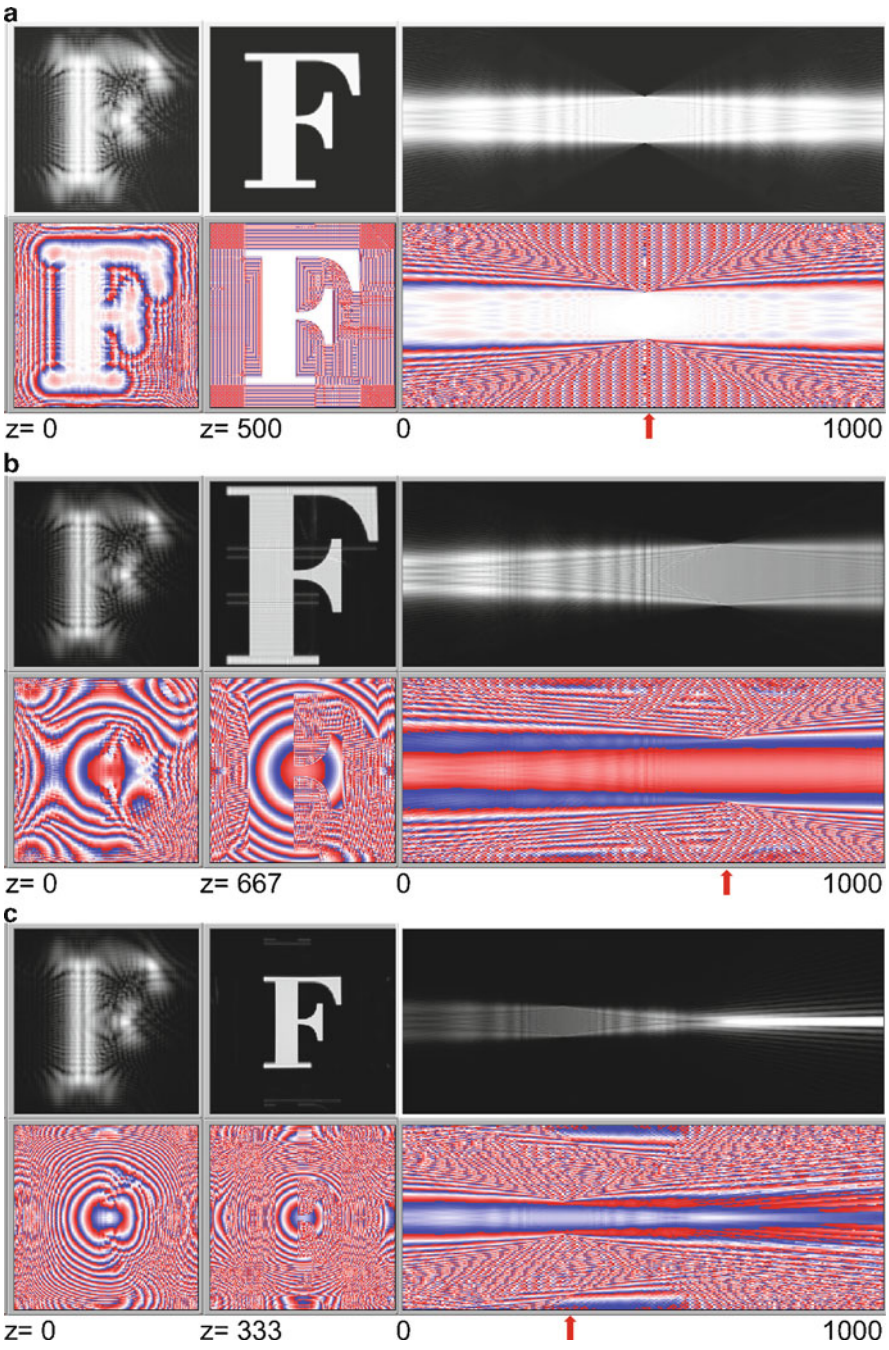

Fig. 5.3 Effect of spherical reference waves. (**a**) The same radius of curvature is used for recording and reconstruction, $R = R' = 1,000\,\mu\text{m}$. (**b**) A larger curvature is used for reconstruction, $R' = 2,000\ \mu\text{m}$. (**c**) A shorter curvature is used for reconstruction, $R' = 500\,\mu\text{m}$. The *arrows* indicate the image locations

When $R' = 2,000\,\mu m$, Fig. 5.3b shows the incomplete compensation of the curvature, and formation of the image at $z = 667\,\mu m$ with magnification $M_x = 1.33$, as expected. Another example with $R' = 500\,\mu m$ in Fig. 5.3c results in $z = 333\,\mu m$ and $M_x = 0.67$.

The above examples show that the holographic image location and magnification are dependent on, and therefore can be controlled by, the choice of wavelengths and reference directions and curvatures. We now give more specific descriptions of configurations frequently used in digital holography experiments [1].

5.2 Digital Gabor Holography

In Gabor holography, the object is illuminated with a single beam of light and there is no separate reference wave (Fig. 5.4). The part of the incident light that is scattered by the object is the object wave and the remainder that does not undergo scattering acts as the reference wave. The method is the more effective the smaller the object is so that the reference is not excessively disturbed. In the simulation example of Fig. 5.5a–c, the object is a thin opaque letter "F" in an otherwise transparent screen (Fig. 5.5a). All the relevant parameters are otherwise the same as in the previous section. A plane wave is transmitted through the screen and propagates to the hologram plane. The intensity pattern on this plane is the hologram (Fig. 5.5b). Illumination of the hologram with another plane wave forms the focused image at the expected distance. But the focused image is also superposed with the blurred twin image, whose focus position is on the opposite side, negative z-distance, of the hologram. If we attempt DGH with an object that consists of transparent letter in an otherwise opaque screen (Fig. 5.5d), then there is not enough reference wave (Fig. 5.5e) and the holographic image does not form (Fig. 5.5f).

Because of the above property and because of the simplicity of the optical setup, Gabor holography is particularly useful for particle or thin fiber image analysis, and the digital Gabor holography (DGH) can provide new capabilities and wider

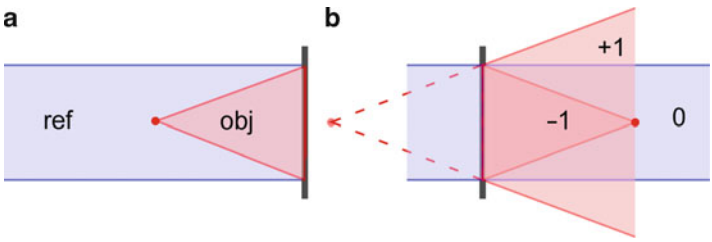

Fig. 5.4 Gabor holography. (**a**) Recording by superposition of the reference wave and its scattered component from a point object, and (**b**) reconstruction of a point image (−1 order) and its defocused twin (+1 order)

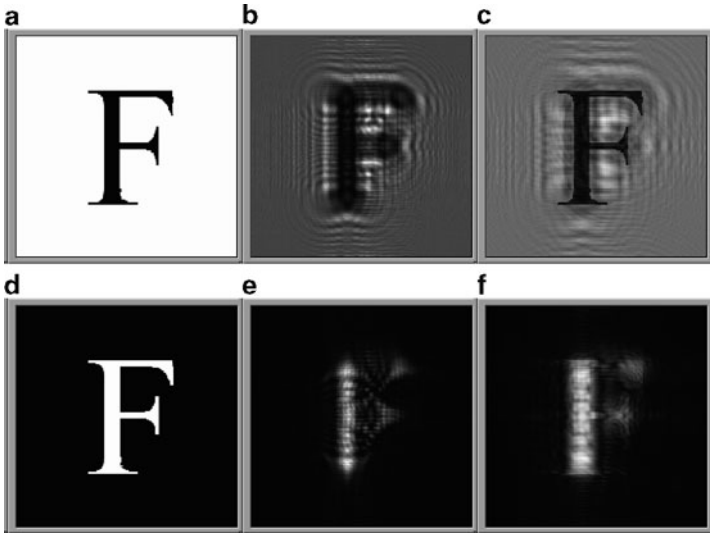

Fig. 5.5 Digital Gabor holography. (**a**) A thin opaque letter in an otherwise opaque screen as the object, (**b**) the diffraction pattern as the hologram, and (**c**) the reconstructed image. (**d**–**f**) Illustrate an attempt at DGH with a thin transparent letter in an otherwise opaque screen. (**d**) Object, (**e**) hologram, and (**f**) image

applications [2–6]. For microscopic particles the twin images are often negligible because even at a relatively short distance the Fraunhofer condition is satisfied and the twin image may be completely defocused.

5.3 Digital In-line Holography

For the in-line holography, a separate reference field is provided in a general alignment with the object field, Fig. 5.6. (Some authors refer to Gabor holography also as in-line holography, but here we will use the term in-line to be more specific as having a separate reference beam.) This allows imaging of objects regardless of its size relative to the field of view. In the example of Fig. 5.7, the object with opaque letter in transparent background produces focused image in a manner similar to the DGH, except that the image also includes the uniform reference as well as the twin image. On the other hand, for the object with transparent letter in opaque background, the in-line configuration is capable of producing a focused image, whereas the DGH is not.

An advantage of in-line DH over DGH is, as seen above, that it does not have a restriction of small object [7–9]. On the other hand, the focused image is superposed with the zero-order and twin-image terms. Therefore, it is usually necessary to find ways to reduce or eliminate the spurious terms. These techniques, to be

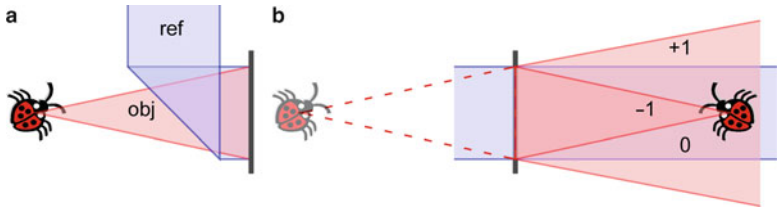

Fig. 5.6 In-line holography. (**a**) In-line superposition of object and reference beams, and (**b**) reconstruction of superposed zero-order and twin images

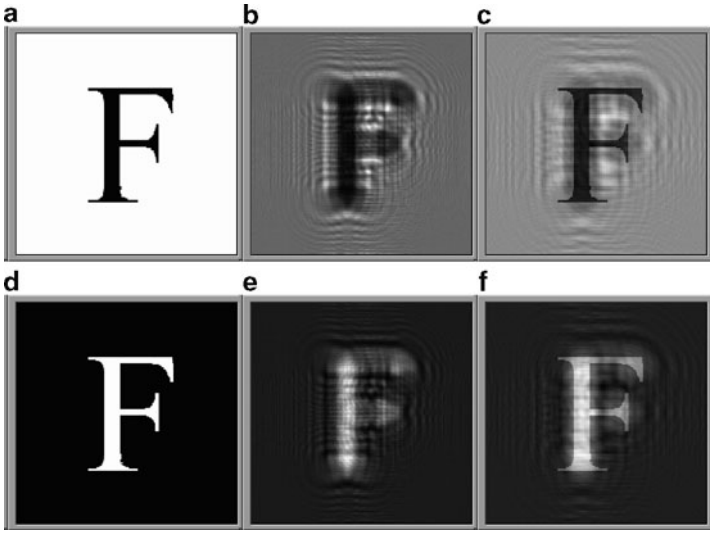

Fig. 5.7 Digital in-line holography. (**a**) A thin opaque letter in an otherwise opaque screen as the object, (**b**) the hologram recorded by the interference of the diffracted object field and the reference, and (**c**) the reconstructed image. (**d–f**) Illustrate digital in-line holography has no trouble imaging a mostly opaque object. (**d**) Object, (**e**) hologram, and (**f**) image

described in Chap. 7, range from relatively simple subtraction of the average intensity from the hologram to the multiexposure phase-shifting methods. Otherwise, one can use one of the off-axis configurations described below. However, most of the off-axis methods reduce the information content of the hologram to one quarter of the pixel count. In a typical digital holography setup, the pixel count is at a premium, and therefore such reduction can be a significant disadvantage. Then the in-line configuration may be considered, though at the expense of multiple exposure or other requirements.

5.4 Digital Image Plane Holography

The object can be placed close to the hologram plane so that the reconstructed image is also near the hologram. We refer to the hologram plane as the plane (or any other plane optically conjugate to it) where the recording takes place. In real space reflection holography applications, this is useful for creating holograms that can be viewed with low coherence light, because the image distance is not very large compared to the coherence length. But in microscopic holography, this would not be useful because there is no magnification, unless one uses a microscope to view the hologram. On the other hand, an objective lens can be used to form near the hologram plane a magnified image of the object Fig. 5.8a. If a plane-wave reference is used for recording and for reconstruction, then the reconstructed image will coincide with the magnified image of the object in amplitude, although the phase will contain the curvature due to the imaging lens.

Alternatively, holographic interference of the object and the plane-wave reference can be formed first and its magnified image projected near the hologram plane (Fig. 5.8b). Equivalently, a separate lens can be used to focus a plane-wave reference to a point conjugate to the back focus of the objective lens, as shown in Fig. 5.8c. In real space holography, illumination of the magnified hologram with a plane wave of the original wavelength will result in an image with unit lateral magnification, relative to the original magnified image, but at a large distance so that the angular size will be the same as if the original unmagnified object was placed in front of the hologram plane. This will also most likely introduce significant aberrations. In order to restore the angular magnification, one has to use a correspondingly magnified wavelength, a mostly unfeasible task.

In digital holographic microscopy, on the other hand, this configuration is particularly flexible because the acquired hologram can be numerically scaled according to the physical dimensions of the object space regardless of the image size on the CCD. In effect a demagnified CCD array is placed near the object position. Once the magnified holographic interference is input to the computer, it is only a matter of assigning the original microscopic frame size and the correct wavelength that was used for creating the holographic interference. The numerically reconstructed image will then correctly represent the amplitude and phase of the original microscopic object space. The curvature matching of the reference wave also has the benefit of reducing fringe frequencies on the CCD, which can reduce aberrations due to residual mismatch between the write and read references.

Image plane digital holography [10] has been useful in a number of different application areas including biological microscopy [11, 12], where it is important to be able to monitor the live specimen being imaged. It is also advantageous for improving light collection efficiency in particle velocimetry [13]. For digital holographic microscopy using low coherence light, one necessarily operates near image plane configuration [14].

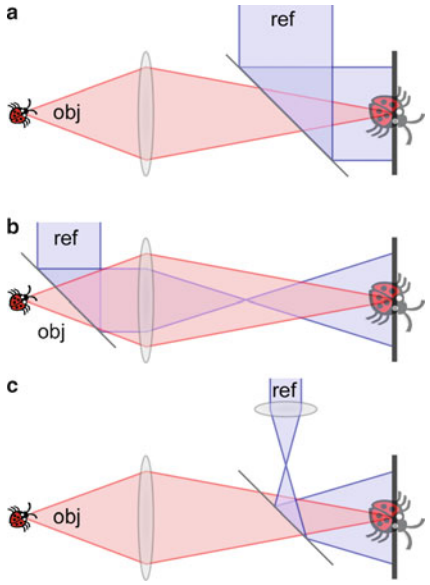

Fig. 5.8 Recording of image plane holograms by projection of a magnified image of the object on the hologram plane, in superposition with (**a**) plane reference wave or (**b**) wavefront curvature-matched reference wave. (**c**) Another method of producing curvature-matched reference wave

5.5 Digital Fourier Holography

As we saw earlier, the field at the back focal plane of a lens is the Fourier transform of the object field at the front focal plane. In a typical configuration for Fourier holography (Fig. 5.9a) the hologram plane is positioned at the back focal plane and a plane-wave reference is produced by focusing the laser at a point on the object plane. In real space holography reconstruction, illumination of the hologram with a plane-reference wave and transmission through a lens produces the inverse Fourier transform, which is the image (Fig. 5.9b). Both of the twin images are in focus at the focal plane of the imaging lens and the zero-order is a small intense spot.

Alternatively, lensless Fourier holography is possible by placing a point source reference on the object plane (Fig. 5.9c) in front of the hologram plane without a lens. From the Fresnel expression of diffraction (2.34), the outer quadratic phase function is canceled by the reference with the same curvature, and the $E_O E_R^*$ term is proportional to the Fourier transform of the object field multiplied by the inner quadratic phase function. Reconstruction proceeds in the same manner as above [15]. The intensity image is not affected by the quadratic phase function.

Both of these methods can be implemented in digital Fourier holography, and the reconstruction is especially simple because it consists of a single Fourier transform of the recorded hologram [16, 17]. Using a small transparent letter "F" as the object (Fig. 5.10a) we illustrate the lensed digital Fourier holography in Fig. 5.10b, c and the lensless digital Fourier holography in Fig. 5.10d, e. The focal length of the lens or the object to hologram distance is 1,000 μm in Fig. 5.10b, d and it is 200 μm in Fig. 5.10c, e.

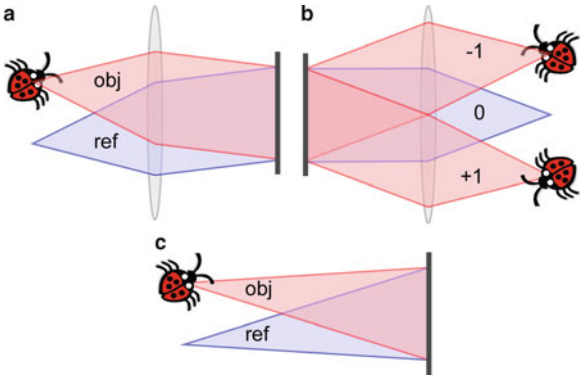

Fig. 5.9 Fourier and lensless Fourier holography. (**a**) Fourier hologram recording using a lens; (**b**) reconstruction by Fourier transform, represented with the Fourier lens; and (**c**) lensless Fourier hologram recording

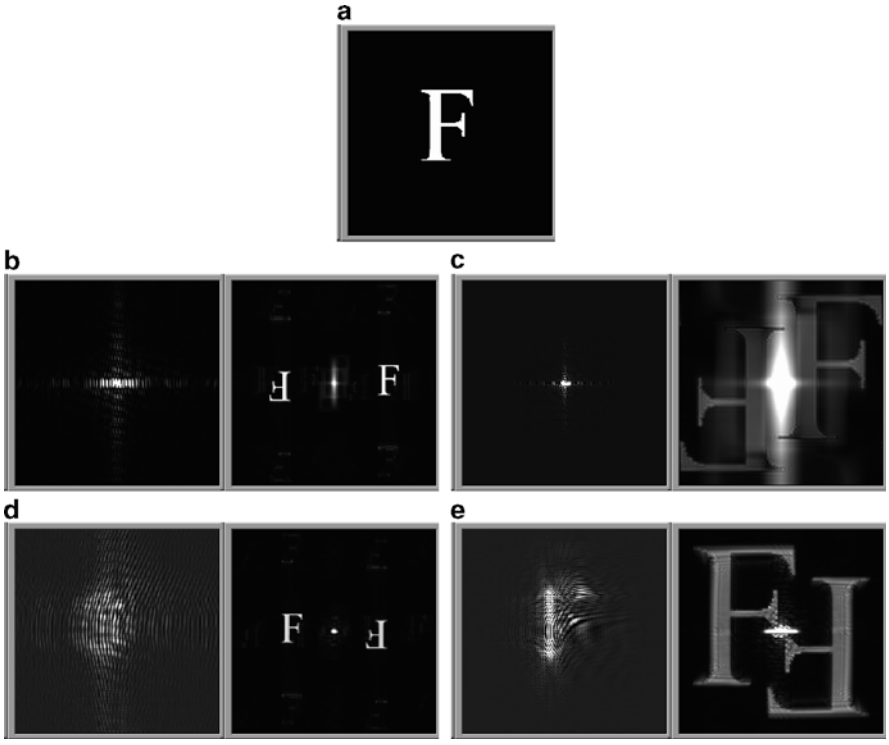

Fig. 5.10 (**a**) The object. Each of the panels (**b–e**) displays the hologram and the reconstructed image. (**b**, **c**) Illustrate digital Fourier holography using a lens with focal length (**b**) 1,000 μm and (**c**) 200 μm. (**d**, **e**) Illustrate lensless digital Fourier holography with the object to hologram distance (**d**) 1,000 μm and (**e**) 200 μm

All the other parameters are as before. The Fourier hologram with lens shows the Fourier transform of the object with interference fringes of the plane-reference wave. The holographic image has the focused twin images on either side of the intense central spot, which is numerically truncated to make the images visible.

As with the Fresnel diffraction, the field size depends on the distance, that is, the focal length or the object to hologram distance, according to

$$X = \frac{N_x \lambda z}{X_0}, \tag{5.4}$$

which for this example is 633 μm in Fig. 5.10b, d or 127 μm in Fig. 5.10c, e. Using the lensless method, the hologram has a more spread-out intensity distribution, but the holographic image amplitude is still identical with the first method. The two methods yield images with opposite orientations. Also note that the distance 200 μm is less than the $z_{\min} = 404\,\mu\text{m}$ of aliasing in Fresnel diffraction and it causes distortion of the images.

In the first digital Fourier microholography experiment of [17], a drop of glycerol placed next to the specimen on a microscope slide acted as the focusing lens to form the point source reference in front of the Fourier lens. There a numerical lens was also introduced to be able to focus the image at varying distances. High resolution microscopy is possible using a relatively simple setup [18, 19] and detailed analysis of image formation in lensless digital Fourier holography is given in [20]. Imaging and analysis of large objects is equally convenient [21]. In lensless Fourier microholography, the object can be placed close to the sensor, which increases the numerical aperture and improves resolution [22]. But this introduces aberration in the reconstruction because of violation of Nyquist frequency requirement. The hologram is expanded and interpolated, followed by multiplication of a transfer function, before Fourier transform, to obtain aberration-free high resolution image. Pedrini et al. [23] make comparison of various interferometer configurations in the context of macroscopic metrology applications.

5.6 Digital Fresnel Holography

The Fresnel holography refers to the configuration where the object is at a finite distance from the hologram plane and is off-axis with respect to a plane-wave reference [24] (Fig. 5.11a). In reconstruction, illumination of the hologram with another plane-wave reference results in images forming at the object position and its mirror position with respect to the hologram, with unit magnification, as shown in Fig. 5.11b. The numerical reconstruction is usually carried out using the Fresnel transform method, which is necessary in order to reconstruct all of the zero-order and the twin images without aliasing. As evident in Fig. 5.11b, the reconstruction area is larger than the hologram area and the Fresnel transform method allows such reconstruction, provided that the image distance is properly chosen. In the simulation example of Fig. 5.12, using mostly the same parameters as before, the object distance is $z_0 = 1,000\,\mu\text{m}$ and is offset from the reference with $k_x/2\pi = (100/256)\,\mu\text{m}^{-1}$. The frame size at $z = 1,000\,\mu\text{m}$ is $N_x \lambda z / X_0 = 633\,\mu\text{m}$ and the

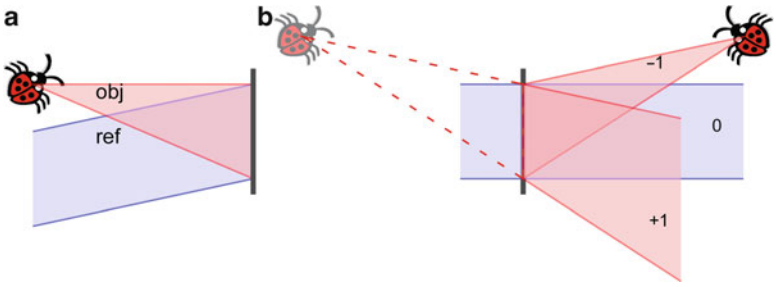

Fig. 5.11 Fresnel holography. (**a**) Recording by off-axis superposition of the object and reference waves, and (**b**) reconstruction of separated zero-order and twin images

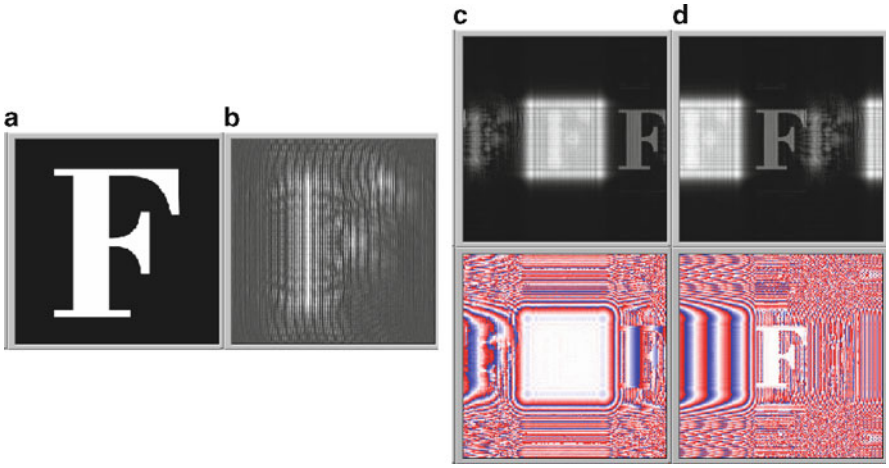

Fig. 5.12 Digital Fresnel holography. (**a**) The object, (**b**) the hologram, (**c**) reconstructed image using normally incident plane-wave reference, and (**d**) reconstructed image using tilted plane-wave reference. Each of the panels (**c**, **d**) display both the amplitude (*upper*) and the phase (*lower*) profiles

reconstruction with a normally incident reference in Fig. 5.12c results in the zero-order at the center and the focused image on one side and the blurred twin on the other. This is to be compared with Fig. 5.11b. If it is desired to have the focused image at the center, then a read reference wave with the same inclination as the write reference can be used. In Fig. 5.12d, the focused image is in the center and the zero-order is moved to the side. Also note that the zero-order consists of the $|E_{\mathrm{R}}|^2$ term as the bright square and the $|E_{\mathrm{O}}|^2$ term as a blurred spot within the square.

In order to accommodate the zero-order and the twin-image terms without aliasing, the object distance has to be large enough so that

$$X = \frac{N_x \lambda z}{X_0} \geq 3X_0 \tag{5.5}$$

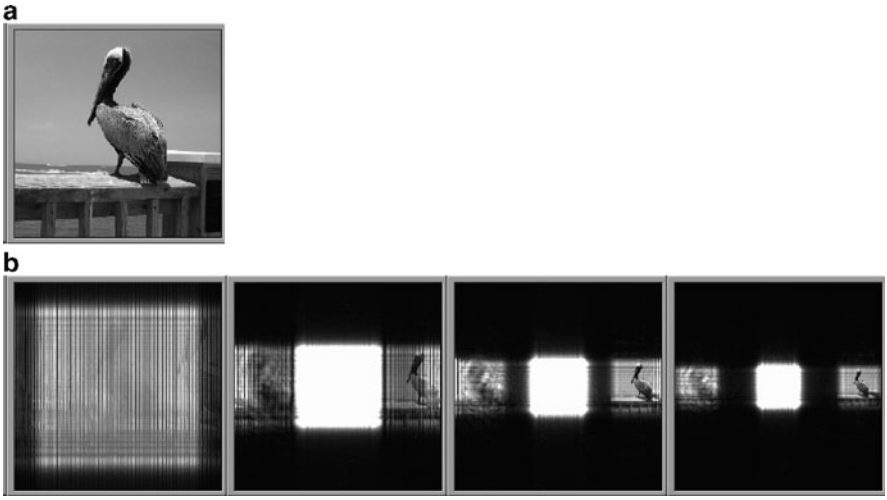

Fig. 5.13 Digital Fresnel hologram image vs. the reconstruction distance (the same as the object distance). (**a**) The object, 256 × 256 μm^2. Images at distances (**b**) 500, (**c**) 1,000, (**d**) 1,500, and (**e**) 2,000 μm

assuming that the object fills the screen size X_0. For our example, this requires $z \geq 1,213\,\mu\text{m}$. An example with an object that fills the screen is shown in Fig. 5.13. The object and the rec.onstruction distances vary as $z = 5,00,1,000,1,500,$ $2,000\,\mu\text{m}$ for Fig. 5.13b–e. Only in Fig. 5.13d, e are the images unhindered by the zero-order or the twin terms.

The variation of the frame size with object distance can be used as an advantage [25]. Placement at a large enough distance and the use of Fresnel transform allow imaging of an object larger than the CCD array size, such as in macroscopic metrology applications [23, 24, 26, 27]. Also an imaging lens can be used to form a magnified [28] or demagnified image of the object, which then propagates to the hologram plane. For example, in [24], a negative lens is used to form a demagnified image of a large object, thus reducing the spatial frequency bandwidth.

References

1. U. Schnars, and W. P. O. Juptner, "Digital recording and numerical reconstruction of holograms," Measurement Science & Technology **13**, R85-R101 (2002).
2. W. B. Xu, M. H. Jericho, I. A. Meinertzhagen, and H. J. Kreuzer, "Digital in-line holography for biological applications," Proceedings of the National Academy of Sciences of the United States of America **98**, 11301–11305 (2001).
3. F. Nicolas, S. Coetmellec, M. Brunel, and D. Lebrun, "Digital in-line holography with a sub-picosecond laser beam," Optics Communications **268**, 27–33 (2006).
4. H. J. Kreuzer, M. J. Jericho, I. A. Meinertzhagen, and W. B. Xu, "Digital in-line holography with photons and electrons," J. Phys.-Condes. Matter **13**, 10729–10741 (2001).

5. J. Garcia-Sucerquia, W. B. Xu, S. K. Jericho, P. Klages, M. H. Jericho, and H. J. Kreuzer, "Digital in-line holographic microscopy," Applied Optics **45**, 836–850 (2006).
6. M. Kempkes, E. Darakis, T. Khanam, A. Rajendran, V. Kariwala, M. Mazzotti, T. J. Naughton, and A. K. Asundi, "Three dimensional digital holographic profiling of micro-fibers," Optics Express **17**, 2938–2943 (2009).
7. G. Pedrini, P. Froning, H. Fessler, and H. J. Tiziani, "In-line digital holographic interferometry," Applied Optics **37**, 6262–6269 (1998).
8. L. Xu, J. M. Miao, and A. Asundi, "Properties of digital holography based on in-line configuration," Optical Engineering **39**, 3214–3219 (2000).
9. S. Grilli, P. Ferraro, S. De Nicola, A. Finizio, G. Pierattini, and R. Meucci, "Whole optical wavefields reconstruction by digital holography," Optics Express **9**, 294–302 (2001).
10. E. Marquardt, and J. Richter, "Digital image holography," Optical Engineering **37**, 1514–1519 (1998).
11. C. J. Mann, L. F. Yu, C. M. Lo, and M. K. Kim, "High-resolution quantitative phase-contrast microscopy by digital holography," Optics Express **13**, 8693–8698 (2005).
12. M. K. Kim, L. F. Yu, and C. J. Mann, "Interference techniques in digital holography," Journal of Optics a-Pure and Applied Optics **8**, S518-S523 (2006).
13. M. P. Arroyo, and J. Lobera, "A comparison of temporal, spatial and parallel phase shifting algorithms for digital image plane holography," Measurement Science & Technology **19**, 074006 (2008).
14. F. Dubois, L. Joannes, and J. C. Legros, "Improved three-dimensional imaging with a digital holography microscope with a source of partial spatial coherence," Applied Optics **38**, 7085–7094 (1999).
15. G. W. Stroke, "Lensless Fourier-Transform Method for Optical Holography," Applied Physics Letters **6**, 201–203 (1965).
16. J. W. Goodman, and R. W. Lawrence, "Digital Image Formation from Electronically Detected Holograms," Applied Physics Letters **11**, 77–79 (1967).
17. W. S. Haddad, D. Cullen, J. C. Solem, J. W. Longworth, A. McPherson, K. Boyer, and C. K. Rhodes, "Fourier-Transform Holographic Microscope," Appl. Opt. **31**, 4973–4978 (1992).
18. M. Gustafsson, M. Sebesta, B. Bengtsson, S. G. Pettersson, P. Egelberg, and T. Lenart, "High-resolution digital transmission microscopy - a Fourier holography approach," Opt. Lasers Eng. **41**, 553–563 (2004).
19. G. Pedrini, P. Froning, H. J. Tiziani, and F. M. Santoyo, "Shape measurement of microscopic structures using digital holograms," Opt. Commun. **164**, 257–268 (1999).
20. C. Wagner, S. Seebacher, W. Osten, and W. Juptner, "Digital recording and numerical reconstruction of lensless Fourier holograms in optical metrology," Appl. Opt. **38**, 4812–4820 (1999).
21. G. Pedrini, S. Schedin, and H. J. Tiziani, "Lensless digital-holographic interferometry for the measurement of large objects," Optics Communications **171**, 29–36 (1999).
22. G. Pedrini, S. Schedin, and H. J. Tiziani, "Aberration compensation in digital holographic reconstruction of microscopic objects," J. Mod. Opt. **48**, 1035–1041 (2001).
23. G. Pedrini, H. J. Tiziani, and Y. L. Zou, "Digital double pulse-TV-holography," Opt. Lasers Eng. **26**, 199–219 (1997).
24. U. Schnars, T. M. Kreis, and W. P. O. Juptner, "Digital recording and numerical reconstruction of holograms: Reduction of the spatial frequency spectrum," Opt. Eng. **35**, 977–982 (1996).
25. M. Jacquot, P. Sandoz, and G. Tribillon, "High resolution digital holography," Optics Communications **190**, 87–94 (2001).
26. U. Schnars, and W. Juptner, "Direct Recording of Holograms by a Ccd Target and Numerical Reconstruction," Appl. Opt. **33**, 179–181 (1994).
27. U. Schnars, and W. P. O. Juptner, "Digital Recording and Reconstruction of Holograms in Hologram Interferometry and Shearography," Appl. Opt. **33**, 4373–4377 (1994).
28. E. Cuche, P. Marquet, and C. Depeursinge, "Simultaneous amplitude-contrast and quantitative phase-contrast microscopy by numerical reconstruction of Fresnel off-axis holograms," Appl. Opt. **38**, 6994–7001 (1999).

Chapter 6
Theoretical Studies of Digital Holography

The diffraction theory is at the basis of development of digital holography and allows calculation of holographic images from the recorded holographic interference patterns [1]. In this chapter, we highlight some of the theoretical tools developed to enhance the capabilities of digital holography and applications.

6.1 Digital Sampling of Hologram

The finite size of and discrete sampling by the CCD array modify the holographic imaging properties that we obtained in Sect. 3.3 [2–13]. As shown in Fig. 6.1, suppose the size of the CCD array is $X_0 \times Y_0$ with $N_x \times N_y$ pixels, so that the pixel pitch is $\delta x_0 \times \delta y_0 = (X_0/N_x) \times (Y_0/N_y)$. Further suppose that the sensitive area of a CCD pixel is $\gamma_x \delta x_0 \times \gamma_y \delta y_0$, where γ_x and γ_y are the fill factors. The CCD sampling function is then written [5–8] as

$$P(x_0, y_0) = \text{rect}\left(\frac{x_0}{X_0}\right)\left[\text{comb}\left(\frac{x_0}{\delta x_0}\right) \odot \text{rect}\left(\frac{x_0}{\gamma \delta x_0}\right)\right], \tag{6.1}$$

where again we abbreviate the y-terms and also drop the subscript from γ. The comb function $\text{comb}(x/\delta x)$ is a series of delta functions with δx interval and the rectangle function $\text{rect}(x/a, y/b)$ has the value one within the rectangle of size $a \times b$ and zero outside. We consider the holographic image formation by point sources as in Sect. 3.3, but in (3.16), we multiply the sampling function $P(x_0, y_0)$ inside the Fresnel diffraction integral, so that

M.K. Kim, *Digital Holographic Microscopy: Principles, Techniques, and Applications*, Springer Series in Optical Sciences 162,
DOI 10.1007/978-1-4419-7793-9_6, © Springer Science+Business Media, LLC 2011

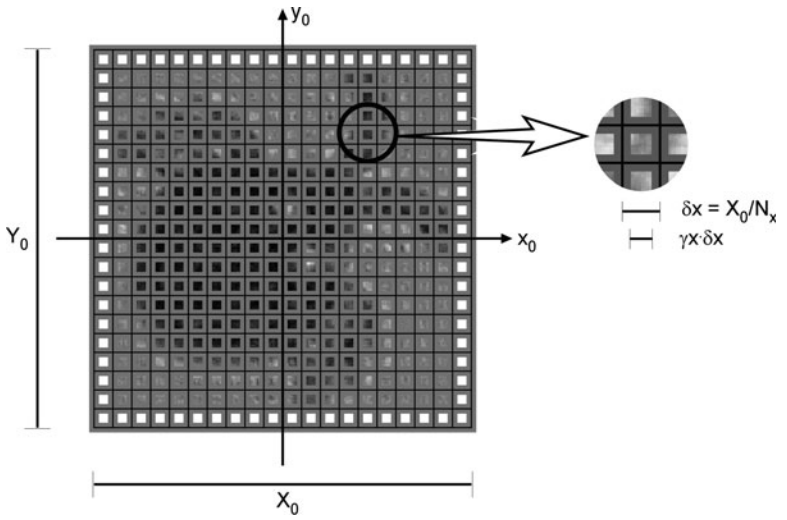

Fig. 6.1 Digital sampling of hologram

$$E^{\pm}(x,y;z) = -\frac{ik'}{2\pi z}\mathfrak{S}_1\mathfrak{S}_2\mathfrak{S}_3 \exp[\pm ik(z_1 - z_2) - ik'(z_3 - z) \pm ik\zeta_{12}] \times \iint\limits_{\Sigma_0} \mathrm{d}x_0 P(x_0) \exp\left[-\frac{ik'}{2}\left(\frac{1}{Z^{\pm}} - \frac{1}{z}\right)x_0^2 + ik'\left(\frac{X^{\pm}}{Z^{\pm}} - \frac{x}{z}\right)x_0 + \frac{ik}{2}\left(\pm\frac{x_{12}^2}{z_{12}} - \frac{\mu x_3^2}{z_3} + \frac{\mu x^2}{z}\right)\right]. \tag{6.2}$$

The effect of the sampling function on the integral is, for a function $f(x_0)$

$$\int\limits_{\Sigma_0} \mathrm{d}x_0 P(x_0) f(x_0) = \sum_{m=-X_0/2\delta x_0}^{X_0/2\delta x_0} \int_{(m-\gamma/2)\delta x_0}^{(m+\gamma/2)\delta x_0} \mathrm{d}x_0 f(x_0). \tag{6.3}$$

Also note that at the position of the holographic image, $z = Z^{\pm}$, and the integral and summation are easily carried out.

$$E^{\pm}(x,y;z) = -\frac{ik'}{2\pi z}\mathfrak{S}_1\mathfrak{S}_2\mathfrak{S}_3 \exp[\pm ik(z_1 - z_2) - ik'(z_3 - z) \pm ik\zeta_{12}] \exp\left[\frac{ik}{2}\left(\pm\frac{{x_{12}}^2}{z_{12}} - \frac{\mu {x_3}^2}{z_3} + \frac{\mu x^2}{z}\right)\right] \times \left\{\gamma\delta x_0 \exp\left[\frac{ik'}{Z^{\pm}}\left(x - X^{\pm}\right)\frac{\delta x_0}{2}\right] \frac{\sin\left[\frac{k'}{Z^{\pm}}\left(x - X^{\pm}\right)\frac{X_0}{2}\right]}{\sin\left[\frac{k'}{Z^{\pm}}\left(x - X^{\pm}\right)\frac{\delta x_0}{2}\right]} \mathrm{sinc}\left[\frac{k'}{Z^{\pm}}\left(x - X^{\pm}\right)\gamma\frac{\delta x_0}{2}\right]\right\}. \tag{6.4}$$

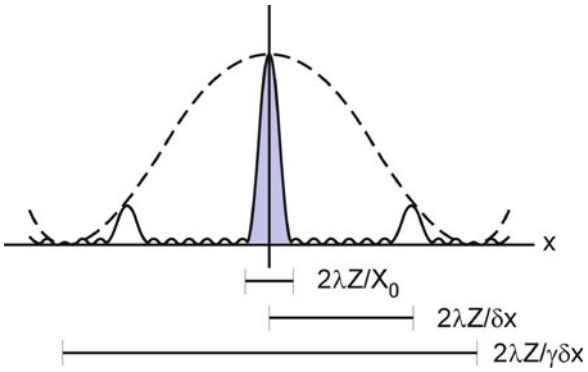

Fig. 6.2 PSF of discretized hologram

The PSF of discretized hologram (6.4) is illustrated in Fig. 6.2. The quantity inside the curly brackets of (6.4) shows the effect of the digital sampling [3]. The sinc function has a width of $4\pi Z^{\pm}/k'\gamma\delta x_0$ between the first zeroes. For a small fill factor $\gamma \to 0$, the image is uniform in amplitude throughout the image plane. On the other hand, integration over the pixel area with larger fill factor results in vignetting, especially for shorter image distance $Z^{\pm}$. The sine-over-sine factor of (6.4) gives the lateral resolution of a point image to be $4\pi Z^{\pm}/k'X_0$, which shows the expected dependence on the numerical aperture of the camera array [14]. Also note that the point image repeats over a period of $4\pi Z^{\pm}/k'\delta x_0$. This period has to be larger than the size of the camera array [4, 15], which leads to the minimum distance $z_{\min} = X^{\pm 2}/2\lambda N$, as seen in Sect. 4.2. To estimate the axial resolution, suppose all three source points are on the z-axis. Then the reconstructed field along the z-axis is given by

$$E^{\pm}(0,0;z) \propto \sum_{m=-X_0/2\delta x_0}^{X_0/2\delta x_0} \int_{(m-\gamma/2)\delta x_0}^{(m+\gamma/2)\delta x_0} \mathrm{d}x_0 \exp\left[-\frac{ik'}{2}\left(\frac{1}{Z^{\pm}}-\frac{1}{z}\right){x_0}^2\right]. \tag{6.5}$$

The integral-sum is close to zero unless the phase of the exponential varies slowly within the range X_0, which leads to the axial resolution being $2\lambda' Z^{\pm 2}/{X_0}^2$.

For a holographic microscopy setup with an objective lens, the source point $\mathcal{E}_1\delta(x-x_1, y-y_1, z-z_1)$ may in fact refer to an object point imaged and magnified by the lens. In that case, $\mathcal{E}_1$ is a point within the PSF of the image, and the description follows as above. Alternatively, and equivalently, $\mathcal{E}_1$ refers to an actual object point and the CCD array refers to its image projected into the object volume through the objective lens. In that case, the CCD array is demagnified by the lens and an object point is spread by a demagnified PSF as well.

The quadratic phase function, also known as chirp function, represents paraxial approximation of a spherical wavefront, and therefore has an important role in much of the diffraction theory. Digital sampling of quadratic phase function and its effect on digital holography image formation have been studied in detail [5, 6, 15, 16].

6.2 Wigner Distribution Function

The Wigner distribution function (WDF) is useful for intuitive visualization of the spatial and spatial-frequency content of a (one-dimensional) image [17–22]. The WDF of a one-dimensional function $f(x)$ is defined as

$$W_f(x,k) \equiv \int_{-\infty}^{\infty} \mathrm{d}x' f\left(x+\frac{1}{2}x'\right) f^*\left(x-\frac{1}{2}x'\right) \exp(-ikx'). \tag{6.6}$$

6.2.1 Basic Properties of WDF

The WDF has a number of interesting properties. The projections of WDF on the x- or k-axis represent the intensity and the power spectrum, respectively:

$$\begin{cases} \int \mathrm{d}k W_f(x,k) = |f(x)|^2, \\ \int \mathrm{d}x W_f(x,k) = \left|\tilde{f}(k)\right|^2, \end{cases} \tag{6.7}$$

where

$$\tilde{f}(k) = \int \mathrm{d}x f(x) \exp(-ikx) \tag{6.8}$$

is the Fourier transform of $f(x)$. In the following discussion, we are mainly interested in the support of the two-dimensional function $W_f(x,k)$ and so ignore overall constant factors from the expressions. The function $f(x)$ can be extracted from $W_f(x,k)$ through a Fourier transform

$$\mathfrak{F}^{-1}\left\{W_f\left(\frac{1}{2}x,k\right)\right\}[x] = \int \mathrm{d}k W_f\left(\frac{1}{2}x,k\right) \exp(ikx) = f(x)f^*(0). \tag{6.9}$$

The WDF of a point source is a one-dimensional delta function, a vertical line in the (x,k)-phase space diagram (Fig. 6.3a) while the WDF of a plane wave is a horizontal line (Fig. 6.3b)

$$f(x) = \exp(ik_x x) \quad \Rightarrow \quad W_f(x,k) = \delta(k-k_x). \tag{6.10}$$

The WDF of a quadratic phase function is a sloped line (Fig. 6.3c)

$$f(x) = \exp\left(i\alpha(x-x_0)^2\right) \quad \Rightarrow \quad W_f(x,k) = \delta(k-2\alpha(x-x_0)). \tag{6.11}$$

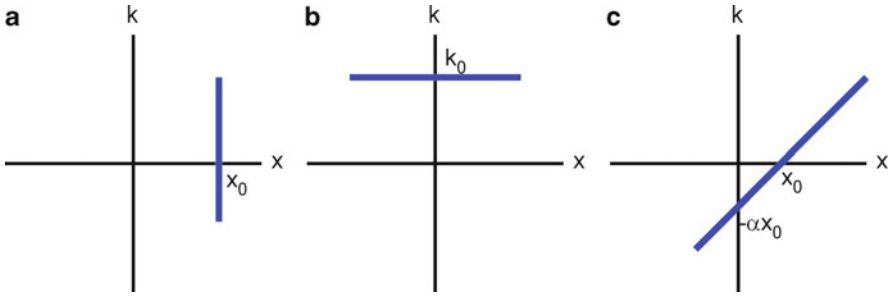

Fig. 6.3 WDF of (**a**) a point source, (**b**) a plane wave, and (**c**) a spherical wave

The Fourier transform of a function corresponds to exchange of x- and k-axes

$$W_{\hat{f}}(k,x) = W_f(x,k). \tag{6.12}$$

The WDF of a product of two functions is the convolution of the WDF's

$$h(x) = f(x)g(x) \quad \Rightarrow \quad W_h(x,k) = W_f(x,k) \odot_k W_g(x,k). \tag{6.13}$$

Combining the last two results, one can see that the multiplication of a function with a quadratic phase function causes shearing in the k-direction

$$f(x)\exp\left(i\alpha x^2\right) \quad \Rightarrow \quad W_f(x, k - 2\alpha x). \tag{6.14}$$

The WDF of the intensity is an autocorrelation

$$W_{|f|^2}(x,k) = W_f \odot_k W_{f^*} = W_f(x,k) \odot_k W_f(x,-k) = W_f \otimes_k W_f{}^*. \tag{6.15}$$

If the Fresnel diffraction is written in the form of (2.33), then its WDF corresponds to a shearing in the x-direction

$$f(x) = \int \mathrm{d}x_0 f_0(x_0) \exp\left(i\alpha(x - x_0)^2\right) \quad \Rightarrow \quad W_f(x,k) = W_{f_0}\left(x - \frac{k}{2\alpha}, k\right). \tag{6.16}$$

6.2.2 *Fourier Transform by a Lens*

We use these properties of WDF to describe various aspects of diffraction in the x–k phase space. For example, consider the Fourier-transforming property of a lens in Fig. 6.4. Suppose the input object has a spatial extent X_0 in the x-direction and a spectral bandwidth B_0 along the k-direction, as shown in Fig. 6.4a. The object is positioned at the front focal plane of the lens of focal length f and a screen is on the back focal plane. The propagation of input field to the lens over a distance $z = f$ is

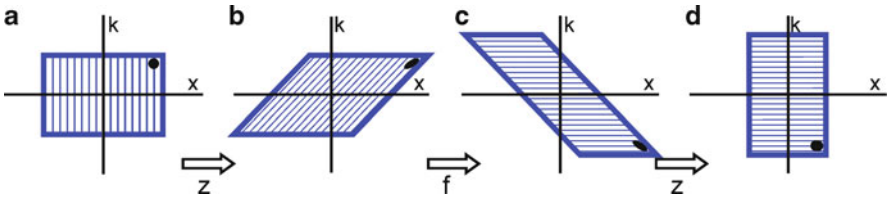

Fig. 6.4 Transformation of WDF during Fourier transform by a lens. (**a**) Input object, (**b**) propagation to the lens, (**c**) quadratic phase of the lens, and (**d**) propagation to the focal plane

described as a Fresnel diffraction, with $\alpha = \kappa/2z$ and $\kappa = 2\pi/\lambda$, which corresponds to a shearing of the WDF in the x-direction by $(f/\kappa)B_0$, as shown in Fig. 6.4b. The quadratic phase of the lens, with $\alpha_f = -(\kappa/2f)$, corresponds to a k-shear of $-(\kappa/f)X_0$, shown in Fig. 6.4c. Another Fresnel propagation to the screen causes an x-shear, so that the WDF acquires a rectangular shape with $X = (f/\kappa)B_0$ and $B = (\kappa/f)X_0$. The black dot and the hatch direction in each diagram provides a guide for how the WDF shape changes through these operations. The WDF has rotated by 90°, which indeed represents a Fourier transform.

6.2.3 *Fourier Holography*

Next consider the process of Fourier transform holography (Fig. 6.5). The rectangular area in Fig. 6.5a represents the WDF of the object, while the thick vertical line is a point source at $x = x_0$ on the object plane. Both the object and the reference pass through the lens in a 2f-system, causing the WDF to rotate by 90° (Fig. 6.5b). Now the hologram records the intensity of the field, that is,

$$I = |E_R|^2 + |E_O|^2 + E_R E_O{}^* + E_R{}^* E_O. \tag{6.17}$$

The WDF of the intensity consists of the four terms

$$\begin{aligned} W_I = {} & W_R \otimes W_R{}^* + W_O \otimes W_O{}^* + W_R(x,k) \odot W_O(x,-k) \\ & + W_R(x,-k) \odot W_O(x,k). \end{aligned} \tag{6.18}$$

In Fig. 6.5c, the thick horizontal line at $k = 0$ is the autocorrelation of the reference and the central vertical rectangle of height $2(\kappa/f)X_0$ is the autocorrelation of the object. The pair of convolutions with the reference gives the upper and the lower rectangles of size $X' = (f/\kappa)B_0$ and $B' = (\kappa/f)X_0$. The reconstruction consists of another Fourier transform that rotates the WDF by 90° again (Fig. 6.5d). The final image consists of the reference spot, the zero-order object, and the well-focused twin images. The object WDF has size $X = X_0$ and $B = B_0$. It is clear that in order to be able to separate the image from the zero-order, the reference point source has to be positioned at $|x_0| > (3/2)X_0$.

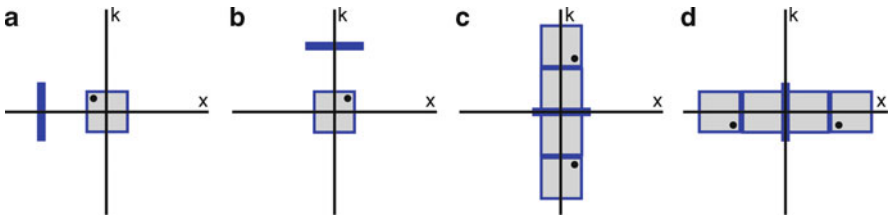

Fig. 6.5 Transformation of WDF during Fourier holography. (**a**) Input object and point source reference, (**b**) Fourier transform by lens, (**c**) intensity of the hologram, and (**d**) Fourier transform

6.2.4 Fresnel Holography

Another example is the Fresnel holography of Fig. 6.6. Here the reference is a plane wave with spatial frequency $k = k_0$, shown as a thick horizontal line in Fig. 6.6a. The object field propagates to the hologram plane over a distance z_0, resulting in the x-shearing by $(z_0/\kappa)B_0$ (Fig. 6.6b). The autocorrelation of the reference is again a thick horizontal line at $k = 0$ of Fig. 6.6c. The autocorrelation of the object is now a rhombus shape, while the two convolutions are the reflected pair of sheared rectangles (parallelograms). For reconstruction, propagation over the same distance z results in the shape of WDF in Fig. 6.6d. When $z = z_0$ exactly, the shearing of the upper parallelogram restores the original rectangular WDF of the object. Separation, in x-direction, of the image from the zero-order is complete if $|k_0| > (3/2)B_0$. Also note that the twin-image WDF is distorted corresponding to a propagation of a distance $2z_0$.

6.2.5 Space–Bandwidth Product

The phase space diagram of Wigner distribution function is also useful for consideration of the space–bandwidth product (SBP), which is proportional to the number of pixels required to represent the image [21]. For a one-dimensional image, it is equal to the area of the rectangle that encloses the WDF. Figure 6.7 shows the WDF of three types of holograms – (a) Fourier, (b) Fresnel, and (c) image plane holograms. For the Fourier hologram, the SBP is X_0B_0, the same as the object itself. For the Fresnel hologram, it is $X_0B_0 + (z_0/\kappa){B_0}^2$. The inverse of the "overhead" SBP, divided by 2π, is called the Fresnel number $N_F = \left[\lambda z_0 {B_0}^2\right]^{-1}$. The hologram needs the same bandwidth as the object but a larger area. For the image plane hologram, the image of the object is formed using a lens of focal length f with a magnification M. The magnification results in the size of WDF $MX_0 \times B_0/M$. But the image also contains a quadratic phase factor $\exp((i\kappa/2fM)x^2)$ and the WDF has a vertical shear, so that the SBP is $X_0B_0 + (\kappa/f)M{X_0}^2$. Referring to Figs. 6.5 and 6.6, these holograms require four times the bandwidth and SBP of the single image terms, two for recording the intensity and two for separating the image from the zero-order.

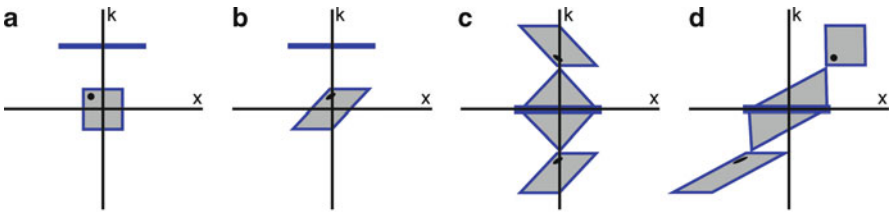

Fig. 6.6 Transformation of WDF during Fresnel holography. (**a**) Input object and plane-wave reference, (**b**) propagation to the hologram plane, (**c**) intensity of the hologram, and (**d**) propagation to the image plane

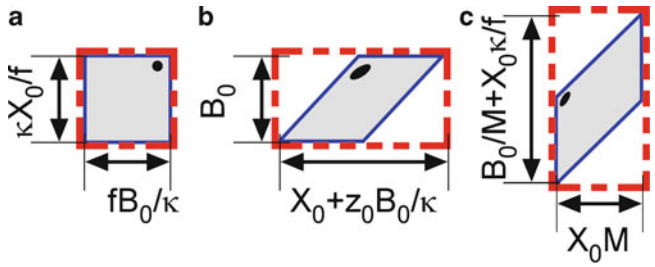

Fig. 6.7 Space–bandwidth of WDF for (**a**) Fourier hologram, (**b**) Fresnel hologram, and (**c**) image plane holograms

6.3 Fractional-Order Fourier Transform

In recent years, the fractional-order Fourier transform (FRFT) has been attracting significant attention in optical processing. In digital holography, in particular, FRFT is seen to be useful for analyzing holographic reconstruction with astigmatic geometry. It also has conceptual significance as a generalization of Fourier transform and provides a connection between Fresnel and Fraunhofer diffraction regimes [18, 23].

Referring to Fig. 6.8, recall that the Fresnel diffraction field $E(x, y; z)$ due to an input field $E_0(x_0, y_0)$ at $z = 0$ is given by, with the usual 1D abbreviation,

$$E(x,y;z) = -\frac{ik}{2\pi z}\exp(ikz)\exp\left(\frac{ik}{2z}x^2\right) \times \iint\limits_{\Sigma_0} \mathrm{d}x_0 E_0(x_0,y_0)\exp\left(\frac{ik}{2z}x_0^2\right)\exp\left(-\frac{ik}{z}xx_0\right). \tag{6.19}$$

The FRFT of order $\alpha \in [0, \pi/2]$ of the function $f(x)$ is defined by

$$\mathfrak{F}_\alpha\{f(u_0)\}[u] = \sqrt{\frac{\exp(i\alpha)}{2\pi i\sin\alpha}}\exp\left(\frac{i}{2}\frac{\cos\alpha}{\sin\alpha}u^2\right), \times \int \mathrm{d}u_0 f(u_0)\exp\left(\frac{i}{2}\frac{\cos\alpha}{\sin\alpha}u^2\right)\exp\left(\frac{-i}{\sin\alpha}uu_0\right), \tag{6.20}$$

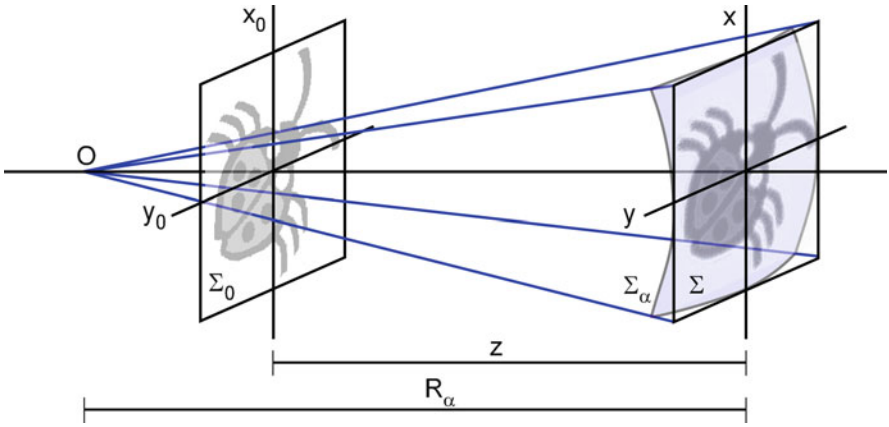

Fig. 6.8 Geometry of fractional-order Fourier transform

which has some resemblance with (6.19) above for Fresnel diffraction. Making the substitutions

$$u_0 = \sqrt{\frac{k}{z}\frac{\sin\alpha}{\cos\alpha}}x_0, \qquad u = \sqrt{\frac{k}{z}\sin\alpha\cos\alpha}x,$$
$$F_0(u_0) = E_0\left(\sqrt{\frac{z}{k}\frac{\cos\alpha}{\sin\alpha}}u_0\right), \quad F(u) = E\left(\sqrt{\frac{z}{k\sin\alpha\cos\alpha}}u\right), \tag{6.21}$$

we obtain

$$F(u) = \exp(ikz)(\cos\alpha)\exp(-i\alpha)\exp\left[\frac{i}{2}(\tan\alpha)u^2\right]\mathfrak{F}_\alpha\{F_0(u_0)\}[u]. \tag{6.22}$$

Therefore, the Fresnel diffraction is a FRFT, except for the last exponential. But

$$\exp\left[\frac{i}{2}(\tan\alpha)u^2\right] = \exp\left[i\frac{k\sin^2\alpha}{2z}x^2\right], \tag{6.23}$$

which is a paraxial approximation of a spherical surface centered at a distance of $R_\alpha = (z/\sin^2\alpha)$ from (x, y) plane. This factor can be compensated for if the diffraction field is observed on the spherical surface or by placing an appropriate lens on the (x, y) plane. Then,

$$F(u) = \exp(ikz)(\cos\alpha)\exp(-i\alpha)\mathfrak{F}_\alpha\{F_0(u_0)\}[u]. \tag{6.24}$$

Note that $\mathfrak{F}_0\{f\} = f$, so that when $z \to 0$, then $\alpha \to 0$ and $F(u) = F_0(u_0)$. Furthermore, $\mathfrak{F}_{\pi/2}\{f\} = \mathfrak{F}\{f\}$, that is, Fourier transform, so that when $z \to \infty$,

then $\alpha \to \pi/2$ and $F(u) \propto \mathfrak{F}\{F_0(u_0)\}[u]$. Thus, as one moves from $z = 0$ to finite distances and then to larger distances, the diffraction field goes from being identical to the input to Fresnel diffraction, and then to Fraunhofer diffraction regimes, as α varies in the range 0 to $\pi/2$.

Discretized form of FRFT has been developed [24, 25]. FRFT may be used in reconstruction from in-line hologram [26], in analyzing tilt and translation of a surface from a single hologram [27], and applied to digital holography of elliptical, astigmatic Gaussian beams [28–30]. It has been used in an iterative feedback loop to synthesize field patterns at multiple focal planes [31].

6.4 Wavelets

The wavelets are a family of functions, obtained from one single function $u(x)$, indexed by two labels as

$$u_{ab}(x) = \frac{1}{a} u\left(\frac{x-b}{a}\right), \tag{6.25}$$

where a represents scaling or frequency and b represents shift. Wavelet transform of a function $f(x)$ is the inner product of the function with the wavelet function:

$$f_{ab} = \langle f(x) \mid u_{ab}(x) \rangle = \int \mathrm{d}x f^*(x) u_{ab}(x). \tag{6.26}$$

As an illustration, we analyze holographic reconstruction using Gabor wavelets [32]. The Gabor wavelets are generated from

$$u(x) = \exp\left(-px^2 + ix\right), \tag{6.27}$$

which is a sinusoidal oscillation with a Gaussian envelope, so that

$$u_{ab}(x) = \frac{1}{a} \exp\left[-p\left(\frac{x-b}{a}\right)^2 + i\left(\frac{x-b}{a}\right)\right]. \tag{6.28}$$

Their Fourier transforms are similarly Gaussian:

$$\tilde{u}(x) = \frac{1}{\sqrt{2p}} \exp\left[-\frac{(1-k)^2}{4p}\right], \tag{6.29}$$

$$\tilde{u}_{ab}(k) = \frac{1}{\sqrt{2p}} \exp\left[-\frac{(1-ak)^2}{4p}\right] \exp(-ikb). \tag{6.30}$$

Lets take a simple case of a purely phase object in superposition with a plane reference wave

$$\begin{cases} E_{\mathrm{O}}(x,y) = \mathscr{E}_{\mathrm{O}} \exp[i\varphi(x,y)], \\ E_{\mathrm{R}}(x,y) = \mathscr{E}_{\mathrm{R}} \exp[i\beta x], \end{cases} \tag{6.31}$$

so that the total intensity is

$$I(x,y) = {\mathscr{E}_{\mathrm{O}}}^2 + {\mathscr{E}_{\mathrm{R}}}^2 + \mathscr{E}_{\mathrm{O}}\mathscr{E}_{\mathrm{R}} \exp[i(\varphi - \beta x)] + \mathscr{E}_{\mathrm{O}}\mathscr{E}_{\mathrm{R}} \exp[-i(\varphi - \beta x)]. \tag{6.32}$$

Take a specific value of y, and consider the intensity a function of x, and further suppose that the phase varies smooth enough that we can write

$$\varphi(x) - \beta x = [\varphi(b) - \beta b] + [\varphi'(b) - \beta](x - b) + \cdots. \tag{6.33}$$

Then the wavelet transform of the intensity is

$$\begin{aligned} I_{ab} =& \left({\mathscr{E}_{\mathrm{O}}}^2 + {\mathscr{E}_{\mathrm{R}}}^2\right)\sqrt{\frac{\pi}{p}}\exp\left(\frac{-1}{4p}\right) \\ &+ \mathscr{E}_{\mathrm{O}}\mathscr{E}_{\mathrm{R}} \exp\{+i[\varphi(b) - \beta b]\}\sqrt{\frac{\pi}{p}}\exp\left(-\frac{1}{4p}[1 + a(\varphi'(b) - \beta)]^2\right) \\ &+ \mathscr{E}_{\mathrm{O}}\mathscr{E}_{\mathrm{R}} \exp\{-i[\varphi(b) - \beta b]\}\sqrt{\frac{\pi}{p}}\exp\left(-\frac{1}{4p}[1 - a(\varphi'(b) - \beta)]^2\right). \end{aligned} \tag{6.34}$$

For positive a, $|I_{ab}|$ is maximum when

$$a = \frac{1}{\varphi'(b) - \beta}, \tag{6.35}$$

which is called the ridge of the wavelet. The wavelet coefficient at the ridge of Gabor wavelet transform is

$$\begin{aligned} I(b) =& \left({\mathscr{E}_{\mathrm{O}}}^2 + {\mathscr{E}_{\mathrm{R}}}^2\right)\sqrt{\frac{\pi}{p}}\exp\left(-\frac{1}{4p}\right) \\ &+ \mathscr{E}_{\mathrm{O}}\mathscr{E}_{\mathrm{R}} \exp\{+i[\varphi(b) - \beta b]\}\sqrt{\frac{\pi}{p}}\exp\left(-\frac{1}{p}\right) \\ &+ \mathscr{E}_{\mathrm{O}}\mathscr{E}_{\mathrm{R}} \exp\{-i[\varphi(b) - \beta b]\}\sqrt{\frac{\pi}{p}}. \end{aligned} \tag{6.36}$$

Choose a sufficiently small value of p, so that

$$I(b) \approx \mathscr{E}_{\mathrm{O}}\mathscr{E}_{\mathrm{R}} \exp\{-i[\varphi(b) - \beta b]\}\sqrt{\frac{\pi}{p}} \tag{6.37}$$

and one can recover the object field by

$$\mathfrak{S}_{\mathrm{O}} \exp[-i\varphi(b)] = \frac{I(b)}{\mathfrak{S}_{\mathrm{R}}} \sqrt{\frac{p}{\pi}} \exp(-i\beta b). \tag{6.38}$$

Wavelet transform has been a useful processing tool in short-coherence interferometry [33, 34], vibration analysis in digital speckle pattern interferometry [35], and profilometry by fringe projection [36]. Diffraction and holography can be looked at from a wavelet framework [37]. A specific type of wavelet called Fresnelet has been devised for analysis of digital holography [38]. Fourier transform is a global operation that is usually used for the analysis of stationary signal, but it has a poor capacity for localizing the signal properties. The ridge of wavelet transform can be used to automatically optimize holographic phase-contrast microscopy, as described above [32, 39], whereas in the conventional methods such as Huygens convolution or angular spectrum, one has to manually filter the angular spectrum.

References

1. E. Wolf, "Determination of Amplitude and Phase of Scattered Fields by Holography," Journal of the Optical Society of America **60**, 18–20 (1970).
2. C. Wagner, S. Seebacher, W. Osten, and W. Juptner, "Digital recording and numerical reconstruction of lensless Fourier holograms in optical metrology," Applied Optics **38**, 4812–4820 (1999).
3. I. Yamaguchi, J. Kato, S. Ohta, and J. Mizuno, "Image formation in phase-shifting digital holography and applications to microscopy," Appl. Opt. **40**, 6177–6186 (2001).
4. L. Onural, "Sampling of the diffraction field," Applied Optics **39**, 5929–5935 (2000).
5. T. M. Kreis, "Frequency analysis of digital holography," Optical Engineering **41**, 771–778 (2002).
6. T. M. Kreis, "Frequency analysis of digital holography with reconstruction by convolution," Optical Engineering **41**, 1829–1839 (2002).
7. C. S. Guo, L. Zhang, Z. Y. Rong, and H. T. Wang, "Effect of the fill factor of CCD pixels on digital holograms: comment on the papers "Frequency analysis of digital holography" and "Frequency analysis of digital holography with reconstruction by convolution"," Optical Engineering **42**, 2768–2771 (2003).
8. T. M. Kreis, "Response to "Effect of the fill factor of CCD pixels on digital holograms: comment on the papers 'Frequency analysis of digital holography' and 'Frequency analysis of digital holography with reconstruction by convolution'", Optical Engineering **42**, 2772–2772 (2003).
9. K. Khare, and N. George, "Direct coarse sampling of electronic holograms," Optics Letters **28**, 1004–1006 (2003).
10. A. Stern, and B. Javidi, "Analysis of practical sampling and reconstruction from Fresnel fields," Optical Engineering **43**, 239–250 (2004).
11. H. Z. Jin, H. Wan, Y. P. Zhang, Y. Li, and P. Z. Qiu, "The influence of structural parameters of CCD on the reconstruction image of digital holograms," Journal of Modern Optics **55**, 2989–3000 (2008).

12. P. Picart, and J. Leval, "General theoretical formulation of image formation in digital Fresnel holography," Journal of the Optical Society of America a-Optics Image Science and Vision **25**, 1744–1761 (2008).
13. D. P. Kelly, B. M. Hennelly, N. Pandey, T. J. Naughton, and W. T. Rhodes, "Resolution limits in practical digital holographic systems," Optical Engineering **48**, 095801 (2009).
14. E. Wolf, "Determination of the Amplitude and the Phase of Scattered Fields by Holography," Journal of the Optical Society of America **60**, 18–20 (1970).
15. L. Onural, "Some mathematical properties of the uniformly sampled quadratic phase function and associated issues in digital Fresnel diffraction simulations," Optical Engineering **43**, 2557–2563 (2004).
16. E. Carcole, J. Campos, and S. Bosch, "Diffraction Theory of Fresnel Lenses Encoded in Low-Resolution Devices," Applied Optics **33**, 162–174 (1994).
17. L. Xu, X. Y. Peng, Z. X. Guo, J. M. Miao, and A. Asundi, "Imaging analysis of digital holography," Optics Express **13**, 2444–2452 (2005).
18. B. M. Hennelly, and J. T. Sheridan, "Generalizing, optimizing, and inventing numerical algorithms for the fractional Fourier, Fresnel, and linear canonical transforms," Journal of the Optical Society of America a-Optics Image Science and Vision **22**, 917–927 (2005).
19. A. Stern, and B. Javidi, "Improved-resolution digital holography using the generalized sampling theorem for locally band-limited fields," Journal of the Optical Society of America a-Optics Image Science and Vision **23**, 1227–1235 (2006).
20. G. Situ, and J. T. Sheridan, "Holography: an interpretation from the phase-space point of view," Optics Letters **32**, 3492–3494 (2007).
21. A. Stern, and B. Javidi, "Space-bandwith conditions for efficient phase-shifting digital holographic microscopy," Journal of the Optical Society of America a-Optics Image Science and Vision **25**, 736–741 (2008).
22. M. Testorf, and A. W. Lohmann, "Holography in phase space," Applied Optics **47**, A70-A77 (2008).
23. P. Pellat-Finet, "Fresnel diffraction and fractional-order Fourier transform," Opt. Lett. **19**, 1388–1390 (1994).
24. Z.-T. Deng, H. J. Caulfield, and M. Schamschula, "Fractional discrete Fourier transforms," Opt. Lett. **21**, 1430–1432 (1996).
25. S. C. Pei, and M. H. Yeh, "Improved discrete fractional Fourier transform," Opt. Lett. **22**, 1047–1049 (1997).
26. Y. Zhang, G. Pedrini, W. Osten, and H. J. Tiziani, "Applications of fractional transforms to object reconstruction from in-line holograms," Optics Letters **29**, 1793–1795 (2004).
27. J. T. Sheridan, and R. Patten, "Holographic interferometry and the fractional Fourier transformation," Opt. Lett. **25**, 448–450 (2000).
28. F. Nicolas, S. Coetmellec, M. Brunel, D. Allano, D. Lebrun, and A. Janssen, "Application of the fractional Fourier transformation to digital holography recorded by an elliptical, astigmatic Gaussian beam," Journal of the Optical Society of America a-Optics Image Science and Vision **22**, 2569–2577 (2005).
29. N. Verrier, S. Coetmellec, M. Brunel, and D. Lebrun, "Digital in-line holography in thick optical systems: application to visualization in pipes," Applied Optics **47**, 4147–4157 (2008).
30. N. Verrier, S. Coetmellec, M. Brunel, D. Lebrun, and A. Janssen, "Digital in-line holography with an elliptical, astigmatic Gaussian beam: wide-angle reconstruction," Journal of the Optical Society of America a-Optics Image Science and Vision **25**, 1459–1466 (2008).
31. J. Hahn, H. Kim, and B. Lee, "Optical implementation of iterative fractional Fourier transform algorithm," Optics Express **14**, 11103–11112 (2006).
32. J. W. Weng, J. G. Zhong, and C. Y. Hu, "Phase reconstruction of digital holography with the peak of the two-dimensional Gabor wavelet transform," Applied Optics **48**, 3308–3316 (2009).
33. P. Sandoz, "Wavelet transform as a processing tool in white-light interferometry," Opt. Lett. **22**, 1065–1067 (1997).

34. R. Recknagel, and G. Notni, "Analysis of white light interferograms using wavelet methods," Opt. Comm. **148**, 122–128 (1998).
35. C. Shakher, R. Kumar, S. K. Singh, and S. A. Kazmi, "Application of wavelet filtering for vibration analysis using digital speckle pattern interferometry," Optical Engineering **41**, 176–180 (2002).
36. J. Zhong, and J. Weng, "Spatial carrier-fringe pattern analysis by means of wavelet transform: wavelet transform profilometry," Appl. Opt. **43**, 4993–4998 (2004).
37. L. Onural, "Diffraction from a Wavelet Point-of-View," Optics Letters **18**, 846–848 (1993).
38. M. Liebling, T. Blu, and M. Unser, "Fresnelets: New multiresolution wavelet bases for digital holography," IEEE Trans. Image Process. **12**, 29–43 (2003).
39. J. W. Weng, J. G. Zhong, and C. Y. Hu, "Digital reconstruction based on angular spectrum diffraction with the ridge of wavelet transform in holographic phase-contrast microscopy," Optics Express **16**, 21971–21981 (2008).

Chapter 7
Suppression of DC and Twin-Image Terms

The intensity distribution on a hologram contains four terms

$$I_H = |E_R + E_O|^2 = |E_R|^2 + |E_O|^2 + E_R{}^* E_O + E_R E_O{}^* \equiv I_R + I_O + \mathcal{E}_O + \mathcal{E}_O^*. \tag{7.1}$$

Of these, normally only one of the last two terms yields the desired holographic image, while the other terms – the zero-order and twin-image terms – only contribute to blurring and interference of the image. This is especially true in in-line configurations where all four terms are superposed on top of each other, but even in off-axis configurations they can limit the number of usable pixels and cause degradation of images. It is therefore a major consideration in any holography system design and there have been developed a fairly large number of techniques addressing the "dc and twin-image problem." Some of these remove the DC term only, while others can suppress the twin image as well.

7.1 Suppression of DC Terms

We illustrate the following methods by simulation examples using the test pattern of Fig. 7.1a, with 256 ×256 pixels of 1 μm pitch and assuming $\lambda = 0.633\,\mu m$. (Note that the group and element numbers of these simulated patterns do not correspond to actual USAF resolution target.) The object and the reconstruction distances are taken to be $z = 1,000\,\mu m$. The in-line hologram of Fig. 7.1b contains all of the four terms of (7.1). The reconstruction in Fig. 7.1c, therefore, shows an in-focus image, $\mathcal{E}_O$, and the defocused twin image, $\mathcal{E}_O{}^*$. It also contains the zero-order reference, I_R, and object, I_O, intensities as blurred background.

A simplest way to deal with the DC term is by subtraction of the average intensity of the hologram $\bar{I}_H$, as is done in Fig. 7.2a [1]. The reconstructed image in Fig. 7.2b is similar to Fig. 7.1c. In this synthesized example, the reference is a

M.K. Kim, *Digital Holographic Microscopy: Principles, Techniques, and Applications*, Springer Series in Optical Sciences 162,
DOI 10.1007/978-1-4419-7793-9_7, © Springer Science+Business Media, LLC 2011

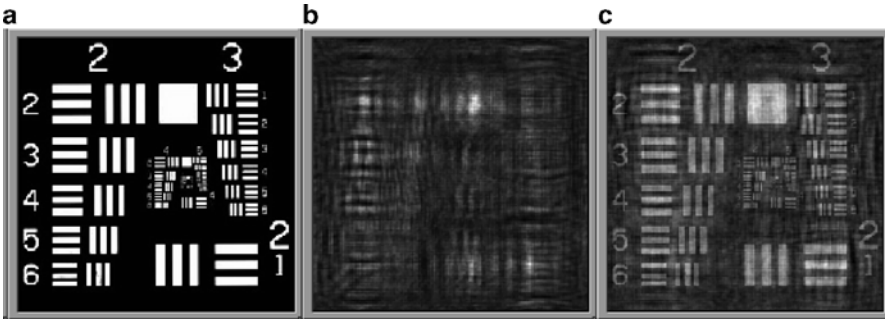

Fig. 7.1 (**a**) Object target pattern, with 256 × 256 μm^2, 256 × 256 pixels; (**b**) hologram I_H; and (**c**) image reconstructed from I_H

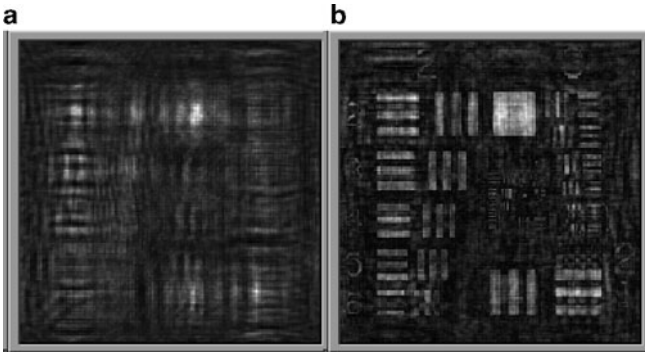

Fig. 7.2 (**a**) $I_H' = I_H - \bar{I}_H$ and (**b**) image reconstructed from I_H'

perfect plane wave, or a constant, and therefore the subtraction of the reference is perfect. In real experiment, the reference may in fact contain nonuniformity. The method may be improved by first taking the Fourier transform of the hologram and zeroing out a central spot of several pixels in diameter, that is, a high pass filtering [1]. Because it still leaves the object component I_O, removal of the reference component alone may not have satisfactory effect. On the other hand, if the reference is much stronger than the object field, then the I_O term may be negligible compared to the other terms and the removal of I_R alone may have a sufficient effect.

The zero-order terms I_R and I_O can be completely removed by taking separate exposures of the reference and object beams as well as the hologram exposure (Fig. 7.3). The reconstructed image Fig. 7.3c is only disturbed by the out-of-focus twin image. Use of the off-axis configuration can separate the twin image and reduce its interference. This method can also reduce the effect of nonuniform reference. The apparatus and the object need to be stable during the multiple exposures, and the method has limitations for dynamic objects.

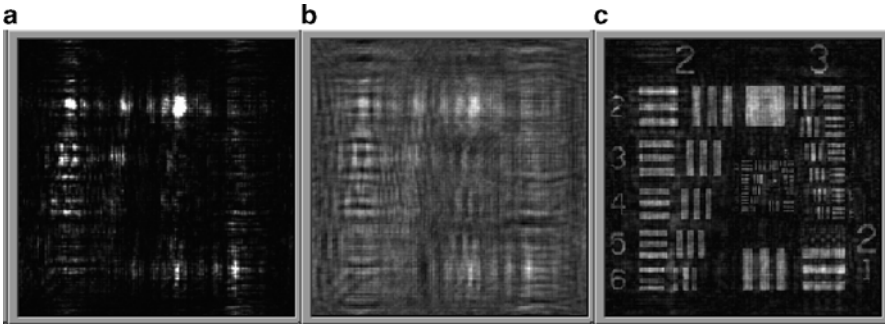

Fig. 7.3 (**a**) I_O, (**b**) $I_H' = I_H - I_R - I_O$, and (**c**) image reconstructed from I_H'

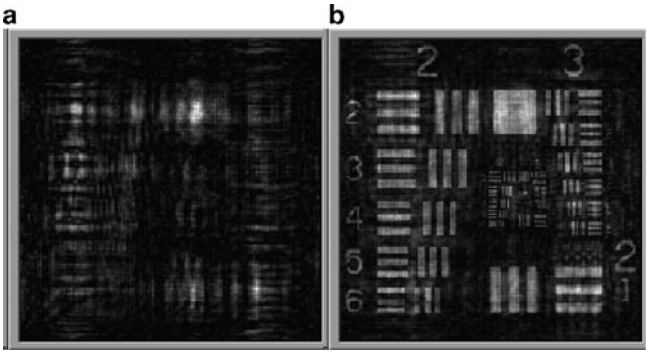

Fig. 7.4 (**a**) I_H' of (7.4) and (**b**) image reconstructed from I_H'

A more efficient method is provided by the example of Fig. 7.4 [2], noting that

$$\begin{aligned}(I_H - I_R)^2 &= I_O(2I_H - I_O) + (E_R{}^* E_O)^2 + (E_R E_O{}^*)^2 \\ &\approx I_O(2I_H - I_O) + 2I_O I_R. \end{aligned} \tag{7.2}$$

The last approximation may be justified if $\mathrm{Im}(E_R{}^* E_O)$ is small. Also assume that $I_R \gg I_O$. Then

$$I_O \approx \frac{(I_H - I_R)^2}{2(I_H + I_R)} \tag{7.3}$$

and

$$\begin{aligned} E_R{}^* E_O + E_R E_O{}^* &= I_H - I_R - I_O \\ &\approx I_H - I_R - \frac{(I_H - I_R)^2}{2(I_H + I_R)} = I_H{}'. \end{aligned} \tag{7.4}$$

This method requires two exposures I_H and I_R to remove the zero-order terms. The reconstructed image in Fig. 7.4b has comparable quality as the previous example.

7.2 Phase-Shifting Methods

Phase-shifting techniques play important roles especially in digital holography, because addition, subtraction, and other manipulations of phase-shifted holograms are easily carried out as simple arithmetic manipulations of numerical arrays. This is in sharp contrast to analog holography. For example, subtraction of two holograms was considered for removal of twin images even in the earliest years of holography development [3]. The subtraction was accomplished by overlap of two hologram prints, one positive and the other negative, in a cumbersome and not very satisfactory process.

The first method requires exposure of two holograms, $I_H(0)$ and $I_H(\alpha)$, while the global phase of the object is shifted by α between the two exposures by, for example, inserting a glass plate [4]. Two additional exposures of I_R and I_O are also taken. Then

$$\begin{cases} I_H(0) - I_R - I_O = E_R E_O{}^* + E_R{}^* E_O, \\ I_H(\alpha) - I_R - I_O = E_R E_O{}'^* e^{-i\alpha} + E_R{}^* E_O e^{i\alpha}, \end{cases} \tag{7.5}$$

so that

$$\begin{aligned} I_H{}' &= [I_H(0) - I_R - I_O] - [I_H(\alpha) - I_R - I_O] e^{i\alpha}, \\ &= E_R{}^* E_O \left(1 - e^{i2\alpha}\right). \end{aligned} \tag{7.6}$$

This method requires four exposures plus the value of phase shift, its optimal value being $\pi/2$. For illustration, Fig. 7.5a shows the angular spectrum (Fourier spectrum) of the hologram $I_H(0)$, with off-axis configuration so that the spectral terms appear separated. It shows the central zero-order and the pair of twin images in the upper right and lower left corners. In contrast, the angular spectrum of the modified hologram $I_H{}'$ in Fig. 7.5b contains only a single spot. Figure 7.5c is the modified hologram $I_H{}'$, and Fig. 7.5d is its reconstructed image.

Alternatively [4], three holograms, I_0, I_1, and I_2, are taken while the object phase is shifted by 0, α_1, and α_2, so that

$$I_m = I_H(\alpha_m) = I_R + I_O + E_R{}^* E_O e^{i\alpha_m} + E_R E_O{}^* e^{-i\alpha_m} \quad (m = 0, 1, 2). \tag{7.7}$$

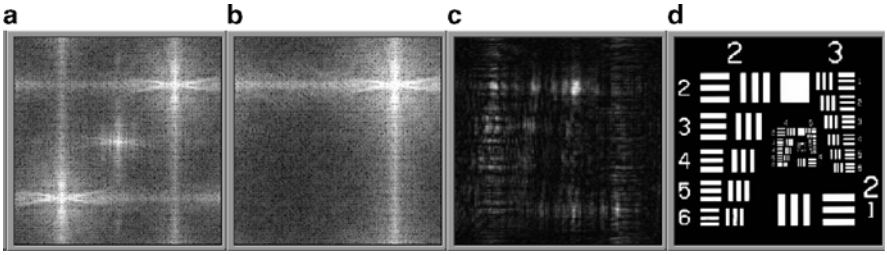

Fig. 7.5 (**a**) Angular spectrum of I_H, (**b**) angular spectrum of I_H' in (7.6), (**c**) I_H', and (**d**) reconstructed image from I_H'. (Angular spectra are plotted in logarithmic intensity scales)

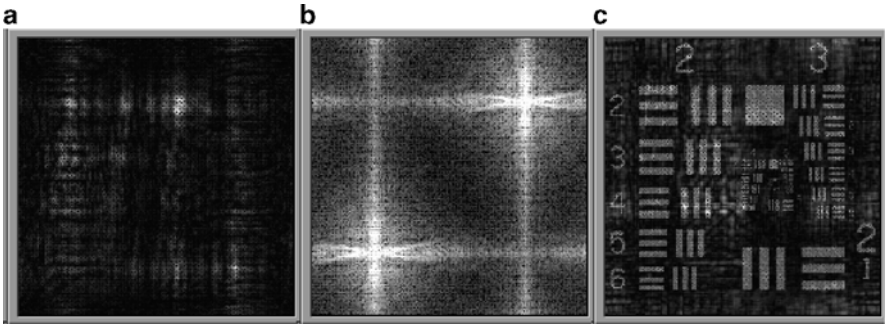

Fig. 7.6 (**a**) The modified hologram I_H' of (7.9), (**b**) its angular spectrum, and (**c**) reconstructed image

Then it follows

$$I_H' = \frac{I_0 - I_1}{1 - e^{-i\alpha_1}} - \frac{I_0 - I_2}{1 - e^{-i\alpha_2}} = {E_R}^* E_0 \left[\frac{1 - e^{i\alpha_1}}{1 - e^{-i\alpha_1}} - \frac{1 - e^{i\alpha_2}}{1 - e^{-i\alpha_2}} \right]. \tag{7.8}$$

The modified hologram and its angular spectrum are essentially the same as in Fig. 7.5. This method needs three camera exposures and the two values of phase shift.

Another method [5, 6] takes two phase-shifted holograms, $I_H(0)$ and $I_H(\alpha)$, to remove the zero-order but not the twin term (Fig. 7.6). For

$$I_H' = I_H(0) - I_H(\alpha) = +E_R^* E_O \left(1 - e^{i\alpha}\right) + E_R {E_O}^* \left(1 - e^{-i\alpha}\right) \tag{7.9}$$

the optimal value of α is π. This method is to be compared with one of the speckle methods in the next section. Other methods of phase shifting in digital holography will be described in detail in Chap. 8.

7.3 Speckle Methods

Instead of phase shifting, one can illuminate the object with speckled light by, for example, sending the laser through a ground glass plate [6, 7]. Two holograms are exposed while the speckle field illuminating the object is randomly changed. The object field arriving at the hologram plane is described as

$$E_{\mathrm{OS}_m} = E_{\mathrm{O}} E_{\mathrm{S}_m} \quad (m = 1, 2), \tag{7.10}$$

where E_{S_m} represents the complex speckle field (Fig. 7.7a) and the holograms (Fig. 7.7b) are

$$I_{\mathrm{H}_m} = I_{\mathrm{R}} + I_{\mathrm{OS}_m} + E_{\mathrm{R}}{}^* E_{\mathrm{O}} E_{\mathrm{S}_m} + E_{\mathrm{R}} E_{\mathrm{O}}{}^* E_{\mathrm{S}_m}{}^*. \tag{7.11}$$

Take separate exposures of the object fields, I_{OS_m}, and subtract from the holograms. Take the difference of the two to obtain the final modified hologram (Fig. 7.7c)

$$\begin{aligned} I_{\mathrm{H}}{}' &= (I_{\mathrm{H}_1} - I_{\mathrm{OS}_1}) - (I_{\mathrm{H}_2} - I_{\mathrm{OS}_2}) \\ &= E_{\mathrm{R}}{}^* E_{\mathrm{O}} (E_{\mathrm{S}_1} - E_{\mathrm{S}_2}) + E_{\mathrm{R}} E_{\mathrm{O}}{}^* (E_{\mathrm{S}_1}{}^* - E_{\mathrm{S}_2}{}^*), \end{aligned} \tag{7.12}$$

which can be compared with (7.9). The image Fig. 7.7d reconstructed from $I_{\mathrm{H}}{}'$ shows clear image of the object. While the image does contain the twin image, it is defocused and speckled into the background.

Speckled holograms can be averaged to obtain twinless image as follows [8]. Let $E_{\mathrm{OS}}(0)$ be the object pattern at $z = 0$ illuminated by the speckle field. Diffraction and propagation to the hologram plane over a distance z is denoted as

$$E_{\mathrm{OS}}(z) = \mathcal{D}_z\{E_{\mathrm{OS}}(0)\} \tag{7.13}$$

and the hologram acquired by the camera is

$$I_{\mathrm{H}} = I_{\mathrm{R}} + I_{\mathrm{OS}} + E_{\mathrm{R}}{}^* E_{\mathrm{OS}}(z) + E_{\mathrm{R}} E_{\mathrm{OS}}{}^*(z). \tag{7.14}$$

Note that $E_{\mathrm{OS}}{}^*(z) = \mathcal{D}_{-z}\{E_{\mathrm{OS}}(0)\}$ and numerically propagate I_{H} by z

$$\begin{aligned} I_{\mathrm{H}}{}' &= |\mathcal{D}_z\{I_{\mathrm{H}}\}|^2 = |\mathcal{D}_z\{I_{\mathrm{R}} + I_{\mathrm{OS}} + E_{\mathrm{R}}{}^* E_{\mathrm{OS}}(z) + E_{\mathrm{R}} E_{\mathrm{OS}}{}^*(z)\}|^2, \\ &= \left|\mathcal{D}_z\{I_{\mathrm{R}} + I_{\mathrm{OS}}\} + E_{\mathrm{R}}{}^* \mathcal{D}_{2z}\{E_{\mathrm{OS}}(0)\} + E_{\mathrm{R}} E_{\mathrm{OS}}{}^*(0)\right|^2. \end{aligned} \tag{7.15}$$

Now if $I_{\mathrm{H}}{}'$ is averaged by repeating the exposure many times, then most of the terms disappear except for the square of the last term.

$$\langle I_{\mathrm{H}}{}' \rangle \approx \left\langle \left| E_{\mathrm{R}} E_{\mathrm{OS}}{}^*(0) \right|^2 \right\rangle = I_{\mathrm{R}} I_{\mathrm{O}}. \tag{7.16}$$

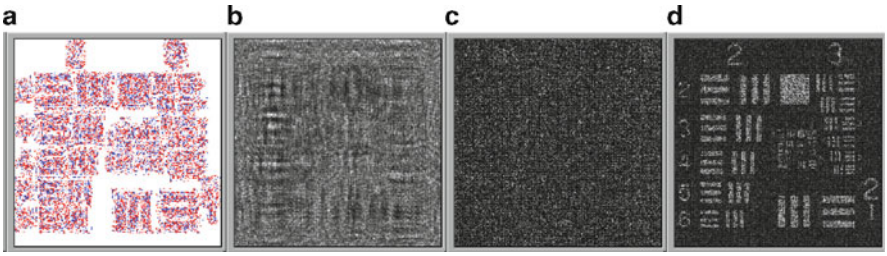

Fig. 7.7 (**a**) Phase of E_{OS_1}, (**b**) I_{H_1}, (**c**) $I_H{}'$, and (**d**) image reconstructed from $I_H{}'$

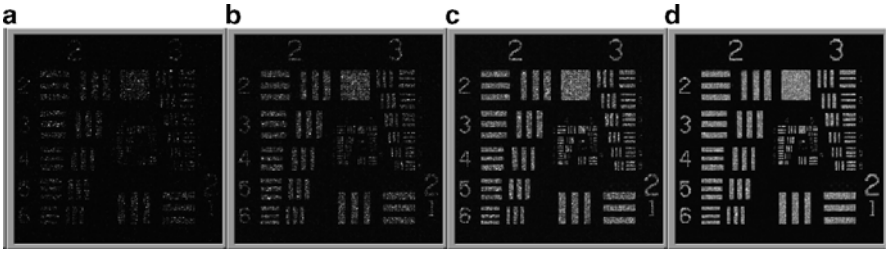

Fig. 7.8 $\langle I_H{}' \rangle$ for $N_{ave} = 1, 4, 16,$ and 64

Convergence is faster if I_R is removed in (7.14), by subtraction of hologram average or angular spectrum filtering. Figure 7.8 shows $\langle I_H{}' \rangle$ for average of 1, 4, 16, and 64 frames.

7.4 Filtering of Angular Spectrum

A very effective and versatile method to suppress the dc and twin image terms is the angular spectrum filtering, or spatial filtering [9]. The method can be used not only to suppress the DC term, but also to select one of the twin first-order terms, as well as to eliminate spurious spectral components due to parasitic reflections and interference, thus improving the quality of the reconstructed image. The method applies to the off-axis hologram, as shown in Fig. 7.9a, where a magnified view of a small area of the hologram displays the interference fringes. Its angular spectrum (Fig. 7.9b) then contains the central zero-order spot as well as a pair of spots for the twin-image terms. Filtering is accomplished numerically by selecting an area – the highlighted circular area in Fig. 7.9b – and zeroing out the rest of the array. The filtered spectrum is then inverse Fourier transformed that yields the modified hologram, which is then used to reconstruct image in Fig. 7.9c by numerical diffraction. The resolution and quality of the reconstructed image depends on the size of the filter, as shown in Fig. 7.10a. If it is too small, the image resolution

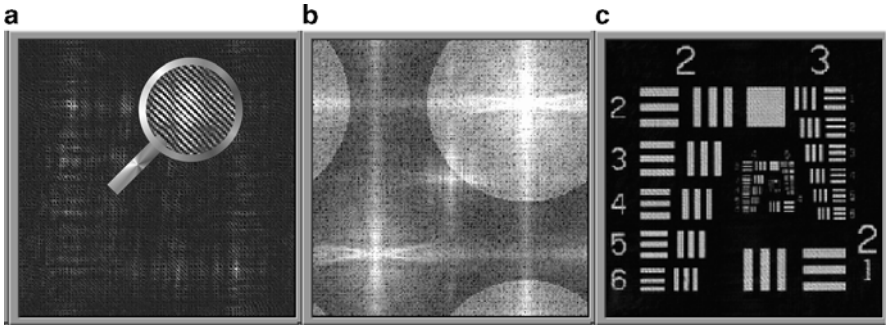

Fig. 7.9 Illustration of angular spectrum filtering. (**a**) The hologram, with a magnified view of a portion highlighting the interference fringes. (**b**) The angular spectrum, with one of the twin-image peaks highlighted with a *brighter circular area*, which is used in the reconstruction of the holographic image in (**c**)

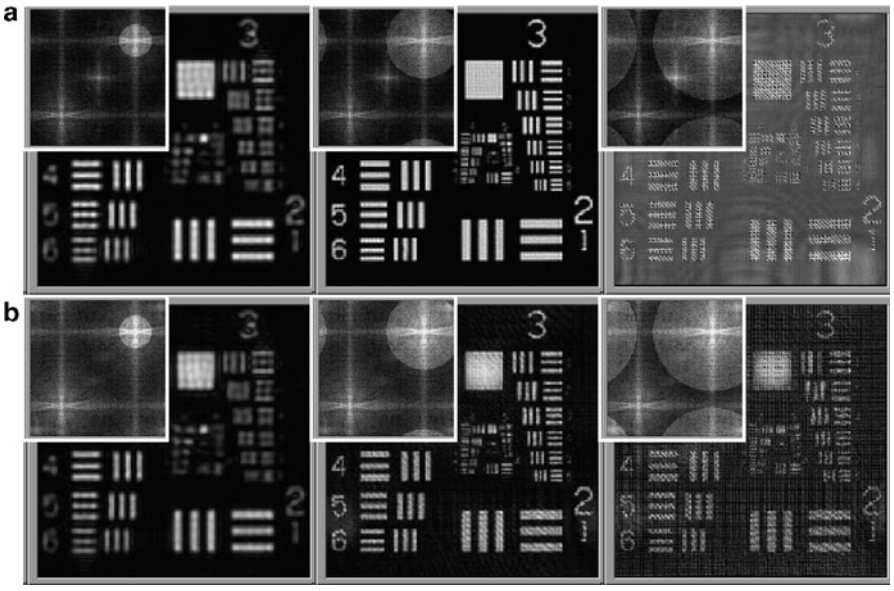

Fig. 7.10 Angular spectrum filtering with varying filter size using (**a**) conventional and (**b**) nonlinear angular spectrum methods. Each frame shows the reconstructed image using the angular spectrum displayed in the *inset*

degrades, and if it is too large and encroaches on the zero-order area, then the image suffers interference and distortion.

Similar effect may be achieved physically by placing an appropriate mask in the Fourier plane of a confocal configuration of lenses [10], but the numerical method affords significant flexibility and versatility. For example, setting the angular

spectrum filter boundary can be automated [11]. The numerical spectral mask can be set up with smoothed, that is, apodized, window function, in order to reduce fringing in the reconstructed image. Separate acquisition and subtraction of reference and object intensities from the hologram can be useful [12], even with the off-axis numerical filtering, by allowing larger bandwidth of the filter. Note that the hologram thus filtered numerically is complex, a feature not feasible in a real space hologram.

An interesting improvement is provided by the nonlinear spatial filtering, [13]. Starting from

$$I_{\mathrm{H}} = I_{\mathrm{R}} + I_{\mathrm{O}} + E_{\mathrm{R}}{}^{*}E_{\mathrm{O}} + E_{\mathrm{R}}E_{\mathrm{O}}{}^{*} \tag{7.17}$$

it follows

$$\frac{I_{\mathrm{H}}}{I_{\mathrm{R}}} = \left(1 + \frac{E_{\mathrm{O}}}{E_{\mathrm{R}}}\right)\left(1 + \frac{E_{\mathrm{O}}{}^{*}}{E_{\mathrm{R}}{}^{*}}\right), \tag{7.18}$$

so that

$$u_{\mathrm{H}} = \log\left(\frac{I_{\mathrm{H}}}{I_{\mathrm{R}}}\right) = \log\left(1 + \frac{E_{\mathrm{O}}}{E_{\mathrm{R}}}\right) + \log\left(1 + \frac{E_{\mathrm{O}}{}^{*}}{E_{\mathrm{R}}{}^{*}}\right). \tag{7.19}$$

The angular spectrum of this expression has only the two twin-image terms and no zero-order term, as shown in Fig. 7.10b. Figure 7.10 compares the effect of varying angular spectrum filter size on the resolution of the reconstructed image, using (Fig. 7.10a) the conventional or (Fig. 7.10b) the nonlinear angular spectrum methods. It shows that the nonlinear AS has no zero-order peak and this allows use of larger AS filter for better resolution, until the filter finally encroaches into the twin-image area.

References

1. T. M. Kreis, and W. P. O. Juptner, "Suppression of the dc term in digital holography," Optical Engineering **36**, 2357–2360 (1997).
2. G. L. Chen, C. Y. Lin, M. K. Kuo, and C. C. Chang, "Numerical suppression of zero-order image in digital holography," Optics Express **15**, 8851–8856 (2007).
3. W. L. Bragg, and G. L. Rogers, "Elimination of the Unwanted Image in Diffraction Microscopy," Nature **167**, 190–191 (1951).
4. Y. Takaki, H. Kawai, and H. Ohzu, "Hybrid holographic microscopy free of conjugate and zero-order images," Applied Optics **38**, 4990–4996 (1999).
5. Y. M. Zhang, Q. N. Lu, and B. Z. Ge, "Elimination of zero-order diffraction in digital off-axis holography," Optics Communications **240**, 261–267 (2004).
6. J. A. H. Ramirez, and J. Garcia-Sucerquia, "Digital off-axis holography without zero-order diffraction via phase manipulation," Optics Communications **277**, 259–263 (2007).

7. N. Demoli, J. Mestrovic, and I. Sovic, "Subtraction digital holography," Applied Optics **42**, 798–804 (2003).
8. D. S. Monaghan, D. P. Kelly, N. Pandey, and B. M. Hennelly, "Twin removal in digital holography using diffuse illumination," Optics Letters **34**, 3610–3612 (2009).
9. E. Cuche, P. Marquet, and C. Depeursinge, "Spatial filtering for zero-order and twin-image elimination in digital off-axis holography," Applied Optics **39**, 4070–4075 (2000).
10. F. Le Clerc, L. Collot, and M. Gross, "Numerical heterodyne holography with two-dimensional photodetector arrays," Optics Letters **25**, 716–718 (2000).
11. J. W. Weng, J. G. Zhong, and C. Y. Hu, "Automatic spatial filtering to obtain the virtual image term in digital holographic microscopy," Applied Optics **49**, 189–195 (2010).
12. L. Xu, J. M. Miao, and A. Asundi, "Properties of digital holography based on in-line configuration," Opt. Eng. **39**, 3214–3219 (2000).
13. N. Pavillon, C. S. Seelamantula, J. Kuhn, M. Unser, and C. Depeursinge, "Suppression of the zero-order term in off-axis digital holography through nonlinear filtering," Applied Optics **48**, H186-H195 (2009).

Chapter 8
Phase-Shifting Digital Holography

The in-line configuration of DH makes use of the full pixel count in forming the holographic image, but the zero-order and the twin-image terms are superposed on the image. Phase-shifting digital holography (PSDH) is a very effective method of removing these terms, introduced by I. Yamaguchi, where the complex field at the hologram is obtained by phase-shifting interferometry [1]. From the complex field at the hologram plane, including the amplitude and phase information, the optical field at any other plane can be obtained by numerical diffraction.

8.1 Basic Principles of PSDH

For simplicity, assume that the reference is a plane wave normally incident on the hologram plane $E_{\mathrm{R}}(x,y) = \mathcal{E}_{\mathrm{R}} \exp(i\alpha)$, where α is a global phase. The object wave has the amplitude $\mathcal{E}_{\mathrm{O}}(x,y)$ and phase $\varphi(x,y)$ distributions, so that

$$E_{\mathrm{O}}(x,y) = \mathcal{E}_{\mathrm{O}}(x,y) \exp[i\varphi(x,y)]. \tag{8.1}$$

Then the interference intensity is

$$\begin{aligned} I_{\alpha}(x,y) &= |E_{\mathrm{R}} + E_{\mathrm{O}}|^2, \\ &= {\mathcal{E}_{\mathrm{R}}}^2 + {\mathcal{E}_{\mathrm{O}}}^2(x,y) + \mathcal{E}_{\mathrm{R}}\mathcal{E}_{\mathrm{O}}(x,y)\mathrm{e}^{i(\varphi-\alpha)} + \mathcal{E}_{\mathrm{R}}\mathcal{E}_{\mathrm{O}}(x,y)\mathrm{e}^{-i(\varphi-\alpha)}, \\ &= {\mathcal{E}_{\mathrm{R}}}^2 + {\mathcal{E}_{\mathrm{O}}}^2(x,y) + 2\mathcal{E}_{\mathrm{R}}\mathcal{E}_{\mathrm{O}}(x,y)\cos[\varphi(x,y) - \alpha]. \end{aligned} \tag{8.2}$$

M.K. Kim, *Digital Holographic Microscopy: Principles, Techniques, and Applications*, Springer Series in Optical Sciences 162,
DOI 10.1007/978-1-4419-7793-9_8, © Springer Science+Business Media, LLC 2011

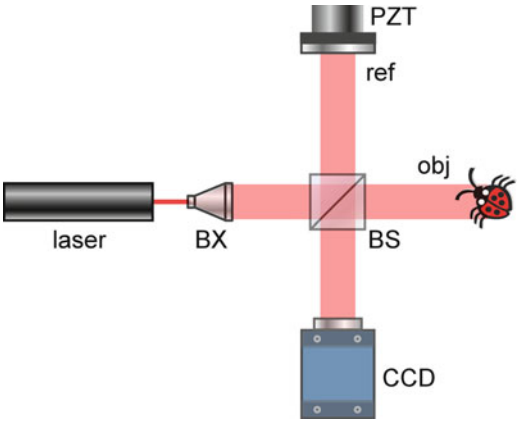

Fig. 8.1 Phase-shifting digital holography with Michelson interferometer. *BX* beam expander, *BS* beam splitter, *PZT* piezo-mounted reference mirror

In the original four-step PSDH [1, 2], four holograms with phase shifts $\alpha = 0$, $\pi/2$, π, $3\pi/2$ are acquired, for example, by using a piezo-mounted reference mirror (Fig. 8.1):

$$\begin{cases} I_0 = \mathcal{E}_\mathrm{R}{}^2 + \mathcal{E}_\mathrm{O}{}^2 + 2\mathcal{E}_\mathrm{R}\mathcal{E}_\mathrm{O}\cos\varphi, \\ I_{\pi/2} = \mathcal{E}_\mathrm{R}{}^2 + \mathcal{E}_\mathrm{O}{}^2 - 2\mathcal{E}_\mathrm{R}\mathcal{E}_\mathrm{O}\sin\varphi, \\ I_\pi = \mathcal{E}_\mathrm{R}{}^2 + \mathcal{E}_\mathrm{O}{}^2 - 2\mathcal{E}_\mathrm{R}\mathcal{E}_\mathrm{O}\cos\varphi, \\ I_{3\pi/2} = \mathcal{E}_\mathrm{R}{}^2 + \mathcal{E}_\mathrm{O}{}^2 + 2\mathcal{E}_\mathrm{R}\mathcal{E}_\mathrm{O}\sin\varphi, \end{cases} \tag{8.3}$$

which are then numerically combined to extract the phase profile

$$\varphi(x,y) = \tan^{-1}\left[\frac{I_{\pi/2} - I_{3\pi/2}}{I_0 - I_\pi}\right] \tag{8.4}$$

and the object field amplitude $\sqrt{E_\mathrm{O}{}^2(x,y)}$ can be obtained by a separate exposure of the object without the reference beam, thus requiring a total of five exposures. The holographic image is then reconstructed from $E_\mathrm{O}(x,y) = \sqrt{E_\mathrm{O}{}^2}\exp[i\varphi]$ (Fig. 8.2).

Alternatively, the complex field can be obtained by [3]

$$E_\mathrm{O}(x,y) = \frac{1}{4\mathcal{E}_\mathrm{R}}\left[(I_0 - I_\pi) + i\left(I_{3\pi/2} - I_{\pi/2}\right)\right]. \tag{8.5}$$

This completely defines the complex optical field $E_\mathrm{O}(x,y;0)$ of the object at the hologram plane, and the diffraction theory can be used to calculate the optical field $E_\mathrm{O}(x,y;z)$ at any distance z from the hologram. These procedures remove the contributions from the zero-order and twin-image terms.

The phase-shifting interferometry (PSI), that is, without the numerical diffraction, has been extensively used in surface metrology and other applications [4].

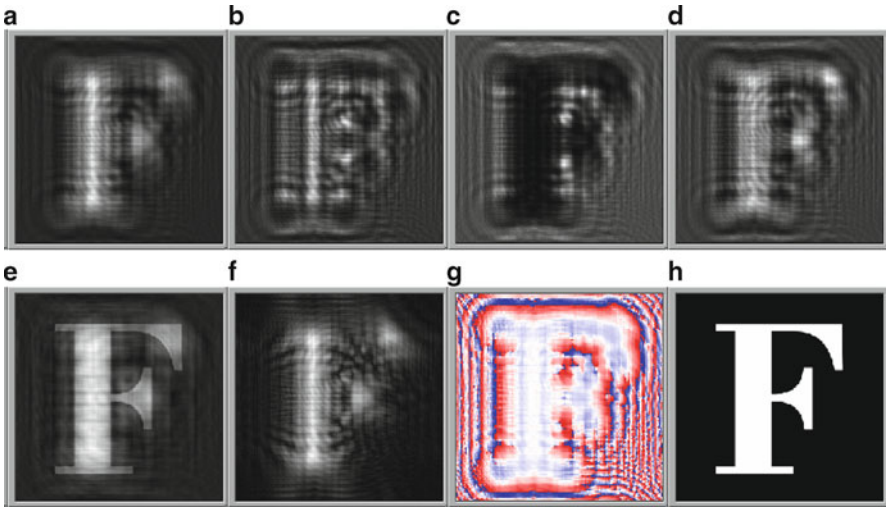

Fig. 8.2 Simulation of PSDH. (**a**) I_0, (**b**) $I_{\pi/2}$, (**c**) I_π, (**d**) $I_{3\pi/2}$, (**e**) image reconstructed from I_0, (**f**) $\sqrt{{E_\mathrm{O}}^2(x,y)}$, (**g**) $\varphi(x,y)$, and (**h**) image reconstructed from $\sqrt{{E_\mathrm{O}}^2}\exp[i\varphi]$

The phase-shifting principle applies equally to noninterferometric fringe projection techniques for 3D surface profiling [5, 6]. Many techniques have been developed for both PSI and PSDH and some of these will be described below [7]. The idea of combining two holograms with a quadrature phase difference was already conceived in the 1950s by Gabor and Goss [8] but the complexity of the optomechanical system was substantial, making its practical implementation very difficult. On the other hand, with the digital implementation, much of the optical manipulations are replaced with numerical operations in a highly efficient and versatile manner, yielding powerful applications in many different areas.

8.2 Reduced Number of Steps

8.2.1 Three-Step Method

The number of required hologram exposures is reduced by one in the three-step PSDH [2]. The interference intensities with three phase shifts 0, α, and β are

$$\begin{cases} I_\alpha = {\mathcal{E}_\mathrm{R}}^2 + {\mathcal{E}_\mathrm{O}}^2 + \mathcal{E}_\mathrm{R}\mathcal{E}_\mathrm{O}\mathrm{e}^{i(\varphi-\alpha)} + \mathcal{E}_\mathrm{R}\mathcal{E}_\mathrm{O}\mathrm{e}^{-i(\varphi-\alpha)}, \\ I_\beta = {\mathcal{E}_\mathrm{R}}^2 + {\mathcal{E}_\mathrm{O}}^2 + \mathcal{E}_\mathrm{R}\mathcal{E}_\mathrm{O}\mathrm{e}^{i(\varphi-\beta)} + \mathcal{E}_\mathrm{R}\mathcal{E}_\mathrm{O}\mathrm{e}^{-i(\varphi-\beta)}, \\ I_0 = {\mathcal{E}_\mathrm{R}}^2 + {\mathcal{E}_\mathrm{O}}^2 + \mathcal{E}_\mathrm{R}\mathcal{E}_\mathrm{O}\mathrm{e}^{i\varphi} + \mathcal{E}_\mathrm{R}\mathcal{E}_\mathrm{O}\mathrm{e}^{-i\varphi}, \end{cases} \tag{8.6}$$

which can be combined to get

$$E_{\mathrm{O}} = \mathcal{E}_{\mathrm{O}} \mathrm{e}^{i\varphi} = \frac{1}{\mathcal{E}_{\mathrm{R}}} \frac{(I_\alpha - I_0)(\mathrm{e}^{i\beta} - 1) - (I_\beta - I_0)(\mathrm{e}^{i\alpha} - 1)}{(\mathrm{e}^{-i\alpha} - 1)(\mathrm{e}^{i\beta} - 1) - (\mathrm{e}^{i\alpha} - 1)(\mathrm{e}^{-i\beta} - 1)}. \tag{8.7}$$

For the case of $\alpha = \pi/2$ and $\beta = -\pi/2$, we have

$$\begin{aligned} E_{\mathrm{O}}(x,y) &= \frac{1-i}{4\mathcal{E}_{\mathrm{R}}}\left[(I_0 - I_{\pi/2}) + i(I_0 - I_{-\pi/2})\right], \\ \varphi(x,y) &= \tan^{-1}\left[\frac{I_0 - I_{-\pi/2}}{I_0 - I_{\pi/2}} - \frac{\pi}{4}\right]. \end{aligned} \tag{8.8}$$

This requires three camera exposures and one intensity measurement.

8.2.2 Two-Step Methods

A two-step method is also possible, for any phase shift $0<\alpha<\pi$ [9]

$$E_{\mathrm{O}}(x,y) = \frac{(I_0 - {\mathcal{E}_{\mathrm{O}}}^2 - {\mathcal{E}_{\mathrm{R}}}^2) - \exp(-i\alpha)(I_\alpha - {\mathcal{E}_{\mathrm{O}}}^2 - {\mathcal{E}_{\mathrm{R}}}^2)}{\mathcal{E}_{\mathrm{R}}[1 - \exp(-2i\alpha)]}, \tag{8.9}$$

which requires three exposures plus one intensity measurement.

It is also possible to have only the two phase-shift exposures to reconstruct the complete object field, as follows [10, 11]. Let $u = {\mathcal{E}_{\mathrm{R}}}^2 + {\mathcal{E}_{\mathrm{O}}}^2$ and write

$$\begin{cases} I_0 = u + 2\mathcal{E}_{\mathrm{R}}\mathcal{E}_{\mathrm{O}} \cos\varphi, \\ I_\alpha = u + 2\mathcal{E}_{\mathrm{R}}\mathcal{E}_{\mathrm{O}} \cos(\varphi - \alpha) = u + 2\mathcal{E}_{\mathrm{R}}\mathcal{E}_{\mathrm{O}}(\cos\varphi\cos\alpha + \sin\varphi\sin\alpha). \end{cases} \tag{8.10}$$

Then

$$\begin{cases} \mathcal{E}_{\mathrm{O}} \cos\varphi = \dfrac{I_0 - u}{2\mathcal{E}_{\mathrm{R}}}, \\ \mathcal{E}_{\mathrm{O}} \sin\varphi = \dfrac{-I_0\cos\alpha + I_\alpha + u(1-\cos\alpha)}{2\mathcal{E}_{\mathrm{R}}\sin\alpha}, \end{cases} \tag{8.11}$$

which leads to

$$4{\mathcal{E}_{\mathrm{R}}}^2(u - {\mathcal{E}_{\mathrm{R}}}^2)\sin^2\alpha = (I_0 - u)^2\sin^2\alpha + [I_0\cos\alpha - I_\alpha + u(1-\cos\alpha)]^2 \tag{8.12}$$

so that

$$au^2 - 2bu + c = 0, \tag{8.13}$$

where

$$\begin{cases} a = 2[1 - \cos\alpha], \\ b = \left[(I_0 + I_\alpha)(1 - \cos\alpha) + 2{\mathcal{E}_\mathrm{R}}^2 u \sin^2\alpha\right], \\ c = \left[I_0^2 + I_\alpha^2 - 2I_0 I_\alpha \cos\alpha + 4{\mathcal{E}_\mathrm{R}}^4 \sin^2\alpha\right]. \end{cases} \tag{8.14}$$

The solution

$$u = \frac{b - \sqrt{b^2 - ac}}{a} \tag{8.15}$$

then allows one to write

$$\begin{aligned} E_\mathrm{O}(x,y) &= \frac{I_0 - u}{2\mathcal{E}_\mathrm{R}} + i\frac{-I_0\cos\alpha + I_\alpha + u(1-\cos\alpha)}{2\mathcal{E}_\mathrm{R}\sin\alpha}, \\ \varphi(x,y) &= \tan^{-1}\left[\frac{-I_0\cos\alpha + I_\alpha + u(1-\cos\alpha)}{(I_0 - u)\sin\alpha}\right]. \end{aligned} \tag{8.16}$$

8.3 Unknown Phase Steps

The above methods allow in principle to extract the complex optical field of the object by combining two or more holograms acquired with fixed phase steps. It may be, however, difficult to precisely control and maintain the phase shift and small errors in phase steps can cause substantial error in the extracted phase profile. A number of methods have been proposed to allow determination of the phase shift by analysis of the hologram images, such as by iterative procedures for estimating the phase shift with improving statistics [12–14].

In a series of papers [15–21], L.Z. Cai et al. have developed methods to extract the arbitrary phase shift and to calculate the complex object field at the hologram. For example [20], suppose we take two holograms with unknown phase shift α:

$$\begin{cases} I_0(x,y) = {\mathcal{E}_\mathrm{R}}^2 + {\mathcal{E}_\mathrm{O}}^2(x,y) + 2\mathcal{E}_\mathrm{R}\mathcal{E}_\mathrm{O}(x,y)\cos[\varphi(x,y)], \\ I_\alpha(x,y) = {\mathcal{E}_\mathrm{R}}^2 + {\mathcal{E}_\mathrm{O}}^2(x,y) + 2\mathcal{E}_\mathrm{R}\mathcal{E}_\mathrm{O}(x,y)\cos[\varphi(x,y) + \alpha]. \end{cases} \tag{8.17}$$

Take their sum and difference

$$\begin{cases} I_0 - I_\alpha = 4\mathcal{E}_\mathrm{R}\mathcal{E}_\mathrm{O}\sin(\varphi + \alpha/2)\sin(\alpha/2) \\ I_0 + I_\alpha = 2{\mathcal{E}_\mathrm{R}}^2 + 2{\mathcal{E}_\mathrm{O}}^2 + 4\mathcal{E}_\mathrm{R}\mathcal{E}_\mathrm{O}\cos(\varphi + \alpha/2)\cos(\alpha/2) \end{cases} \tag{8.18}$$

and take the following averages over all pixels of the frame

$$\begin{cases} \left\langle (I_0 - I_\alpha)^2 \right\rangle = 4{\mathcal{E}_\mathrm{R}}^2 \langle {\mathcal{E}_\mathrm{O}}^2 \rangle (1 - \cos\alpha), \\ \langle I_0 + I_\alpha \rangle = 2{\mathcal{E}_\mathrm{R}}^2 + 2\langle {\mathcal{E}_\mathrm{O}}^2 \rangle. \end{cases} \tag{8.19}$$

This averaging assumes that the phase distribution is sufficiently random, that is, its histogram is sufficiently uniform in the $[0, 2\pi]$ interval, and that the amplitude and phase are not statistically correlated. Then the phase shift α can be calculated from the two holograms, I_0 and I_α, plus the constant reference intensity ${\mathcal{E}_\mathrm{R}}^2$ by

$$\alpha = \cos^{-1}\left[1 - \frac{\left\langle (I_0 - I_\alpha)^2 \right\rangle}{2{\mathcal{E}_\mathrm{R}}^2 \left(\langle I_0 + I_\alpha \rangle - 2{\mathcal{E}_\mathrm{R}}^2 \right)}\right]. \tag{8.20}$$

With the knowledge of α, one can also calculate the object intensity ${\mathcal{E}_\mathrm{O}}^2(x, y)$ by applying $\sin^2(\varphi + \alpha/2) + \cos^2(\varphi + \alpha/2) = 1$ to (8.18) to write

$${\mathcal{E}_\mathrm{O}}^4 - b{\mathcal{E}_\mathrm{O}}^2 + \frac{1}{4}c = 0, \tag{8.21}$$

where

$$\begin{aligned} b &= I_0 - I_\alpha + 2{\mathcal{E}_\mathrm{R}}^2 \cos\alpha, \\ c &= \left(I_0 + I_\alpha - 2{\mathcal{E}_\mathrm{R}}^2\right)^2 + \frac{(I_0 - I_\alpha)^2}{\tan^2(\alpha/2)}, \end{aligned} \tag{8.22}$$

so that

$${\mathcal{E}_\mathrm{O}}^2 = \frac{1}{2}\left[b - \sqrt{b^2 - c}\right], \tag{8.23}$$

which is valid for ${\mathcal{E}_\mathrm{R}}^2 > {\mathcal{E}_\mathrm{O}}^2$. And finally the complex object field $E_\mathrm{O}(x, y)$ can be calculated from (8.16) above.

Alternatively [21], one can go back to (8.12) and write it as

$$a\cos^2\alpha - 2b\cos\alpha + c = 0, \tag{8.24}$$

where

$$\begin{cases} a = 4{\mathcal{E}_\mathrm{R}}^2 \left(u - {\mathcal{E}_\mathrm{R}}^2\right), \\ b = (u - I_0)(u - I_\alpha), \\ c = (I_0 - u)^2 + (I_\alpha - u)^2 - 4{\mathcal{E}_\mathrm{R}}^2 \left(u - {\mathcal{E}_\mathrm{R}}^2\right). \end{cases} \tag{8.25}$$

Again, take average of (8.24) over all pixels, before solving it for $\cos\alpha$,

$$\cos\alpha = \frac{\langle b\rangle \pm \sqrt{\langle b\rangle^2 - \langle a\rangle\langle c\rangle}}{\langle a\rangle}. \tag{8.26}$$

8.4 Techniques of PSDH

8.4.1 Phase-Shifting Methods

The phase-shift is most often achieved by using a reference mirror mounted on a piezoelectric transducer (e.g., PZT) [1]. Phase-shifting can also be accomplished by using liquid-crystal phase retarder [3, 9, 22], acousto-optic modulator [23], or between polarization components transmitted through quarter-wave plates [24, 25]. For multiwavelength holography, the phase-shifting by PZT is wavelength-dependent, and can lead to errors and noise [26]. An achromatic phase shifter, consisting of a half-wave plate sandwiched between a pair of quarter-wave plates, was used to record tri-color digital hologram [27, 28]. In spectral or wavelength phase-shifting [29–31], the phase shift is achieved by shift in wavelength of a tunable light source, through $\Delta\varphi = 2\pi z\Delta\lambda/\lambda^2$. A spiral phase plate or a SLM (spatial light modulator) with computer-generated spiral phase pattern can be used where the phase shift is achieved by rotation of the phase plate [32]. Some of the various phase-shifting methods are compared in [33].

Use of SLM, such as liquid crystal or micromirror array allows faster switching time and stability against micromechanical vibrations. Furthermore, different parts of an optical beam can acquire different phase shifts. This is especially useful in several of common-path and low-coherence interferometer configurations and techniques, as will be described in later chapters.

8.4.2 Heterodyne Digital Holography

Instead of phase-shifting in discrete steps, the phase can be varied in continuous manner, integrating the time-dependent light intensity over finite intervals. For example, the relative phase between the reference and object fields can be varied linearly in time, which is equivalent to having a frequency offset between the two [34]. If the reference and object fields are written as

$$\begin{cases} E_{\mathrm{R}}(x,y;t) = \mathcal{E}_{\mathrm{R}}\exp(-i\omega_{\mathrm{R}}t), \\ E_{\mathrm{O}}(x,y) = \mathcal{E}_{\mathrm{O}}(x,y)\exp[i\varphi(x,y) - i\omega_{\mathrm{O}}t], \end{cases} \tag{8.27}$$

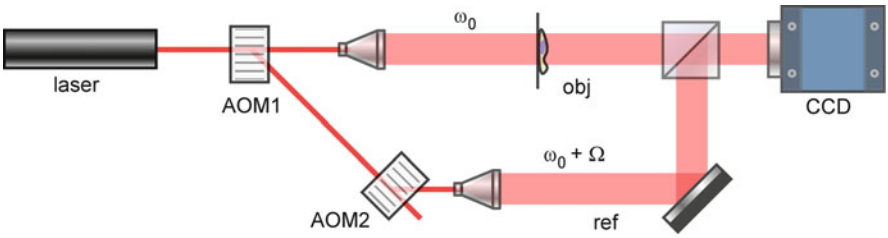

Fig. 8.3 Heterodyne DH configuration. *AOMs* acousto-optic modulators

with $\omega_R - \omega_O = \Omega$, then the interference intensity is time-dependent

$$I(x, y; t) = \mathcal{E}_R{}^2 + \mathcal{E}_O{}^2(x, y) + 2\mathcal{E}_R\mathcal{E}_O(x, y)\cos[\varphi(x, y) - \Omega t]. \tag{8.28}$$

Four exposures may be taken at $t = 2\pi n/N\Omega$ ($N = 4$, $n = 0, 1, 2, 3$) to obtain the four quadrature interference images and proceed to derive the complex object field $E_O(x, y) = \mathcal{E}_O(x, y)\exp[i\varphi(x, y)]$. (To be more precise, one needs to integrate (8.28) over the exposure time of each camera frame, but the result is essentially the same.) The camera frame rate is therefore $f_{CCD} = N\Omega/2\pi$, where in this case $N = 4$. The frequency offset is typically created by using a pair of acousto-optic modulators (AOM), as depicted in Fig. 8.3. The heterodyne digital holography [34–36] solves a major problem of PSDH of precisely controlling the phase shift. The RF frequencies of the AOMs can be easily controlled with high precision and coherence, compared to micromechanical control of PZTs. In [36], by combining heterodyne DH and off-axis configuration with angular spectrum filtering, noise associated with the dc and twin-image terms are effectively eliminated as well as noise due to spurious interference, leading to quantum limit of single photo-electron per pixel. Alternatively, digital holography was demonstrated at the photon-counting level using a *xy*-scanned optical fiber tip connected to a photon-counting detector [37]. Digital hologram with illumination as low as 43 counts per second produced clear reconstruction image.

Instead of linear variation of phase (frequency shifting), the phase may be modulated sinusoidally [38]. This is useful in PZT-based system, which obviously cannot move linearly for indefinite period of time, though the analysis becomes more involved. The interference intensity with sinusoidal phase modulation is written as

$$I(x, y; t) = \bar{I}(x, y) + A(x, y)\cos[\varphi(x, y) + \psi\sin(\Omega t + \theta)] \tag{8.29}$$

where $\bar{I}(x, y)$ is the dc term, $A(x, y)$ is the fringe amplitude, ψ is the phase modulation amplitude, Ω is the modulation frequency, and θ is the phase angle of the phase modulation. The average intensity of the nth integration bucket is

$$I_n(x, y) = \frac{1}{\tau}\int_{(n-1)\tau}^{n\tau} I(x, y; t)\mathrm{d}t, \tag{8.30}$$

which can be carried out using Bessel expansion, and the phase function $\varphi(x, y)$ can be calculated [38]. Some of the characteristics and advantages of sinusoidal phase modulation are similar to the linear phase modulation (i.e., frequency shifting or heterodyne digital holography).

8.4.3 Asynchronous Digital Holography

In asynchronous digital holography of [39], the object and reference arms are frequency shifted by 100 Hz using a pair of offset AOMs, causing a phase shift between two exposures. The phase shift is measured by sinusoid-fitting and quantitative phase profile is then obtained by Hilbert transform. In [40], instead of consecutive exposures using AOMs, a Wollaston prism is used to generate two interferograms spatially separated and phase shifted. Subnanometer fluctuations of a MDA-MB-468 human breast cancer cell was measured on ms time scale. A phase profile movie of a beating myocyte of rat heart is obtained.

8.4.4 Parallel Phase-Shifting

In the above PSDH methods, two or more holograms are acquired sequentially as the phase of the reference beam is stepped. This is sometimes referred to as the temporal phase shifting, and has inherent speed limitation because of the multiple exposure. There have been various efforts to increase the speed of PSDH process so that it can be used for dynamic systems. In [41], multiple cameras are used to record interferograms with different phase shifts, which in this case is effected by different diffraction orders of a Fourier plane grating. The multicamera system tends to be cumbersome and costly, as well as being technically challenging to achieve and maintain exact pixelwise registration. Awatsuji et al. has proposed the use of phase mosaic patterns inserted into the reference, so that adjacent pixels with different phase steps can be combined to obtain a final pixel value, depicted in Fig. 8.4. Four-, three-, and two-step phase mosaics have been considered [42–45]. In the absence of commercially available phase shift arrays, demonstration experiments had to synthesize such array from multiple phase-shifted holograms generated in the conventional manner. It is worth noting that the idea of dividing a hologram into strips or checkerboard patterns with quadrature phase shift has been mentioned in Gabor's original attempt at phase shift holography [8].

8.4.5 Fractional Talbot Effect

An interesting way to generate phase mosaic is provided by the fractional Talbot effect [46]. When a two-dimensional binary amplitude grating is illuminated with a

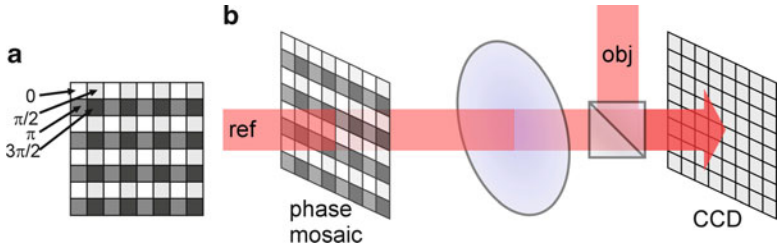

Fig. 8.4 Parallel phase shifting. The phase mosaic patterns (**a**) is imaged on the CCD array in (**b**)

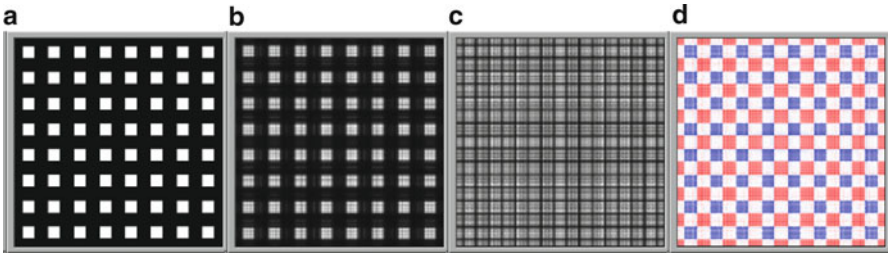

Fig. 8.5 Fractional Talbot effect. The input pattern (**a**) and the diffraction pattern at Talbot distance Z_T (**b**). The diffraction pattern at $1.25\,Z_T$, showing the (**c**) amplitude and (**d**) phase (*white* = 0, *light red* = $\pi/2$, *light blue* = $-\pi/2$)

plane wave, replicas of the grating appear periodically at distances multiple of the Talbot distance $z_T = 2d^2/\lambda$, where d is the grating period. In addition, a superposition of laterally shifted replicas of the grating but weighted by different phase factors, called Fresnel images, appear at fractions of the Talbot distance

$$z_T{}' = z_T\left(q + \frac{n}{m}\right), \tag{8.31}$$

where q and $0<n<m$ are integers. This provides a periodic three-step phase distribution with uniform irradiance that can provide the reference illumination for parallel phase shifting. When $n/m = 1/4$ or $3/4$, a 2×2 superpixel contains phase shifts of 0, $\pi/2$, $\pi/2$, and π, as shown in Fig. 8.5. This pattern can be projected on the CCD and used as the reference, and the three-step phase-shifting algorithm can be applied.

8.4.6 Spatial Phase-Shifting

The method of extracting the phase profile from a single interferogram containing spatial carrier frequency is sometimes referred to as spatial phase shifting, which includes the usual off-axis holography configuration [33, 47]. In a method called

spatial carrier phase shift method or sinusoid-fitting method [48, 49], a single interferogram is used to fit sinusoids over the slowly varying interference envelope. This requires a single interferogram exposure but at the expense of the spatial resolution. It operates on the interference fringes at the image plane, does not require Fourier transform, and is valid if the phase changes slowly over several pixels, so that

$$\varphi(x,y) = -\tan^{-1}\left[\frac{I(x+\Delta x,y) - I(x-\Delta x,y)}{I(x+\Delta x,y) - 2I(x,y) + I(x-\Delta x,y)} \tan\frac{k_0 \Delta x}{2}\right], \tag{8.32}$$

where $I(x,y)$ is the interference pattern, k_0 is the carrier fringe frequency and Δx is the pixel pitch. A more general method that works for curved reference wave as well as plane wave was introduced in [50].

8.5 Errors and Noise in PSDH

Error in phase shift in reconstruction relative to the phase shift in recording can lead to incomplete cancellation of the dc and conjugate terms. The miscalibration may be due to nonlinearity and nonrepeatability of the phase shifters. An extra interferometric arm may be adopted for in situ monitoring of phase shift, at the expense of more complicated instrumentation [51]. Errors and noise also arise from digitization, thermal noise, shot noise, mechanical vibrations, instability of light intensity, and speckle interference [47]. There have been many studies for optimal minimization and compensation of errors and noise in both PSI [52, 53] and PSDH [3, 47, 54–58].

One way to estimate and correct the error is by minimizing the error in the reconstructed amplitude image compared to the object [54]. A more general method is given in [15, 18, 20], where the phase shift between two exposures is calculated based on a statistical consideration of the interferogram, and its correction for intensity instability is also given [59]. In heterodyne digital holography [35], a difference frequency between the object and reference beams is set up using acousto-optic modulators so that the phase shift between consecutive CCD frames can be controlled with much higher precision. An analysis of noise and sensitivity of PSDH has been made in [56].

References

1. I. Yamaguchi, and T. Zhang, "Phase-shifting digital holography," Optics Letters **22**, 1268–1270 (1997).
2. I. Yamaguchi, J. Kato, S. Ohta, and J. Mizuno, "Image formation in phase-shifting digital holography and applications to microscopy," Applied Optics **40**, 6177–6186 (2001).

3. S. C. Lai, B. King, and M. A. Neifeld, "Wave front reconstruction by means of phase-shifting digital in-line holography," Optics Communications **173**, 155–160 (2000).
4. K. Creath, "Phase measurements interferometry techniques," in *Progress in Optics*, E. Wolf, ed. (Elsevier Science, New York, 1988), pp. 349–393.
5. P. S. Huang, and S. Zhang, "Fast three-step phase-shifting algorithm," Applied Optics **45**, 5086–5091 (2006).
6. B. Pan, Q. Kemao, L. Huang, and A. Asundil, "Phase error analysis and compensation for nonsinusoidal waveforms in phase-shifting digital fringe projection profilometry," Optics Letters **34**, 416–418 (2009).
7. T. Kreis, *Handbook of holographic interferometry: Optical and digital methods* (Wiley-VCH, 2005).
8. D. Gabor, and W. P. Goss, "Interference Microscope with Total Wavefront Reconstruction," J. Opt. Soc. Am. **56**, 849–858 (1966).
9. Y. Takaki, H. Kawai, and H. Ohzu, "Hybrid holographic microscopy free of conjugate and zero-order images," Applied Optics **38**, 4990–4996 (1999).
10. X. F. Meng, L. Z. Cai, X. F. Xu, X. L. Yang, X. X. Shen, G. Y. Dong, and Y. R. Wang, "Two-step phase-shifting interferometry and its application in image encryption," Optics Letters **31**, 1414–1416 (2006).
11. J. P. Liu, and T. C. Poon, "Two-step-only quadrature phase-shifting digital holography," Optics Letters **34**, 250–252 (2009).
12. Z. Y. Wang, and B. T. Han, "Advanced iterative algorithm for phase extraction of randomly phase-shifted interferograms," Optics Letters **29**, 1671–1673 (2004).
13. X. F. Xu, L. Z. Cai, X. F. Meng, G. Y. Dong, and X. X. Shen, "Fast blind extraction of arbitrary unknown phase shifts by an iterative tangent approach in generalized phase-shifting interferometry," Optics Letters **31**, 1966–1968 (2006).
14. Hae Y. Yun, and Chung K. Hong, "Interframe intensity correlation matrix for self-calibration in phase-shifting interferometry," Appl. Opt. **44**, 4860–4869 (2005).
15. L. Z. Cai, Q. Liu, and X. L. Yang, "Phase-shift extraction and wave-front reconstruction in phase-shifting interferometry with arbitrary phase steps," Optics Letters **28**, 1808–1810 (2003).
16. J. A. Ferrari, and E. Garbusi, "Comment on "phase-shift extraction and wave-front reconstruction in phase-shifting interferometry with arbitrary phase steps" [2003 OL 28 1808]," Optics Letters **29**, 1257–1258 (2004).
17. L. Z. Cai, Q. Liu, and X. L. Yang, "Reply to comment on "phase-shift extraction and wave-front reconstruction in phase-shifting interferometry with arbitrary phase steps" [2003 OL 28 1808]," Optics Letters **29**, 1259–1260 (2004).
18. L. Z. Cai, Q. Liu, and X. L. Yang, "Generalized phase-shifting interferometry with arbitrary unknown phase steps for diffraction objects," Optics Letters **29**, 183–185 (2004).
19. X. F. Xu, L. Z. Cai, Y. R. Wang, X. F. Meng, H. Zhang, G. Y. Dong, and X. X. Shen, "Blind phase shift extraction and wavefront retrieval by two-frame phase-shifting interferometry with an unknown phase shift," Optics Communications **273**, 54–59 (2007).
20. X. E. Xu, L. Z. Cai, Y. R. Wang, X. E. Meng, W. J. Sun, H. Zhang, X. C. Cheng, G. Y. Dong, and X. X. Shen, "Simple direct extraction of unknown phase shift and wavefront reconstruction in generalized phase-shifting interferometry: algorithm and experiments," Optics Letters **33**, 776–778 (2008).
21. X. F. Meng, L. Z. Cai, Y. R. Wang, X. L. Yang, X. F. Xu, G. Y. Dong, X. X. Shen, and X. C. Cheng, "Wavefront reconstruction by two-step generalized phase-shifting interferometry," Optics Communications **281**, 5701–5705 (2008).
22. D. W. Griffin, "Phase-shifting shearing interferometer," Opt. Lett. **26**, 140–142 (2001).
23. E. B. Li, J. Q. Yao, D. Y. Yu, J. T. Xi, and J. Chicharo, "Optical phase shifting with acousto-optic devices," Optics Letters **30**, 189–191 (2005).
24. T. Kiire, S. Nakadate, and M. Shibuya, "Digital holography with a quadrature phase-shifting interferometer," Applied Optics **48**, 1308–1315 (2009).

25. T. Kiire, S. Nakadate, and M. Shibuya, "Simultaneous formation of four fringes by using a polarization quadrature phase-shifting interferometer with wave plates and a diffraction grating," Applied Optics **47**, 4787–4792 (2008).
26. I. Yamaguchi, T. Matsumura, and J. Kato, "Phase-shifting color digital holography," Optics Letters **27**, 1108–1110 (2002).
27. J. Kato, I. Yamaguchi, and T. Matsumura, "Multicolor digital holography with an achromatic phase shifter," Optics Letters **27**, 1403–1405 (2002).
28. M. Roy, G. Cox, and P. Hariharan, "Low-coherence interference microscopy with an improved switchable achromatic phase-shifter," Opt. Express **13**, 9125–9130 (2005).
29. K. Hibino, R. Hanayama, J. Burke, and B. F. Oreb, "Tunable phase-extraction formulae for simultaneous shape measurement of multiple surfaces with wavelength-shifting interferometry," Opt. Express **12**, 5579–5594 (2004).
30. I. Yamaguchi, T. Ida, M. Yokota, and K. Yamashita, "Surface shape measurement by phase-shifting digital holography with a wavelength shift," Applied Optics **45**, 7610–7616 (2006).
31. D. Kim, J. W. You, and S. Kim, "White light on-axis digital holographic microscopy based on spectral phase shifting," Optics Express **14**, 229–234 (2006).
32. C. S. Guo, X. Cheng, X. Y. Ren, J. P. Ding, and H. T. Wang, "Optical vortex phase-shifting digital holography," Optics Express **12**, 5166–5171 (2004).
33. M. P. Arroyo, and J. Lobera, "A comparison of temporal, spatial and parallel phase shifting algorithms for digital image plane holography," Measurement Science & Technology **19**, 13 (2008).
34. F. Le Clerc, L. Collot, and M. Gross, "Numerical heterodyne holography with two-dimensional photodetector arrays," Optics Letters **25**, 716–718 (2000).
35. M. Atlan, M. Gross, and E. Absil, "Accurate phase-shifting digital interferometry," Optics Letters **32**, 1456–1458 (2007).
36. M. Gross, and M. Atlan, "Digital holography with ultimate sensitivity," Optics Letters **32**, 909-911 (2007).
37. M. Yamamoto, H. Yamamoto, and Y. Hayasaki, "Photon-counting digital holography under ultraweak illumination," Optics Letters **34**, 1081–1083 (2009).
38. A. Dubois, "Phase-map measurements by interferometry with sinusoidal phase modulation and four integrating buckets," J. Opt. Soc. Am. A **18**, 1972–1979 (2001).
39. K. J. Chalut, W. J. Brown, and A. Wax, "Quantitative phase microscopy with asynchronous digital holography," Optics Express **15**, 3047–3052 (2007).
40. N. T. Shaked, M. T. Rinehart, and A. Wax, "Dual-interference-channel quantitative-phase microscopy of live cell dynamics," Optics Letters **34**, 767–769 (2009).
41. O. Y. Kwon, D. M. Shough, and R. A. Williams, "Stroboscopic phase-shifting interferometry," Opt. Lett. **12**, 855 (1987).
42. Y. Awatsuji, M. Sasada, and T. Kubota, "Parallel quasi-phase-shifting digital holography," Applied Physics Letters **85**, 1069–1071 (2004).
43. Y. Awatsuji, A. Fujii, T. Kubota, and O. Matoba, "Parallel three-step phase-shifting digital holography," Applied Optics **45**, 2995–3002 (2006).
44. Y. Awatsuji, T. Tahara, A. Kaneko, T. Koyama, K. Nishio, S. Ura, T. Kubota, and O. Matoba, "Parallel two-step phase-shifting digital holography," Applied Optics **47**, D183–D189 (2008).
45. T. Nomura, S. Murata, E. Nitanai, and T. Numata, "Phase-shifting digital holography with a phase difference between orthogonal polarizations," Applied Optics **45**, 4873–4877 (2006).
46. L. Martinez-Leon, M. Araiza, B. Javidi, P. Andres, V. Climent, J. Lancis, and E. Tajahuerce, "Single-shot digital holography by use of the fractional Talbot effect," Optics Express **17**, 12900–12909 (2009).
47. C. Remmersmann, S. Sturwald, B. Kemper, P. Langehanenberg, and G. von Bally, "Phase noise optimization in temporal phase-shifting digital holography with partial coherence light sources and its application in quantitative cell imaging," Applied Optics **48**, 1463–1472 (2009).

48. E. Vikhagen, "Tv Holography - Spatial-Resolution and Signal Resolution in Deformation Analysis," Appl. Opt. **30**, 420–425 (1991).
49. G. Pedrini, H. J. Tiziani, and Y. L. Zou, "Digital double pulse-TV-holography," Opt. Lasers Eng. **26**, 199–219 (1997).
50. M. Liebling, T. Blu, and M. Unser, "Complex-wave retrieval from a single off-axis hologram," J. Opt. Soc. Am. A-Opt. Image Sci. Vis. **21**, 367–377 (2004).
51. T. Zhang, and I. Yamaguchi, "Three-dimensional microscopy with phase-shifting digital holography," Optics Letters **23**, 1221–1223 (1998).
52. Q. Liu, L. Z. Cai, and M. Z. He, "Digital correction of wave-front errors caused by detector nonlinearity of second order in phase-shifting interferometry," Optics Communications **239**, 223–228 (2004).
53. R. Langoju, A. Patil, and P. Rastogi, "Phase-shifting interferometry in the presence of nonlinear phase steps, harmonics, and noise," Optics Letters **31**, 1058–1060 (2006).
54. C. S. Guo, L. Zhang, H. T. Wang, J. Liao, and Y. Y. Zhu, "Phase-shifting error and its elimination in phase-shifting digital holography," Opt. Lett. **27**, 1687–1689 (2002).
55. M. D. Stenner, and M. A. Neifeld, "Motion compensation and noise tolerance in phase-shifting digital in-line holography," Optics Express **14**, 4286–4299 (2006).
56. M. Gross, M. Atlan, and E. Absil, "Noise and aliases in off-axis and phase-shifting holography," Appl. Opt. **47**, 1757–1766 (2008).
57. X. F. Xu, L. Z. Cai, Y. R. Wang, X. F. Meng, X. C. Cheng, H. Zhang, G. Y. Dong, and X. X. Shen, "Correction of wavefront reconstruction errors caused by light source intensity instability in phase-shifting interferometry," Journal of Optics a-Pure and Applied Optics **10**, 085008 (2008).
58. J. Schmit, and K. Creath, "Extended averaging technique for derivation of error-compensating algorithms in phase-shifting interferometry," Appl. Opt. **34**, 3610–3619 (1995).
59. X. F. Xu, L. Z. Cai, Y. R. Wang, X. F. Meng, X. C. Cheng, H. Zhang, G. Y. Dong, and X. X. Shen, "Correction of wavefront reconstruction errors caused by light source intensity instability in phase-shifting interferometry," J. Opt. A-Pure Appl. Opt. **10**, 6 (2008).

Chapter 9
Numerical Techniques of Digital Holography

Beyond the basic numerical diffraction methods, there are many DH techniques that take full advantage of the ability to numerically manipulate the optical field represented as an array of complex numbers. These techniques have unique capabilities, and are distinct from and generally more versatile than the conventional image processing methods that apply on intensity images.

9.1 Numerical Focusing

One of the most familiar characteristics of holography is the three-dimensional content of the image information. So in digital holography, starting from a single hologram acquired by the camera, and possibly preprocessed to suppress unwanted dc or twin terms, one can reconstruct the image at various distances simply by changing the distance value in the numerical diffraction, in a manner analogous to turning of the focusing knob on a microscope or other imaging instruments [1]. Figure 9.1 gives an example of such numerical focusing.

Furthermore, in some applications such as in microscopy and particle analysis, it is useful or required to be able to automatically determine the best focus of an image. One may apply a sharpness metric, a well-developed current technology. There are auto-focusing techniques that are unique to digital holography. In [2], it is shown that the average pixel value

$$M = \frac{1}{N_{\text{pixels}}} \sum_{\text{all pixels}} p_{ij} \tag{9.1}$$

can be used as a focus metric because it goes through an extremum at the best focal plane. For an amplitude object the M-value is a minimum and for a phase object it is a maximum. Examples in Fig. 9.2 show that the extrema are fairly sharp, although the

M.K. Kim, *Digital Holographic Microscopy: Principles, Techniques, and Applications*, Springer Series in Optical Sciences 162,
DOI 10.1007/978-1-4419-7793-9_9, © Springer Science+Business Media, LLC 2011

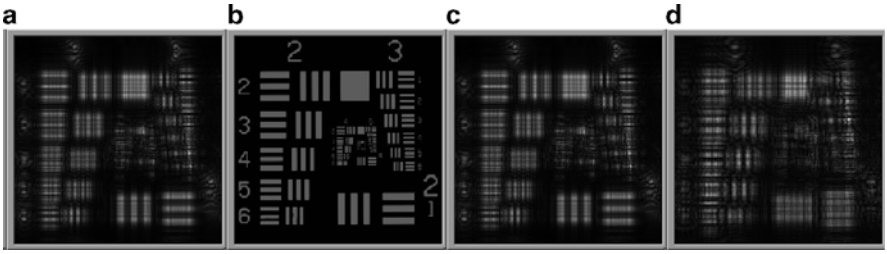

Fig. 9.1 Numerical focusing with $z = -100,\ 0,\ +100,\ +200\,\mu m$ relative to the expected image distance

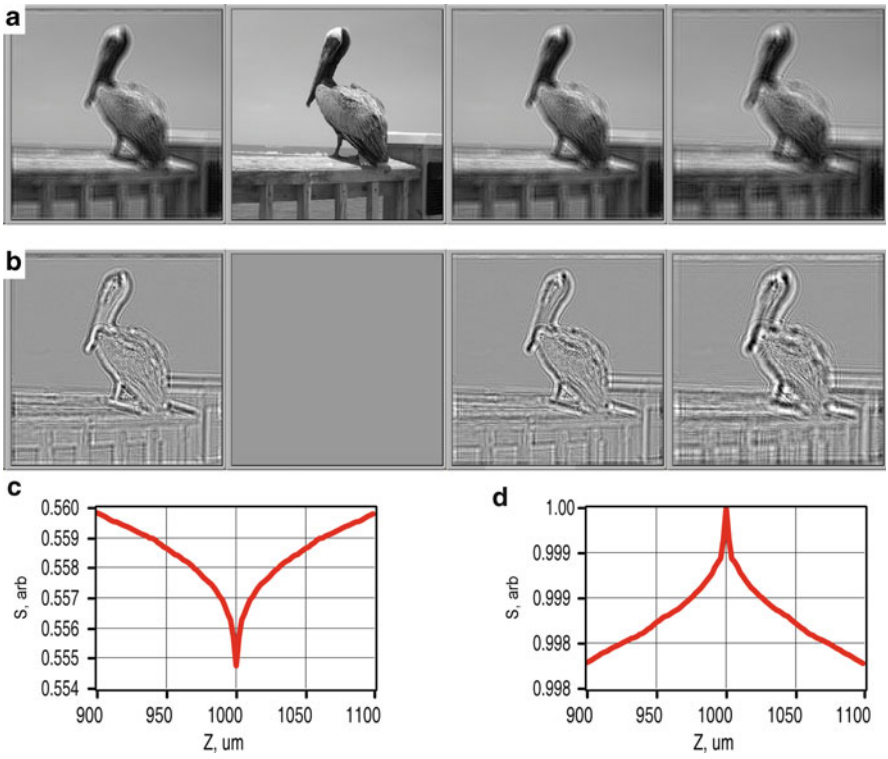

Fig. 9.2 Focus detection by average amplitude. (**a**) Reconstructed images of a gray-scale amplitude object at $z = -50,\ 0,\ +50,\ +100\,\mu m$ relative to the expected image distance; (**b**) reconstructed images of a phase-only object, i.e., the phase retardation is proportional to the gray scale of the object in (**a**); (**c**) focus metric vs. distance for the amplitude object (**a**); (**d**) for the phase object (**b**)

size of the peak is only a few percent. If the object is a mixture of amplitude and phase, then the extremum may be modified or even disappear.

Another signature of the focal plane is provided by the phase behavior [3]. In Fig. 9.3, the object is an opaque particle in a transparent background. The amplitude

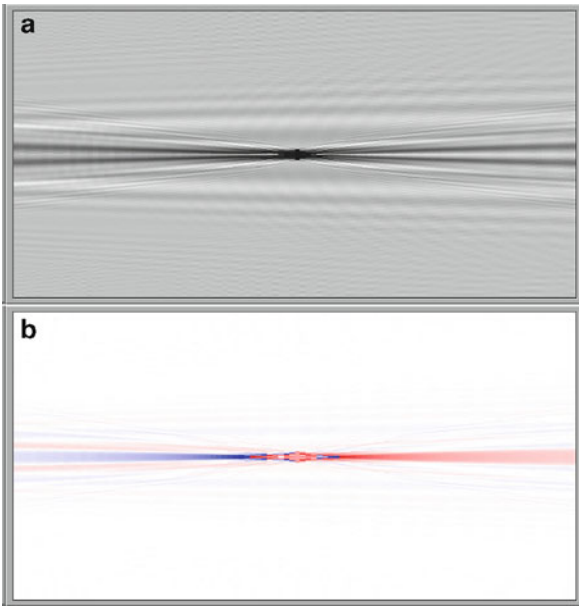

Fig. 9.3 Phase reversal across the focal plane of an opaque particle of diameter 10 μm. The panels represent propagation of $z = -250$ to $+250$ μm and lateral field size of $X = 256$ μm

image goes through a minimum at the focus, as expected, while the phase image changes sign across the focal plane. The phase reversal may also occur for a phase object, for example, a transparent particle in a bright background, and for these the amplitude may also change sign relative to the background. But the behavior is dependent on the size of the phase discontinuity and may not be robust enough for practical applications, compared to the amplitude object. On the other hand, a spherical particle may behave much as an opaque particle because of the large scattering and the phase reversal may be a useful method of focus detection.

A number of auto-focusing methods are analyzed in [4], including weighted spectral analysis, variance of gray value distribution, cumulated edge detection by gradient calculation, and cumulated edge detection by Laplace filtering. Variance and Laplacian of Gaussian are analyzed as a focus measure in [5]. The focal plane of particles can also be determined by maximizing the correlation coefficient [6].

9.1.1 Extended Focus

In [7], a sequence of digital holograms are recorded as a MEMS component undergoes axial displacement. The focus displacement is tracked by monitoring the phase image of DH and this information is in turn used to track the reconstruction distance. Using a similar logic in [8], an entire inclined surface of a MEMS component is imaged in focus by using the phase image to determine the focal distance of small areas of the surface and reconstructing the segments separately

using the corresponding focus distances. In [9], a volume containing many particles is imaged with all the particles in focus by determining the best focus for a region of interest around each particle. Extended focus imaging of macroscopic objects is demonstrated in a similar manner [10]. Extended focus imaging is shown to improve the precision of quantitative phase microscopy by digital holography [11].

From the basic equations for formation of holographic image, it is clear that if the hologram is stretched by a factor α, then the image magnification increases by α and the image distance increases by α^2. This effect can be utilized in DH by numerical expansion of the hologram array in a very flexible manner [12, 13]. Through an adaptive deformation of digital hologram, it is possible to put different objects at different distances simultaneously in focus. In particular, if the hologram is stretched in quadratic proportion of a lateral direction, then the focus distance varies linearly along that direction, bringing all parts of a tilted plane into focus.

9.2 Pixel Resolution Control

As we noted earlier, the Fresnel transform method (FTM) of numerical diffraction has pixel resolution, δx, proportional to the propagation distance, z,

$$\delta x = \frac{\lambda z}{N_x \delta x_0}, \tag{9.2}$$

where δx_0 is the pixel size on the input frame. Together with the minimum reconstruction distance, $z_{\min} = {X_0}^2/N\lambda$, the FTM has a significant constraint on the size and resolution of the reconstructed image. On the other hand, the Huygens convolution method (HCM) and the angular spectrum method (ASM) have constant frame size, so that objects larger than the camera frame cannot be properly imaged without using additional imaging optics.

9.2.1 Zero-Padding Method

For example, Fig. 9.4a is a simulated hologram of a resolution target with a field size $X_0 = 256\,\mu\text{m}$ and $N_x = 256$ pixels so that $\delta x_0 = 1\mu\text{m}$. The object distance is $z_0 = 1{,}200\,\mu\text{m}$. The hologram is preprocessed to remove the dc and twin terms. The Fig. 9.4b is reconstructed from Fig. 9.4a by FTM. At the reconstruction distance $z = 1{,}200\,\mu\text{m}$, the new resolution is $\delta x = (\lambda z/N_x \delta x_0) = 2.97\,\mu\text{m}$ and the field size $X = N_x \delta x = 760\,\mu\text{m}$, and therefore the target pattern occupies a small portion of the frame. A magnified detail of the dotted square in Fig. 9.4b is shown in Fig. 9.4c, containing 53 pixels across.

In order to maintain the same resolution, the hologram is padded with enough zeroes to make $\delta x' = (\lambda z/N_x' \delta x_0) = \delta x_0$, that is $N_x' = (\lambda z/\delta {x_0}^2) = 760$.

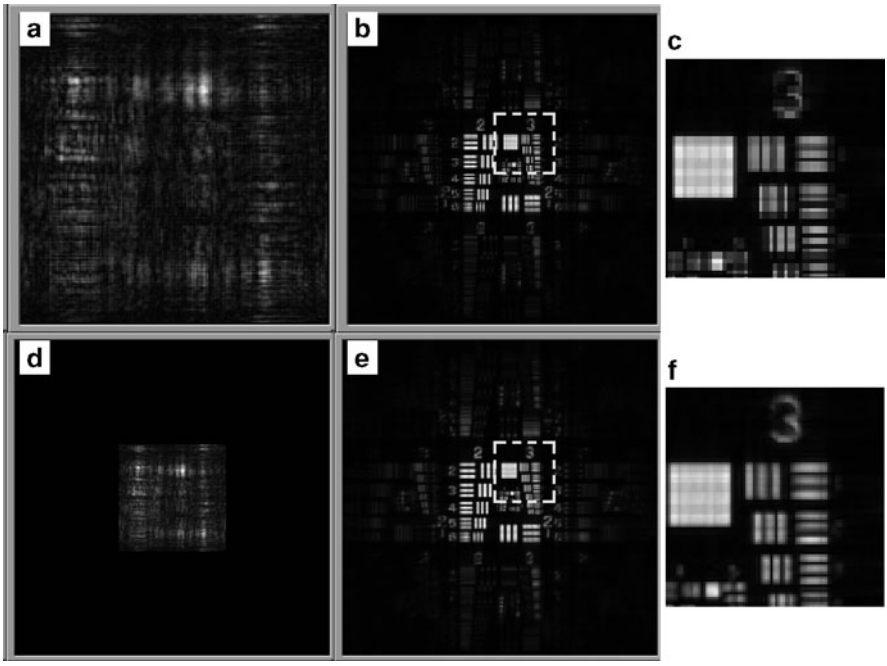

Fig. 9.4 Zero-padding method. (**a**) Simulated hologram with 256 × 256 pixels; (**b**) reconstruction from (**a**) by FTM; (**c**) a detail of the dotted square in (**b**) with 53 × 53 pixels; (**d**) the hologram with padded zeroes with total 760 × 760 pixels; (**e**) reconstruction from (**e**) by FTM; (**f**) a detail of the dotted square in (**e**) with 157 × 157 pixels

Figure 9.4d is the zero-padded hologram and Fig. 9.4e is the image reconstructed from Fig. 9.4d. Figure 9.4f is a magnified detail of the dotted square of Fig. 9.4e, but it now contains 157 pixels across. It maintains the resolution of $\delta x = 1\,\mu\text{m}$. For reconstruction at various distances, different number of zeroes are padded and the central $N_x = 256$ pixels can be cropped to maintain the same field and resolution. The method is straightforward but it does increase the computational load.

9.2.2 Two-Step Propagation Method

A two-step FTM method [14, 15] uses an intermediate plane to propagate over two distances z_1 and z_2 so that $z = z_1 + z_2$. Then

$$\delta x_1 = \frac{\lambda z_1}{N \delta x_0} \tag{9.3}$$

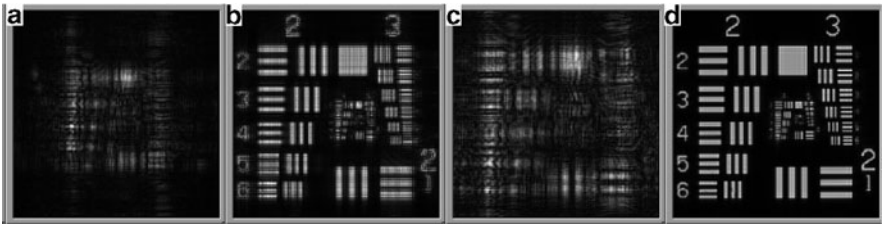

Fig. 9.5 Two-step propagation methods. (**a**) FTM propagation of $z_1 = 600$ μm, where $X_1 = 380$ μm; (**b**) another FTM of (**a**) for $z_2 = 600$ μm, to result in $X_2 = 256$ μm. (**c**) ASM propagation of $z_1 = 796$ μm, where $X_1 = 256$ μm; (**d**) FTM of (**c**) for $z_2 = 404$ μm to obtain $X_2 = 256$ μm

and

$$\delta x_2 = \frac{\lambda z_2}{N \delta x_1} = \frac{z_2}{z_1} \delta x_0. \tag{9.4}$$

The ratio between z_1 and z_2 can be adjusted so that the final resolution δx_2 matches the desired resolution δx. In particular, to maintain the same pixel size in the input and output planes, the propagation over z can be carried out in two half-steps of $z/2$, as shown in Fig. 9.5a, b.

On the other hand, with the two-step FTM, the partial steps z_1 and z_2 must also each satisfy the minimum distance requirement. A more flexible method [16] first propagates to z_1 by ASM, which does not have minimum distance requirement but maintains the same pixel resolution, followed by another propagation of $z_2 = z - z_1$ using FTM. The values of z_1 and z_2 are chosen so that

$$z_2 = \frac{X_0^2}{\lambda N_x} \tag{9.5}$$

and $z_1 = z - z_2$. The result shown in Fig. 9.5d has better quality than Fig. 9.5b.

9.3 Optical Phase Unwrapping

The phase images generated by digital holography, as well as most other phase imaging techniques, suffer from modulo 2π ambiguities. An object whose optical thickness variation exceeds the wavelength produces wrapped phase images, with discontinuities at every 2π of the phase profile. Numerous phase unwrapping algorithms have been developed [17, 18], but it remains challenging to find solutions that can efficiently address all different types of phase topologies. This is because most of the unwrapping procedures are based on different strategies to

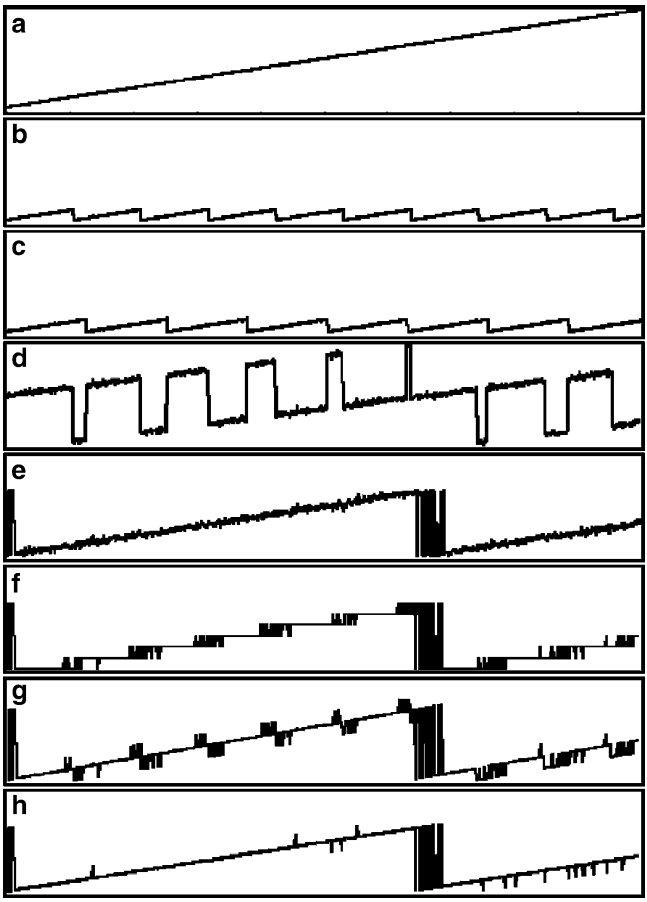

Fig. 9.6 Optical phase unwrapping. (**a**) Height profile $z(x)$ of a slanted plane of maximum height 5 μm; (**b**, **c**) phase profiles $\varphi_1(x,y)$ and $\varphi_2(x,y)$ with $\lambda_1 = 0.532$ μm and $\lambda_2 = 0.633$ μm, respectively; (**d**) $\Delta\varphi = \varphi_1 - \varphi_2$; (**e**) add 2π wherever $\Delta\varphi<0$; (**f**) $\text{int}[\Phi_{12}'\Lambda_{12}/\lambda_1]2\pi$; (**g**) $\Phi_{12} = \varphi_1 + \text{int}[\Phi_{12}'\Lambda_{12}/\lambda_1]2\pi$; (**h**) clean up glitches by adding or subtracting λ_1 if $\left|\Phi_e - \Phi_g\right| \geq \lambda_1/2$ [19]

find the phase discontinuities and to make judgments on how to stitch the discontinuous regions. Most often the algorithms are computationally demanding and have difficulty handling different types of phase topologies. Optical phase unwrapping (OPU) based on multiwavelength digital holography offers a method that is fast, efficient, and deterministic [19, 20].

For example, two holograms of the same object are acquired using two different wavelengths, λ_1 and $\lambda_2 (\lambda_2 > \lambda_1$ for definiteness), and the phase images $\varphi_1(x,y)$ and $\varphi_2(x,y)$ are produced from them (Fig. 9.6). Each of these profiles range in phase

from 0 to 2π and the corresponding optical thickness profiles range up to λ_1 or λ_2. Now subtracting the two, $\Delta\varphi = \varphi_1 - \varphi_2$, followed by adding 2π wherever $\Delta\varphi<0$, results in a new phase image $\Phi_{12}{}'$ that ranges from 0 to 2π, whose effective wavelength, or the synthetic wavelength [21–23], is given by

$$\Lambda_{12} = \frac{\lambda_2\lambda_1}{\lambda_2 - \lambda_1} \tag{9.6}$$

The new phase image handles optical thickness variations up to Λ_{12}, which can be made large enough to cover the object's maximum thickness variation by choosing small enough wavelength difference. If, however, the original phase images have certain amount of noise, say $\varepsilon 2\pi$, then the new phase image contains the same amount of phase noise, which translates to noise in the optical thickness profile, $\varepsilon\Lambda_{12}$ instead of $\varepsilon\lambda_1$, amplified by the same factor as the synthetic wavelength magnification. The noise can be reduced back to the original level, by using the new phase map as a guide to decide how to unwrap the φ_1 phase map. That is, the new phase map is given by

$$\Phi_{12} = \varphi_1 + \text{int}\left[\frac{\Phi_{12}{}'\Lambda_{12}}{\lambda_1}\right]2\pi, \tag{9.7}$$

where int stands for integer quotient. This scheme works unless the amplified noise exceeds the original wavelength, $\varepsilon\Lambda_{12}>\lambda_1$, which sets the minimum difference wavelength, and therefore the maximum synthetic wavelength:

$$\lambda_2 - \lambda_1 > \varepsilon\lambda_2; \qquad \Lambda_{12} < \frac{\lambda_1}{\varepsilon} \tag{9.8}$$

If the noise is more excessive, or a larger synthetic wavelength is needed, there are hierarchical methods using three or more wavelengths [24, 25]. For example, start from λ_1 and choose $\lambda_2>\lambda_1$ such that $\Lambda_{12}<\frac{\lambda_1}{\varepsilon}$ and

$$\lambda_2 = \frac{\Lambda_{12}\lambda_1}{\Lambda_{12} - \lambda_1}. \tag{9.9}$$

The noise associated with the new phase map of Λ_{12} is $\varepsilon_{12} = \varepsilon\lambda_1/\Lambda_{12}$. Next choose $\lambda_3>\lambda_2$ such that $\Lambda_{23}<(\Lambda_{12}/\varepsilon_{12})$ and

$$\lambda_3 = \frac{\Lambda_{23}\lambda_2}{\Lambda_{23} - \lambda_2}. \tag{9.10}$$

Now use Λ_{12} and Λ_{13} as the two new phase maps to form a new combination

$$\Lambda_{23} = \frac{\Lambda_{13}\Lambda_{12}}{\Lambda_{13} - \Lambda_{12}}. \tag{9.11}$$

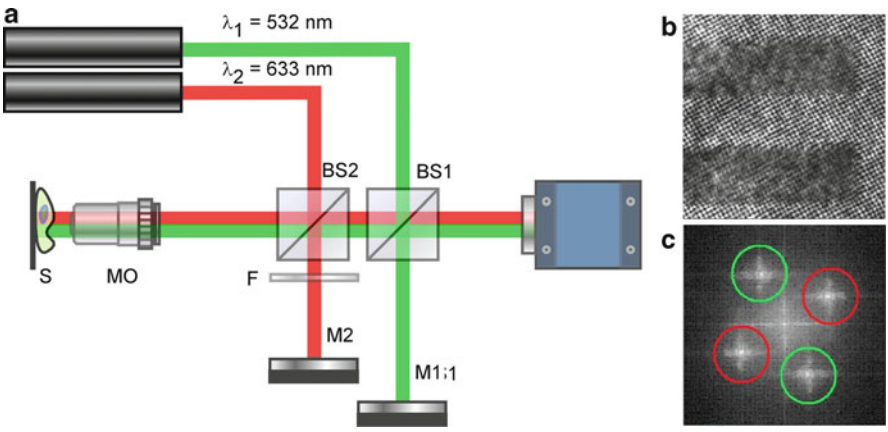

Fig. 9.7 (**a**) Two-wavelength holographic interferometer. (**b**) A detail of a hologram showing the two sets of fringes in orthogonal directions. (**c**) Angular spectrum of (**b**) showing the two pairs of peaks for the *green* and *red* lasers [26]

The noise associated with Λ_{23} is $\varepsilon_{23} = \varepsilon\lambda_1/\Lambda_{23}$. In general, the nth wavelength $\lambda_n > \lambda_{n-1}$ is chosen such that $\Lambda_{n-1,n} < (\Lambda_{n-2,n-1}/\varepsilon_{n-2,n-1})$ and

$$\lambda_n = \frac{\Lambda_{n-1,n}\lambda_{n-1}}{\Lambda_{n-1,n} - \lambda_{n-1}}.$$

Then use $\Lambda_{n-2,n-1}$ and $\Lambda_{n-2,n}$ as the two new phase maps to form a new combination

$$\Lambda_{n-1,n} = \frac{\Lambda_{n-2,n}\Lambda_{n-2,n-1}}{\Lambda_{n-2,n} - \Lambda_{n-2,n-1}} = \frac{\lambda_n\lambda_{n-1}}{\lambda_n - \lambda_{n-1}}. \tag{9.12}$$

The noise associated with $\Lambda_{n-1,n}$ is $\varepsilon_{n-1,n} = \varepsilon\lambda_1/\Lambda_{n-1,n}$. The process continues until $\Lambda_{n-1,n}$ is large enough for the z-range of the object.

The optical phase unwrapping method was applied to quantitative phase microscopy in [20, 27]. Two-wavelength OPU can be achieved with single exposure digital holography, by angular multiplexing [26, 28–30], as shown in Fig. 9.7. The double interferometer consists of one common object arm and two separate reference arms illuminated by two different wavelength lasers. The reference arms are aligned so that the fringes of the two wavelengths are perpendicular to each other. On the angular spectrum the peaks appear as two distinct pairs, so that the holographic images can be processed separately by selecting the appropriate peak for each wavelength. Figure 9.8 is an example of a DHM phase image of the surface of a polished coal sample, unwrapped by OPU. Evidently, the software-based method has difficulty handling isolated areas of phase profile, while the OPU generates correct phase profile regardless of the topology. The OPU consists of only several algebraic and Boolean operations, and therefore is very fast and computational demand is low. The method is entirely deterministic, not depending on any estimations of topology of a pixel's neighborhood.

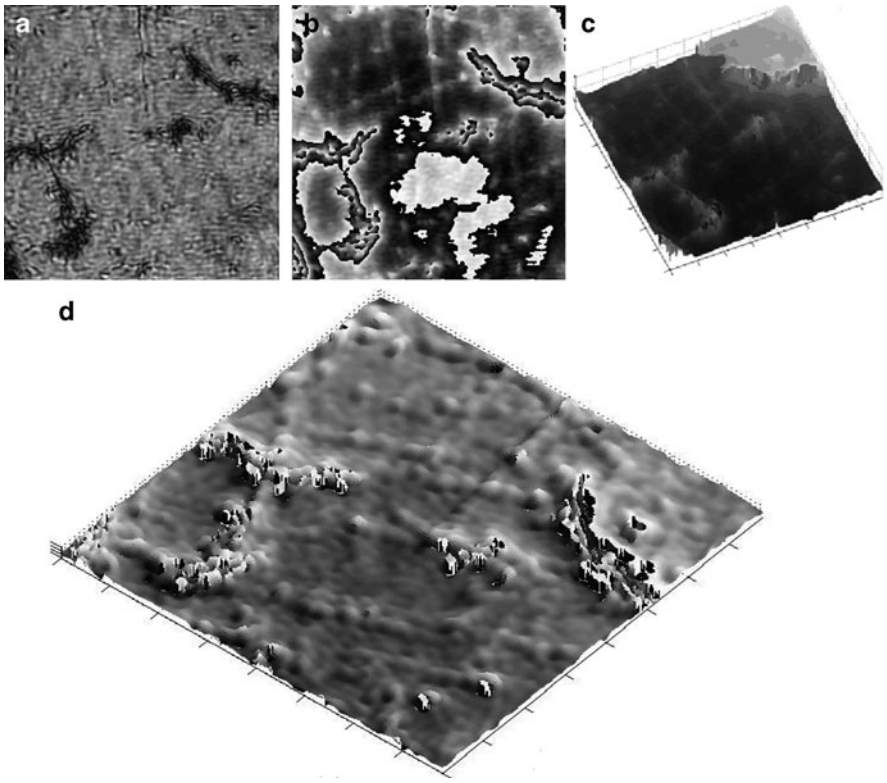

Fig. 9.8 Two-wavelength optical phase unwrapping on images of a porous coal sample. (**a**) Amplitude image. (**b**) Single-wavelength phase image reconstructed with $\lambda_1 = 532\,\text{nm}$. (A second phase image with $\lambda_2 = 633\,\text{nm}$ is not shown.) (**c**) Software unwrapped phase images from (**b**). (**d**) 3D rendering of the dual-wavelength unwrapped phase image [26]

For macroscopic measurements with thickness range of centimeters, the wavelength difference needs to be $\sim 10^{-5}\lambda$ or several GHz in frequency difference, which can be produced by laser cavity modulation [31] or electrooptic modulation. For microscopic imaging of <50 μm thick biological cells, say, the wavelength difference needs to be $\Delta\lambda$>5 nm, which would require separate lasers or a tunable laser. For larger wavelength differences, the image formation may be affected by chromatic aberration of the system. The optical elements or the object itself may have chromatic aberration, or in the case of Fresnel transform method for numerical diffraction, the reconstructed image size depends on the wavelength. In DH, it is a simple matter to compensate for the aberration by adjustment of the reconstruction distance [32] or by subtracting reference holograms without the object [33]. Three-wavelength OPU has been demonstrated with three LED's, three laser diodes, or a tunable dye laser as light sources [34–36].

Simultaneous acquisition of multiwavelength holograms can be achieved by using tri-color CCD sensors [37, 38]. A means to determine the precise wavelengths

during OPU experiment is available [39]. Instead of multiple wavelengths, one may shift the illumination angle to achieve similar phase unwrapping effect [40]. Phase unwrapping is also effected by varying reconstruction distances [41]. The OPU method is fast enough for real-time vibration analysis [31, 42].

9.4 Diffraction Between Tilted Planes

Conventional diffraction theory usually describes propagation of optical field between parallel planes perpendicular to the optical axis. The ability to directly calculate the holographic image on an arbitrarily inclined plane would be useful in many different applications, such as inspection of fiber segments, characterization of integrated optics components, imaging of tissue surfaces, and particle field imaging with seeded laminar flow patterns [43, 44]. Diffraction between tilted planes have been studied by a number of authors [45–49] and fairly complete descriptions are provided in [50–52]. It has been applied to holographic reconstruction with varying view angle [53, 54] and to reconstruction of tomographic images of digital interference holography on variable planes of inclination [44, 55]. Wavelet transform approach has also been applied to reconstruction on tilted planes [43].

As depicted in Fig. 9.9a, we are in general interested in the propagation of optical field from the input plane $\Sigma_0'(x_0', y_0')$ to the output plane $\Sigma'(x', y')$, either or both of which may be tilted with respect to the optical axis. A general strategy is to use intermediate planes $\Sigma_0(x_0, y_0)$ and $\Sigma(x, y)$ that are perpendicular to the optic axis. One first calculates propagation from Σ_0' to Σ_0, which can be accomplished by rotation in the Fourier domain, as described below. This is followed by propagation between parallel planes $\Sigma_0(z = -Z)$ and $\Sigma(z = 0)$, using conventional methods based on traditional diffraction theory. Finally, propagation from Σ to the tilted output plane Σ' is handled by another Fourier rotation.

The method of Fourier rotation is illustrated with the configuration of Fig. 9.9b, where the output plane is tilted by an angle β around the y-axis while the input plane is normal to the optical axis. Let the optical field at the input plane be

$$E_{\Sigma_0}(x_0, y_0) = E_0(x_0, y_0). \tag{9.13}$$

Then its angular spectrum

$$A_0\left(k_x, k_y\right) = \mathcal{F}\{E_0\} = \frac{1}{2\pi} \int_{\Sigma_0} \mathrm{d}x_0 \mathrm{d}y_0 E_0(x_0, y_0) \exp\left[-i\left(k_x x_0 + k_y y_0\right)\right] \tag{9.14}$$

is the amplitude of a plane wave component

$$\psi(x, y, z) = \exp\left[i\left(k_x x + k_y y + k_z z\right)\right] \tag{9.15}$$

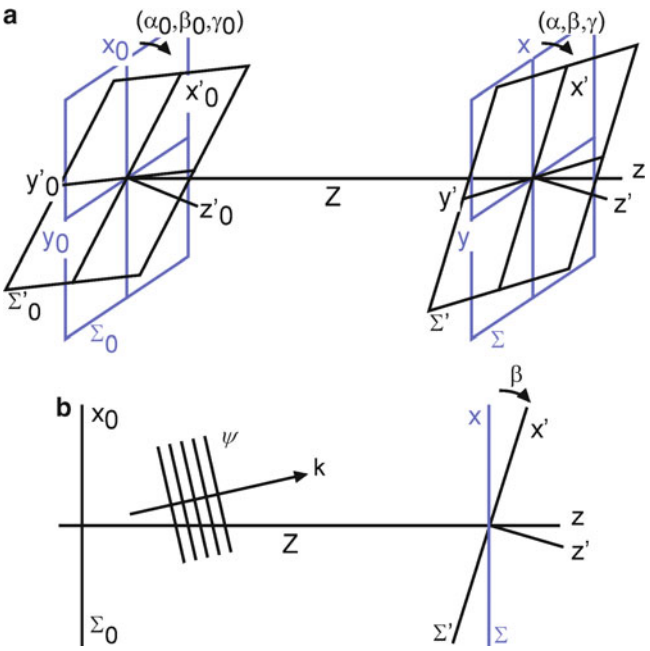

Fig. 9.9 Geometry of diffraction between tilted planes. (**a**) General rotation of input and output planes. (**b**) Simpler case of only the output plane tilted around the *y*-axis by β

that propagates along the direction $\mathbf{k} = \left(k_x, k_y, k_z\right)$, where

$$k_z = \sqrt{k^2 - {k_x}^2 - {k_y}^2}. \tag{9.16}$$

As we saw in Chap. 2, the optical field at any distance $Z + z$ from the Σ_0-plane is

$$E(x, y, z) = \frac{1}{2\pi} \int_{\Xi_0} \mathrm{d}k_x \mathrm{d}k_y A_0\left(k_x, k_y\right) \exp\left[i\left(k_x x + k_y y + k_z (Z + z)\right)\right]. \tag{9.17}$$

This can be rewritten in the coordinate system of (x', y', z') by noting that

$$\begin{bmatrix} x \\ y \\ z \end{bmatrix} = \begin{bmatrix} x' \cos\beta - z' \sin\beta \\ y' \\ x' \sin\beta + z' \cos\beta \end{bmatrix} \tag{9.18}$$

and

$$\begin{bmatrix} k_x \\ k_y \\ k_z \end{bmatrix} = \begin{bmatrix} k_x' \cos\beta - k_z' \sin\beta \\ k_y' \\ k_x' \sin\beta + k_z' \cos\beta \end{bmatrix} \tag{9.19}$$

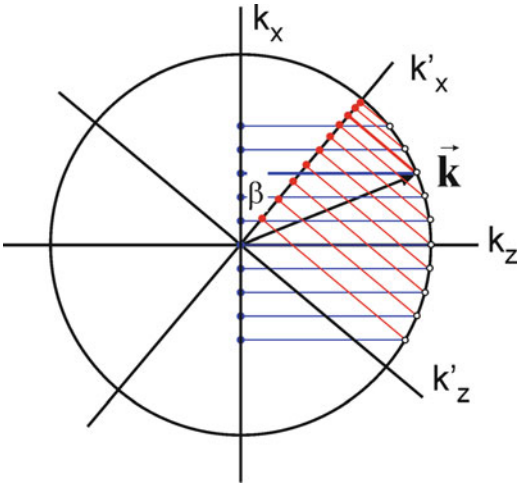

Fig. 9.10 Mapping of discrete frequency intervals under rotation

and using the Jacobian determinant

$$\begin{aligned} \mathrm{d}k_x \mathrm{d}k_y &= \mathrm{d}k_x' \mathrm{d}k_y' \left| \frac{\partial(k_x, k_y)}{\partial(k_x', k_y')} \right|, \\ &= \mathrm{d}k_x' \mathrm{d}k_y' \left| \frac{\partial k_x}{\partial k_x'} \frac{\partial k_y}{\partial k_y'} - \frac{\partial k_x}{\partial k_y'} \frac{\partial k_y}{\partial k_x'} \right|, \\ &= \mathrm{d}k_x' \mathrm{d}k_y' \left(\cos\beta + \frac{k_x'}{k_z'} \sin\beta \right). \end{aligned} \tag{9.20}$$

The field on the Σ'-plane with $z' = 0$ is then

$$\begin{aligned} E_{\Sigma'}(x', y') = &\frac{1}{2\pi} \int_{\Sigma_0} \mathrm{d}k_x' \mathrm{d}k_y' \exp\left[i\left(k_x' x' + k_y y' \right) \right] \\ &\times \left\{ \begin{array}{l} A_0\left(k_x' \cos\beta - k_z' \sin\beta, k_y' \right) \left(\cos\beta + \dfrac{k_x'}{k_z'} \sin\beta \right) \\ \qquad \times \exp[i(k_x' \sin\beta + k_z' \cos\beta) Z] \end{array} \right\} \end{aligned} \tag{9.21}$$

with $k_z' = \sqrt{k^2 - k_x'^2 - k_y'^2}$. Analytically, this is an inverse Fourier transform of the quantity in curly brackets.

Problem arises when this is discretized for numerical diffraction because of the nonlinear transform of (9.18) and (9.19). In Fig. 9.10, the blue dots on the vertical axis represent the uniformly sampled spatial frequencies k_x, while the corresponding wave vector $\mathbf{k}$ is on the circle (Ewald sphere) of radius k. When the $\mathbf{k}$-vector is projected on the k_x'-axis, it is clear that the sampling on this axis is nonuniform (red dots). Possible solutions are to use an algorithm for nonuniformly sampled Fourier transform [56, 57] or to interpolate the spectrum onto uniform sampling points.

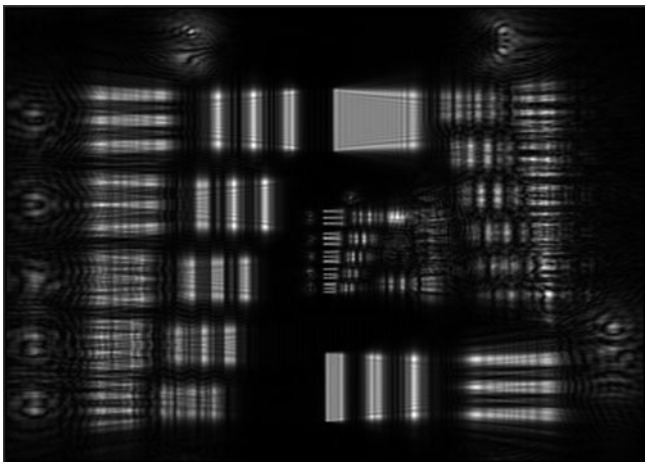

Fig. 9.11 Diffraction of resolution target pattern of 256 × 256 μm^2 tilted at 45°. The plane is at focus at the center vertical line

A third alternative, especially when the tilt is only around a single axis, is to numerically integrate one axis (k_x' in our example) without the benefit of FFT and to apply FFT for the other axis (k_y' in our example) (Fig. 9.11). Depending on the application, this may be satisfactory in speed and accuracy. Another problem to note is that although the k_x range is centered at zero, the k_x' is in general not centered at zero, which imparts a carrier frequency on the output field. This needs to be compensated by shifting the center of k_x'-axis.

9.5 Aberration Compensation

Aberration arises when the optical wavefront of an imaging system is deformed in an unintended manner. Recall that Gabor's original intention for lensless imaging by holography was to avoid the aberration problems of electron lenses. Reconstruction of wavefront by holography also leads to the ability to control and manipulate the wavefront in order to compensate for the aberration. Leith & Upatnieks demonstrated recording of wavefront aberration by holography and use of the hologram as a correction plate for the imaging system [58]. Digital holography offers further flexibility and versatility in sensing and control of aberrations.

For example, suppose an imaging system conveys the optical field of an object as E_O but imperfections in the system adds aberration E_a to the object field, preventing formation of a perfect image. Interference with a reference field E_R results in a hologram, one of its twin-image terms being of the form $(E_O + E_a)E_R^*$. The aberration term can be eliminated if one acquires another hologram without the object in place, so that the corresponding term is $E_a E_R^*$. Now if this hologram is

subtracted from the first, the resulting numerical hologram has the object field without aberration, $E_O E_R^*$. This is digital implementation of the concept of correction plate in [58]. At least in principle, this results in complete elimination of aberration without the need to know any details of the aberration. The aberration of the imaging system can be measured once and used for imaging of any objects, as long as the imaging parameters do not change. A possible drawback is that it requires at least two exposures of holograms.

There are techniques for achieving aberration compensation from a single hologram. These usually presume that the object has flat or empty areas, such as in MEMS devices [59] or substrate areas of cell culture, or if the sample is known to be thin with flat background or substrate [60]. Lowest order aberration is the tilt of wave front that may result from misalignment of object and reference or, equivalently, misregistration of center of angular spectrum filter. This can be corrected by use of correspondingly tilted reference plane wave. Note that because of the discrete intervals of spatial frequencies, the tilt may not always be eliminated by adjustment of the angular spectrum filter and use of tilted reference plane wave is then necessary. Next order is the spherical aberration, which may arise from defocus of the real space imaging system [61] or numerical focus of digital holography. It also often arises when the object and reference waves have mismatched curvatures. This can be compensated for by using quadratic curvature of numerical reference wave [62–64]. Adjustment of aberration parameters can be automated for efficiency and accuracy. Automatic compensation of higher order terms of Zernike polynomials has been demonstrated [65]. Generalizing further, the concept of numerical parametric lens has been introduced that can shift, magnify, and compensate aberrations [66]. A partial compensation of aberration without detailed knowledge of aberration parameters is possible by in effect high-pass filtering a small central portion of a twin-image diffraction order in angular spectrum. This assumes that aberration is mostly low-order and that the specimen does not have interesting low-frequency features [67]. In [68], the parabolic phase front is subtracted using a lateral shear approach. Compensation of astigmatism is demonstrated that accompanies anamorphism of grating-reflected image [69] or tilted plane [47]. Assuming the microscope objective is the critical place where aberrations enter the system, insertion of reference beam before the objective lens can reduce differential aberration between the object and reference fields [70], although this may be difficult with the short working distance of most microscope systems. Compensation of chromatic aberration has been demonstrated [33].

References

1. S. Grilli, P. Ferraro, S. De Nicola, A. Finizio, G. Pierattini, and R. Meucci, "Whole optical wavefields reconstruction by digital holography," Optics Express **9**, 294–302 (2001).
2. F. Dubois, C. Schockaert, N. Callens, and C. Yourassowsky, "Focus plane detection criteria in digital holography microscopy by amplitude analysis," Optics Express **14**, 5895–5908 (2006).

3. W. D. Yang, A. B. Kostinski, and R. A. Shaw, "Phase signature for particle detection with digital in-line holography," Optics Letters **31**, 1399–1401 (2006).
4. P. Langehanenberg, B. Kemper, D. Dirksen, and G. von Bally, "Autofocusing in digital holographic phase contrast microscopy on pure phase objects for live cell imaging," Applied Optics **47**, D176-D182 (2008).
5. M. L. Tachiki, M. Itoh, and T. Yatagai, "Simultaneous depth determination of multiple objects by focus analysis in digital holography," Applied Optics **47**, D144–D153 (2008).
6. Y. Yang, B. S. Kang, and Y. J. Choo, "Application of the correlation coefficient method for determination of the focal plane to digital particle holography," Applied Optics **47**, 817–824 (2008).
7. P. Ferraro, G. Coppola, S. D. Nicola, A. Finizio, and G. Pierattini, "Digital holographic microscope with automatic focus tracking by detecting sample displacement in real time," Opt. Lett. **28**, 1257–1259 (2003).
8. P. Ferraro, S. Grilli, and D. Alfieri, "Extended focused image in microscopy by digital holography," Optics Express **13**, 6738–6749 (2005).
9. M. Antkowiak, N. Callens, C. Yourassowsky, and F. Dubois, "Extended focused imaging of a microparticle field with digital holographic microscopy," Optics Letters **33**, 1626–1628 (2008).
10. C. P. McElhinney, B. M. Hennelly, and T. J. Naughton, "Extended focused imaging for digital holograms of macroscopic three-dimensional objects," Applied Optics **47**, D71–D79 (2008).
11. T. Colomb, N. Pavillon, J. Kuhn, E. Cuche, C. Depeursinge, and Y. Emery, "Extended depth-of-focus by digital holographic microscopy," Optics Letters **35**, 1840–1842 (2010).
12. P. Ferraro, M. Paturzo, P. Memmolo, and A. Finizio, "Controlling depth of focus in 3D image reconstructions by flexible and adaptive deformation of digital holograms," Optics Letters **34**, 2787–2789 (2009).
13. M. Paturzo, and P. Ferraro, "Creating an extended focus image of a tilted object in Fourier digital holography," Optics Express **17**, 20546–20552 (2009).
14. F. C. Zhang, I. Yamaguchi, and L. P. Yaroslavsky, "Algorithm for reconstruction of digital holograms with adjustable magnification," Optics Letters **29**, 1668–1670 (2004).
15. D. Y. Wang, J. Zhao, F. Zhang, G. Pedrini, and W. Osten, "High-fidelity numerical realization of multiple-step Fresnel propagation for the reconstruction of digital holograms," Applied Optics **47**, D12–D20 (2008).
16. L. F. Yu, and M. K. Kim, "Pixel resolution control in numerical reconstruction of digital holography," Optics Letters **31**, 897–899 (2006).
17. T. R. Judge, C. G. Quan, and P. J. Bryanstoncross, "Holographic Deformation Measurements by Fourier-Transform Technique with Automatic Phase Unwrapping," Opt. Eng. **31**, 533–543 (1992).
18. M. A. Schofield, and Y. Zhu, "Fast phase unwrapping algorithm for interferometric applications," Opt. Lett. **28**, 1194–1196 (2003).
19. J. Gass, A. Dakoff, and M. K. Kim, "Phase imaging without 2-pi ambiguity by multiwavelength digital holography," Opt. Lett. **28**, 1141–1143 (2003).
20. D. Parshall, and M. K. Kim, "Digital holographic microscopy with dual-wavelength phase unwrapping," Appl. Opt. **45**, 451–459 (2006).
21. J. C. Wyant, "Testing Aspherics Using Two-Wavelength Holography," Applied Optics **10**, 2113–2118 (1971).
22. Y. Y. Cheng, and J. C. Wyant, "Two-wavelength phase shifting interferometry," Appl. Opt. **23**, 4539–4543 (1984).
23. K. Creath, "Step height measurement using two-wavelength phase-shifting interferometry," Appl. Opt. **26**, 2810–2816 (1987).
24. W. Nadeborn, P. Andra, and W. Osten, "A robust procedure for absolute phase measurement," Optics and Lasers in Engineering **24**, 245–260 (1996).
25. C. Wagner, W. Osten, and S. Seebacher, "Direct shape measurement by digital wavefront reconstruction and multiwavelength contouring," Opt. Eng. **39**, 79–85 (2000).

26. A. Khmaladze, A. Restrepo-Martinez, M. Kim, R. Castaneda, and A. Blandon, "Simultaneous dual-wavelength reflection digital holography applied to the study of the porous coal samples," Appl. Opt. **47**, 3203–3210 (2008).
27. J. Gass, A. Dakoff, and M. K. Kim, "Phase imaging without 2 pi ambiguity by multiwavelength digital holography," Opt. Lett. **28**, 1141–1143 (2003).
28. J. Kuhn, T. Colomb, F. Montfort, F. Charriere, Y. Emery, E. Cuche, P. Marquet, and C. Depeursinge, "Real-time dual-wavelength digital holographic microscopy with a single hologram acquisition," Opt. Express **15**, 7231–7242 (2007).
29. A. Khmaladze, M. Kim, and C. M. Lo, "Phase imaging of cells by simultaneous dual-wavelength reflection digital holography," Opt. Express **16**, 10900–10911 (2008).
30. J. Kuhn, F. Charriere, T. Colomb, E. Cuche, F. Montfort, Y. Emery, P. Marquet, and C. Depeursinge, "Axial sub-nanometer accuracy in digital holographic microscopy," Meas. Sci. Technol. **19**, 8 (2008).
31. G. Pedrini, P. Froning, H. J. Tiziani, and M. E. Gusev, "Pulsed digital holography for high-speed contouring that uses a two-wavelength method," Appl. Opt. **38**, 3460–3467 (1999).
32. P. Ferraro, L. Miccio, S. Grilli, M. Paturzo, S. De Nicola, A. Finizio, R. Osellame, and P. Laporta, "Quantitative Phase Microscopy of microstructures with extended measurement range and correction of chromatic aberrations by multiwavelength digital holography," Opt. Express **15**, 14591–14600 (2007).
33. S. De Nicola, A. Finizio, G. Pierattini, D. Alfieri, S. Grilli, L. Sansone, and P. Ferraro, "Recovering correct phase information in multiwavelength digital holographic microscopy by compensation for chromatic aberrations," Optics Letters **30**, 2706–2708 (2005).
34. N. Warnasooriya, and M. K. Kim, "LED-based multi-wavelength phase imaging interference microscopy," Opt. Express **15**, 9239–9247 (2007).
35. N. Warnasooriya, and M. Kim, "Quantitative phase imaging using three-wavelength optical phase unwrapping," J. Mod. Opt. **56**, 85–92 (2009).
36. C. J. Mann, P. R. Bingham, V. C. Paquit, and K. W. Tobin, "Quantitative phase imaging by three-wavelength digital holography," Optics Express **16**, 9753–9764 (2008).
37. P. Tankam, P. Picart, D. Mounier, J. M. Desse, and J. C. Li, "Method of digital holographic recording and reconstruction using a stacked color image sensor," Applied Optics **49**, 320–328 (2010).
38. M. T. Rinehart, N. T. Shaked, N. J. Jenness, R. L. Clark, and A. Wax, "Simultaneous two-wavelength transmission quantitative phase microscopy with a color camera," Optics Letters **35**, 2612–2614 (2010).
39. D. Carl, M. Fratz, M. Pfeifer, D. M. Giel, and H. Hofler, "Multiwavelength digital holography with autocalibration of phase shifts and artificial wavelengths," Applied Optics **48**, H1-H8 (2009).
40. D. V. Prieto, and J. Garcia-Sucerquia, "Three-dimensional surface contouring of macroscopic objects by means of phase-difference images," Applied Optics **45**, 6381–6387 (2006).
41. A. Khmaladze, T. Epstein, and Z. Chen, "Phase unwrapping by varying the reconstruction distance in digital holographic microscopy," Optics Letters **35**, 1040–1042 (2010).
42. Y. Fu, G. Pedrini, B. M. Hennelly, R. M. Groves, and W. Osten, "Dual-wavelength image-plane digital holography for dynamic measurement," Opt. Lasers Eng. **47**, 552–557 (2009).
43. D. Lebrun, A. M. Benkouider, S. Coetmellec, and M. Malek, "Particle field digital holographic reconstruction in arbitrary tilted planes," Optics Express **11**, 224–229 (2003).
44. L. F. Yu, and M. K. Kim, "Wavelength scanning digital interference holography for variable tomographic scanning," Optics Express **13**, 5621–5627 (2005).
45. D. Leseberg, "Computer-Generated 3-Dimensional Image Holograms," Applied Optics **31**, 223–229 (1992).

46. N. Delen, and B. Hooker, "Free-space beam propagation between arbitrarily oriented planes based on full diffraction theory: a fast Fourier transform approach," Journal of the Optical Society of America a-Optics Image Science and Vision **15**, 857–867 (1998).
47. S. D. Nicola, A. Finizio, G. Pierattini, P. Ferraro, and D. Alferi, "Angular spectrum method with correction of anamorphism for numerical reconstruction of digital holograms on tilted planes," Optics Express **13**, 9935 (2005).
48. R. P. Muffoletto, J. M. Tyler, and J. E. Tohline, "Shifted Fresnel diffraction for computational holography," Optics Express **15**, 5631–5640 (2007).
49. K. Matsushima, "Shifted angular spectrum method for off-axis numerical propagation," Optics Express **18**, 18453–18463 (2010).
50. K. Matsushima, "Formulation of the rotational transformation of wave fields and their application to digital holography," Applied Optics **47**, D110–D116 (2008).
51. K. Matsushima, H. Schimmel, and F. Wyrowski, "Fast calculation method for optical diffraction on tilted planes by use of the angular spectrum of plane waves," J. Opt. Soc. Am. A **20**, 1755–1762 (2003).
52. S. J. Jeong, and C. K. Hong, "Pixel-size-maintained image reconstruction of digital holograms on arbitrarily tilted planes by the angular spectrum method," Applied Optics **47**, 3064–3071 (2008).
53. L. F. Yu, Y. F. An, and L. L. Cai, "Numerical reconstruction of digital holograms with variable viewing angles," Optics Express **10**, 1250–1257 (2002).
54. Y. Takaki, and H. Ohzu, "Hybrid holographic microscopy: visualization of three-dimensional object information by use of viewing angles," Applied Optics **39**, 5302–5308 (2000).
55. L. F. Yu, and M. K. Kim, "Variable tomographic scanning with wavelength scanning digital interference holography," Optics Communications **260**, 462–468 (2006).
56. A. Dutt, and V. Rokhlin, "Fast Fourier-Transforms for Nonequispaced Data .2.," Applied and Computational Harmonic Analysis **2**, 85–100 (1995).
57. A. F. Ware, "Fast approximate Fourier transforms for irregularly spaced data," Siam Review **40**, 838–856 (1998).
58. J. Upatnieks, A. V. Lugt, and E. N. Leith, "Correction of lens aberrations by means of holograms," Appl. Opt. **5**, 589–593 (1966).
59. P. Ferraro, S. De Nicola, A. Finizio, G. Coppola, S. Grilli, C. Magro, and G. Pierattini, "Compensation of the inherent wave front curvature in digital holographic coherent microscopy for quantitative phase-contrast imaging," Applied Optics **42**, 1938–1946 (2003).
60. L. Miccio, D. Alfieri, S. Grilli, P. Ferraro, A. Finizio, L. De Petrocellis, and S. D. Nicola, "Direct full compensation of the aberrations in quantitative phase microscopy of thin objects by a single digital hologram," Applied Physics Letters **90**, 3 (2007).
61. S. De Nicola, P. Ferraro, A. Finizio, S. Grilli, and G. Pierattini, "Experimental demonstration of the longitudinal image shift in digital holography," Optical Engineering **42**, 1625–1630 (2003).
62. E. Cuche, P. Marquet, and C. Depeursinge, "Simultaneous amplitude-contrast and quantitative phase-contrast microscopy by numerical reconstruction of Fresnel off-axis holograms," Applied Optics **38**, 6994–7001 (1999).
63. A. Stadelmaier, and J. H. Massig, "Compensation of lens aberrations in digital holography," Optics Letters **25**, 1630–1632 (2000).
64. J. L. Di, J. L. Zhao, W. W. Sun, H. Z. Jiang, and X. B. Yan, "Phase aberration compensation of digital holographic microscopy based on least squares surface fitting," Optics Communications **282**, 3873–3877 (2009).
65. T. Colomb, E. Cuche, F. Charriere, J. Kuhn, N. Aspert, F. Montfort, P. Marquet, and C. Depeursinge, "Automatic procedure for aberration compensation in digital holographic microscopy and applications to specimen shape compensation," Applied Optics **45**, 851–863 (2006).
66. T. Colomb, F. Montfort, J. Kuhn, N. Aspert, E. Cuche, A. Marian, F. Charriere, S. Bourquin, P. Marquet, and C. Depeursinge, "Numerical parametric lens for shifting, magnification, and complete aberration compensation in digital holographic microscopy," Journal of the Optical Society of America a-Optics Image Science and Vision **23**, 3177–3190 (2006).

67. T. Colomb, J. Kuhn, F. Charriere, C. Depeursinge, P. Marquet, and N. Aspert, "Total aberrations compensation in digital holographic microscopy with a reference conjugated hologram," Opt. Express **14**, 4300–4306 (2006).
68. P. Ferraro, D. Alferi, S. De Nicola, L. De Petrocellis, A. Finizio, and G. Pierattini, "Quantitative phase-contrast microscopy by a lateral shear approach to digital holographic image reconstruction," Optics Letters **31**, 1405–1407 (2006).
69. S. De Nicola, P. Ferraro, A. Finizio, and G. Pierattini, "Correct-image reconstruction in the presence of severe anamorphism by means of digital holography," Optics Letters **26**, 974–976 (2001).
70. W. J. Zhou, Y. J. Yu, and A. Asundi, "Study on aberration suppressing methods in digital micro-holography," Optics and Lasers in Engineering **47**, 264–270 (2009).

Chapter 10
Special Techniques of Digital Holography

Here we highlight special techniques of DH that combine the numerical processing capabilities with variations on the hardware configurations. In this and the following chapters, we survey some of the large number of novel techniques and capabilities that are made possible by digital processing of holograms. We will also see that many of these techniques finally provide highly effective solutions to problems that have been known in conventional holography.

10.1 Synthetic Aperture Methods

The resolution of DH image is determined by the numerical aperture of the optical system including the CCD array, or equivalently by the range of spatial frequencies captured by the system. The resolution can be improved, therefore, by increasing the effective aperture of the system. Since in practice the CCD array size is limited, an alternative is to translate the camera in the lateral (xy) directions and acquire many holograms, which are then stitched together (Fig. 10.1a). Precision in stitching can be achieved by overlapping parts of the holograms and maximizing the correlation peak. The result is a higher resolution image equivalent to one obtained by a large size hologram. This has been demonstrated in lensless Fourier [1] or Gabor [2] configurations, or using a line scan camera [3] or a fixed pair of cameras [4]. Instead of translating the camera, the object plane in Fresnel configuration can be tilted to a range of angles [5] (Fig. 10.1b), as well as tilting the illumination angle of the object [6] (Fig. 10.1c). The concept of aperture synthesis has been utilized in many different systems, such as synthetic aperture radar (SAR), radio and optical telescope arrays, and sonars. In airborne SAR, the length of the flight path is the effective aperture size, greatly increasing the resolution in the

M.K. Kim, *Digital Holographic Microscopy: Principles, Techniques, and Applications*, Springer Series in Optical Sciences 162,
DOI 10.1007/978-1-4419-7793-9_10, © Springer Science+Business Media, LLC 2011

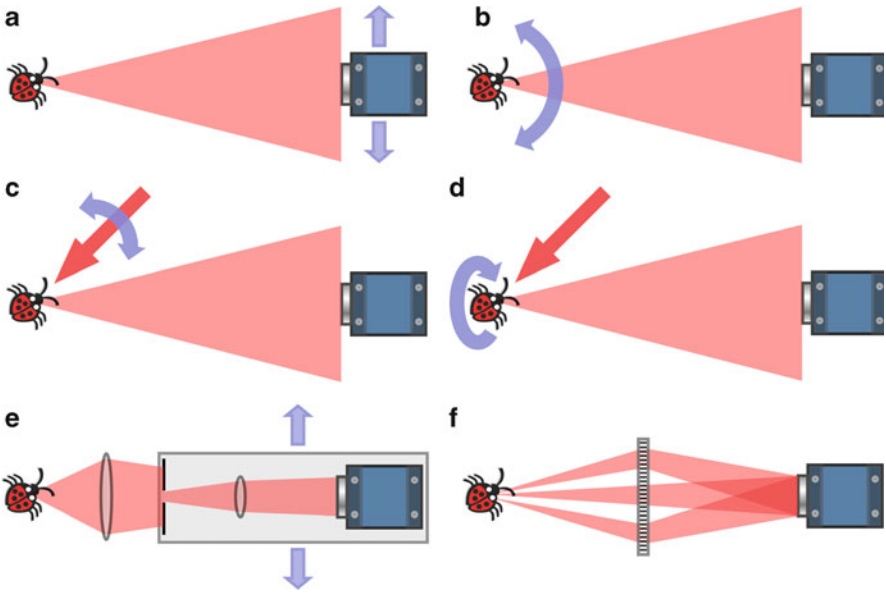

Fig. 10.1 Methods for aperture synthesis. (**a**) Translate the camera, (**b**) tilt the object plane, (**c**) scan the illumination angle, (**d**) rotate the object, (**e**) scan across the Fourier plane, and (**f**) use a diffraction grating

direction of flight, while the resolution in range is provided by the frequency sweep of the side-looking radar. A close analogue in optical implementation has been demonstrated using a tunable laser and tilting the object plane [7].

A large hologram captures a larger portion of the diffraction field, resulting in the increased resolution. Or, one can use the same size hologram but capture or redirect higher-frequency components which tend to diffract out of the system aperture faster than the lower frequency components. This gives an alternative approach of coherent superposition of angular spectra in the Fourier domain. In [8], the Fourier plane aperture, an imaging lens, and the CCD camera are translated together across the Fourier plane (Fig. 10.1e). Similar effect can be achieved by varying the object illumination angle [9] or by rotating the object in its plane while holding the illumination at an oblique angle [10, 11] (Fig. 10.1d). Angular multiplexing of three object-reference pairs derived from a single pulsed laser is used in [12].

A grating can be used to redirect high-frequency diffraction components that otherwise would leave the imaging system, and thus increase the resolution [13] (Fig. 10.1f). A linear grating improves the resolution in one direction, while a hexagonal grating allows super-resolution in both lateral directions [14]. In [15], a 2D VCSEL (vertical cavity surface emitting laser) array is used for illumination and a number of laser elements are turned on in sequence to illuminate the optical

system with varying tilt angles. This scheme of super-resolution is also used in a common-path interferometer [16] and a type of Fourier domain interferometer [17]. These interferometers will be described in some detail in Chap. 11. Synthetic aperture effect is also demonstrated in a multiplane phase retrieval system [6]. In [18], the camera scan and a double numerical propagation technique is used to achieve free-viewpoint imaging of 3D scenes demonstrating full parallax and occlusion effects of objects.

10.2 Multiplane Phase Retrieval

An intensity measurement, in general, does not yield phase information of the optical field. In order to obtain both amplitude and phase information, measurement of at least two quantities is required – two equations for two unknowns. This so-called phase problem leads to the twin-image problem of holography, and also arises in X-ray crystallography and various inverse scattering applications such as optical diffraction tomography. A number of methods are available for phase retrieval from intensity measurements and they can be grouped according to being iterative or noniterative. Noniterative methods are deterministic and numerically efficient but tend to have instability against initial condition. Iterative methods tend to be computationally intensive but can have better stability and be accommodating. Examples are described below.

10.2.1 Noniterative Methods

Consider the intensity of the holographic interference field between a reference $E_{\mathrm{R}}(x,y;z) = \mathcal{E}_{\mathrm{R}} \exp(ikz)$ and object $E_{\mathrm{O}}(x,y;z)$, assumed to be much weaker than the reference, $|E_{\mathrm{O}}(x,y;z)| \ll \mathcal{E}_{\mathrm{R}}$,

$$I(z) = {\mathcal{E}_{\mathrm{R}}}^2 + \mathcal{E}_{\mathrm{R}} \exp(ikz) {E_{\mathrm{O}}}^*(z) + \mathcal{E}_{\mathrm{R}} \exp(-ikz) E_{\mathrm{O}}(z), \tag{10.1}$$

where, for brevity, we omit (x,y) dependence of fields. The object field $E_{\mathrm{O}}(z)$ is related to the input field $E_{\mathrm{O}}(0)$ through a convolution

$$E_{\mathrm{O}}(z) = E_{\mathrm{O}}(0) \odot S(z), \tag{10.2}$$

where, in Fresnel approximation,

$$S(z) = \frac{ik}{2\pi z} \exp(ikz) \exp\left[\frac{ik}{2z}\left(x^2 + y^2\right)\right]. \tag{10.3}$$

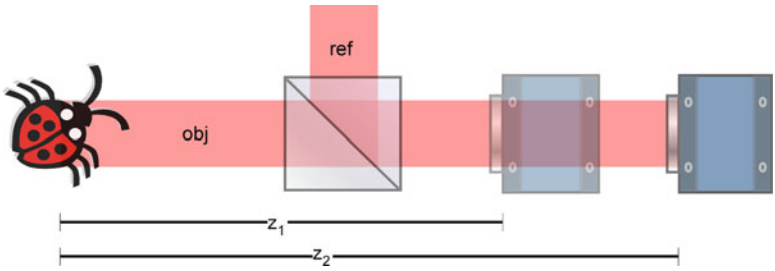

Fig. 10.2 Acquisition of in-line holograms at two distances

Notations are a little simpler if we write

$$S'(z) = \frac{ik}{2\pi z} \exp\left[\frac{ik}{2z}\left(x^2 + y^2\right)\right] \tag{10.4}$$

so that

$$E_{\mathrm{O}}(z) = \exp(ikz) E_{\mathrm{O}}(0) \odot S'(z). \tag{10.5}$$

Note that

$$\begin{cases} S'(-z) = S'^{*}(z), \\ S'(z_1) \odot S'(z_2) = S'(z_1 + z_2), \end{cases} \tag{10.6}$$

and the transfer function is

$$\tilde{S'}(z) = -\frac{1}{2\pi} \exp\left[-\frac{iz}{2k}\left({k_x}^2 + {k_y}^2\right)\right], \tag{10.7}$$

where the Fourier transform is denoted as $\tilde{f} = \mathcal{F}\{f\}$. The intensity function is

$$I(z) = {\mathcal{E}_{\mathrm{R}}}^2 + \mathcal{E}_{\mathrm{R}} {E_{\mathrm{O}}}^{*}(0) \odot S'^{*}(z) + \mathcal{E}_{\mathrm{R}} E_{\mathrm{O}}(0) \odot S'(z). \tag{10.8}$$

If the object is purely absorptive, then $E_{\mathrm{O}}(0)$ is real and it can be obtained, in principle, by deconvolution $(\odot^{-1})$

$$E_{\mathrm{O}}(0) = \frac{1}{\mathcal{E}_{\mathrm{R}}} \left[I(z) - {\mathcal{E}_{\mathrm{R}}}^2\right] \odot^{-1} \left[S'^{*}(z) + S'(z)\right]. \tag{10.9}$$

For the general case of the object having both absorptive and phase profiles, the problem is under-specified. At least two measurements are required, for example, at two distances [19] (Fig. 10.2):

$$I_1 = I(z_1) = {\mathcal{E}_\mathrm{R}}^2 + \mathcal{E}_\mathrm{R} {E_\mathrm{O}}^*(0) \odot {S'}^*(z_1) + \mathcal{E}_\mathrm{R} E_\mathrm{O}(0) \odot S'(z_1),$$
$$I_2 = I(z_2) = {\mathcal{E}_\mathrm{R}}^2 + \mathcal{E}_\mathrm{R} {E_\mathrm{O}}^*(0) \odot {S'}^*(z_2) + \mathcal{E}_\mathrm{R} E_\mathrm{O}(0) \odot S'(z_2). \tag{10.10}$$

We can eliminate ${E_\mathrm{O}}^*(0)$ by forming

$$D_1 = \frac{1}{\mathcal{E}_\mathrm{R}} \left(I_1 - {\mathcal{E}_\mathrm{R}}^2\right) \odot S'(z_1) = {E_\mathrm{O}}^*(0) + E_\mathrm{O}(0) \odot S'(2z_1),$$
$$D_2 = \frac{1}{\mathcal{E}_\mathrm{R}} \left(I_2 - {\mathcal{E}_\mathrm{R}}^2\right) \odot S'(z_2) = {E_\mathrm{O}}^*(0) + E_\mathrm{O}(0) \odot S'(2z_2), \tag{10.11}$$

and subtracting

$$D_1 - D_2 = E_\mathrm{O}(0) \odot [S'(2z_1) - S'(2z_2)]. \tag{10.12}$$

Solve for $\tilde{E}_O(0)$ in the Fourier domain

$$\tilde{E}_\mathrm{O}(0) = \frac{\tilde{D}_1 - \tilde{D}_2}{\tilde{S}'(2z_1) - \tilde{S}'(2z_2)}. \tag{10.13}$$

The input field $E_\mathrm{O}(0)$ can then be obtained by inverse Fourier transform. Equation (10.13) is valid except where the denominator vanishes. Regularization of the singularities is then necessary.

Another noniterative method is provided in [20, 21], which starts by writing the holographic field, again assuming weak object field compared to reference, as

$$E(z) = E_\mathrm{R}(z) + E_\mathrm{O}(z) = E_\mathrm{R}(z)\{1 + u(z)\} \approx E_\mathrm{R}(z) \exp[u(z)], \tag{10.14}$$

where

$$u(z) \equiv \frac{E_\mathrm{O}(z)}{E_\mathrm{R}(z)} = \frac{\exp(-ikz)}{\mathcal{E}_\mathrm{R}} E_\mathrm{O}(z) = u(0) \odot S'(z). \tag{10.15}$$

The intensity function is

$$I(z) = |E(z)|^2 = \mathcal{E}_\mathrm{R}^2 \exp[u(z) + u^*(z)]. \tag{10.16}$$

Now take the logarithm

$$\mathcal{I}(z) \equiv \log \frac{I(z)}{\mathcal{E}_R^2} = u(z) + u^*(z) = u(0) \odot S'(z) + u^*(0) \odot {S'}^*(z) \tag{10.17}$$

and its Fourier transform

$$\tilde{\mathcal{I}}(z) = \tilde{u}(0)\tilde{S}'(z) + \tilde{u}^*(0)\tilde{S}'^*(z). \tag{10.18}$$

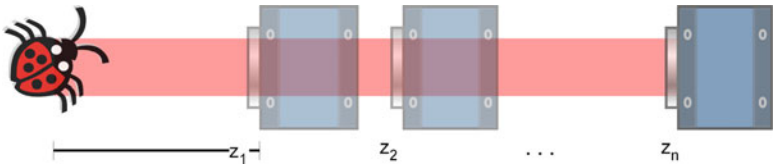

Fig. 10.3 Acquisition of object intensity at multiple distances

Repeat the measurement at another distance $z + \Delta z$

$$\tilde{\mathcal{I}}(z + \Delta z) = \tilde{u}(0)\tilde{S}'(z)\,\tilde{S}'(\Delta z) + \tilde{u}^*(0)\,\tilde{S}'^*(z)\,\tilde{S}'^*(\Delta z) \tag{10.19}$$

and $\tilde{u}^*(0)$ can be eliminated by forming

$$\tilde{\mathcal{I}}(z + \Delta z)\,\tilde{S}'(\Delta z) - \tilde{\mathcal{I}}(z) = \tilde{u}(0)\,\tilde{S}'(z)\left[\tilde{S}'(\Delta z) - 1\right] \tag{10.20}$$

so that

$$\tilde{u}(0) = \frac{\tilde{\mathcal{I}}(z + \Delta z)\tilde{S}'(\Delta z) - \tilde{\mathcal{I}}(z)}{\tilde{S}'(z)\left[\tilde{S}'(\Delta z) - 1\right]} \tag{10.21}$$

and the input field $E_{\mathrm{O}}(0)$ can be calculated from here.

10.2.2 Iterative Methods

Iterative methods use intensity measurements at two or more distances from the object (Fig. 10.3). A method based on the Gerchberg–Saxton–Fienup algorithm uses holograms recorded at two different distances and a large number of iteration cycles [22]. A many-plane method [22–24] starts from an intensity measurement I_1 at z_1 and a complex field $E_1 = \sqrt{I_1}\exp(i\varphi_1)$ is assumed, where the trial phase φ_1 may be taken to be a constant. The field is then numerically propagated to another distance z_2 to obtain the complex field there as $E_2 = \mathcal{E}_2 \exp(i\varphi_2)$. Here the amplitude is replaced with the measured value $\mathcal{E}_2{}' = \sqrt{I_2}$. The new field $E_2{}' = \mathcal{E}_2{}'\exp(i\varphi_2)$ is then propagated to another distance z_3, and so on. At each step n the intensity error is calculated between the measured value I_n and the calculated value $|E_n|^2$ and the process terminates when the error is smaller than the set threshold, or when the error ceases to decrease as the case may be. One can use a finite number of measurements $I_1, I_2, \ldots, I_N$ and revert from I_N to I_1 before continuing. These methods are based on intensity measurements of object field propagation requiring no reference fields, and therefore have important applications in X-ray and electron microscopy, where appropriate coherent sources and interferometer configurations are not readily available [25].

In another example of iterative method [26], from the interference intensity function

$$I(x,y) = {\mathcal{E}_\mathrm{R}}^2 + {\mathcal{E}_\mathrm{O}}^2(x,y) + \mathcal{E}_\mathrm{R}\mathcal{E}_\mathrm{O}\cos[\varphi(x,y) - \varphi_\mathrm{R}] \tag{10.22}$$

one can write

$$\varphi(x,y) - \varphi_\mathrm{R} = \cos^{-1}\frac{I(x,y) - {\mathcal{E}_\mathrm{R}}^2 - {\mathcal{E}_\mathrm{O}}^2(x,y)}{\mathcal{E}_\mathrm{R}\mathcal{E}_\mathrm{O}}, \tag{10.23}$$

where the reference field is $E_\mathrm{R}(x,y) = \mathcal{E}_\mathrm{R}\exp[i\varphi_\mathrm{R}]$ and the object field

$$E_\mathrm{O}(x,y) = \mathcal{E}_\mathrm{O}(x,y)\exp[i\varphi(x,y)]. \tag{10.24}$$

The object amplitude $\mathcal{E}_\mathrm{O}(x,y) = \sqrt{|\mathcal{E}_\mathrm{O}|^2}$ is available from object intensity measurement, the only unknown being the sign of the phase function $\varphi(x,y) - \varphi_\mathrm{R}$, which is determined in an iterative loop, as detailed in [26].

10.2.3 Other Methods of Phase Retrieval

Retrieval of phase is possible by noninterferometric measurements of intensities at multiple distances. In phase space tomography, the Wigner distribution function is reconstructed from intensity measurements, by calculating Fractional-order Fourier transforms that correspond to projections of the Wigner distribution along different directions of the phase space [27, 28]. Differential focusing of intensity image is used to solve the so-called transport of intensity equation to yield the quantitative phase profile, that does not even require unwrapping [29–31]. Differential measurement of intensity at two planes is used for enhanced edge detection [32].

10.3 Dynamic Systems

In order to image a dynamic system, one needs fast or short exposures of the hologram. This can be achieved using a correspondingly fast camera, as was done in [33] using a 4,000 frames-per-second camera to image the random motion of a balloon. Often the limitation on the camera speed is stringent in terms of cost and availability. A more common approach is to use pulsed lasers to shorten the illumination instead of the exposure. A nanosecond pulsed laser is a convenient source for capturing a hologram of fast moving macroscopic objects [34]. Consecutive exposures of two holograms can be used for imaging deformation or displacement between the exposures. Special techniques have been developed for exposures with time delays shorter than milliseconds. For time delay in the tens

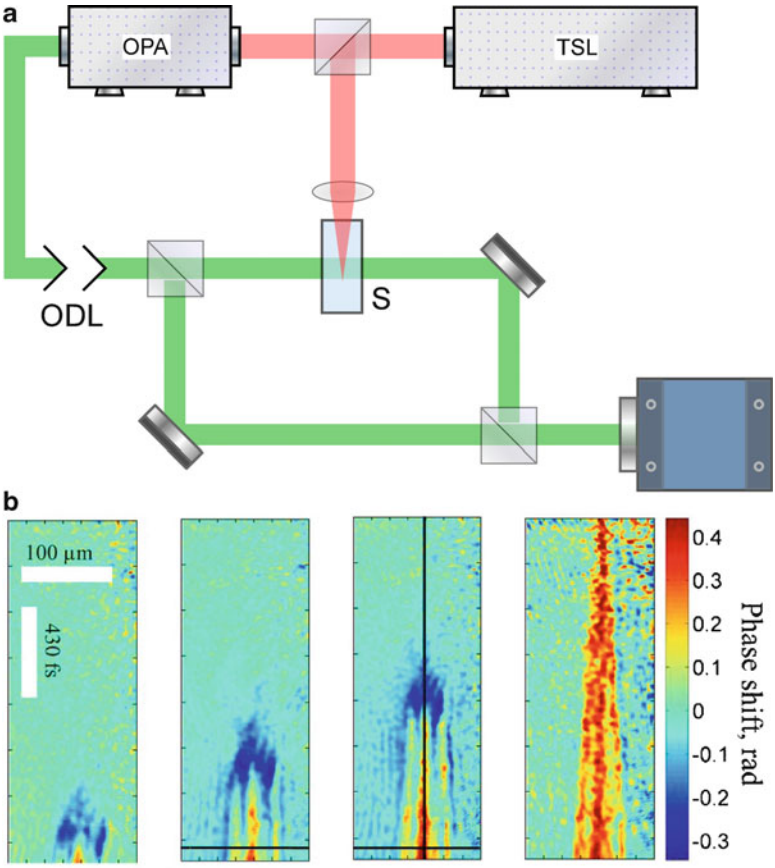

Fig. 10.4 Holography with optical time delay. (**a**) *TSL* femtosecond Ti:sapphire laser (800 nm, 130 fs), *OPA* optical parametric amplifier (550 nm, 30 fs), *ODL* optical delay line, *S* sample cell containing water. (**b**) Laser-induced plasma filament formation, imaged with quantitative phase microscopy by digital holography. (Reprinted from [40] by permission of OSA)

of microseconds, one can use the ability of a CCD camera to make charge transfer to the shift registers in a few microseconds between the exposures [35, 36]. For faster delays, one has to use a single exposure to capture the multiple time-delayed events. This is achieved by optically setting up the multiple delays and inserting them into the interferometer with different angular orientations, so that the angular spectrum of the hologram contains several pairs of spectral peaks. These pairs are incoherent with respect to each other because of the time delay and can be analyzed separately to produce corresponding number of independent holograms. This technique was used with nanosecond [37] or femtosecond [38, 39] delays to image laser-induced ionization of air. If the experiment is repeatable, a delay line can be stepped while making multiple exposures, as in [40] where a femtosecond laser and an optical delay line is used to image the formation and evolution of laser-induced plasma filament in water (Fig. 10.4).

A technique for complete characterization of spatial, temporal, and phase profiles of a femtosecond pulse has been developed using a wavelength-multiplexed digital holography [41, 42]. A slightly rotated two-dimensional diffractive optical element and a variable-wavelength filter together generate multiple spectrally resolved digital holograms that are simultaneously captured in a single frame.

10.4 Noise Reduction

The speckle is a well-known source of noise in coherent imaging such as digital holography. Yet, systematic studies of speckle noise on digital holography appear lacking especially for the phase image reconstruction. In [43], the speckle noise of reconstructed intensity image is seen to be aggravated by the relatively small aperture of digital holograms. For phase images, the behavior of speckle noise is expected to be very different and usually significantly less aggravating, as one may also glean from some of the simulation images of numerical diffraction in Chap. 4. For intensity images, a common way to reduce the speckle noise is by averaging of several holograms while some of the imaging parameters change, such as the wavelength [44] or the object illumination angle [45]. Alternatively, digital postprocessing of the hologram by various filtering operations can improve the image quality [46]. Use of low coherence light can be an effective method for reducing the noise, and will be described in Chap. 12.

Axial subnanometer high precision profiles of calibrated chromium step was achieved by using reference calibrated hologram (RCH) reconstruction method, a temporal averaging procedure and a specific dual-wavelength DHM arrangement [47]. Influence of shot noise on phase measurement was studied in [48, 49], where it was also found that at low photon flux, the phase accuracy is limited by the readout noise of the CCD, while at higher intensities the phase accuracy is limited by fluctuations in the optical setup.

10.5 Nonlinear Optics

10.5.1 Imaging of NLO Materials

There are two distinct areas that DHM has been used regarding nonlinear optics (NLO), both of which can lead to significant expansions of applications. In one, DHM is used to characterize NLO materials and processes. For example, DHM is used to visualize light-induced refractive index changes in lithium niobate and other photorefractive crystals [50]. DHM was used to measure the refractive index change resulting from waveguide formation in Ti:sapphaire crystal or glass by femtosecond laser writing [51, 52]. P. Ferraro's group has made a series of studies

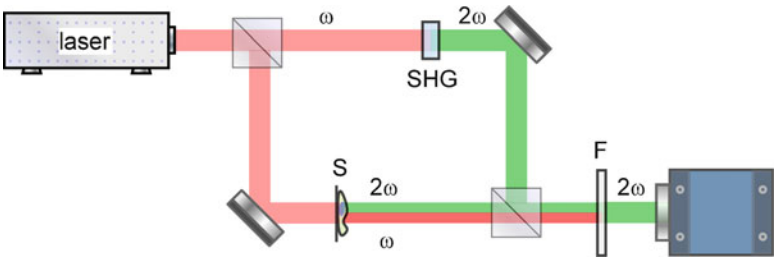

Fig. 10.5 Configuration for holography with SHG light. *SHG* second harmonic generator, *S* sample object with SHG signal, *F* green filter

of nonlinear crystals using digital holography. Topography of microstructures of ~60 nm thickness fabricated on bulk lithium niobate surface has been imaged [53]. Electrooptic phase retardation, domain reversal, and periodic poling in congruent lithium niobate are monitored in situ by DH-QPM [54–56]. Light-induced refractive index changes in the photorefractive phase grating is measured with a sensitivity of better than 10^{-5} [57]. Defect dependence of the internal field in lithium niobate is studied using DH-QPM and the value of the internal field is found to grow in proximity of defects and to vanish far from them [58]. Formation of bright spatial soliton (i.e., self-focusing) is characterized [59, 60].

10.5.2 Digital Holography by NLO Light

In the other area, DHM is made a part of the NLO process. For example, in harmonic holography the second harmonic signal generated in the object, for example, photorefractive nanocrystals, interferes with the reference of the harmonic wavelength, as depicted in Fig. 10.5 [61]. Harmonic holography is used to image the amplitude and phase profiles of second harmonic signal generated at the glass–air interface of a microscope slide under focused femtosecond laser illumination [62]. SHG (second harmonic generation) nanoparticles are used in mammalian cells as markers for harmonic holography in [63]. SHG from cellular and subcellular structures of biological specimens, including starch granules, corn seed, and muscle fibrils, are used for label-free imaging of these structures [64]. In [65], phase measurement technique of SHG in harmonic holography experiment is described that gives ~10 nm precision of axial position of nanoparticles.

In another example, DHM is used to measure the complex optical profile of the output from a propagation through a nonlinear medium [66] (Fig. 10.6). Ordinarily, because of the intensity-dependent phase distortion in nonlinear media, it is not possible to form an image through such material. Phase conjugation processes can undo such distortion, but they require repropagation back through the nonlinear medium to recover the original image. Instead, the complex optical field is obtained by holographic interference, followed by numerical propagation through the

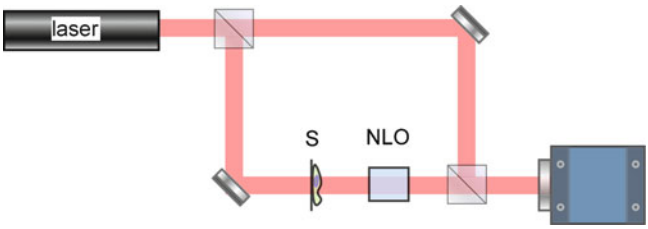

Fig. 10.6 Optical configuration for imaging through a NLO material using digital holography. *S* object to be imaged, *NLO* nonlinear optical material. (Adapted from [66])

nonlinear material using a theoretical model of the nonlinear propagation, obtaining a numerical image of the input field. Alternatively, phase conjugation can be implemented using an SLM. In [67, 68], SHG signals, after passing through a turbid medium, is imaged by DHM. The resulting complex optical field is then imposed on the SLM, from which a laser beam propagates back through the turbid medium and focuses precisely on the original point source.

10.6 Optical Parameters of Digital Holography

10.6.1 Color Digital Holography

Ability to reconstruct holographic images in full color can be of interest in 3D display applications, as well as in full-color imaging of microscopic and macroscopic objects. For example, in [69], the three lines at 636.0, 537.8, and 441.6 nm of a HeCd laser are used to illuminate a PSDH system with a color CCD camera. Holograms from the three color channels are separately processed using Fresnel transform or convolution methods. For Fresnel method, the three holographic images have different sizes according to the wavelengths and therefore resizing of the holograms is necessary. The three holograms are then combined to produce a full-color hologram. Disparity in laser power in the three lines is handled by appropriate weighting factors before color composition. Wavelength mismatch in PZT-based phase shift can be avoided by using achromatic phase shifter [70]. In [71], three separate lasers at 633, 532, and 473 nm are used together with a monochrome camera to acquire three holograms in sequence. Three-dimensional color image fusion has been demonstrated [72].

In [73], chromatic aberration in color holography is compensated for by adjusting the imaging distances of the three color channels until the phase differences between the channels are minimized. Use of lensless Fourier configuration in [71] assures precise transverse superposition of reconstructed images. Image fusion technique with multiresolution wavelet decomposition is shown to increase the details and contrast of 3D reconstructed images obtained by multiwavelength digital holography [72].

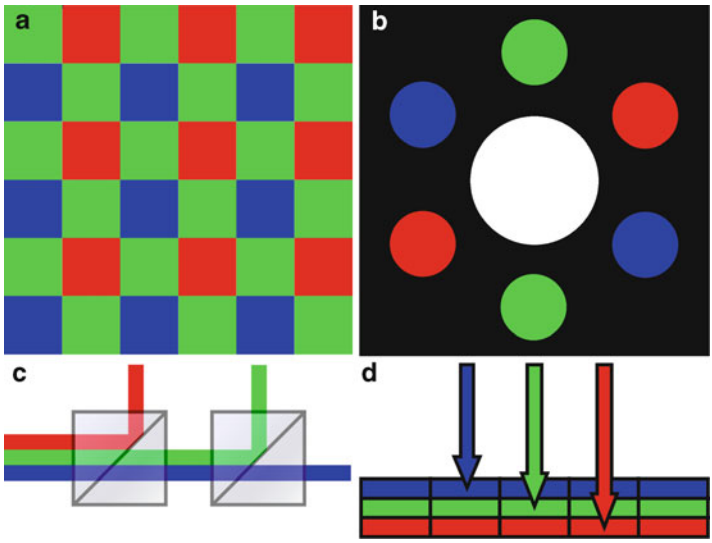

Fig. 10.7 Methods to acquire the three color channels simultaneously. (**a**) Bayer color mosaic on CCD sensor array, (**b**) angular multiplexing, (**c**) use of dichroic beam splitters and separate cameras, and (**d**) stacked photodiode sensors. (Adapted from [75])

The three color channels may be acquired in sequence using a single monochrome camera [74], but for applications involving dynamic scenes, simultaneous acquisition of the channels is necessary. Figure 10.7 illustrates and compares methods for simultaneous recording of color holograms [75]. In Fig. 10.7d, three layers of photodiodes are stacked, the spectral selectivity being provided by the penetration depth of photons in silicon: 0.2 μm for blue photons, 2 μm for green photons and 3 μm for red photons. The structure can provide a limited spectral selectivity but the spatial resolution is maximal [75]. A more readily available approach (Fig. 10.7a) is to use the conventional Bayer mosaic of color sensors [69, 70]. Thus the spectral cross-talk is minimized but the spatial resolution is reduced. Because this type of color sensor is common, the approach may be a good compromise when the spatial resolution is not critical. One may use three separate monochrome cameras with an appropriate set of color filters or dichroic beam splitters (Fig. 10.7c). This maximizes both the spectral selectivity and spatial resolution, but at significant cost increase and optomechanical complexity. In Fig. 10.7b, the color channels are separated in the spatial frequency domain [76, 77]. The object is illuminated by a collinear beams of the three color lasers, while the reference beams impinge on the camera from three different directions, thus producing three separate directions of interference fringes and three pairs of angular spectrum peaks. (Alternatively, the reference beams may be collinear while the object is illuminated from three angles, although this arrangement may be more prone to errors due to mismatch of object illumination.) The method uses a single monochrome camera. The spectral selectivity is good but the spatial resolution is reduced.

One notes that these methods are relevant not only for generating color holography but also for some of the multiwavelength holographic interferometry, with two or three wavelengths well-separated over the visible spectrum.

10.6.2 Polarization Digital Holography

Polarization has a number of useful applications in conventional holography, such as polarization multiplexing, logical operations, and birefringence imaging [78]. Using DH, one can determine simultaneously the distributions of intensity, phase, and polarization state at the surface of a specimen on the basis of a single image acquisition [79, 80]. Two reference waves with orthogonal polarization states interfere with the object wave to permit determination of all the components of the Jones vector of the object wave front [81, 82]. The two reference waves can be arranged in angular multiplexing similar to the multicolor configuration of Fig. 10.7d. This was used to analyze the birefringence of stressed polymethyl methacrylate (PMMA) [79] and optical fiber [83].

10.6.3 Other Wavelengths and Particles

Since early in the history of holography, the principle has been applied to many other parts of electromagnetic spectrum as well as particle waves. Digital holography has also been demonstrated and applied in nonvisible or nonoptical radiation.

Infrared radiation from CO_2 laser has been used for digital holography using pyroelectric or microbolometer sensor array as the camera [84–86]. A vidicon was used for holography with 1.3 μm superluminescent source to overcome the low quantum efficiency of CCD in the infrared [87].

Digital holography of millimeter wave with intensity detector and separate reference beam has been demonstrated and may be useful for imaging nonconducting materials and objects [88]. Microwave holography with a geostationary satellite was used for measurement and adjustment of a radio telescope [89]. In an optical-THz hybrid system of [90], a THz beam profile is detected by optical holography. A two-wavelength phase unwrapping has been demonstrated in THz interferometry [91].

It is difficult to produce mutually coherent object and reference beams of X-ray to extract the phase information. Gabor type in-line digital holography has been demonstrated using 32 nm soft X-ray generated by focusing Ti:sapphire laser into a gas cell [92], with resultant resolution of 800 nm. Use of 193 nm deep UV from excimer laser also yielded similar resolution [93]. The low resolution is due to the difficulty of achieving NA of the imaging system higher than 0.01–0.02 in this range. In [94], holograms using different X-ray energies 220–330 eV (5.6–3.8 nm) near carbon absorption were combined to differentiate organic materials. Coherent X-ray free electron laser source has been used in lensless Fourier holography configuration by using an opaque mask with two apertures: one for placement of

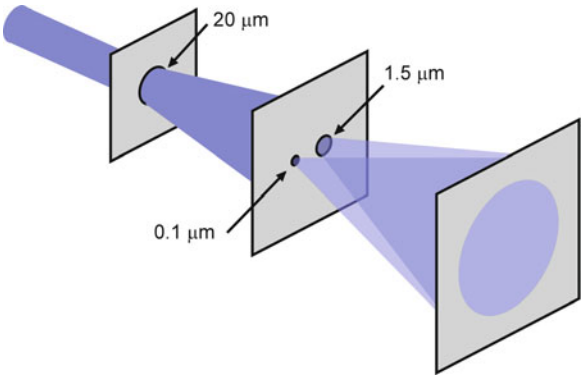

Fig. 10.8 Digital Fourier holography of 1.59 nm X-ray. Lithographically manufactured mask contains 1.5 μm sample aperture and 0.1 μm reference aperture. (Adapted from [96])

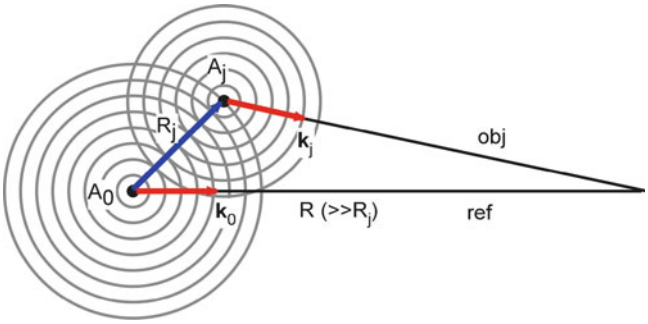

Fig. 10.9 The inside source principle. A_0 is the source atom, whose radiation scatters off a neighbor A_j. The scattered and unscattered components interfere to form the hologram. (Adapted from [98])

the specimen and the other as reference point source [95, 96] (Fig. 10.8). Random magnetic domain structure in a Co/Pt multilayer film was obtained with 50 nm spatial resolution. Off-axis Fresnel configuration digital holography has also been demonstrated using a pair of X-ray waveguides, achieving 10 nm spatial resolution at 10.4 keV photon energy [97]. X-ray holography can in principle yield atomic resolution, provided one has sources or detectors of nanometer-scale pixel size. The so-called "inside source" or "inside detector" concept uses the atoms or nuclei of the sample as sources or detectors [98] (Fig. 10.9).

References

1. J. H. Massig, "Digital off-axis holography with a synthetic aperture," Optics Letters **27,** 2179–2181 (2002).
2. L. Martinez-Leon, and B. Javidi, "Synthetic aperture single-exposure on-axis digital holography," Optics Express **16**, 161–169 (2008).

3. J. L. Di, J. L. Zhao, H. Z. Jiang, P. Zhang, Q. Fan, and W. W. Sun, "High resolution digital holographic microscopy with a wide field of view based on a synthetic aperture technique and use of linear CCD scanning," Applied Optics **47**, 5654–5659 (2008).
4. T. Kreis, and K. Schluter, "Resolution enhancement by aperture synthesis in digital holography," Optical Engineering **46**, 055803–055807 (2007).
5. R. Binet, J. Colineau, and J. C. Lehureau, "Short-range synthetic aperture imaging at 633 nm by digital holography," Applied Optics **41**, 4775–4782 (2002).
6. P. Almoro, G. Pedrini, and W. Osten, "Aperture synthesis in phase retrieval using a volume-speckle field," Optics Letters **32**, 733–735 (2007).
7. M. Bashkansky, R. L. Lucke, E. Funk, L. J. Rickard, and J. Reintjes, "Two-dimensional synthetic aperture imaging in the optical domain," Opt. Lett. **27**, 1983–1985 (2002).
8. F. Le Clerc, M. Gross, and L. Collot, "Synthetic-aperture experiment in the visible with on-axis digital heterodyne holography," Optics Letters **26**, 1550–1552 (2001).
9. J. R. Price, P. R. Bingham, and C. E. Thomas, "Improving resolution in microscopic holography by computationally fusing multiple, obliquely illuminated object waves in the Fourier domain," Applied Optics **46**, 827–833 (2007).
10. S. A. Alexandrov, T. R. Hillman, T. Gutzler, and D. D. Sampson, "Synthetic aperture fourier holographic optical microscopy," Physical Review Letters **97**, 168102 (2006).
11. T. R. Hillman, T. Gutzler, S. A. Alexandrov, and D. D. Sampson, "High-resolution, wide-field object reconstruction with synthetic aperture Fourier holographic optical microscopy," Optics Express **17**, 7873–7892 (2009).
12. C. J. Yuan, H. C. Zhai, and H. T. Liu, "Angular multiplexing in pulsed digital holography for aperture synthesis," Optics Letters **33**, 2356–2358 (2008).
13. C. Liu, Z. G. Liu, F. Bo, Y. Wang, and J. Q. Zhu, "Super-resolution digital holographic imaging method," Applied Physics Letters **81**, 3143–3145 (2002).
14. M. Paturzo, F. Merola, S. Grilli, S. De Nicola, A. Finizio, and P. Ferraro, "Super-resolution in digital holography by a two-dimensional dynamic phase grating," Optics Express **16**, 17107–17118 (2008).
15. V. Mico, Z. Zalevsky, P. Garcia-Martinez, and J. Garcia, "Superresolved imaging in digital holography by superposition of tilted wavefronts," Applied Optics **45**, 822–828 (2006).
16. V. Mico, Z. Zalevsky, and J. Garcia, "Superresolution optical system by common-path interferometry," Optics Express **14**, 5168–5177 (2006).
17. V. Mico, Z. Zalevsky, P. Garcia-Martinez, and J. Garcia, "Synthetic aperture superresolution with multiple off-axis holograms," Journal of the Optical Society of America a-Optics Image Science and Vision **23**, 3162–3170 (2006).
18. T. Nakatsuji, and K. Matsushima, "Free-viewpoint images captured using phase-shifting synthetic aperture digital holography," Applied Optics **47**, D136-D143 (2008).
19. M. H. Maleki, and A. J. Devaney, "Noniterative Reconstruction of Complex-Valued Objects from 2 Intensity Measurements," Optical Engineering **33**, 3243–3253 (1994).
20. Y. Zhang, G. Pedrini, W. Osten, and H. J. Tiziani, "Reconstruction of in-line digital holograms from two intensity measurements," Optics Letters **29**, 1787–1789 (2004).
21. G. Situ, J. P. Ryle, U. Gopinathan, and J. T. Sheridan, "Generalized in-line digital holographic technique based on intensity measurements at two different planes," Applied Optics **47**, 711–717 (2008).
22. Y. Zhang, G. Pedrini, W. Osten, and H. J. Tiziani, "Whole optical wave field reconstruction from double or multi in-line holograms by phase retrieval algorithm," Optics Express **11**, 3234–3241 (2003).
23. A. Anand, G. Pedrini, W. Osten, and P. Almoro, "Wavefront sensing with random amplitude mask and phase retrieval," Optics Letters **32**, 1584–1586 (2007).
24. A. Anand, and B. Javidi, "Three-dimensional microscopy with single-beam wavefront sensing and reconstruction from speckle fields," Optics Letters **35**, 766–768 (2010).
25. Y. X. Zhang, and X. Y. Zhang, "Reconstruction of a complex object from two in-line holograms," Optics Express **11**, 572–578 (2003).
26. T. Nakamura, K. Nitta, and O. Matoba, "Iterative algorithm of phase determination in digital holography for real-time recording of real objects," Applied Optics **46**, 6849–6853 (2007).

27. M. G. Raymer, M. Beck, and D. F. McAlister, "Complex wave-field reconstruction using phase-space tomography," Phys. Rev. Lett. **72**, 1137–1140 (1994).
28. D. F. Mcalister, M. Beck, L. Clarke, A. Mayer, and M. G. Raymer, "Optical-Phase Retrieval by Phase-Space Tomography and Fractional-Order Fourier-Transforms," Optics Letters **20**, 1181–1183 (1995).
29. A. Barty, K. A. Nugent, D. Paganin, and A. Roberts, "Quantitative optical phase microscopy," Optics Letters **23**, 817–819 (1998).
30. D. Paganin, and K. A. Nugent, "Noninterferometric phase imaging with partially coherent light," Phys. Rev. Lett. **80**, 2586–2589 (1998).
31. T. E. Gureyev, A. Pogany, D. M. Paganin, and S. W. Wilkins, "Linear algorithms for phase retrieval in the Fresnel region," Optics Communications **231**, 53–70 (2004).
32. C. S. Guo, Q. Y. Yue, G. X. Wei, L. L. Lu, and S. J. Yue, "Laplacian differential reconstruction of in-line holograms recorded at two different distances," Optics Letters **33**, 1945–1947 (2008).
33. C. Perez-Lopez, M. H. De La Torre-Ibarra, and F. M. Santoyo, "Very high speed cw digital holographic interferometry," Optics Express **14**, 9709–9715 (2006).
34. S. Schedin, G. Pedrini, H. J. Tiziani, and F. M. Santoyo, "All-fibre pulsed digital holography," Optics Communications **165**, 183–188 (1999).
35. G. Pedrini, P. Froning, H. J. Tiziani, and M. E. Gusev, "Pulsed digital holography for high-speed contouring that uses a two-wavelength method," Applied Optics **38**, 3460–3467 (1999).
36. C. Perez-Lopez, F. M. Santoyo, G. Pedrini, S. Schedin, and H. J. Tiziani, "Pulsed digital holographic interferometry for dynamic measurement of rotating objects with an optical derotator," Applied Optics **40**, 5106–5110 (2001).
37. Z. W. Liu, M. Centurion, G. Panotopoulos, J. Hong, and D. Psaltis, "Holographic recording of fast events on a CCD camera," Optics Letters **27**, 22–24 (2002).
38. X. L. Wang, and H. C. Zhai, "Pulsed digital micro-holography of femto-second order by wavelength division multiplexing," Optics Communications **275**, 42–45 (2007).
39. X. L. Wang, H. C. Zhai, and G. G. Mu, "Pulsed digital holography system recording ultrafast process of the femtosecond order," Optics Letters **31**, 1636–1638 (2006).
40. T. Balciunas, A. Melninkaitis, G. Tamosauskas, and V. Sirutkaitis, "Time-resolved off-axis digital holography for characterization of ultrafast phenomena in water," Optics Letters **33**, 58–60 (2008).
41. P. Gabolde, and R. Trebino, "Single-shot measurement of the full spatio-temporal field of ultrashort pulses with multi-spectral digital holography," Optics Express **14**, 11460–11467 (2006).
42. P. Gabolde, and R. Trebino, "Single-frame measurement of the complete spatiotemporal intensity and phase of ultrashort laser pulses using wavelength-multiplexed digital holography," Journal of the Optical Society of America B-Optical Physics **25**, A25-A33 (2008).
43. X. O. Cai, and H. Wang, "The influence of hologram aperture on speckle noise in the reconstructed image of digital holography and its reduction," Optics Communications **281**, 232–237 (2008).
44. T. Nomura, M. Okamura, E. Nitanai, and T. Numata, "Image quality improvement of digital holography by superposition of reconstructed images obtained by multiple wavelengths," Applied Optics **47**, D38-D43 (2008).
45. C. G. Quan, X. Kang, and C. J. Tay, "Speckle noise reduction in digital holography by multiple holograms," Optical Engineering **46**, 6 (2007).
46. J. Maycock, B. M. Hennelly, J. B. McDonald, Y. Frauel, A. Castro, B. Javidi, and T. J. Naughton, "Reduction of speckle in digital holography by discrete Fourier filtering," Journal of the Optical Society of America a-Optics Image Science and Vision **24**, 1617–1622 (2007).
47. J. Kuhn, F. Charriere, T. Colomb, E. Cuche, F. Montfort, Y. Emery, P. Marquet, and C. Depeursinge, "Axial sub-nanometer accuracy in digital holographic microscopy," Measurement Science & Technology **19**, 074007 (2008).

48. F. Charriere, B. Rappaz, J. Kuhn, T. Colomb, P. Marquet, and C. Depeursinge, "Influence of shot noise on phase measurement accuracy in digital holographic microscopy," Optics Express **15**, 8818–8831 (2007).
49. F. Charriere, T. Colomb, F. Montfort, E. Cuche, P. Marquet, and C. Depeursinge, "Shot-noise influence on the reconstructed phase image signal-to-noise ratio in digital holographic microscopy," Applied Optics **45**, 7667–7673 (2006).
50. J. L. Zhao, P. Zhang, J. B. Zhou, D. X. Yang, D. S. Yang, and E. P. Li, "Visualizations of light-induced refractive index changes in photorefractive crystals employing digital holography," Chin. Phys. Lett. **20**, 1748–1751 (2003).
51. V. Apostolopoulos, L. Laversenne, T. Colomb, C. Depeursinge, R. P. Salathe, M. Pollnau, R. Osellame, G. Cerullo, and P. Laporta, "Femtosecond-irradiation-induced refractive-index changes and channel waveguiding in bulk Ti3+: Sapphire," Applied Physics Letters **85**, 1122–1124 (2004).
52. R. Osellame, N. Chiodo, V. Maselli, A. Yin, M. Zavelani-Rossi, G. Cerullo, P. Laporta, L. Aiello, S. De Nicola, P. Ferraro, A. Finizio, and G. Pierattini, "Optical properties of waveguides written by a 26 MHz stretched cavity Ti : sapphire femtosecond oscillator," Optics Express **13**, 612–620 (2005).
53. S. De Nicola, P. Ferraro, A. Finizio, S. Grilli, G. Coppola, M. Iodice, P. De Natale, and M. Chiarini, "Surface topography of microstructures in lithium niobate by digital holographic microscopy," Measurement Science & Technology **15**, 961–968 (2004).
54. S. Grilli, P. Ferraro, M. Paturzo, D. Alfieri, and P. De Natale, "In-situ visualization, monitoring and analysis of electric field domain reversal process in ferroelectric crystals by digital holography," Optics Express **12**, 1832–1842 (2004).
55. M. de Angelis, S. De Nicola, A. Finizio, G. Pierattini, P. Ferraro, S. Grilli, M. Paturzo, L. Sansone, D. Alfieri, and P. De Natale, "Two-dimensional mapping of electro-optic phase retardation in lithium niobate crystals by digital holography," Optics Letters **30**, 1671–1673 (2005).
56. S. Grilli, M. Paturzo, L. Miccio, and P. Ferraro, "In situ investigation of periodic poling in congruent LiNbO3 by quantitative interference microscopy," Measurement Science & Technology **19**, 7 (2008).
57. M. de Angelis, S. De Nicola, A. Finizio, G. Pierattini, P. Ferraro, S. Pelli, G. Righini, and S. Sebastiani, "Digital-holography refractive-index-profile measurement of phase gratings," Applied Physics Letters **88**, 3 (2006).
58. M. Paturzo, P. Ferraro, S. Grilli, D. Alfieri, P. De Natale, M. de Angelis, A. Finizio, S. De Nicola, G. Pierattini, F. Caccavale, D. Callejo, and A. Morbiato, "On the origin of internal field in Lithium Niobate crystals directly observed by digital holography," Optics Express **13**, 5416–5423 (2005).
59. M. Paturzo, L. Miccio, S. De Nicola, P. De Natale, and P. Ferraro, "Amplitude and phase reconstruction of photorefractive spatial bright-soliton in LiNbO3 during its dynamic formation by digital holography," Optics Express **15**, 8243–8251 (2007).
60. F. Merola, L. Miccio, M. Paturzo, S. De Nicola, and P. Ferraro, "Full characterization of the photorefractive bright soliton formation process using a digital holographic technique," Measurement Science & Technology **20**, 045301 (2009).
61. Y. Pu, M. Centurion, and D. Psaltis, "Harmonic holography: a new holographic principle," Applied Optics **47**, A103-A110 (2008).
62. E. Shaffer, N. Pavillon, J. Kuhn, and C. Depeursinge, "Digital holographic microscopy investigation of second harmonic generated at a glass/air interface," Optics Letters **34**, 2450–2452 (2009).
63. C.-L. Hsieh, R. Grange, Y. Pu, and D. Psaltis, "Three-dimensional harmonic holographic microcopy using nanoparticles as probes for cell imaging," Opt. Express **17**, 2880–2891 (2009).
64. O. Masihzadeh, P. Schlup, and R. A. Bartels, "Label-free second harmonic generation holographic microscopy of biological specimens," Optics Express **18**, 9840–9851 (2010).

65. E. Shaffer, P. Marquet, and C. Depeursinge, "Real time, nanometric 3D-tracking of nanoparticles made possible by second harmonic generation digital holographic microscopy," Optics Express **18**, 17392–17403 (2010).
66. C. Barsi, W. J. Wan, and J. W. Fleischer, "Imaging through nonlinear media using digital holography," Nat. Photonics **3**, 211–215 (2009).
67. M. Cui, and C. H. Yang, "Implementation of a digital optical phase conjugation system and its application to study the robustness of turbidity suppression by phase conjugation," Optics Express **18**, 3444–3455 (2010).
68. C. L. Hsieh, Y. Pu, R. Grange, and D. Psaltis, "Digital phase conjugation of second harmonic radiation emitted by nanoparticles in turbid media," Optics Express **18**, 12283–12290 (2010).
69. I. Yamaguchi, T. Matsumura, and J. Kato, "Phase-shifting color digital holography," Optics Letters **27**, 1108–1110 (2002).
70. J. Kato, I. Yamaguchi, and T. Matsumura, "Multicolor digital holography with an achromatic phase shifter," Optics Letters **27**, 1403–1405 (2002).
71. J. L. Zhao, H. Z. Jiang, and J. L. Di, "Recording and reconstruction of a color holographic image by using digital lensless Fourier transform holography," Optics Express **16**, 2514–2519 (2008).
72. B. Javidi, P. Ferraro, S. H. Hong, S. De Nicola, A. Finizio, D. Alfieri, and G. Pierattini, "Three-dimensional image fusion by use of multiwavelength digital holography," Optics Letters **30**, 144–146 (2005).
73. P. Ferraro, S. Grilli, L. Miccio, D. Alfieri, S. De Nicola, A. Finizio, and B. Javidi, "Full color 3-D imaging by digital holography and removal of chromatic aberrations," J. Disp. Technol. **4**, 97–100 (2008).
74. P. Almoro, M. Cadatal, W. Garcia, and C. Saloma, "Pulsed full-color digital holography with a hydrogen Raman shifter," Applied Optics **43**, 2267–2271 (2004).
75. P. Tankam, P. Picart, D. Mounier, J. M. Desse, and J. C. Li, "Method of digital holographic recording and reconstruction using a stacked color image sensor," Applied Optics **49**, 320–328 (2010).
76. J. Kuhn, T. Colomb, F. Montfort, F. Charriere, Y. Emery, E. Cuche, P. Marquet, and C. Depeursinge, "Real-time dual-wavelength digital holographic microscopy with a single hologram acquisition," Optics Express **15**, 7231–7242 (2007).
77. A. Khmaladze, M. Kim, and C. M. Lo, "Phase imaging of cells by simultaneous dual-wavelength reflection digital holography," Optics Express **16**, 10900–10911 (2008).
78. T. Todorov, L. Nikolova, K. Stoyanova, and N. Tomova, "Polarization Holography .3. Some Applications of Polarization Holographic Recording," Applied Optics **24**, 785–788 (1985).
79. T. Colomb, P. Dahlgren, D. Beghuin, E. Cuche, P. Marquet, and C. Depeursinge, "Polarization imaging by use of digital holography," Applied Optics **41**, 27–37 (2002).
80. T. Nomura, B. Javidi, S. Murata, E. Nitanai, and T. Numata, "Polarization imaging of a 3D object by use of on-axis phase-shifting digital holography," Optics Letters **32**, 481–483 (2007).
81. T. Colomb, E. Cuche, F. Montfort, P. Marquet, and C. Depeursinge, "Jones vector imaging by use of digital holography: simulation and experimentation," Optics Communications **231**, 137–147 (2004).
82. M. Yokota, Y. Terui, and I. Yamaguchi, "Analysis of polarization state by digital holography with polarization modulation," Opt. Rev. **13**, 405–409 (2006).
83. T. Colomb, F. Durr, E. Cuche, P. Marquet, H. G. Limberger, R. P. Salathe, and C. Depeursinge, "Polarization microscopy by use of digital holography: application to optical-fiber birefringence measurements," Applied Optics **44**, 4461–4469 (2005).
84. E. Allaria, S. Brugioni, S. De Nicola, P. Ferraro, S. Grilli, and R. Meucci, "Digital holography at 10.6 mu m," Optics Communications **215**, 257–262 (2003).
85. S. De Nicola, P. Ferraro, S. Grilli, L. Miccio, R. Meucci, P. K. Buah-Bassuah, and F. T. Arecchi, "Infrared digital reflective-holographic 3D shape measurements," Optics Communications **281**, 1445–1449 (2008).

86. N. George, K. Khare, and W. Chi, "Infrared holography using a microbolometer array," Applied Optics **47**, A7–A12 (2008).
87. L. Repetto, R. Chittofrati, E. Piano, and C. Pontiggia, "Infrared lensless holographic microscope with a vidicon camera for inspection of metallic evaporations on silicon wafers," Optics Communications **251**, 44–50 (2005).
88. R. J. Mahon, J. A. Murphy, and W. Lanigan, "Digital holography at millimetre wavelengths," Optics Communications **260**, 469–473 (2006).
89. H. Yu, "Microwave holography measurement and adjustment of 25-m radio telescope of Shanghai," Microw. Opt. Technol. Lett. **49**, 467–470 (2007).
90. Y. Zhang, W. Zhou, X. Wang, Y. Cui, and W. Sun, "Terahertz digital holography," Strain **44**, 380–385 (2008).
91. X. K. Wang, L. Hou, and Y. Zhang, "Continuous-wave terahertz interferometry with multi-wavelength phase unwrapping," Applied Optics **49**, 5095–5102 (2010).
92. A. S. Morlens, J. Gautier, G. Rey, P. Zeitoun, J. P. Caumes, M. Kos-Rosset, H. Merdji, S. Kazamias, K. Casson, and M. Fajardo, "Submicrometer digital in-line holographic microscopy at 32 nm with high-order harmonics," Optics Letters **31**, 3095–3097 (2006).
93. G. Pedrini, F. C. Zhang, and W. Osten, "Digital holographic microscopy in the deep (193 nm) ultraviolet," Applied Optics **46**, 7829–7835 (2007).
94. A. Rosenhahn, R. Barth, F. Staier, T. Simpson, S. Mittler, S. Eisebitt, and M. Grunze, "Digital in-line soft x-ray holography with element contrast," Journal of the Optical Society of America a-Optics Image Science and Vision **25**, 416–422 (2008).
95. I. McNulty, J. Kirz, C. Jacobsen, E. H. Anderson, M. R. Howells, and D. P. Kern, "High-Resolution Imaging by Fourier-Transform X-Ray Holography," Science **256**, 1009–1012 (1992).
96. S. Eisebitt, J. Luning, W. F. Schlotter, M. Lorgen, O. Hellwig, W. Eberhardt, and J. Stohr, "Lensless imaging of magnetic nanostructures by X-ray spectro-holography," Nature **432**, 885–888 (2004).
97. C. Fuhse, C. Ollinger, and T. Salditt, "Waveguide-based off-axis holography with hard x rays," Physical Review Letters **97**, 4 (2006).
98. G. Faigel, and M. Tegze, "X-ray holography," Reports on Progress in Physics **62**, 355–393 (1999).

Chapter 11
Digital Holographic Microscopy

Microscopy is one of the main research and application areas of digital holography. Direct access to the phase as well as amplitude profiles makes quantitative phase microscopy by digital holography (DH-QPM) particularly powerful and versatile. A number of techniques of DH are developed especially for microscopy imaging and these are made possible because of the particular imaging characteristics of DH. Digital holographic and interferometric principles are the basis of many other techniques of QPM with novel capabilities. A survey is given of the wide and very active field of research in DHM techniques and applications. We begin with a brief background on optical microscopy.

11.1 Optical Microscope Basics

11.1.1 Optical Configuration

A typical microscope optical train is depicted in Fig. 11.1. The collector lens produces an image of the lamp at the condenser aperture, which is optically conjugate with the objective back focal plane and the eyepoint of the eyepiece or ocular. With the Koehler illumination, the sample specimen is illuminated with a more or less collimated beam, and its images are formed at the focal plane of the tube lens and at the camera plane. The specimen is also conjugate with the field diaphragm. In the infinity configuration, the space between the objective lens and the tube lens can accommodate various auxiliary components, such as beam splitter for epi-illumination and phase plate for phase-contrast imaging, without introducing aberrations. The field diaphragm defines the illuminated area of the specimen and the condenser aperture controls the brightness of the illumination as

M.K. Kim, *Digital Holographic Microscopy: Principles, Techniques, and Applications*, Springer Series in Optical Sciences 162,
DOI 10.1007/978-1-4419-7793-9_11, © Springer Science+Business Media, LLC 2011

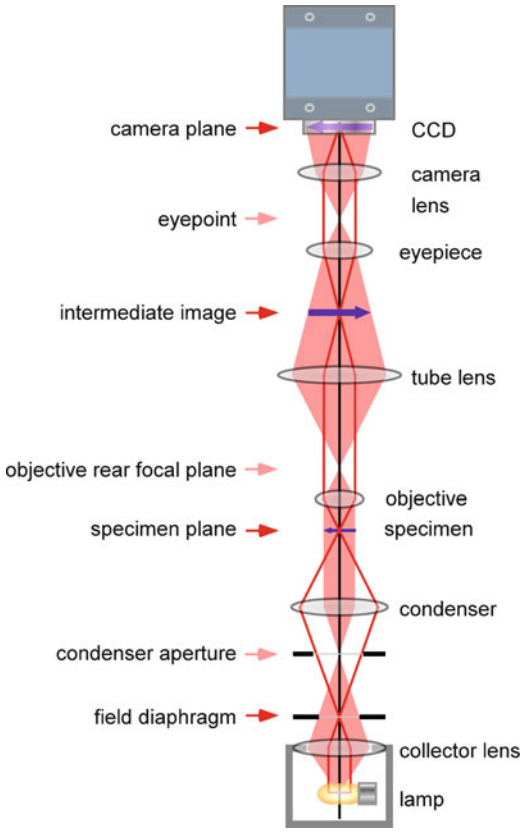

Fig. 11.1 Compound microscope optical train

well as the condenser numerical aperture. The illustration of Fig. 11.1 is for transmission imaging. For reflection imaging with epi-illumination, the illumination light is introduced from above the objective lens, by inserting a beam splitter, so that the objective lens functions also as condenser lens. With the inverted microscope configuration, the illumination is at the top and all the imaging components from objective to camera are below the specimen stage, the optical path usually folded with mirrors for space consideration. Inverted configuration provides better convenience and space for manipulation and control of live cells, for example.

In the traditional finite optical system (RMS: Royal Microscopy Society standard), the objective lens forms an intermediate image at the distance 160 mm, called the tube length, and the eyepiece magnifies this intermediate image. There is no tube lens. Because of the proliferation of auxiliary components inserted into the tube, such as for DIC or epifluorescence, the infinity configuration is more common in research-grade microscopes.

11.1.2 Magnification

If the lateral size of the specimen is x_o. The size of the intermediate image x_i is

$$x_i = x_o \frac{f_t}{f_o} = x_o \, M_o, \tag{11.1}$$

where f_o is the objective focal length and f_t is the tube lens focal length. The objective magnification M_o is specified with a standard tube focal length $f_t = 200\,\text{mm}$, in infinity configuration. A combination of the eyepiece and the camera lenses form the final image on the camera plane.

For magnification of the eyepiece, the eyepiece is considered to form a virtual image at a standard distance of 250 mm with the intermediate image just outside its front focus: for example, a 10× eyepiece has focal length 25 mm. The total magnification is the product of the objective M_o and the eyepiece M_e magnifications.

$$M = M_o \times M_e. \tag{11.2}$$

11.1.3 Resolution

The lateral resolution is determined by the numerical aperture, NA, of the objective lens:

$$\text{NA} = n \sin\theta, \tag{11.3}$$

where n is the index of refraction between the specimen and the objective and θ is the half angular aperture of the objective. The lateral resolution of the specimen plane is then

$$\delta x_o = 0.61 \frac{\lambda}{\text{NA}} \tag{11.4}$$

As a rule of thumb, for NA slightly larger than one, the lateral resolution can be expected to be about half of the wavelength. This assumes that the condenser NA matches or exceeds the objective NA. If the NAs do not match, then a more accurate expression is

$$\delta x_o = 1.22 \frac{\lambda}{\text{NA}_o + \text{NA}_c}, \tag{11.5}$$

where NA_o and NA_c refer to the objective and condenser NAs, respectively. For example, for collimated laser illumination, $NA_c = 0$ and the resolution is twice larger, that is, poorer, than NA-matched incoherent illumination. The axial resolution is also determined by the NA:

$$\delta z_o = \frac{n\lambda}{NA^2}. \tag{11.6}$$

11.1.4 Objective Lenses

The objective lens is obviously the most critical element of a microscope. Various levels of three main types of aberration corrections determine the grades of a lens: spherical aberration, chromatic aberration, and field curvature. An achromat corrects for axial chromatic aberration at two wavelengths, red (656 nm) and blue (486 nm), and for spherical aberration at green (546 nm). Plan achromats also correct for the field curvature. Fluorite lenses correct for both chromatic and spherical aberration at two or three wavelengths. Plan fluorite also corrects for field curvature and plan apochromat has the highest degree of correction at four or five wavelengths. Oil (1.515) or water (1.333) immersion lenses, when used with appropriate liquid, yield higher NA and improved resolution. One should also use standard cover slip (thickness 170 μm and index 1.515) with these objectives in order to preserve the aberration correction. Special purpose objective lenses are used for various microscopy techniques such as interference microscopy, phase-contrast microscopy, and scanning confocal microscopy.

11.1.5 Eye

For visual observation, the eye becomes a part of the optical imaging system. Ideally, the exit pupil (eyepoint) of the eyepiece coincides with the pupil of the eye. Visual resolution or acuity is constrained physically by the retinal photoreceptor spacing of about 5 μm (or 0.7 arc minutes for 25 mm distance from cornea to retina), although the vision process involves the complex processing by the visual cortex and the actual acuity can vary significantly above or below the physical limit. Then the visual resolution of an object at a distance 250 mm is nominally 50 μm. This leads to the minimum resolvable distance on the specimen plane to be $50/M$ μm, which needs to be larger than the resolution of the objective. The maximum useful magnification is then approximately $M_{max} \sim 200\,NA$, beyond which the magnification is said to be empty.

11.1.6 Camera

For digital imaging, a CCD camera substitutes for the eye. Digital imaging has mostly replaced traditional film-based imaging because of a number of important advantages, including the immediacy of visual feedback, quantitative image measurements, high sensitivity, and a large number of image-processing techniques available, which are the same reasons for the growing development and applications of digital holography. As a critical element in the imaging system, one needs to consider a number of operational parameters of CCD camera, including spatial pixel resolution, gray-scale resolution, frame rate, dynamic range, and noise [1].

11.2 Optical Microscopy Techniques

Brief descriptions of some of the main types of modern optical microscopies are given for the purpose of introducing typical problems encountered in microscopy and possible approaches for solving those problems. Full technical descriptions are found in many excellent sources, including [2, 3].

11.2.1 Bright Field Microscopy

This is the most common imaging mode of standard optical microscopy, where the light is transmitted through or reflected from most of the field of view, and the variation in transmittance or reflectance provides the contrast. The basic principle is generally familiar and operations relatively simple. Often various dyes are used in order to enhance the contrast of an otherwise transparent sample (Fig. 11.2).

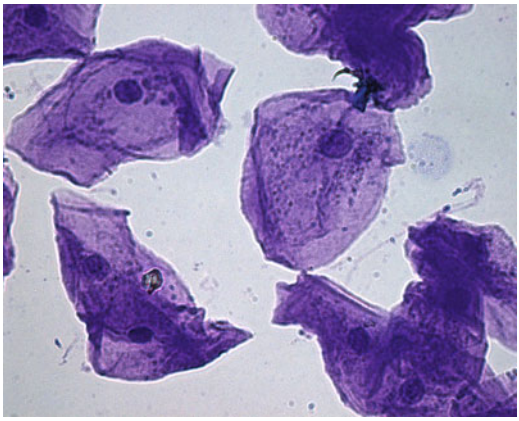

Fig. 11.2 Bright field microscopy image of stained cheek cells. (From http://washington.uwc.edu/about/wayne.schaefer/TissuesPage.htm, courtesy of Prof. W. Schaefer, Univ. Wisconsin)

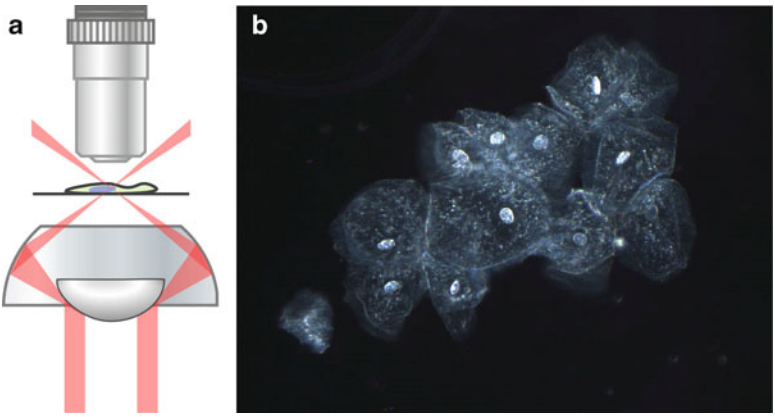

Fig. 11.3 (**a**) Dark-field condenser. (**b**) Dark-field microscopy image of cheek cells. (Courtesy of Prof. B.J. Cha, Univ. South Florida, Medicine)

11.2.2 Dark-Field Microscopy

For microscopy of objects with little variations in the intensity transmittance or reflectance, it is difficult to obtain visible contrast in bright field microscopy. With oblique illumination, most of the direct light beam does not enter the pupil of the optical system except for those scattered from particles, edges, and other irregularities in the specimen, (Fig. 11.3). From Fourier optics point of view, the dark-field microscopy performs high-pass filtering that attenuates low-frequency components.

11.2.3 Zernike Phase-Contrast Microscopy

The Zernike phase-contrast microscope (ZPC) makes transparent phase objects visible by converting phase variations into intensity variations. This is achieved by spatial filtering diffracted and undiffracted components of light transmitted through the specimen and introducing a phase shift between the two components (Fig. 11.4). It employs an annular aperture at the condenser aperture and a phase plate of matching pattern at the objective back focal plane. Depending on the relative magnitude of index of refraction of the ring pattern in the phase plate vs. its background, one obtains positive or negative phase contrast, which results in reversal of brightness of areas with larger or smaller indices of refraction in the specimen. In order to improve interference contrast, the phase ring may be coated with metal or dielectric film so that the undiffracted intensity is comparable to diffracted component. A significant artifact is the so-called halo effect of diffuse bright area surrounding the boundary of abrupt optical density change, which is due to the finite width of the condenser annulus and the phase ring being slightly larger

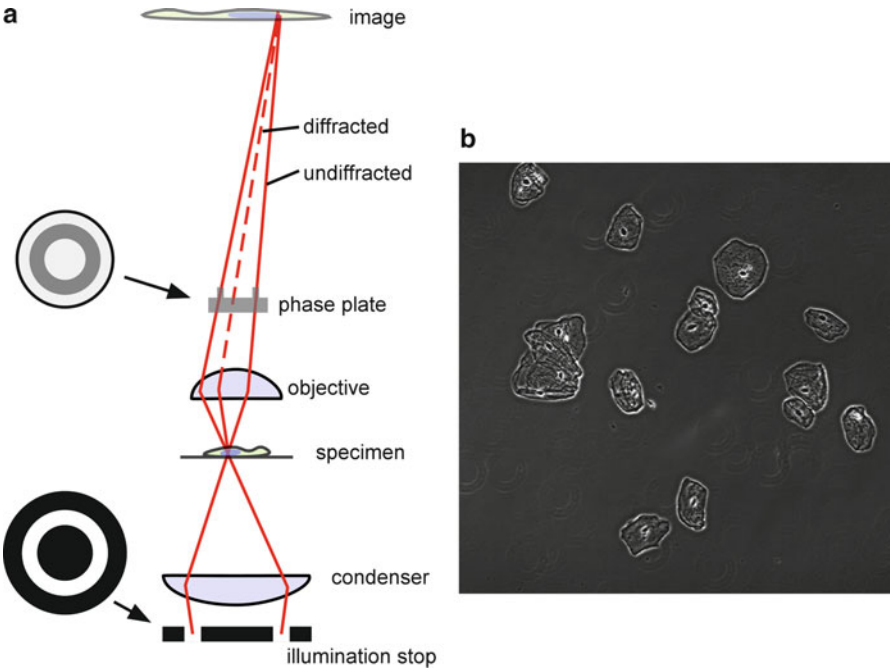

Fig. 11.4 (**a**) Optical system for Zernike phase-contrast microscopy. (**b**) ZPC image of cheek cells. (Courtesy of Prof. B.J. Cha, Univ. South Florida, Medicine)

than the image of the annulus. Use of different index material for sample suspension can reduce or even reverse the halo. Special apodized phase plate can also be used to reduce the halo effect. The ZPC has widespread use in imaging live cells, tissues, and microorganisms, as well as intracellular components such as the membrane, nuclei, mitochondria, chromosomes, and cytoplasmic granules. Highly refined modern ZPC, together with digital image processing, makes it even possible to sense the variation in index due to the presence of a small number of protein molecules.

11.2.4 Differential Interference Contrast

In Nomarski or differential interference contrast (DIC) microscopy, the e- and o- polarization components are separated by use of a Wollaston prism near the condenser aperture (Fig. 11.5). The lateral shear is typically a fraction of a micron. The two components pass through, or reflect from, the specimen and are made to converge and interfere with each other behind the objective back focal plane. The amount of shear is controlled by translating the Wollaston prisms. There are some variations such as use of Nomarski prism or de Senarmont compensator.

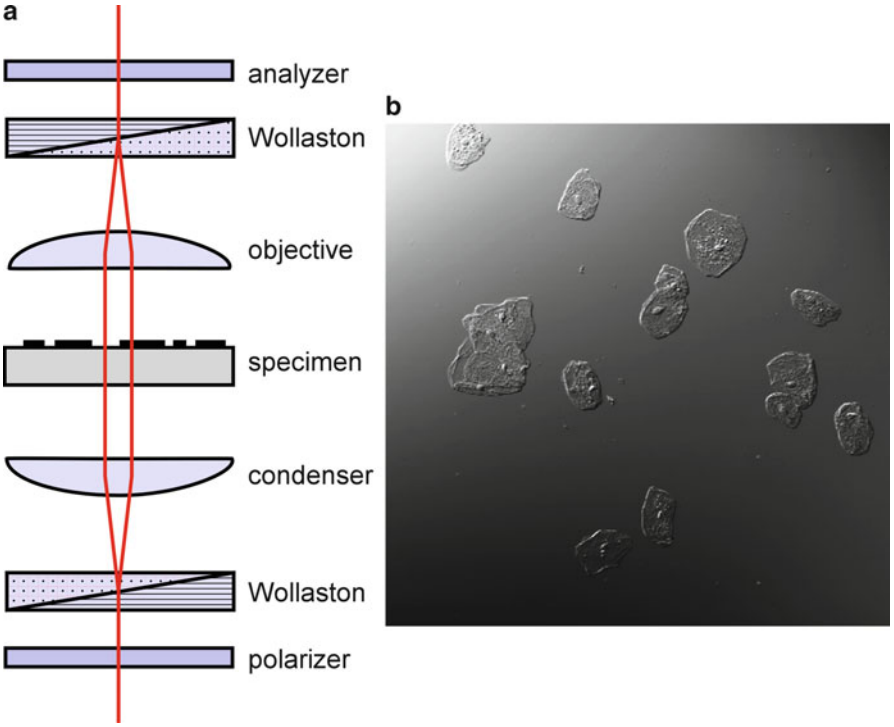

Fig. 11.5 (**a**) Optical system for DIC microscopy. (**b**) DIC image of cheek cells. (Courtesy of Prof. B.J. Cha, Univ. South Florida, Medicine)

The two components acquire phase difference when the optical thickness has a slope in the direction of the shear. A DIC image is characterized by its appearance of three-dimensional relief that emphasizes lines and edges across the shear direction. High resolution, wide range of contrast control, seemingly straightforward interpretation of images, absence of significant artifacts, and good optical sectioning properties account for the popularity of DIC microscopy. In particular, DIC has excellent sensitivity for imaging very small features together with those much larger, such as bacterial flagella and intracellular microtubules and other organelles. Interpretation of DIC images does need to consider the absence of contrast in the direction perpendicular to the shear and it is more difficult to use in thick or birefringent materials.

11.2.5 Interference Microscopy

Both Watson and Linnik microscope configurations are based on Michelson interferometer (Fig. 11.6a, b). In Watson, a single objective lens images the interference of the specimen and the reference, whereas in Linnik, the two arms are separately imaged with matching objectives before superposition and interference. Linnik allows shorter working distance and higher magnification but matched

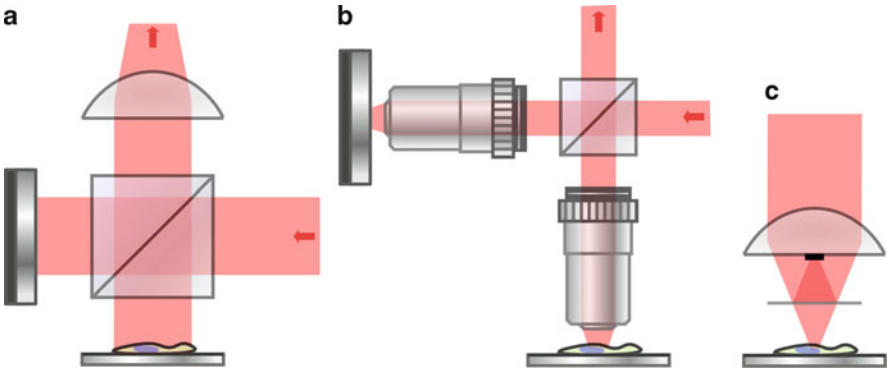

Fig. 11.6 Interference microscopy configurations. (**a**) Watson, (**b**) Michelson (or Linnik), and (**c**) Mirau

objectives is costly and alignment with low-coherence light is more critical. The Mirau objective uses half-silvered mirror and a reference mirror spot on the objective front surface (Fig. 11.6c). The almost common-path configuration provides mechanical stability and is used in optical profilometry applications.

11.2.6 Polarization Microscopy

Crossed polarizers reveal birefringence of the specimen placed in between. Many biological tissues and cells exhibit birefringence and these can display bright interference colors using polarization microscopy. Polarization microscopy used in crystallography can yield quantitative information on the birefringence and structures of the crystal.

11.2.7 Fluorescence Microscopy

The fluorescence microscopy is a highly versatile and essential tool in biomedical and materials sciences and many powerful techniques have been developed. The basic principle is straightforward: excitation of molecules of a specimen with higher energy (shorter wavelength) photons result in emission of lower energy (longer wavelength, or Stokes) photons, under specific conditions. The power of fluorescence microscopy stems from the specificity of the process: the molecules emit specific wavelengths when excited by specific wavelengths under possibly additional conditions such as temperature, pH, electric, or magnetic fields, etc. The fluorescence microscopy is also a zero-background imaging technique, particularly when epi-illumination is employed. Some biomolecules exhibit fluorescence (autofluorescence), but most often fluorophores (or fluorochromes) are added that bind or migrate to specific cellular and intracellular components and fluoresce with high efficiency.

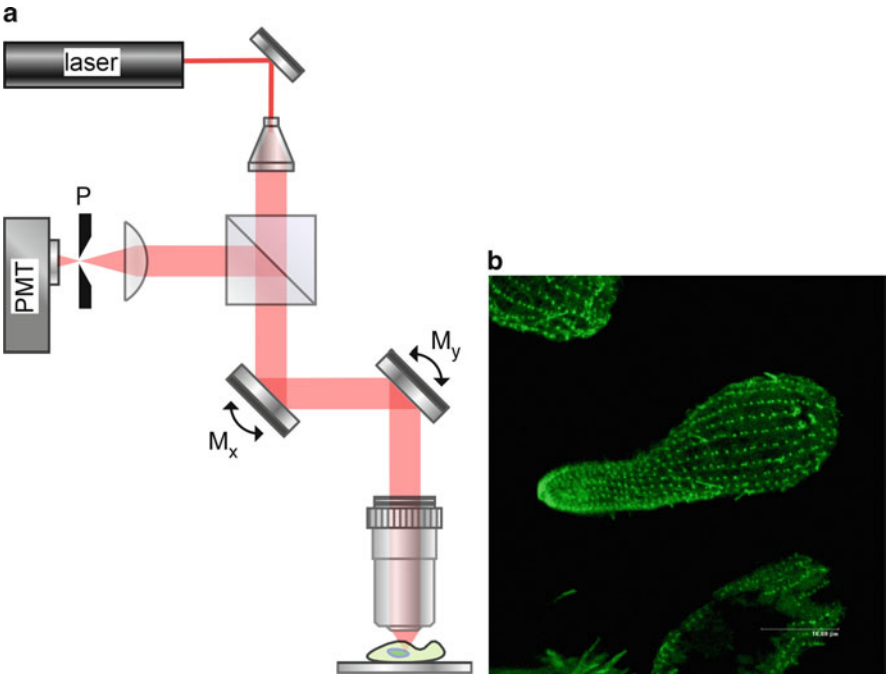

Fig. 11.7 (**a**) Optical system for confocal laser scanning microscopy. M_x *and* M_y scanning mirrors, *P* pinhole, *PMT* photomultiplier tube. (**b**) Confocal microscopy image of Beta-tubulin in tetrahymena cell, visualized using green fluorescent protein. (From http://en.wikipedia.org/wiki/Confocal_microscopy, under GNU Free Documentation License)

The discovery of green fluorescence protein (GFP) and development of many other fluorescent proteins covering all of the visible spectrum has been of tremendous impact in genetic science as well as other areas of biomedical science and engineering. A large number of powerful techniques, some with interesting acronyms – such as FRET, FLIM, FISH, FRAP, and FLIP – have been developed that exploit rich variety of physical, chemical, and optical interactions that affect fluorescence.

11.2.8 Confocal Laser Scanning Microscopy

With conventional wide-field fluorescence microscopy, the fluorescence is emitted from the entire illuminated volume of the specimen, which often obscures the signals from the focal plane. In confocal scanning microscopy, pinholes are used to illuminate a single focal point within the specimen volume and to collect scattered or fluorescence photons emanating only from the focus, blocking photons from the rest of the volume (Fig. 11.7). Two-dimensional optically sectioned image is acquired, usually inside a computer, by raster scanning the focal point over

the field. Three-dimensional volume image can be built up by stacking the 2D optical sections for a range of specimen planes. Confocal fluorescence microscopy principle is extended to multiphoton and harmonic generation microscopy as well.

Scanning of the illumination focus and descanning, so that the signal photons arrive at the stationary detection pinhole, are achieved in a number of different ways. First, the sample stage can be scanned, which keeps the optical system relatively simple but the mass of the stage limits the scan speed. Most confocal microscopes for biomedical study scans the focal spot within stationary specimen volume, using galvanometer-driven scan mirrors or acousto-optic deflectors, or a combination thereof, typically at a rate of one 2D frame per second. Parallel scanning of many pinholes can be achieved by a spinning Nipkow disk, one side of which is illuminated with a broad laser beam, allowing video rate imaging. Light throughput, and signal strength, can be improved by a microlens array on the disk.

11.2.9 Multiphoton Excitation and Nonlinear Optical Microscopy

Use of multiphoton (two- or three-photon) excitation of fluorescence or harmonic generation leads to nth power dependence of the generated signal as a function of the excitation intensity, where n is the number of photons involved. This leads to a number of unique advantages over single photon fluorescence. Because of the nonlinear dependence, the excitation laser intensity is high enough only at the focus and therefore the signal is emitted only from the focus region. Scanning microscopy is possible without using pinholes. The excitation laser is usually in the infrared, where the phototoxicity is significantly lower than in visible or UV. Most often pulsed emission from mode-locked lasers are used so that laser intensity is concentrated in picosecond or femtosecond pulses while average intensity is still relatively low. The short wavelength fluorescence or NLO light is emitted only from the focus. The phototoxicity and photobleaching is insignificant for the remainder of the sample volume, a situation very different from single photon confocal microscopy. The long wavelength excitation also leads to significantly longer depth of penetration allowing optical section microscopy of thicker tissues.

11.3 Digital Holographic Microscopy

A basic digital holographic microscopy (DHM) setup consists of an illumination source, an interferometer with microscopic imaging optics, a digitizing camera, and a computer with necessary programs.

11.3.1 Light Source

Most often a laser is used for illumination with the necessary coherence to produce interference. All different types of lasers have been used, from the ubiquitous HeNe laser and diode laser, to diode-pumped and doubled YAG laser (often referred to simply as a solid-state laser), argon laser, as well as tunable dye laser and Ti:sapphire laser. For multiwavelength techniques, two or more of different lasers may be coupled into the interferometer, or a tunable laser may be employed. There are also low-coherence techniques for the purpose of reducing speckle and spurious interference noise or generating contour or tomographic images. A short-pulse (picosecond or femtosecond) laser may be used or a tunable laser may be turned into a broadband source by removing the tuning element. Even an LED typically has 10 μm or so coherence length, which can be sufficient for the thickness of microscopic specimen.

11.3.2 Interferometers

The two main types of interferometers are the Michelson and the Mach–Zehnder type interferometers. The Michelson interferometer (Fig. 11.8a), is appropriate for reflective object, though it is also possible to arrange for double-pass transmission, by placing transparent specimen on a mirror. The Mach–Zehnder interferometer (Fig. 11.8b) is more suitable for transmissive objects. It requires more components but offers more flexibility in alignment, especially when the microscopic imaging optics are used. One can also modify the Mach–Zehnder configuration for reflective object by adding more beam splitters, as shown in Fig. 11.8c, where the short arm in the upper right corner is useful especially for short coherence length source, where the optical paths need precise balancing. In these diagrams, the shaded paths represent the beams of undiffracted illumination and the red lines indicate the image forming rays. In the illustrated examples, the object is illuminated by a plane wave and the magnification is provided by the microscope objective lens and imaging lens combination. The reference beam is focused at a point conjugate to the back focal plane of the objective lens, so that it arrives at the CCD plane with the same wavefront curvature as the object wave [4], except for an offset in the angle of incidence for off-axis holography, and any residual mismatch of wavefront curvature can be compensated for by numerical techniques as described earlier.

Each of these arrangements can have variations. One can omit lenses in the object and reference arms altogether for Fresnel holography configuration. If a lens in reference arm positions a focus at a conjugate point of the object plane, then itbecomes a lensless Fourier configuration. One can place the objective lens so that an intermediate image plane is conjugate with the reference focus, for lensed Fourier holography. Formation of an intermediate image may add some flexibility and easier access to a Fourier plane. The wavefront curvature

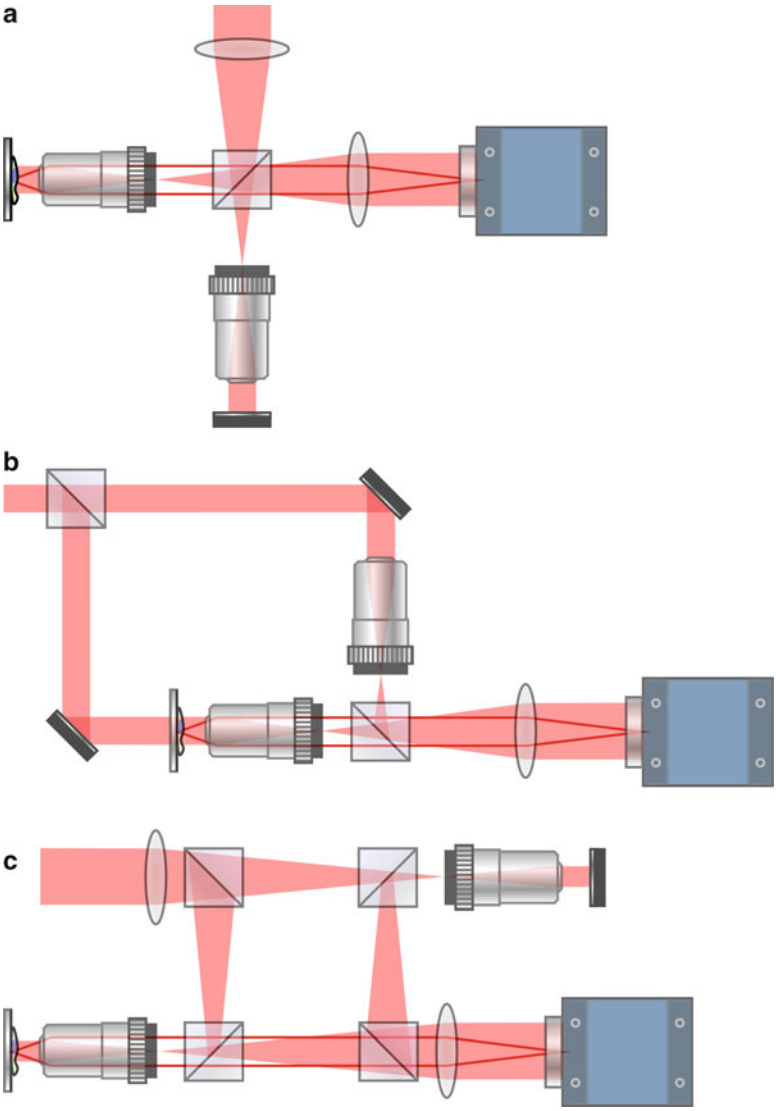

Fig. 11.8 Interferometer configurations for digital holographic microscopy. (**a**) Michelson (or Linnik), (**b**) Mach–Zehnder, and (**c**) modified Mach–Zehnder

matching between the object and reference arms is also optional but may be beneficial for minimizing possible secondary aberrations due to excessive fringe frequencies at the CCD plane. One can delete the reference arm altogether for Gabor holography. The examples in Fig. 11.8 have the CCD focused near the object plane, for image plane holography. This may have the advantage of being able to easily monitor the object scene even when holography reconstruction is not turned on. The illustrations are also

Fig. 11.9 Lyncée Tec DHM T1000 digital holographic microscope. (Courtesy of Dr. Yves Emery, Lyncée Tec SA)

for infinity configuration, so that the insertion of beam splitters and other components cause minimal aberration. We also note that, unlike conventional low-coherence interferometry, the focusing lens in the reference arm does not need precise match with the objective lens, its only function being approximate matching of the wavefront curvatures. There are many versatile techniques in digital holography that compensates for various types of aberrations and imperfections of the optical system, and therefore, in comparison with conventional microscopy, the optical and mechanical requirements can be significantly less stringent.

The interferometers may also include various apertures, attenuators, and polarization optics to control the reference and object intensity ratio. The polarization optics may also be used for the specific purpose of birefringence imaging. There may also be various types of modulators such as piezo-mounted optics, liquid crystal phase modulator, acousto-optic or electro-optic modulators to establish modulated signals. As in conventional microscopy, immersion-type objective lens has been shown to enhance the NA and resolution [5]. For quick optical setup and experimentation, horizontal layout of optics may be easier but the vertical orientation of specimen is incompatible with most cellular microscopy. Vertical arrangement of optics using vertical breadboard or a cage system is more appropriate so that the specimen can be placed horizontally. Upright (illumination of object from below) or inverted (illumination from above) microscope configurations are possible [6]. Alternatively, the holographic interferometer may be built around a laboratory optical microscope, by introducing the reference beam through one of the access ports [7]. Complete digital holographic optical microscopes are now available commercially as well (Fig. 11.9).

11.3.3 Camera

Typically a CCD or, more recently, CMOS cameras are used to capture and digitize the holographic interference pattern. The pixel size of these devices is several microns with pixel count of up to $1{,}000 \times 1{,}000$ or so. These parameters are the main limiting factors in the DHM resolution and prescribes the range of applications, but one would expect them to continue to improve in the coming years. The captured hologram pattern is digitized by the camera, or a frame grabber, and input to the computer as a 2D array of integers with 8-bit or higher gray-scale resolution. Often in standard DH experiments, the sensitivity and noise of CCD is not a central issue, at least not to the extent that it is in fluorescence microscopy, for example. This is because DH is a two-step indirect imaging method, where the pattern acquired by the camera is processed before numerically constructing the final image. The relationship between these two is more convoluted. In particular, the noise in the phase image from DH behaves quite differently from the intensity image [8]. The CCD sensitivity does become important in low-light DH techniques, such as in dark-field DH of nanoparticles [9].

11.3.4 Computer

The main task of the computer is to carry out the numerical diffraction in order to compute the holographic image as an array of 2D complex numbers. The software package would include components for image acquisition and camera interface control, holographic calculations, and image rendering and processing. The acquisition component establishes communication with the camera and other components of the microscope, setting the laser power, camera exposure levels, timing modes and synchronizations. It performs image acquisition in the different modes, as well as some preprocessing of images, for example, background subtraction. Holographic calculations may use angular spectrum or other methods and provide for numerical focusing. Special numerical techniques may be included, such as optical phase unwrapping, aberration compensation, differential holography, and automatic focusing and tracking, as described in Chap. 9. At the current stage of digital holography development, most researchers rely on in-house development of software package. User-friendly interface is important for rendering the image data in a consistent and flexible manner, as well as for calibration, measurements and postprocessing of the images. An efficient and robust means of storing, archiving, and retrieving image data and associated metadata is also important. To reduce computation times for numerical diffraction, hardware accelerations have been demonstrated using FPGA (field programmable gate array) or GPU (graphic processing unit) [10, 11].

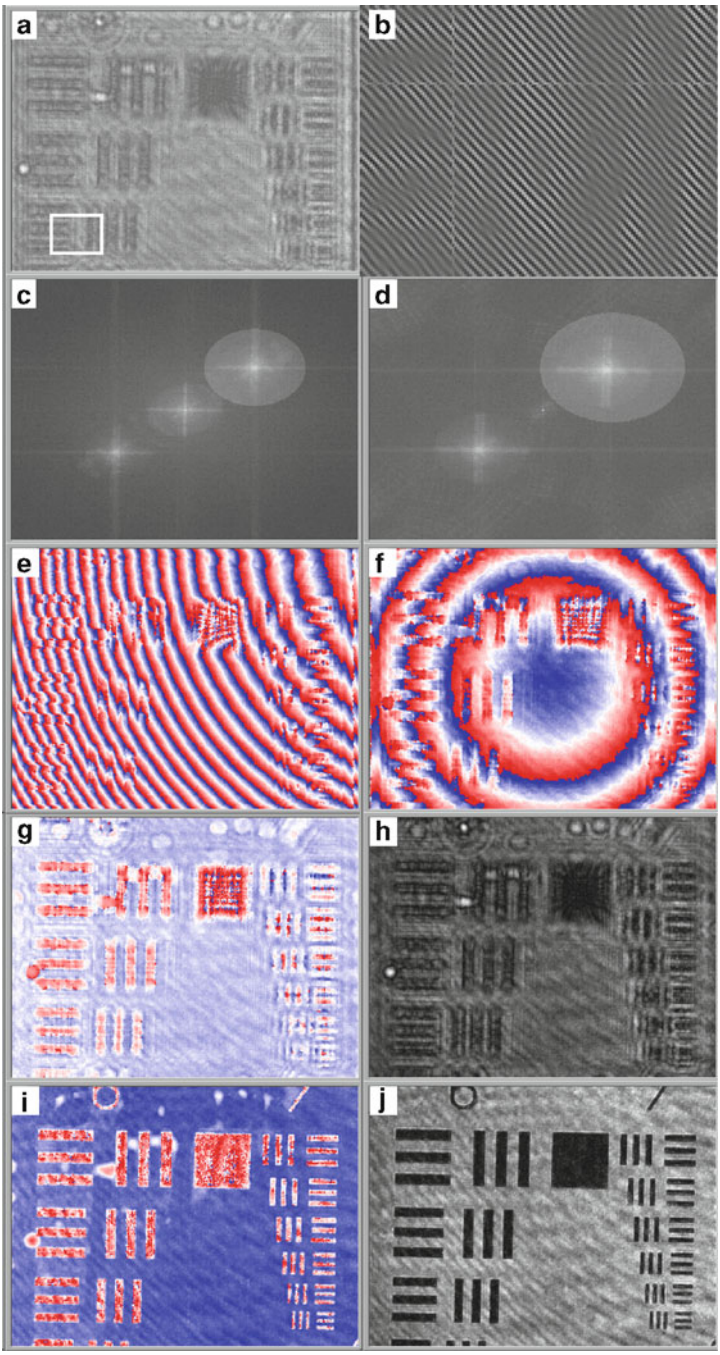

Fig. 11.10 Digital holographic microscopy process, $269 \times 202\,\mu m^2$, $1{,}024 \times 768$ pixels (**a**) Hologram; (**b**) a detail of the *small white rectangle* in (**a**); (**c**) angular spectrum including zero-order terms; (**d**) angular spectrum after subtraction of object and reference intensities from

11.3.5 Examples

An example of the DHM process is shown in Fig. 11.10, using a resolution target with FOV (field of view) 269 × 202 μm^2 and 1,024 × 768 pixels. The wavelength used was 635 nm. Figure 11.10a is the hologram acquired by the CCD camera, with a detail of a small area (small white rectangle) shown in Fig. 11.10b, where the interference fringes are visible. Its angular spectrum (Fourier transform) in Fig. 11.10c shows the zero-order and the twin-image peaks. One of the twin terms may be selected, but the zero-order peak limits the size of the filter (highlighted circular area). The zero-order peak can be suppressed if one takes separate exposures of the object and reference without interference and subtracts from the hologram, as shown in Fig. 11.10d. Now the numerical bandpass filter can be larger, and the resolution of the reconstructed image improved. When the filtered spectrum is then inverse Fourier transformed, one usually finds aberrations due to wavefront curvature and slope mismatch, as in the phase profile Fig. 11.10e. First, the center of the numerical filter is fine-adjusted to coincide the spectrum peak, resulting in the new phase profile in Fig. 11.10f. The phase curvature is due to a slight mismatch in the curvatures of the object and reference beams during hologram exposure. It is not necessary to physically fine-adjust the position of the lenses. The same effect can be achieved much more conveniently by multiplying a spherical wavefront to the hologram, and setting the radius of curvature until the curvature of the phase profile disappears, as in Fig. 11.10g. The corresponding amplitude image (Fig. 11.10h) is the reconstructed image at the hologram plane. Finally, numerically propagate the hologram an appropriate distance, $z = 100$ μm, so that the image comes into focus. The resulting in-focus phase and amplitude images are shown in Fig. 11.10i, j. As we have seen in previous chapters, additional numerical techniques can be applied to compensate for other types of aberrations, or to further process the image in various ways. The phase images' color scale ranges the $[-\pi, \pi]$ interval, corresponding to one wavelength of optical path length. Although the resolution target is a flat two-dimensional object, and thus without interesting topographic variations, the phase image (Fig. 11.10i) shows that there are some smudges of materials less than a wavelength thick at several spots on the surface. Also note that the dark bar and square areas represent almost opaque metallic film, and therefore the light intensity is low. The low signal causes larger noise in the phase profile for these areas.

Fig. 11.10 (continued) the hologram, with the *brighter circular area* for bandpass filter; (**e**) reconstructed phase profile at hologram plane, without any corrections; (**f**) phase profile after correct centering of the filtered angular spectrum; (**g**) phase profile after compensation of the spherical wave curvature; (**h**) the amplitude image at the hologram plane corresponding to the phase image (**g**); (**i**) phase image after numerical propagation to the object focus distance $z = 100$ μm; and (**j**) the focused amplitude image

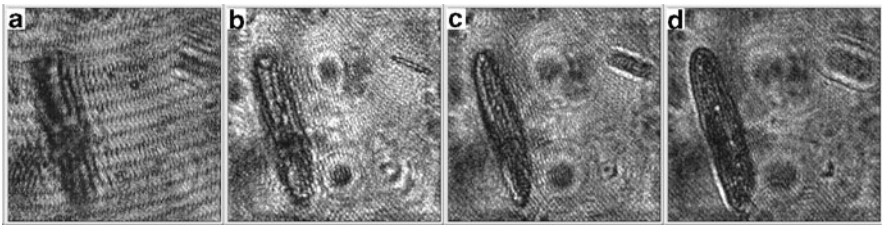

Fig. 11.11 (**a**) A hologram of paramecium and euglenas (80 × 80 μm^2). (**b–d**) Reconstructed amplitude images at $z = 100, 150, 200$ μm [12]

A well-known distinctive feature of holography is the three-dimensional content of the image information. In DHM, a single hologram is used to reconstruct the optical field at any distance from the hologram, within the limitation of the approximation method used. For example, Fig. 11.11a is a hologram of paramecium and several euglenas in water, with FOV 80 × 80 μm^2 and 464 × 464 pixels. From the single hologram, the images are calculated at various distances, showing the paramecium and a euglena coming into focus at depths approx. 100 μm apart. The numerical focusing emulates the turning of the focus knob on a conventional microscope. A movie of holograms is acquired in real time, several frames of which are shown in Fig. 11.12a, which is then postprocessed to produce the amplitude (Fig. 11.12b) and phase movies (Fig. 11.12c). In the scene, the paramecium and the euglenas swim not only in lateral directions but also in varying depths. In conventional video microscopy, the focal plane would be fixed and whatever happened to be in that plane would be recorded, but information on objects not in the focal plane would be permanently lost. With DHM, the holographic movie can be processed by calculating the images while adjusting the reconstruction distances to track a particular specimen as it swims up and down in the three-dimensional object volume. In effect, the holographic movie is a complete four-dimensional space-time record of the object volume.

11.3.6 Comparisons of Analog and Digital Holographic Microscopy

There are a number of significant distinctions between the analog (AH) and digital (DH) holographies. Most obviously, DH does not involve photochemical processing. Therefore, DH is orders of magnitude faster and can be performed at video rate. Additional hardware required in DH is the CCD camera and a computer, while eliminating the need for dark room facility and the supply of chemicals. Furthermore, because of the high sensitivity of CCD compared to photographic emulsion, the exposure time is reduced by orders of magnitude. For example, a CCD pixel of 100 μm^2 can detect as few as several photons, whereas a similar

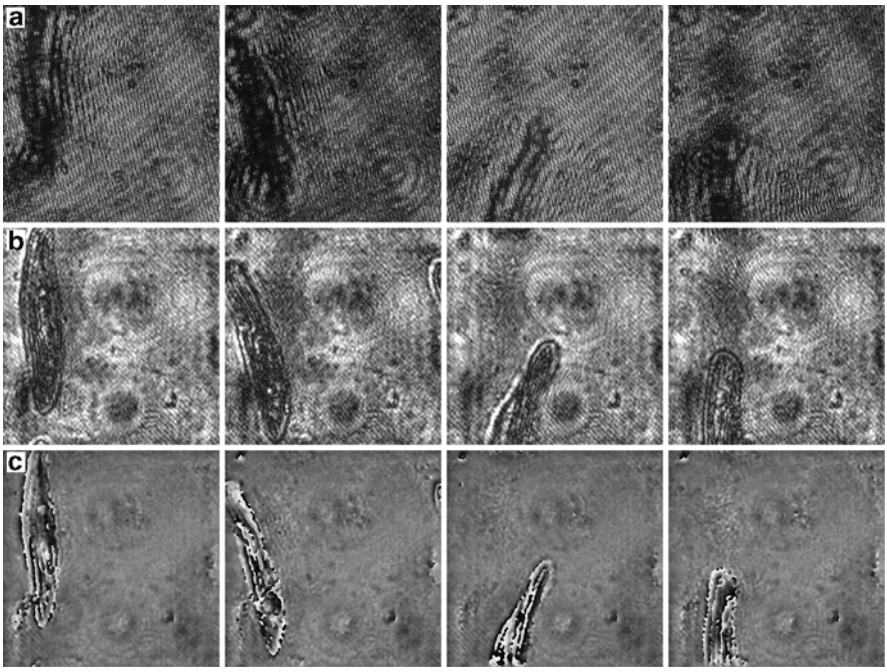

Fig. 11.12 (**a**) Several frames of a holographic movie of paramecium and euglenas. (**b**) Amplitude and (**c**) phase movies reconstructed from the holographic frames, while adjusting reconstruction distance to maintain the paramecium in focus [12]

area of a high-sensitivity photographic plate requires many millions of photons. Even when comparing exposures of individual pixels or grains, CCD can be orders of magnitude more sensitive. Short exposure time in turn implies much reduced requirement on the mechanical stability of the apparatus. Heavy optical tables with vibration isolation are often not as critical as in AH. On the other hand, the main issue of DH is the low resolution. A typical CCD pixel is several microns across, while the grains on a photographic emulsion may be two orders of magnitude finer. This limits the spatial frequency of the fringes and therefore the angular size of the object to about a few degrees for DH, while full 180° is possible for AH. The familiar parallax effect of display holograms of AH is more difficult in DH [13]. The real strength of DH, however, is the whole range of powerful numerical techniques that can be applied once the hologram is input to a computer. One simple but significant example relates to the microscopic imaging, where a lens is used to magnify the hologram FOV to match the CCD size. Once the computer reads the hologram into an array, one only needs to specify the dimension of the FOV and the wavelength, and proceed to compute the numerical diffraction. In AH, however, in order to properly read out the magnified or demagnified hologram, the wavelength also needs to be scaled proportionately, a task that is

highly cumbersome at the least and infeasible in most cases. Another example is the holographic interferometry using multiple wavelengths. In AH interferometry, multiple holograms are produced and repositioned exactly, and ideally each hologram needs to be illuminated with a different wavelength, which can be physically impossible. Most often the superposed holograms are illuminated with a single wavelength and the resulting aberrations are unavoidable. In DH reconstruction, however, use of various wavelengths only amounts to assigning numbers and the superposition simply consists of addition of several numerical arrays. There is no limitation on the number of arrays and, furthermore, there are ways to preprocess the arrays to compensate for chromatic and other aberrations if present. More examples of the power of numerical processing in DH have been described in previous chapters.

11.4 Quantitative Phase Microscopy by DHM

The optical phase of the light transmitted through transparent objects can convey quantitative information about the object, such as its physical thickness and index of refraction [14], which in turn are functions of physical density or chemical concentration properties. High-precision measurements of optical phase can thus reveal subtle changes in these parameters that accompany cellular processes. In order to obtain quantitative phase images, one can perform interferometric measurement of a focused beam of light on an object and scan the beam over the object in a raster fashion. Optical profilers based on scanning interferometer are especially well suited for imaging applications in materials science, as in MEMS and nanofabrication, because of the high precision obtainable and the static nature of the objects being imaged. On the other hand, the speed constraint and mechanical complexity of scanning interferometer can significantly restrict the range of applications in biology, where one needs to make observations of dynamic processes under widely varying environments.

Digital holography is a very effective process for achieving high-precision quantitative phase microscopy. The phase image is immediately and directly available as soon as the 2D complex array of the holographic image is calculated. A single hologram exposure is required. It does not involve raster scanning. Most importantly, the phase image is a quantitative representation of the object profile with nanometer, and even subnanometer, precision [15–17]. An example of DHM imaging of a SKOV3 ovarian cancer cells is shown in Fig. 11.13, where Fig. 11.13a is the hologram and Fig. 11.13b is the reconstructed amplitude image, analogous to what one would see through a conventional microscope. The phase image in Fig. 11.13c indicates that the cells apparently have thickness of several microns, and therefore the phase profile varies by several cycles of 2π radians. A public-domain phase unwrapping algorithm is used to remove the 2π discontinuities in Fig. 11.13d, and it is rendered in pseudo-color pseudo-3D perspective in Fig. 11.13e. The apparent height profile is the profile of optical thickness that

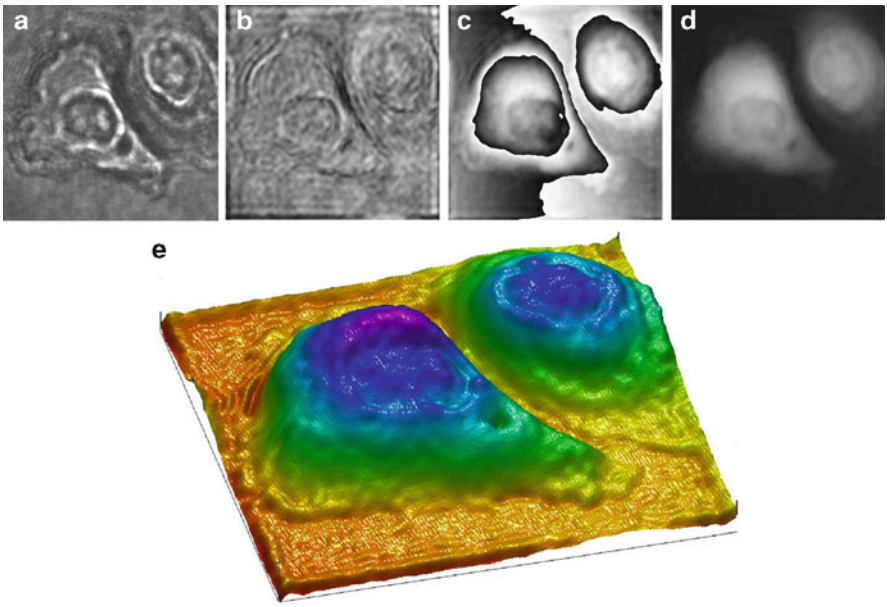

Fig. 11.13 Digital holographic microscopy of SKOV3 ovarian cancer cells (60×60 μm^2, 404×404 pixels): (**a**) hologram, (**b**) amplitude image, (**c**) phase image, (**d**) unwrapped phase image, and (**e**) phase image in pseudo-color pseudo-3D view [18]

includes both physical thickness and index variation, and one needs to use caution in interpreting such images. Figure 11.14 displays a few more examples of DH-QPM images, including a layer of onion cells (Fig. 11.14a), a mouth epithelial cell (Fig. 11.14b), several red blood cells (Fig. 11.14c), and a small quartz crystal in common sand (Fig. 11.14d).

11.5 Cell Microscopy and Other Applications

The quantitative phase microscopy (QPM) is perhaps the most important aspect of DHM because it allows optical thickness measurements with nanometric accuracy in a single-shot wide-field acquisition and it yields such phase profiles without some of the difficulties associated with other phase imaging methods. QPM is therefore a very important and active area of research and applications in digital holography. We survey some examples of applications in cell microscopy here.

C. Depeursinge et al. have pioneered the DH-QPM with the original demonstration of nanometric surface profiling [15] and have carried out quantitative cellular imaging and characterization studies. Living mouse cortical neurons are imaged (Fig. 11.15) and their reaction to hypotonic shock is quantitatively measured [19, 20].

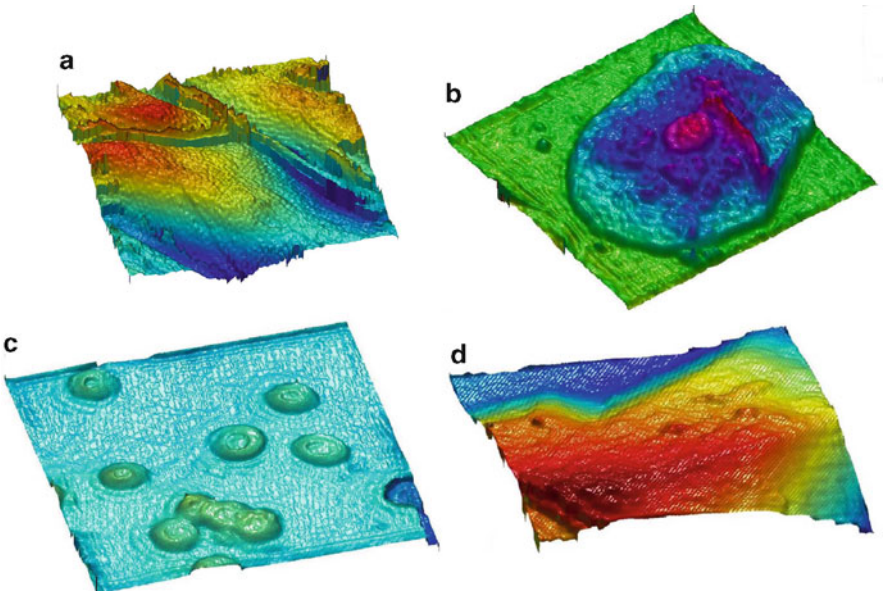

Fig. 11.14 Examples of quantitative phase microscopy by digital holography. (**a**) Onion cells, (**b**) mouth epithelial cell, (**c**) red blood cells, and (**d**) small quartz crystal in common sand

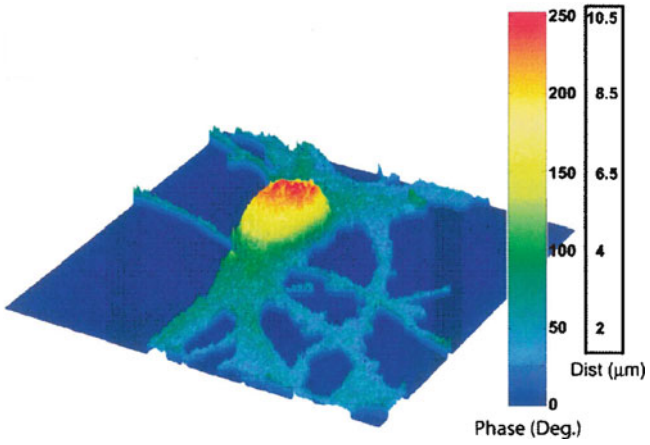

Fig. 11.15 Perspective image in false color of the phase distribution obtained with DHM of living mouse cortical neuron in culture. (Reprinted from [19] by permission of OSA)

In order to decouple the physical thickness and index of refraction, they have devised a decoupling procedure, where two holograms are taken while the cells are immersed in standard perfusion solution and a second solution with the same osmolarity (to avoid cell volume variation) but with a different refractive index. Phase images $\varphi_1(x, y)$ and

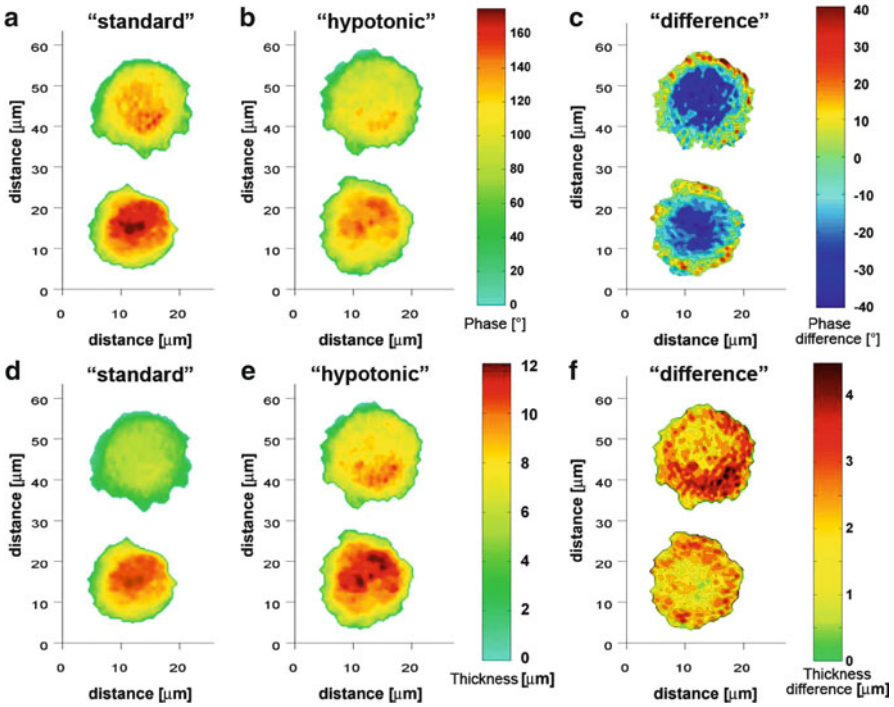

Fig. 11.16 (*Upper panels*) Quantitative phase images of two neuronal cell bodies before (**a**, "standard") and 3 min after the onset of the hypotonic shock (**b**, "hypotonic"). (**c**) Color-coded distribution of phase difference resulting from the subtraction of the "standard" image from the "hypotonic" image. Neuronal cell body boundaries have been identified by a gradient-based edge detection algorithm. (*Lower panels*) Morphometry of 2 cell bodies before (**d**) and 3 min after the onset (**e**) of a hypotonic shock. Here the z-axis (cellular thickness) is expressed in micrometers. These values were obtained using the results of the decoupling procedure. (**f**) Color-coded distribution of thickness variations resulting from the subtraction of the "standard" image to the "hypotonic" image. (Reprinted from [20] by permission of OSA)

$\varphi_2(x, y)$ from the two holograms are combined to yield separately the index $n_c(x, y)$ and physical height $h_c(x, y)$ profiles:

$$n_c(x, y) = \frac{\varphi_1}{\varphi_1 - \varphi_2}\delta n + n_m, \tag{11.7}$$

$$h_c(x, y) = \frac{\lambda}{2\pi}\frac{\varphi_1 - \varphi_2}{\delta n}, \tag{11.8}$$

where n_m and $n_m + \delta n$ are the indices of the two solutions. The technique is applied to quantifying the morphological changes following hypotonic shock of cells, where the cells are consecutively subjected to the standard perfusion solution and a hypotonic solution reducing the extracellular osmolarity by 37%. The hypotonic solution produces a decrease in the phase signal which reaches a plateau after 2 min, as displayed in Fig. 11.16. But when the decoupling technique is applied, the physical

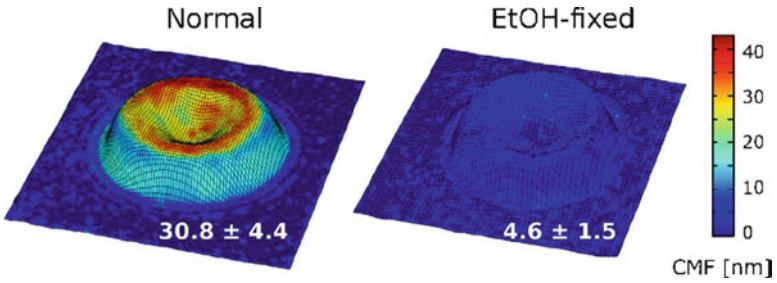

Fig. 11.17 Normal cell membrane fluctuations (CMF) displayed as color code over the shape of the RBC for a representative normal and ethanol-fixed cells. *Insets* contain the mean ± SD (nm) of the CMF of the analyzed regions for each representative cell. (Reprinted from [22] by permission of Elsevier Inc.)

thickness profile shows the expected swelling of the neurons. The decoupling technique allows accurate measurement of index of refraction to obtain the indices of red blood cells $n_{\mathrm{RBC}} = 1.394 \pm 0.008$ and neurons $n_{\mathrm{neuron}} = 1.380 \pm 0.007$ [21]. They have also found the fluctuation of red blood cell membranes to be 35.9 ± 8.9 nm in normal state, while that of ethyl alcohol-fixed cells showed much reduced fluctuations 4.7 ± 0.5 nm (Fig. 11.17) [22]. Fission yeast cell cycle is studied by monitoring dry mass production rate and dry mass surface density in wild-type and mutant fission yeast cells [23]. Another method to decouple the physical thickness is by using a single buffer containing absorptive dye (sulforhodamine) and utilizing the sharp dispersion near an absorption peak for two-wavelength measurement [24].

Bally et al. have studied human cancer cells by DHM [7, 25, 26]. For example, Fig. 11.18 shows initial swelling or rounding of a pancreatic cancer cell in response to anticancer drug taxol, followed by its collapse over a 4 h period. The morphological change is quantified in Fig. 11.18b. Similarly, osmotic volume changes in tumorous hepatocytes have been imaged in response to NaCl solution [27]. The phase image from DHM accounts for the variation of the optical thickness, which is a product of both the physical thickness and the index of refraction. The two can be decoupled if one of the two parameters is known. Profiles of index of refraction in pancreatic cancer cell can be obtained by confining the cell in a chamber of known thickness [28].

Kim et al. have obtained high-quality image of fixed SKOV-3 (human ovarian cancer cells) with approximately 0.5 μm lateral resolution and better than 10 nm optical height noise [18]. Holographic time-lapse movies of mouse embryo fibroblast cell in mitosis as well as real-time movies of paramecium and euglena are obtained in [12]. Optical phase unwrapping in single-shot dual-wavelength hologram acquisition has significant advantages in imaging of dynamic cellular phenomena [29]. They have developed a technique to image the phase profile of total internal reflection for studying cell–substrate adhesion, detailed in the next section [30]. Quantitative phase images recorded during the process of laser microsurgery

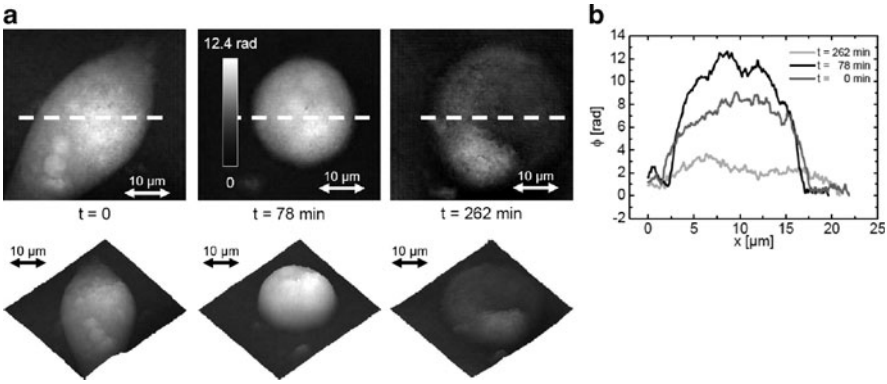

Fig. 11.18 (**a**) Monitoring of a living PaTu8988S cell after addition of an anticancer drug (taxol) to the cell culture medium. Apoptosis induces morphological changes such as cell rounding and finally cell collapse. *Upper row*: gray-level coded unwrapped phase distribution at $t = 0$, $t = 78$ min, and $t = 262$ min after taxol addition. *Lower row*: corresponding pseudo 3D representations of the phase data. (**b**) Cross-sections through the measured optical path length changes corresponding to the *dashed white lines* in the phase distributions of (**a**) (Reprinted from [7] by permission of SPIE)

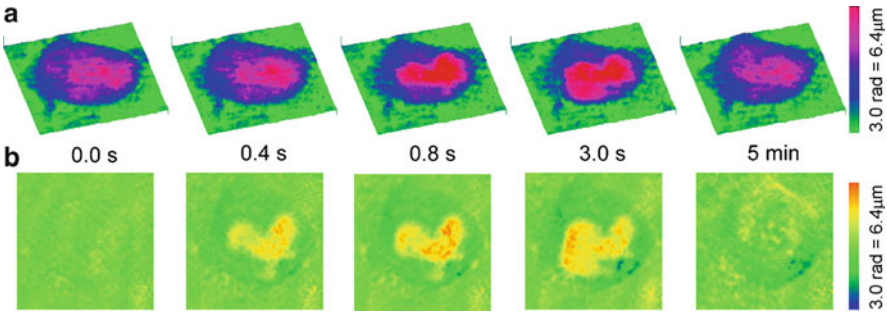

Fig. 11.19 (**a**) DH phase images of rat kangaroo kidney epithelial (PTK2) cells after laser microsurgery. (**b**) Difference phase image relative to $t = 0.0$ s. Scale bar: 10 µm, $n = 1.38$ [31]

of PTK2 (rat kangaroo kidney epithelial) cells, goldfish retinal rod cells, and human red blood cells allowed evaluation of dynamic changes in cell morphology in real time [31] (Fig. 11.19).

In [32], three-dimensional trajectories of many living fibrosarcoma cells embedded in a 3D collagen gel have been obtained, where the use of low-coherence light source reduced spurious speckle noise. DH-QPM is used in [33] to monitor the morphological changes during trypsinization (a process which causes cell thickness change but not its index of refraction), hypo-osmotic, and apoptosis processes. The activity of TRPV1 (transient receptor potential vanilloid type-1) was measured by DH-QPM, which detects cell surface topology perturbations that follow Ca^{2+} entry of plasma membrane [34].

11.6 Special Techniques of DHM

11.6.1 Total Internal Reflection Digital Holographic Microscopy

Many cells move by crawling over surfaces. Axons grow over long distances, macrophages and neutrophils crawl to sites of infection, fibroblasts migrate through connective tissues and cancer cells metastasize. The mechanics of cellular motion involves an orchestrated set of activities that include the protrusion of pseudopodia, the formation of new adhesions, the development of traction, and the release of previous adhesions. Current primary tools for imaging and studying these surface processes are the total internal reflection fluorescence microscopy (TIRFM) [35] and interference reflection microscopy (IRM) [36–39]. In TIRFM, only the fluorophores present within the distance of evanescent field emit the fluorescence signal, while the rest of the cell body remains dark, thus dramatically enhancing the contrast of cellular adhesion. While this technique provides excellent functional imaging, information on the morphology of the cellular membrane surface is largely absent [40]. In the interference reflection microscopy, light waves reflected from the two surfaces of the cell–substrate interface produce interference fringes, thus allowing estimation of the interface thickness profile. While this method allows qualitative interpretation of the surface profile, the interference image of the interface is usually complicated by the reflection image of the cell body and its contents.

The technique of total internal reflection holographic microscopy (TIRHM) was introduced to apply the quantitative phase microscopy by digital holography in the imaging of the phase profile of light in total internal reflection [30, 41]. While in total internal reflection all of the incident light energy is reflected, the evanescent field can interact with any materials present on the surface resulting in the modulation of the phase of the reflected light. Digital holography detects and images this phase profile with high sensitivity. Figure 11.20 depicts the geometry of TIRHM, where the incident light enters the prism and is TIR-reflected from the top surface

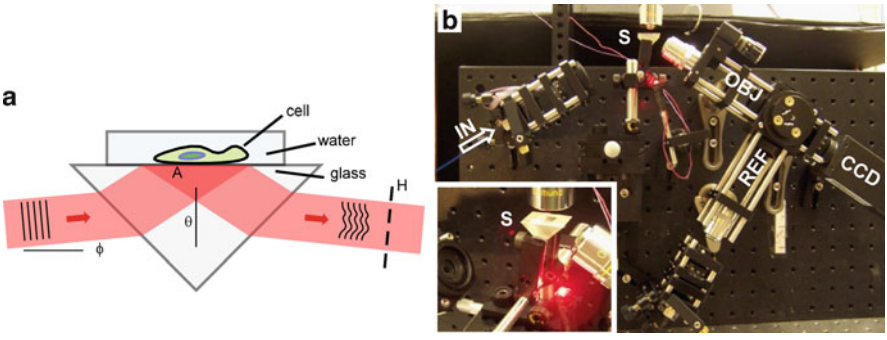

Fig. 11.20 (**a**) TIR prism with object beam and aqueous cellular sample. *A* prism surface, *H* hologram plane, θ angle of incidence. (**b**) TIRHM system on a vertical plate. TIR prism at apex. *Inset*: TIR prism close-up

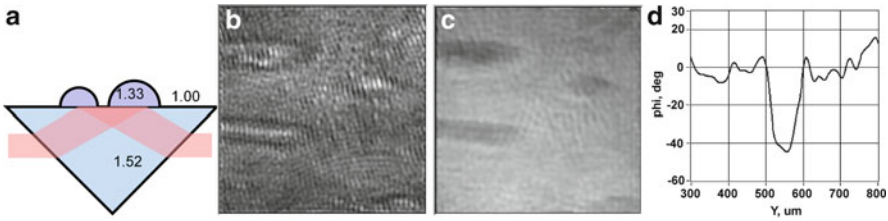

Fig. 11.21 (**a**) General configuration of water droplets placed on prism. (**b**) Amplitude and (**c**) phase images of light reflected from the prism. Field of view is approximately $300 \times 900\ \mu m^2$. (**d**) Graph of cross-section along a vertical line through a water drop in (**c**) [30]

provided the incidence angle is larger than the critical angle between the prism glass and the material in contact with the prism surface. The reflected light exiting the prism then contains the phase modulation due to the interaction of the evanescent field and the material on the prism. The camera is focused on a plane perpendicular to the propagation direction, such as the plane H in Fig. 11.20. Numerical diffraction is calculated from the plane H to the object plane, which is the prism face A, and therefore the calculation involves the technique of diffraction between tilted planes, described in Chap. 9. The prism is incorporated into a Mach–Zehnder interferometer to produce the hologram.

Consider the reflection of light, of vacuum wavelength λ_0, across a boundary between two dielectric media with indices $n_1 > n_2$. The reflection coefficients are given by the familiar Fresnel equations. When the angle of incidence θ_1 is greater than the critical angle $\theta_c = \sin^{-1}(n_2/n_1)$, and the polarization is normal to the plane of incidence (*s*-polarization), the reflection coefficient is complex with unit magnitude

$$r_\perp = \exp(-2i\varphi_\perp), \tag{11.9}$$

where the reflection phase is given by

$$\varphi_\perp = \tan^{-1} \frac{\sqrt{n_1{}^2 \sin^2\theta_1 - n_2{}^2}}{n_1 \cos\theta_1}, \tag{11.10}$$

which depends on the index of the second medium. Any variation of the index n_2 leads to corresponding variation in the reflection phase $2\varphi_\perp$. Figure 11.21 demonstrates such phase shift imaged by TIRHM for water droplets or 50/50 mixture of water/ethylene glycol on the glass prism surface. The size of the phase shift was found to be consistent with (11.10).

A more relevant configuration for the study of cellular adhesion involves two interfaces, as depicted in Fig. 11.22. In order to obtain phase-only signature

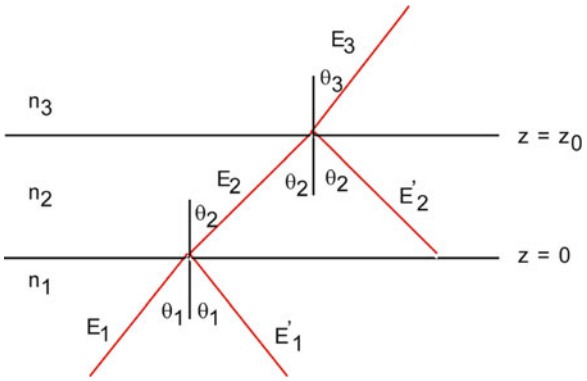

Fig. 11.22 Geometry of frustrated TIR (fTIR)

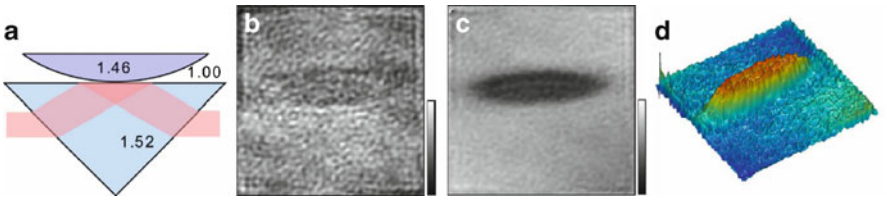

Fig. 11.23 (**a**) General configuration of quartz lens placed on prism. (**b**) Amplitude and (**c**) phase images of light reflected from the prism. (**d**) Pseudo-color perspective rendering of (**c**). Field of view is approximately 260 × 780 μm^2 [30]

in the reflected field, the TIR condition must be met at least for n_1/n_3 interface. The reflection coefficient for *s*-polarization is then

$$r_\perp = \left(\frac{E'_1}{E_1}\right)_\perp = \frac{(h_1 - i\eta_2)(\eta_2 + \eta_3) + (h_1 + i\eta_2)(\eta_2 - \eta_3)\exp(-2\varphi_0\eta_2)}{(h_1 + i\eta_2)(\eta_2 + \eta_3) + (h_1 - i\eta_2)(\eta_2 - \eta_3)\exp(-2\varphi_0\eta_2)}, \quad (11.11)$$

where

$$h_i = n_i \cos\theta_i = \sqrt{{n_i}^2 - {n_1}^2 \sin^2\theta_1} = i\eta_i \quad (i = 1, 2, 3) \quad (11.12)$$

and

$$\varphi_0 = 2\pi z_0/\lambda_0. \quad (11.13)$$

This mode of TIRHM imaging is demonstrated in Fig. 11.23, where a fused quartz lens of known curvature is placed on the prism surface. The resulting holographic image shows little amplitude contrast but the phase image clearly displays the presence of the lens. Filling the air gap with other materials such as ethylene glycol

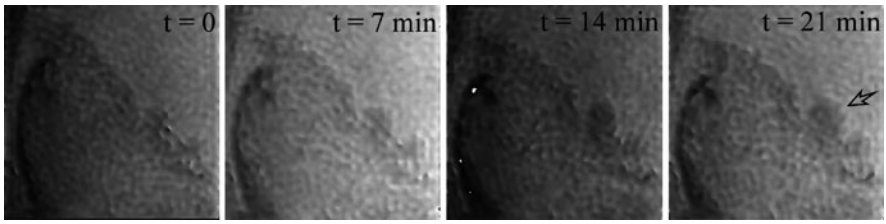

Fig. 11.24 TIRHM images of *Amoeba proteus* pseudopod activity at 7-min intervals [41]

and water is shown to vary the observed phase shift according to (11.11). Given the 115 mm curvature of the lens surface, the air gap varies up to 75 nm across the horizontal FOV, and the phase shift is observed within the 50 nm or so evanescent layer.

In Fig. 11.24, an amoeba proteus cell placed on the prism is imaged by TIRHM, where pseudopod movement, captured at 7 min intervals, may be discerned by thrust activity, designated at the arrow, between phase captures relative to the overall relaxation, shift, and counterclockwise rotation for the feature in general. The darker areas near the active pseudopod presumably indicate tighter adhesion to the surface.

11.6.2 Multimode Microscopy from a Single Hologram

As we noted earlier, there are a number of techniques available in optical microscopy for generating intensity contrast images from transparent phase objects, such as Zernike phase contrast and DIC. But these require delicate and expensive optical elements and their precise alignment. Zernike requires matched apertures and phase plate. DIC requires Wollaston prism pairs, etc. In DHM, on the other hand, it has been shown that the direct access to the full complex optical field makes it possible to manipulate the numerical representation of the optical field as if using real space optics [42]. In Fig. 11.25 several images of red blood cells are displayed, generated from a single hologram. The amplitude image in Fig. 11.25a is analogous to conventional bright field. The quantitative phase image in Fig. 11.25b is generated as described above. During the numerical reconstruction of the image, the angular spectrum is available. In addition to suppressing the dc and twin-image terms, other types of numerical filters can be applied to the angular spectrum to achieve different contrast effects. For example, a numerical filter in the form of $1 - \delta(k_x, k_y)$ suppresses dc background from the image, where k_x and k_y are spatial frequencies. For thin specimen, the resulting intensity image is proportional to $\varphi^2(x, y)$, where φ is the phase profile of the object, minus the overall average phase value. This is equivalent to the image generated by conventional dark-field microscopy,

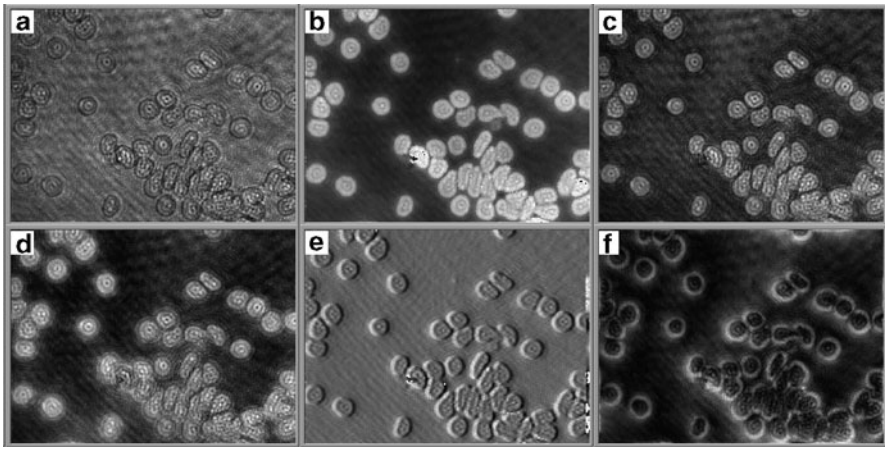

Fig. 11.25 Multimode contrast generation from a single hologram of red blood cells. (**a**) Amplitude contrast, (**b**) quantitative phase contrast, (**c**) dark field, (**d**) Zernike phase contrast, (**e**) DIC, and (**f**) spiral DIC

Fig. 11.25c. Since it cannot distinguish $+\varphi(x,y)$ and $-\varphi(x,y)$, some structural information is lost. If we take instead $1-(1-i)\delta(k_x,k_y)$ as the filter function, then its intensity image is proportional to $[1+\varphi(x,y)]^2$, which is essentially the image obtained by the positive Zernike phase-contrast microscopy (Fig. 11.25d). The polarity can be reversed for negative ZPC by using $1-(1+i)\delta(k_x,k_y)$. For the DIC effect, one takes $\exp\left[2\pi i\left(k_x\Delta_x+k_y\Delta_y\right)\right]$ as the filter, where Δ_x and Δ_y are the lateral shears. Images reconstructed from the filtered and unfiltered spectra are combined, and one can extract an image corresponding to $\varphi\left(x+\Delta_x,y+\Delta_y\right)-\varphi(x,y)$, as shown in Fig. 11.25e. This is equivalent to the conventional DIC. Finally, use of the filter $\exp(i\theta)$, where θ is the polar angle in the frequency domain, leads to an image which corresponds to the convolution of the original image with $r^{-2}\exp(i\theta')$, where r and θ' are the radius and polar angle in real space. This yields the spiral DIC image, which is very sensitive to phase jumps [43], such as at edges (Fig. 11.25f).

These methods of numerical contrast generation are fast, taking only one or a few extra steps of processing in the frequency domain. They preserve full resolution and dynamic range of unfiltered images. If the phase variation is more than 2π, then the contrast generation can produce artifacts, but this can be avoided if the multi-wavelength OPU is used as described above. These methods are to be distinguished with more commonly used image-processing methods that are used mostly on the intensity images, such as edge enhancement, unsharp mask, etc., whereas the above procedures apply only to holographic images represented with complex numbers. Most significantly, all different types of contrast can be generated from a single hologram without requiring different pieces of hardware or their delicate alignment.

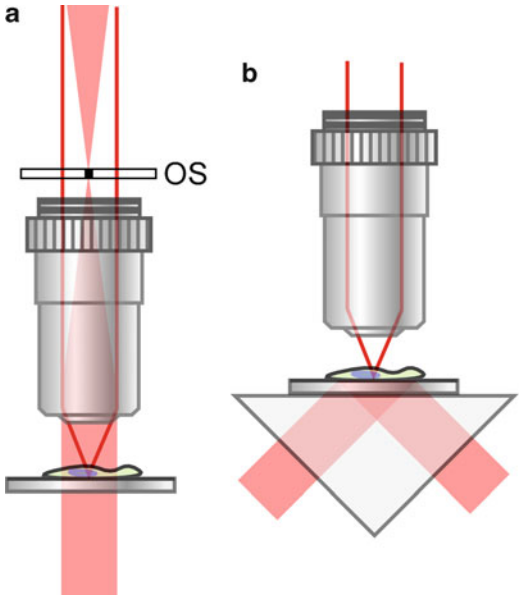

Fig. 11.26 Dark-field illumination for DHM. (**a**) An optical stop (OS) placed at the back focal plane of the objective and (**b**) use of the evanescent field of TIR

11.6.3 Dark-Field DHM

In Fig. 11.26a, dark-field microscopy is achieved by placing an optical stop at the back focal plane of the objective lens [44]. Undiffracted light is blocked, transmitting only diffracted light. The configuration is incorporated in Mach–Zehnder interferometer for digital holography for improved detection of objects smaller than the optical resolution with the refocusing capability yielded by digital holography. Although emulated dark-field digital holography is possible by numerical filtering of the dc component, as we have seen above, the physical stop removes the dc component from the imaging system thus allowing full use of the camera dynamic range for the detection of weak signals, for example, from nanoparticles. Dark-field DH can also be achieved by using the evanescent field of total internal reflection, which was combined with heterodyne DH for high-sensitivity nanoparticle imaging [45–47].

11.6.4 DH Interferometer with a Beam-Splitter Cube

An interesting interferometer configuration is introduced in [48, 49], using a single beam-splitter (BS) cube, Fig. 11.27. A diverging spherical wave from a pinhole illuminates two adjacent sides of the BS with the semireflecting layer oriented along the general direction of the propagation. The two halves of the beam refract

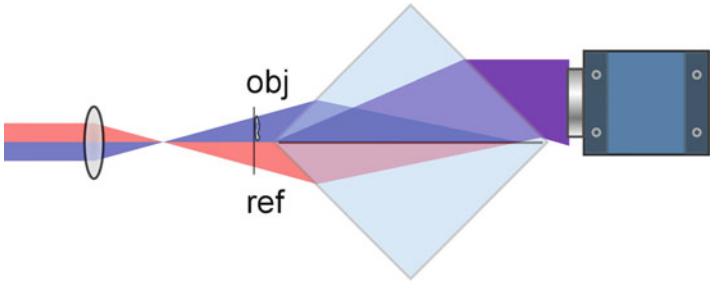

Fig. 11.27 Beam-splitter cube interferometer. The *blue half* and *red half* split and combine to form interference in the *purple region*. One of the halves (*blue*) contains the object and the cube may be tilted slightly for off-axis holography. (Adapted from [49])

from the BS surfaces and transmit through or reflect from opposite sides of the BS's semireflecting hypotenuse, which then combine and exit the BS forming the interference. The sample is placed in the path of one of the half beams. The single-cube beam splitter thus carries out both the beam splitting and beam combining functions simultaneously. The common-path configuration has advantages of simplicity, minimal number of components, insensitivity to vibration, and self-compensation of wave front curvature.

11.6.5 Lens-Free On-Chip Holographic Microscopy

In Fig. 11.28, an incoherent point source illuminates the entire area of a CMOS sensor and the sample plane is placed a short distance (less than a millimeter) from the sensor. The diffraction pattern on the sensor constitutes the in-line hologram with a very large field of view, namely the size of the sensor array (a few millimeters across), laterally separated objects creating uncorrelated subholograms [50]. Polarizers and a thin plate of birefringent crystal is used to establish differential interference. The hologram with the differential interference is then numerically reconstructed, yielding DIC holographic images. Because of the close proximity of the object plane to the sensor plane, the illumination aperture can be large, whereas in conventional lenless holography, the object is placed closer to the aperture for magnification. But the increase in field of view comes at the expense of resolution, which is limited by the pixel size (a few micrometers) of the sensor. To overcome this limitation, super-resolution is obtained by multiple exposure of subpixel shifted holograms [51]. But the hologram shift is achieved not by shifting of the sensor or the object, which requires submicron mechanical precision, but by shifting the illumination aperture. Because of the geometry, shifting of the aperture by 100 μm results in the hologram shift of 0.5 μm. The result is a 0.6 μm resolution over the entire 24 mm^2 field of view.

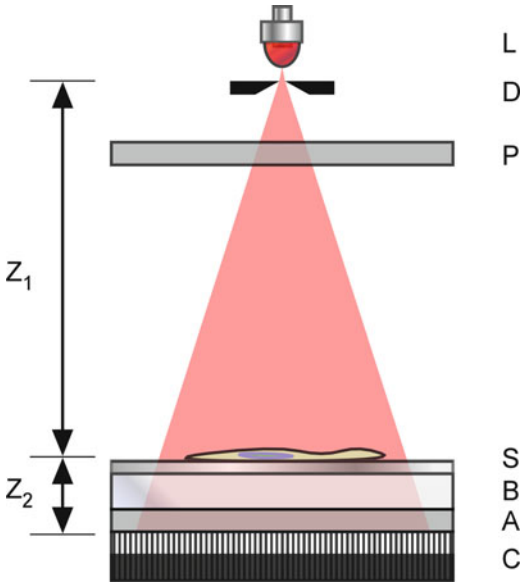

Fig. 11.28 DIC microscopy by lensless holographic imaging. *L* incoherent light source, *D* large aperture pinhole (50–100 μm), *P* polarizer, *S* sample on glass, *B* uniaxial birefringent crystal, *A* analyzer, *C* CCD array. z_1 (5–10 cm) is much larger than z_2 (~1 mm). The orientation of the first polarizer is adjusted to control the differential phase contrast while the analyzer is fixed at ~45° with respect to the birefringent crystal orientation. (Adapted from [50])

11.7 Other Methods of Quantitative Phase Microscopy

11.7.1 Fourier Phase Microscopy

The Fourier phase microscope (FPM) has a configuration that somewhat resembles the Zernike phase microscope but with the spatial phase filter replaced with a spatial light modulator to allow phase-shift image acquisition in a common-path interferometer [52, 53], as depicted in Fig. 11.29. The lens projects a Fourier transform of the input field on the SLM. The undiffracted, zero-frequency component impinges on the central spot on the SLM, and acts as the reference, while the rest of the SLM area receives the higher frequency components containing the structural information of the object. The center spot is phase shifted in four quadrature steps and the resulting four interferograms are combined as in phase-shifting interferometry. Stability of the common-path configuration leads to extremely low noise of 0.15 nm in optical path and the use of low-coherence (but with good spatial coherence by passing through a single mode fiber) illumination field, as opposed to laser radiation, contributes to the sensitivity of the method. Similar concept is implemented with different names, such as the point diffraction interferometer [54] and phase-shifting Gabor holography [55].

11.7.2 Hilbert Phase Microscopy

A Mach–Zehnder interferometer is set up with the object imaged on the CCD at the output plane and the reference tilted at large enough angle so that the interference

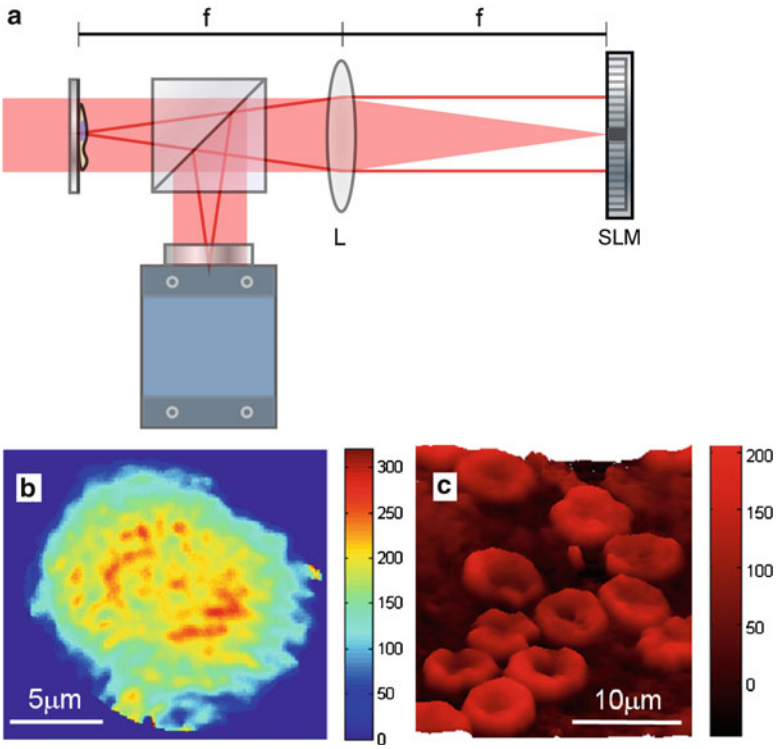

Fig. 11.29 (**a**) Fourier phase microscope. *L* Fourier transform lens, *SLM* spatial light modulator. (Adapted from [52].) (**b**) FPM image of a HeLa cell undergoing mitosis. (**c**) Whole blood smear. The *color bars* represent optical path length in nanometers. (Reprinted from [52] by permission of OSA)

pattern has a high spatial carrier frequency. The phase of the object optical field can be extracted by using the Hilbert transform [56]. The Hilbert phase microscopy (HPM) allows quantitative phase microscopy from single-shot interferograms, with the acquisition rate only limited by the camera speed, but the resolution is limited by the fringe frequency. In [57], the refractive index profile of a HeLa cell was obtained by Hilbert phase microscopy and using a microfluidic chamber, where the cell takes on the known height of the chamber. The technique is used for refractometry of mouse tissue slices of brain, spleen, and liver [58]. The spatial power spectra of the phase images reveal power law behavior with different exponents for each tissue type, which opens a possibility of stain-free characterization and diagnostics of biological structures.

11.7.3 Diffraction Phase Microscopy

In diffraction phase microscopy (DPM) [59], a phase grating is placed at a plane conjugate to the object plane, which generates various diffraction orders (Fig. 11.30).

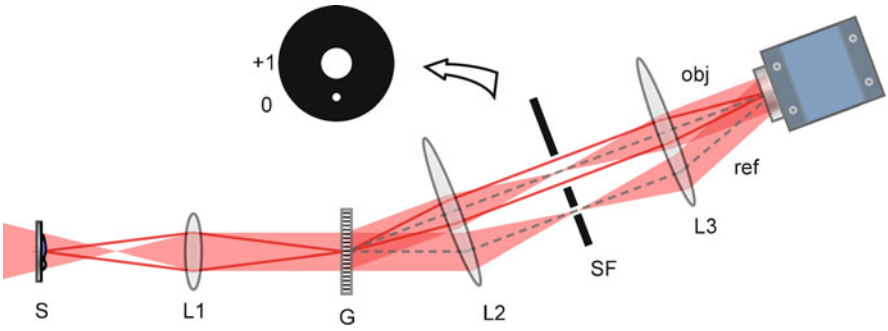

Fig. 11.30 Optical system for diffraction phase microscopy. *S* sample, L_1 imaging lens, *G* grating, L_2 Fourier transform lens, *SF* spatial filter, L_3 inverse Fourier transform lens (Adapted from [59].)

A spatial filter with two apertures is used to select the zero-order and the first-order diffraction. The smaller aperture passes the dc component of the object spectrum, and is used as the reference field, while the larger aperture passes all of the object spectrum. The two components are combined on the CCD plane, and the recorded interference is Hilbert transformed to retrieve the phase profile of the object. The single-shot common-path technique yielded subnanometer optical pathlength-equivalent noise level, and was used to measure the membrane fluctuation of live red blood cells. The technique was combined with epifluorescence microscopy in [60].

11.7.4 Quantitative DIC

An extension of DIC for quantitative phase microscopy uses phase shifting by precise stepping of DIC bias to convert the DIC intensities to linear phase gradients in one shear direction [61]. Orthogonal directions of shear and Fourier space integration using a modified spiral phase transform leads to quantitative phase imaging.

A single-shot linear method uses no polarization optics but places a Ronchi grating a short distance from an intermediate image plane of the object [62]. This generates a zero-order and first-order copies of the image field, which are slightly offset laterally from each other, Fig. 11.31: that is, the lateral shift of DIC is accomplished by the clever arrangement of the grating and the image position, without Wollaston prism or other polarization optics. The spatial filter passes the two diffraction orders, which are combined on the CCD plane, which is focused on the grating plane. The hologram is a superposition of two copies of the object field slightly out of focus and slightly shifted laterally. Digital holography reconstruction yields a DIC-like image, that is, a profile of phase gradient along the shear direction. In order to obtain full 2D phase profile, a 2D Ronchi grating (i.e., a checkerboard pattern) is used to simultaneously record two orthogonal fringes, followed by spiral phase integration of the two orthogonally sheared phase profiles. Increasing the illumination NA also demonstrated optical sectioning property similar to conventional DIC.

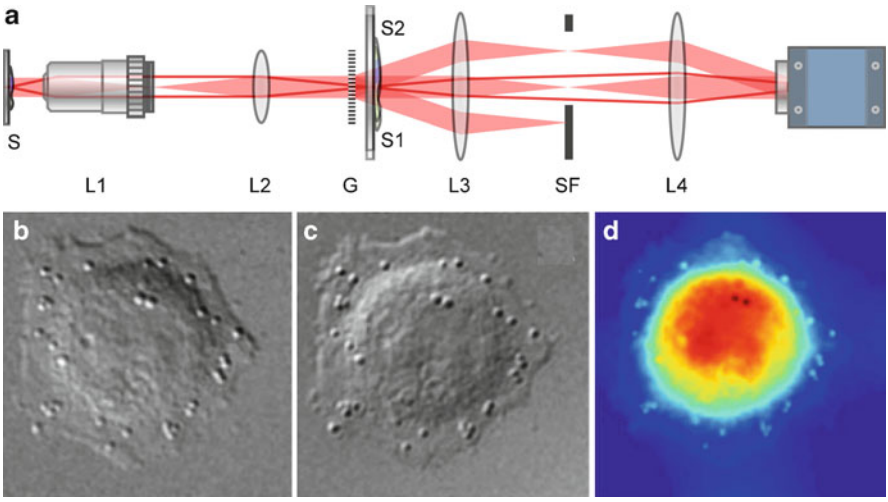

Fig. 11.31 (**a**) Quantitative DIC optical setup. *S* sample, L_1 objective lens, L_2 relay lens, *G* Ronchi grating, S_1 *and* S_2 intermediate image plane containing two (or more) laterally shifted images of the sample, L_3 *and* L_4 Fourier transform lens pair. (Adapted from [62].) (**b**, **c**) A pair of DIC images of a HeLa cell reconstructed from a single exposure hologram. (**d**) 2D unwrapped phase image obtained by spiral integration. (Reprinted from [62] by permission of OSA)

The above technique may be compared with the numerical shearing of digital hologram [63], Fig. 11.32. A phase image from digital holography is numerically sheared, that is, shifted by a small number of pixels, which is then subtracted from the original. The resulting shearogram is integrated along the direction of the shear which produces quantitative phase profile along that direction. Together with another shearogram in the orthogonal direction, a complete 2D phase profile is obtained. A distinct advantage of this and the preceding techniques is that the phase profile does not require unwrapping, as long as the shear is not large enough to introduce phase jump within the shear distance.

11.7.5 Spiral Phase-Contrast Microscopy

The $\pi/2$ phase step at the Fourier plane of conventional PCM is replaced with a spiral (also referred to as vortex, or helical) phase profile of the form $\exp(i\varphi)$, where φ is the polar angle [43]. This leads to convolution of the image with the Fourier transform of the phase function, $\exp(i\varphi)/r^2$. The method uses no polarization optics, is highly sensitive to phase gradients, and, unlike Nomarski DIC, the sensitivity is isotropic and highlights all edges regardless of the direction of the gradient. It is capable of detecting 1% or less of 2π phase jumps. Further manipulation of the center of the phase profile can yield DIC-like images with directional relief effect, but with improved resolution [64]. For phase objects of several wavelengths thickness,

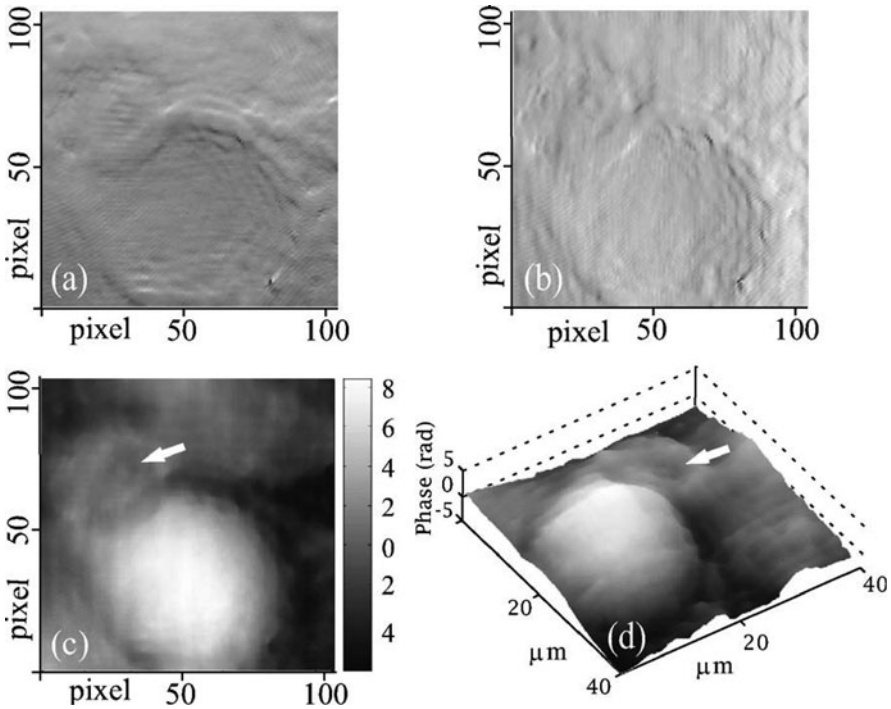

Fig. 11.32 Shearograms of a mouse cell along (**a**) *x* and (**b**) *y* directions. (**c**) 2D phase profile and (**d**) its pseudo-3D rendering. (Reprinted from [63] by permission of OSA)

the spiral phase contrast can also produce spiral contours of the thickness profile [65] (Fig. 11.33). Quantitative phase profile can be achieved by phase-shift spiral phase microscopy by numerical postprocessing of a sequence of at least three shadow-effect images, recorded with different phase offsets between the zero-order Fourier spot, and the remaining, spiral filtered part of the image field [66].

11.7.6 Low-Coherence Interference Microscopy

Low-coherence interference microscopy can generate quantitative phase images by using phase-shifting technique. For example, [67] describes full-field phase-shifting interference microscopy with halogen lamp, where the interferometer also includes a SLD beam detected by a photodiode for active stabilization, to obtain phase noise corresponding to optical path length of 1.3 nm. In [68], a low-coherence light source (halogen lamp with 2 μm coherence length) is used in a Linnik interferometer configuration with phase shifting. For accurate phase shifting with low-coherence light, seven phase steps are acquired and combined. Two phase profiles are obtained, one with double-pass transmission through the specimen (Fig. 11.34a) and one with reflection from within the specimen (Fig. 11.34b),

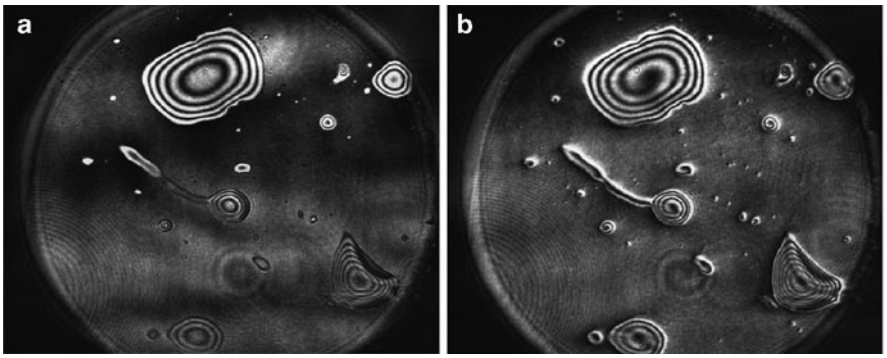

Fig. 11.33 Interferogram of an oil drop smeared on a glass coverslip. (**a**) Normal contourlike interference fringes. (**b**) Spiral interferogram after filtering with the modified spiral phase filter. (Reprinted from [65] by permission of OSA)

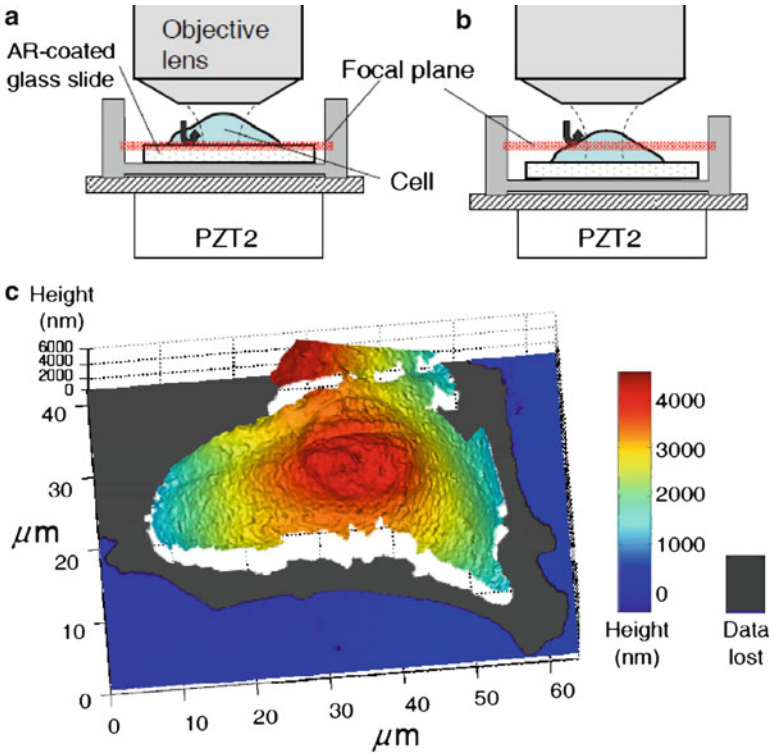

Fig. 11.34 (**a**) Focal condition for measuring the transmission mode phase image, (**b**) focal condition for measuring the reflection mode phase change, and (**c**) quantitative topography of a MCF7 human breast cancer cell surface. (Reprinted from [68] by permission of OSA)

the two modes being separated by virtue of the low coherence. This allowed determination of the physical thickness and refractive index profiles of a MCF-7 human breast cancer cell (Fig. 11.34c).

Phase shifting by piezo-mounted mirror is highly dependent on the wavelength, and therefore can be problematic for broadband source. Achromatic phase shifting is possible by using geometric phase modulator (GPM). A conventional GPM consists of a half-wave plate, sandwiched between two quarter wave plates and two polarizers. Rotation of the half-wave plate determines the amount of phase shift. Use of ferro-electric liquid crystal device in place of the half-wave plate allows fast switching of the phase shift [69].

References

1. G. C. Holst, and T. S. Lomheim, *CMOS/CCD sensors and camera systems* (JCD Publishing, 2007).
2. D. B. Murphy, *Fundamentals of light microscopy and electronic imaging* (Wiley-Liss, 2001).
3. J. Mertz, *Introduction to Optical Microscopy* (Roberts & Co, 2009).
4. W. J. Qu, C. O. Choo, V. R. Singh, Y. J. Yu, and A. Asundi, "Quasi-physical phase compensation in digital holographic microscopy," Journal of the Optical Society of America a-Optics Image Science and Vision **26**, 2005–2011 (2009).
5. J. Garcia-Sucerquia, W. B. Xu, M. H. Jericho, and H. J. Kreuzer, "Immersion digital in-line holographic microscopy," Optics Letters **31**, 1211–1213 (2006).
6. M. Kim, S. Hong, S. Shim, K. Soh, S. Shin, J. Y. Son, J. Lee, and J. Kim, "Plane wave illumination for correct phase analysis and alternative phase unwrapping in dual-type, transmission and reflection. three-dimensional digital holographic microscopy," Optical Engineering **49**, 055801 (2010).
7. B. Kemper, D. Carl, A. Hoink, G. Von Bally, I. Bredebusch, and J. Schnekenburger, "Modular digital holographic microscopy system for marker free quantitative phase contrast imaging of living cells," SPIE **6191**, 61910 T (2006).
8. F. Charriere, B. Rappaz, J. Kuhn, T. Colomb, P. Marquet, and C. Depeursinge, "Influence of shot noise on phase measurement accuracy in digital holographic microscopy," Optics Express **15**, 8818–8831 (2007).
9. B. Bhaduri, N. K. Mohan, and M. P. Kothiyal, "(1, N) spatial phase-shifting technique in digital speckle pattern interferometry and digital shearography for nondestructive evaluation," Optical Engineering **46**, 051009 (2007).
10. T. Lenart, M. Gustafsson, and V. Owall, "A hardware acceleration platform for digital holographic imaging," J. Signal Process. Syst. Signal Image Video Technol. **52**, 297–311 (2008).
11. T. Shimobaba, Y. Sato, J. Miura, M. Takenouchi, and T. Ito, "Real-time digital holographic microscopy using the graphic processing unit," Optics Express **16**, 11776–11781 (2008).
12. C. J. Mann, L. F. Yu, and M. K. Kim, "Movies of cellular and sub-cellular motion by digital holographic microscopy," Biomed. Eng. Online **5**, 21 (2006).
13. T. Nakatsuji, and K. Matsushima, "Free-viewpoint images captured using phase-shifting synthetic aperture digital holography," Applied Optics **47**, D136-D143 (2008).
14. J. Beuthan, O. Minet, J. Helfmann, M. Herrig, and G. Muller, "The spatial variation of the refractive index in biological cells," Physics in Medicine and Biology **41**, 369–382 (1996).
15. E. Cuche, F. Bevilacqua, and C. Depeursinge, "Digital holography for quantitative phase-contrast imaging," Optics Letters **24**, 291–293 (1999).

16. E. Cuche, P. Marquet, and C. Depeursinge, "Simultaneous amplitude-contrast and quantitative phase-contrast microscopy by numerical reconstruction of Fresnel off-axis holograms," Applied Optics **38**, 6994–7001 (1999).
17. J. Kuhn, F. Charriere, T. Colomb, E. Cuche, F. Montfort, Y. Emery, P. Marquet, and C. Depeursinge, "Axial sub-nanometer accuracy in digital holographic microscopy," Measurement Science & Technology **19**, 074007 (2008).
18. C. J. Mann, L. F. Yu, C. M. Lo, and M. K. Kim, "High-resolution quantitative phase-contrast microscopy by digital holography," Optics Express **13**, 8693–8698 (2005).
19. P. Marquet, B. Rappaz, P. J. Magistretti, E. Cuche, Y. Emery, T. Colomb, and C. Depeursinge, "Digital holographic microscopy: a noninvasive contrast imaging technique allowing quantitative visualization of living cells with subwavelength axial accuracy," Opt. Lett. **30**, 468–470 (2005).
20. B. Rappaz, P. Marquet, E. Cuche, Y. Emery, C. Depeursinge, and P. J. Magistretti, "Measurement of the integral refractive index and dynamic cell morphometry of living cells with digital holographic microscopy," Optics Express **13**, 9361–9373 (2005).
21. B. Rappaz, A. Barbul, F. Charriere, J. Kuhn, P. Marquet, R. Korenstein, C. Depeursinge, and P. J. Magistretti, "Erythrocytes analysis with a digital holographic microscope," SPIE **6631**, 66310 H (2007).
22. B. Rappaz, A. Barbul, A. Hoffmann, D. Boss, R. Korenstein, C. Depeursinge, P. J. Magistretti, and P. Marquet, "Spatial analysis of erythrocyte membrane fluctuations by digital holographic microscopy," Blood Cells Mol. Dis. **42**, 228–232 (2009).
23. B. Rappaz, E. Cano, T. Colomb, J. Kuhn, C. Depeursinge, V. Simanis, P. J. Magistretti, and P. Marquet, "Noninvasive characterization of the fission yeast cell cycle by monitoring dry mass with digital holographic microscopy," J. Biomed. Opt. **14**, 034049 (2009).
24. B. Rappaz, F. Charriere, C. Depeursinge, P. J. Magistretti, and P. Marquet, "Simultaneous cell morphometry and refractive index measurement with dual-wavelength digital holographic microscopy and dye-enhanced dispersion of perfusion medium," Optics Letters **33**, 744–746 (2008).
25. B. Kemper, D. Carl, J. Schnekenburger, I. Bredebusch, M. Schafer, W. Domschke, and G. von Bally, "Investigation of living pancreas tumor cells by digital holographic microscopy," J. Biomed. Opt. **11**, 034005 (2006).
26. B. Kemper, and G. von Bally, "Digital holographic microscopy for live cell applications and technical inspection," Applied Optics **47**, A52-A61 (2008).
27. D. Carl, B. Kemper, G. Wernicke, and G. Bally, "Parameter-optimized digital holographic microscope for high-resolution living-cell analysis," Appl. Opt. **43**, 6536–6544 (2004).
28. B. Kemper, S. Kosmeier, P. Langehanenberg, G. von Bally, I. Bredebusch, W. Domschke, and J. Schnekenburger, "Integral refractive index determination of living suspension cells by multifocus digital holographic phase contrast microscopy," J. Biomed. Opt. **12**, 054009 (2007).
29. A. Khmaladze, M. Kim, and C. M. Lo, "Phase imaging of cells by simultaneous dual-wavelength reflection digital holography," Optics Express **16**, 10900–10911 (2008).
30. W. M. Ash, and M. K. Kim, "Digital holography of total internal reflection," Optics Express **16**, 9811–9820 (2008).
31. L. F. Yu, S. Mohanty, J. Zhang, S. Genc, M. K. Kim, M. W. Berns, and Z. P. Chen, "Digital holographic microscopy for quantitative cell dynamic evaluation during laser microsurgery," Optics Express **17**, 12031–12038 (2009).
32. F. Dubois, C. Yourassowsky, O. Monnom, J. C. Legros, O. Debeir, P. Van Ham, R. Kiss, and C. Decaestecker, "Digital holographic microscopy for the three-dimensional dynamic analysis of in vitro cancer cell migration," J. Biomed. Opt. **11**, 054032 (2006).
33. M. Kemmler, M. Fratz, D. Giel, N. Saum, A. Brandenburg, and C. Hoffmann, "Noninvasive time-dependent cytometry monitoring by digital holography," J. Biomed. Opt. **12**, 064002 (2007).

34. A. Ligresti, L. De Petrocellis, D. H. P. de la Ossa, R. Aberturas, L. Cristino, A. S. Moriello, A. Finizio, M. E. Gil, A. I. Torres, J. Molpeceres, and V. Di Marzo, "Exploiting Nanotechnologies and TRPV1 Channels to Investigate the Putative Anandamide Membrane Transporter," PLoS One **5**, 10239 (2010).
35. D. Axelrod, "Cell-Substrate Contacts Illuminated by Total Internal-Reflection Fluorescence," Journal of Cell Biology **89**, 141–145 (1981).
36. A. S. G. Curtis, "Mechanism of Adhesion of Cells to Glass - Study by Interference Reflection Microscopy," Journal of Cell Biology **20**, 199–215amp; (1964).
37. H. Verschueren, "Interference Reflection Microscopy in Cell Biology - Methodology and Applications," Journal of Cell Science **75**, 279–301 (1985).
38. J. Schilling, K. Sengupta, S. Goennenwein, A. Bausch, and E. Sackmann, "Absolute interfacial distance measurements by dual-wavelength reflection interference contrast microscopy," Phys. Rev. E **69**, 021901 (2004).
39. L. Limozin, and K. Sengupta, "Quantitative Reflection Interference Contrast Microscopy (RICM) in Soft Matter and Cell Adhesion," Chemphyschem **10**, 2752–2768 (2009).
40. P. S. Carney, and J. C. Schotland, "Three-dimensional total internal reflection microscopy," Opt. Lett. **26**, 1072 (2001).
41. W. M. Ash, L. G. Krzewina, and M. K. Kim, "Quantitative imaging of cellular adhesion by total internal reflection holographic microscopy," Applied Optics **48**, H144–H152 (2009).
42. C. Liu, Y. S. Bae, W. Z. Yang, and D. Y. Kim, "All-in-one multifunctional optical microscope with a single holographic measurement," Optical Engineering **47**, 087001 (2008).
43. S. Furhapter, A. Jesacher, S. Bernet, and M. Ritsch-Marte, "Spiral phase contrast imaging in microscopy," Opt. Express **13**, 689–694 (2005).
44. F. Dubois, and P. Grosfils, "Dark-field digital holographic microscopy to investigate objects that are nanosized or smaller than the optical resolution," Optics Letters **33**, 2605–2607 (2008).
45. M. Atlan, M. Gross, P. Desbiolles, E. Absil, G. Tessier, and M. Coppey-Moisan, "Heterodyne holographic microscopy of gold particles," Optics Letters **33**, 500–502 (2008).
46. E. Absil, G. Tessier, M. Gross, M. Atlan, N. Warnasooriya, S. Suck, M. Coppey-Moisan, and D. Fournier, "Photothermal heterodyne holography of gold nanoparticles," Optics Express **18**, 780–786 (2010).
47. N. Warnasooriya, F. Joud, P. Bun, G. Tessier, M. Coppey-Moisan, P. Desbiolles, M. Atlan, M. Abboud, and M. Gross, "Imaging gold nanoparticles in living cell environments using heterodyne digital holographic microscopy," Optics Express **18**, 3264–3273 (2010).
48. W. J. Qu, K. Bhattacharya, C. O. Choo, Y. J. Yu, and A. Asundi, "Transmission digital holographic microscopy based on a beam-splitter cube interferometer," Applied Optics **48**, 2778–2783 (2009).
49. W. J. Qu, Y. J. Yu, C. O. Choo, and A. Asundi, "Digital holographic microscopy with physical phase compensation," Optics Letters **34**, 1276–1278 (2009).
50. C. Oh, S. O. Isikman, B. Khademhosseinieh, and A. Ozcan, "On-chip differential interference contrast microscopy using lensless digital holography," Optics Express **18**, 4717–4726 (2010).
51. W. Bishara, T. W. Su, A. F. Coskun, and A. Ozcan, "Lensfree on-chip microscopy over a wide field-of-view using pixel super-resolution," Optics Express **18**, 11181–11191 (2010).
52. G. Popescu, L. P. Deflores, J. C. Vaughan, K. Badizadegan, H. Iwai, R. R. Dasari, and M. S. Feld, "Fourier phase microscopy for investigation of biological structures and dynamics," Optics Letters **29**, 2503–2505 (2004).
53. N. Lue, W. S. Choi, G. Popescu, T. Ikeda, R. R. Dasari, K. Badizadegan, and M. S. Feld, "Quantitative phase imaging of live cells using fast Fourier phase microscopy," Appl. Opt. **46**, 1836–1842 (2007).
54. C. Iemmi, A. Moreno, and J. Campos, "Digital holography with a point diffraction interferometer," Optics Express **13**, 1885–1891 (2005).
55. V. Mico, J. Garcia, Z. Zalevsky, and B. Javidi, "Phase-shifting Gabor holography," Optics Letters **34**, 1492–1494 (2009).

56. T. Ikeda, G. Popescu, R. R. Dasari, and M. S. Feld, "Hilbert phase microscopy for investigating fast dynamics in transparent systems," Optics Letters **30**, 1165–1167 (2005).
57. N. Lue, G. Popescu, T. Ikeda, R. R. Dasari, K. Badizadegan, and M. S. Feld, "Live cell refractometry using microfluidic devices," Opt. Lett. **31**, 2759–2761 (2006).
58. N. Lue, J. Bewersdorf, M. D. Lessard, K. Badizadegan, R. R. Dasari, M. S. Feld, and G. Popescu, "Tissue refractometry using Hilbert phase microscopy," Optics Letters **32**, 3522–3524 (2007).
59. G. Popescu, T. Ikeda, R. R. Dasari, and M. S. Feld, "Diffraction phase microscopy for quantifying cell structure and dynamics," Optics Letters **31**, 775–777 (2006).
60. Y. Park, G. Popescu, K. Badizadegan, R. R. Dasari, and M. S. Feld, "Diffraction phase and fluorescence microscopy," Opt. Express **14**, 8263–8268 (2006).
61. S. V. King, A. Libertun, R. Piestun, C. J. Cogswell, and C. Preza, "Quantitative phase microscopy through differential interference imaging," J. Biomed. Opt. **13**, 024020 (2008).
62. D. Fu, S. Oh, W. Choi, T. Yamauchi, A. Dorn, Z. Yaqoob, R. R. Dasari, and M. S. Feld, "Quantitative DIC microscopy using an off-axis self-interference approach," Optics Letters **35**, 2370–2372 (2010).
63. P. Ferraro, D. Alferi, S. De Nicola, L. De Petrocellis, A. Finizio, and G. Pierattini, "Quantitative phase-contrast microscopy by a lateral shear approach to digital holographic image reconstruction," Optics Letters **31**, 1405–1407 (2006).
64. A. Jesacher, S. Furhapter, S. Bernet, and M. Ritsch-Marte, "Shadow effects in spiral phase contrast microscopy," Phys. Rev. Lett. **94**, 233902 (2005).
65. S. Furhapter, A. Jesacher, S. Bernet, and M. Ritsch-Marte, "Spiral interferometry," Optics Letters **30**, 1953–1955 (2005).
66. S. Bernet, A. Jesacher, S. Furhapter, C. Maurer, and M. Ritsch-Marte, "Quantitative imaging of complex samples by spiral phase contrast microscopy," Optics Express **14**, 3792–3805 (2006).
67. X. H. Li, T. Yamauchi, H. Iwai, Y. Yamashita, H. J. Zhang, and T. Hiruma, "Full-field quantitative phase imaging by white-light interferometry with active phase stabilization and its application to biological samples," Optics Letters **31**, 1830–1832 (2006).
68. T. Yamauchi, H. Iwai, M. Miwa, and Y. Yamashita, "Low-coherent quantitative phase microscope for nanometer-scale measurement of living cells morphology," Optics Express **16**, 12227–12238 (2008).
69. M. Roy, G. Cox, and P. Hariharan, "Low-coherence interference microscopy with an improved switchable achromatic phase-shifter," Opt. Express **13**, 9125–9130 (2005).

Chapter 12
Low-Coherence and Tomographic Techniques

Digital holography using low-coherence light source has distinct imaging characteristics and applications. A number of special techniques have been developed to take advantage of such distinct characteristics of interference by low-coherence light. Topographic and tomographic imaging follow naturally from the well-established and still evolving field of low-coherence interferometry. A very significant contribution by digital holography is the possibility of holographic recording of white light or fluorescence. Although some of the principles have been known in conventional holography, recording of extended objects under white light illumination suffers from precipitous degradation of interference contrast due to noninterfering background. DH-related techniques, such as phase shifting, allow efficient removal of the background. Some of these may develop into powerful and practical new imaging technologies.

12.1 Techniques of Low-Coherence Digital Holographic Microscopy

Holography is a coherent process. The optical path of the object beam has to match that of the reference beam, in order to obtain visible interference fringes. If a source of short coherence length is used, then only the part of the object that matches the reference path within the coherence length produces holographic interference. This is both a problem and advantage. The optical alignment needs to be more precise and the fringe visibility tends to be lower because of the noninterfering background. On the other hand, this also leads to optical sectioning capability, where the holographic reconstruction highlights a section of the object image, while suppressing image of the other parts of the object. It also leads to significant

M.K. Kim, *Digital Holographic Microscopy: Principles, Techniques, and Applications*, Springer Series in Optical Sciences 162,
DOI 10.1007/978-1-4419-7793-9_12, © Springer Science+Business Media, LLC 2011

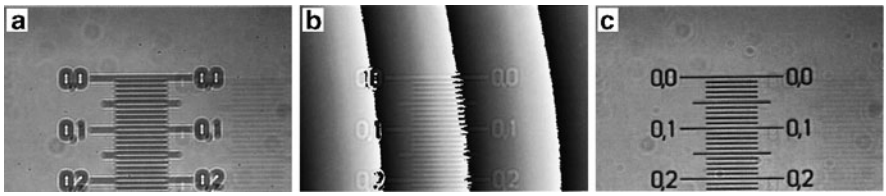

Fig. 12.1 Example of refocusing capability with a digital holography microscope on a metric scale (100 divisions/mm), illuminated with a LED. (**a**) Intensity of the defocus, (**b**) phase of the defocus image, and (**c**) computer-refocused image. The refocus distance is 80 μm. (Reprinted from [1] by permission of OSA)

reduction of the coherent noise due to spurious interference with various surfaces of the optical system, thus improving the quality of the holographic image.

12.1.1 Low-Coherence Sources

Short coherence can arise from short pulse length of the laser light, or a broad spectral width. Useful sources for low-coherence digital holography (LCDH) include femtosecond or picosecond lasers, low-coherence laser diodes (LD), superluminescent diodes (SLD), and high-brightness LEDs. Dubois et al. [1] describe image formation of digital holographic microscopy using low-coherence sources, by spatial filtering a LED. Digitally reconstructed images showed image quality and focusing characteristics similar to white light microscopy, while also providing low-noise quantitative phase images (Fig. 12.1). In [2], a laser diode is used in a lensless holography configuration with temporal phase shifting, to record a hologram at a distance of 45 mm from the object and reconstruct the image that displays sectioning capability of depth close to the coherence length of 20 μm. It is also demonstrated that LCDH can image through a few hundred micrometer depth of scattering medium and produce tomographic images of biological specimen [3]. In [4], an 80-fs laser pulses are used to generate tomographic images of porcine cornea and iris. Another lensless configuration – a Gabor configuration with a point source illumination – with a spatial-filtered LED illumination is also demonstrated to produce proper holographic image [5]. In [6], a red LED and a HeNe laser are compared for digital holographic microscopy, finding that an LED represents a quasi-monochromatic light source of coherence length 16.5 μm, which may be increased by a decrease of the spatial filter pinhole. The dispersion increases effective coherence length, but the contrast of the hologram decreases with imbalance of dispersion between object and reference arms.

Low coherence can be emulated, that is the speckle noise can be reduced, by averaging. For example, in [7], many holograms of the same scene are recorded while a diffuser changes the speckle pattern on the object illumination. Summation of the resulting holograms leads to reduction of speckles and improved resolution in the reconstructed images.

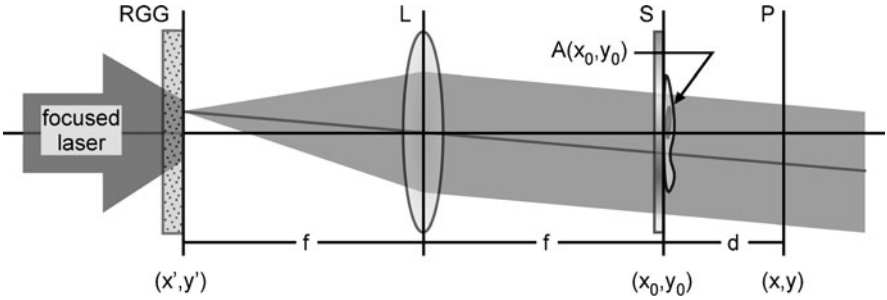

Fig. 12.2 Geometry of partial coherence illumination. *RGG* Rotating ground glass, *L* condenser lens, *S* sample plane, *P* focus plane of the camera. (Adapted from [8])

12.1.2 Rotating Ground Glass

F. Dubois et al. have described a very effective and flexible method for generating partial spatial coherence source by sending a laser beam through a rotating ground glass [8], which was applied to imaging of biological cells as well as for particle flow analysis [9]. If the ground glass rotates fast enough that the phase at any point on it varies over the range $[0, 2\pi]$ during the camera exposure, then these points can be considered completely incoherent with respect to each other: that is, the mutual coherence function over the illuminated area of the (x', y') plane of Fig. 12.2 is a delta function. Consider one such point source illuminating the object plane (x_0, y_0) through the condenser lens L, with both (x', y') and (x_0, y_0) planes positioned at the focal planes of the lens of focal length f. The light arriving at the object plane is a tilted plane wave $\exp[-i(k/f)(x'x_0 + y'y_0)]$. The object has complex transmission coefficient $A(x_0, y_0)$, so that the object wave leaving the (x_0, y_0) plane is

$$E_0(x_0, y_0) = A(x_0, y_0) \exp\left[-i\frac{k}{f}(x'x_0 + y'y_0)\right]. \tag{12.1}$$

This field propagates to the (x, y) plane over a distance z, where the camera is focused. The field at the (x, y) plane is described with the Fresnel diffraction expression

$$\begin{aligned} E(x, y; z) &= -\frac{ik}{z}\exp(ikz)\exp\left[\frac{ik}{2z}x^2\right]\mathcal{F}\left\{A(x_0)\exp\left[-i\frac{k}{f}x'x_0\right]\exp\left[\frac{ik}{2z}{x_0}^2\right]\right\}[k_x], \\ &= -\frac{ik}{2\pi z}\exp(ikz)\exp\left[\frac{ik}{2z}x^2\right]\mathcal{F}\{A(x_0)\}[k_x] \odot \mathcal{F}\left\{\exp\left[\frac{ik}{2z}{x_0}^2\right]\exp\left[-i\frac{k}{f}x'x_0\right]\right\}[k_x], \end{aligned} \tag{12.2}$$

where we again abbreviate the (y)-terms for brevity and also make use of the convolution theorem. The first Fourier transform is the object spatial frequency

spectrum $\tilde{A}(k_x, k_y)$, with $k_x = kx/z$ and $k_y = ky/z$, and the second Fourier transform is easily calculated so that

$$\begin{aligned} E(x,y;z) &= -\frac{ik}{2\pi z}\exp(ikz)\exp\left[\frac{ik}{2z}x^2\right]\tilde{A}(k_x)\odot\frac{iz}{k}\exp\left[-\frac{iz}{2k}\left(\frac{k}{f}x'+k_x\right)^2\right], \\ &= \frac{1}{2\pi}\exp(ikz)\exp\left[\frac{ik}{2z}x^2\right]\iint \mathrm{d}k_x'\tilde{A}(k_x')\exp\left[-\frac{iz}{2k}\left(\frac{k}{f}x'+k_x-k_x'\right)^2\right], \\ &= \frac{1}{2\pi}\exp(ikz)\exp\left[-\frac{izk}{2f^2}x'^2-\frac{ik}{f}x'x\right]\mathcal{F}^{-1}\left\{\tilde{A}(k_x')\exp\left[-\frac{iz}{2k}k_x'^2\right]\right\}\left[\frac{z}{f}x'+x\right]. \end{aligned} \tag{12.3}$$

The reference field $E_\mathrm{R}(x,y;z)$, in a Mach–Zehnder interferometer, is equivalent to a copy of this field (12.3) but without the modulation by the object $A(x_0, y_0)$, so that

$$\begin{aligned} E_\mathrm{R}(x,y;z) = {} & \frac{1}{2\pi}\exp(ikz)\exp\left[-\frac{izk}{2f^2}x'^2-\frac{ik}{f}x'x\right] \\ & \times\mathcal{F}^{-1}\left\{\delta(k_x')\exp\left[-\frac{iz}{2k}k_x'^2\right]\right\}\left[\frac{z}{f}x'+x\right]. \end{aligned} \tag{12.4}$$

The fields interfere and the camera records the summation of all intensities contributed by the incoherent source points on the (x', y') plane with a distribution $P(x', y')$

$$\begin{aligned} I(x,y;z) &= \iint \mathrm{d}x'P(x')|E+E_\mathrm{R}|^2, \\ &= \frac{1}{4\pi^2}\iint \mathrm{d}x'P(x')\left|\mathcal{F}^{-1}\left\{\left[\tilde{A}(k_x')+\delta(k_x')\right]\exp\left[-\frac{iz}{2k}k_x'^2\right]\right\}\left[\frac{z}{f}x'+x\right]\right|^2. \end{aligned} \tag{12.5}$$

Through the use of phase-shifting method, one of the holographic terms can be extracted

$$\begin{aligned} I^+(x,y;z) &= \frac{1}{4\pi^2}\iint \mathrm{d}x'P(x')\mathcal{F}^{-1}\left\{\tilde{A}(k_x')\exp\left[-\frac{iz}{2k}k_x'^2\right]\right\}\left[\frac{z}{f}x'+x\right], \\ &= -\frac{1}{4\pi^2}\frac{f}{z}P'\odot\mathcal{F}^{-1}\left\{\tilde{A}(k_x')\exp\left[-\frac{iz}{2k}k_x'^2\right]\right\}(x), \end{aligned} \tag{12.6}$$

where

$$P'(x) = P\left(-\frac{f}{z}x\right). \tag{12.7}$$

The spectrum of $I^+(x;z)$ is

$$\tilde{I}^+(k_x,k_y;z) = -\frac{1}{4\pi^2}\frac{f}{z}\tilde{P}'(k_x)\left\{\tilde{A}(k_x)\exp\left[-\frac{iz}{2k}{k_x}^2\right]\right\}. \tag{12.8}$$

The quantity in the curly bracket is the spectrum one obtains at the (x,y) plane if the object is illuminated with a normally incident plane wave. This spectrum is multiplied, that is, low-pass filtered, by the spectrum of the scaled illumination profile $P'(x,y)$. For example, take

$$P(x) = \exp\left[-\frac{x^2}{a^2}\right] \tag{12.9}$$

so that

$$\tilde{P}'(k_x) = \frac{a^2z^2}{2f^2}\exp\left[-\frac{a^2z^2}{4f^2}{k_x}^2\right], \tag{12.10}$$

which is a Gaussian of width $\Delta k_x = 2f/az$. The low-pass filter becomes narrower as the refocus distance z increases. If we take the threshold of resolution loss to be where the quadratic phase in (12.8) becomes π, then the effective coherence length of the source is

$$z_{\max} = \frac{2f^2}{\pi k a^2}. \tag{12.11}$$

The effective coherence length can be adjusted by varying the laser spot size a on the ground glass. Figure 12.3 shows reconstructed images at three distances and two different spot sizes. Larger spot size reduces spurious interference as well reducing the depth of focus, as expected of a low-coherence source.

12.1.3 Fresnel Incoherent Correlation Holography

In [10], a SLM under a computer control is used as a diffractive optical element (DOE). The DOE is in effect a superposition of a plane mirror and a quadratic phase function, by sharing 50/50 portions of all the pixels. For better clarity, Fig. 12.4 illustrates the principle of Fresnel incoherent correlation holography (FINCH) assuming a transmissive SLM, which acts as if a superposition of a plane window and a converging lens. An object is illuminated with a white light and a color filter narrows the bandwidth enough for proper operation of the DOE. Upon transmission through the SLM, the light from a point scatterer on the object results in two

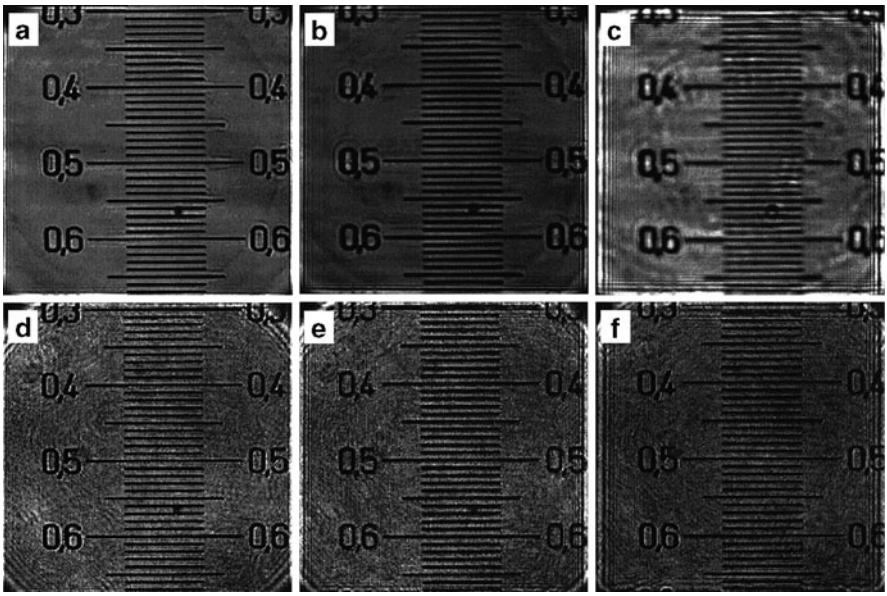

Fig. 12.3 Refocusing property and spatial coherence. (**a**–**c**) Are with speckle size of 12 μm (low coherence), while (**d**–**f**) are with speckle size of 200 μm (high coherence). The refocus distances for each row are $d = 50$, 100, and 200 μm. (Reprinted from [8] by permission of OSA)

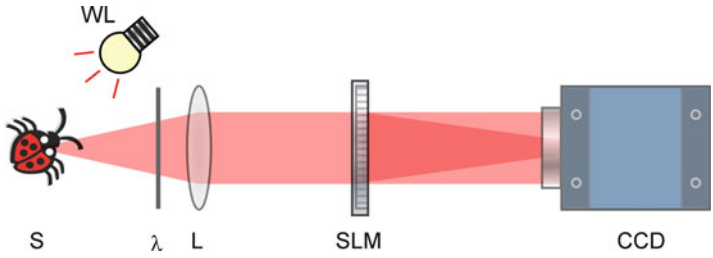

Fig. 12.4 FINCH optical setup. *WL* white light source, *S* sample object, λ color filter, *L* lens, *SLM* spatial light modulator, *CCD* camera

components, one a collimated beam without deflection and the other a converging spherical wave. The two components are coaxial and therefore produces a Fresnel zone interference pattern, which can be recorded by a camera and numerically reconstructed to form a point image. For an extended object under spatially incoherent illumination, the Fresnel zones superpose incoherently, rapidly reducing the fringe contrast. This has been known to be a common problem in many of the incoherent holography techniques. Again, numerical processing by digital holography provides a powerful solution to an old problem. Phase shifting is applied by introducing a relative phase between the plane and quadratic phase parts of the

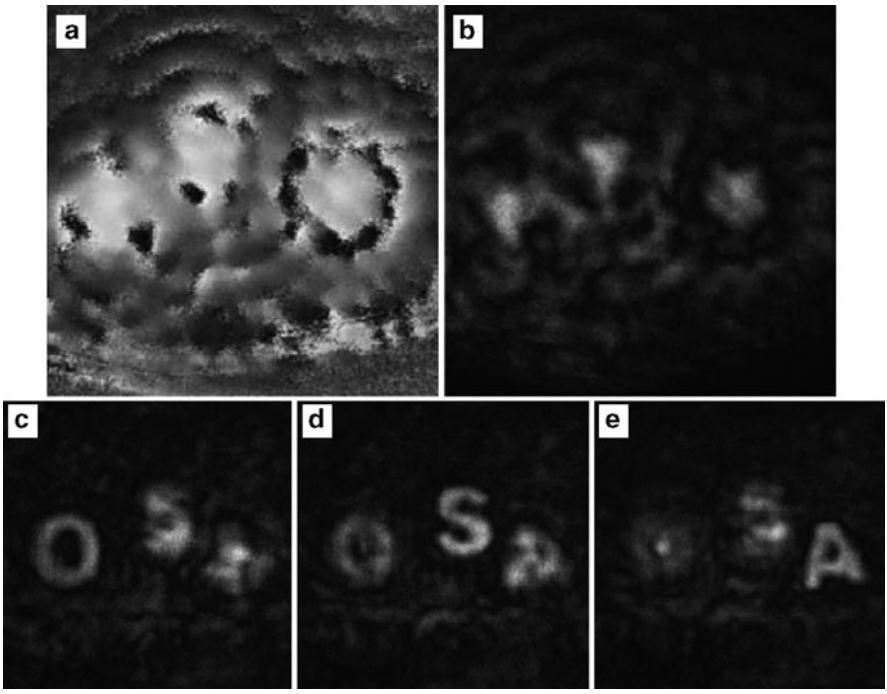

Fig. 12.5 Holographic imaging of 3D objects under white light illumination by FINCH. (**a**) Amplitude and (**b**) phase of the complex hologram. (**c**–**e**) Show reconstruction at different distances. (Reprinted from [10] by permission of OSA)

DOE, and taking several exposures while stepping the phase shift. This eliminates the dc and conjugate terms from the Fresnel zones, yielding a complex hologram corresponding to a single conjugate term (Fig. 12.5). Image reconstruction proceeds as in ordinary digital holography. Numerical focusing of objects at different distances under arc lamp illumination have been clearly demonstrated. Holographic recording and imaging of multicolor fluorescence has been demonstrated as well (Fig. 12.6) [11, 12].

12.1.4 Achromatic Fringe System

We may note some of the low coherence techniques developed for conventional holography. In the achromatic fringe system of Fig. 12.7, a collimated beam illuminates a diffraction grating G at plane P_1 [13]. The lens L_2 focuses various diffraction orders on the plane P_2, where a pair of pinholes select two of the diffraction orders. The hologram is recorded on the plane P_4, which is the image of the grating formed by the lens L_2. The image is in fact a superposition of the two

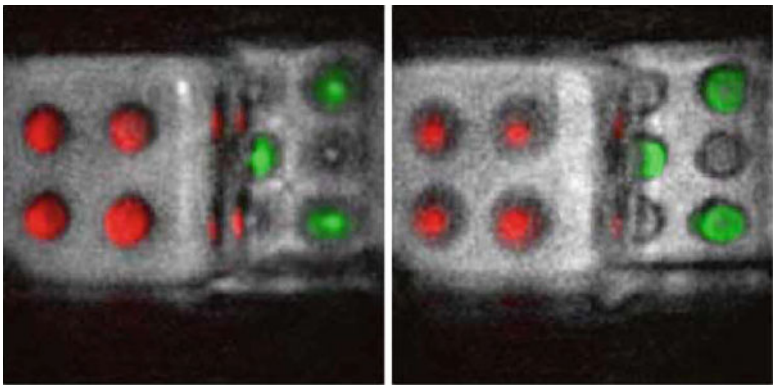

Fig. 12.6 Holographic imaging of fluorescent color 3D objects by FINCH. (Reprinted from [11] by permission of OSA)

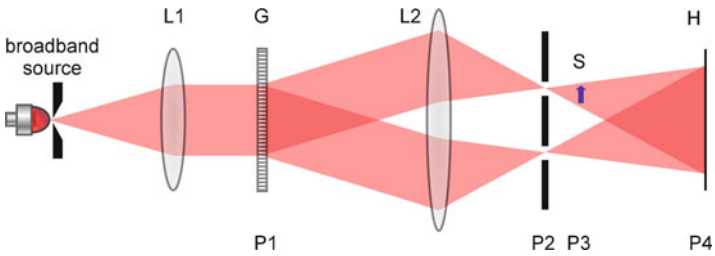

Fig. 12.7 Grating achromatic interferometer. (Adapted from [13])

diffraction orders. The image formation does not depend on the wavelength. A transparency or silhouette placed at P_3 in front of one of the pinholes modifies one of the grating images, thus recording the information as a modulated fringe on P_4, as in ordinary off-axis hologram. But the coherence requirement is only similar to Gabor hologram, much less stringent than ordinary off-axis hologram.

12.1.5 Triangular Interferometer

A triangular interferometer is depicted in Fig. 12.8, which contains two lenses L_1 and L_2 of respective focal lengths f_1 and f_2 separated by a distance $f_1 + f_2$. If an object is placed at the front focal plane A of f_1, then an image of magnification $-f_2/f_1$ forms at the plane B, which is a focal plane of L_2. But if A also happens to be a focal plane of f_2, then another image of magnification $-f_1/f_2$ forms on B. If the field on A is a spherical wave from a point source, then the field on B is an interference of two spherical waves of different curvatures, resulting in a Fresnel zone pattern (FZP), which can be used to form a holographic image of the original

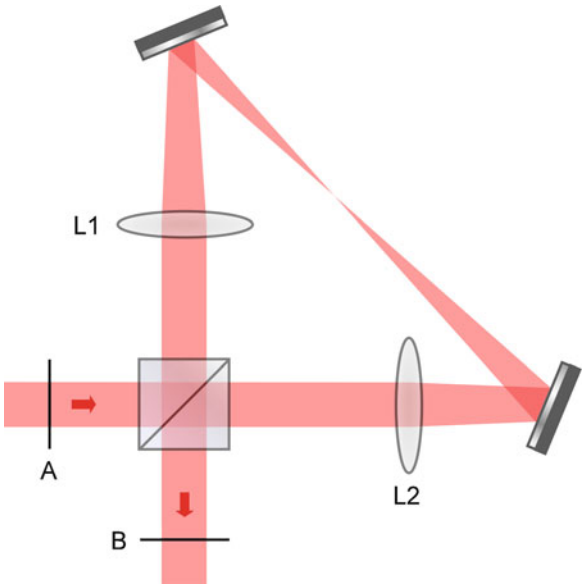

Fig. 12.8 Triangular interferometer. Each of A and B is a focal plane of both L_1 and L_2, which are separated at confocal distance through the hypotenuse

point source [14]. A serious drawback is that as more point sources are added, the various FZP's add incoherently, adding dc background and twin-image contributions. A digital holography demonstration of the concept, with phase shifting by using discrete polarization components and multiple cameras, has been demonstrated to significantly reduce the dc and twin problems [15].

12.1.6 Conoscopic Holography

In conoscopic holography, a cone of light emitted from each object point passes through a length of birefringent crystal. If the crystal axis is along its length, the ordinary rays propagate with isotropic speed forming spherical waves. But extraordinary rays have speed that depends on the direction of propagation, forming elliptic wavefronts. The two polarization components emerge from the crystal as two approximately spherical waves of different curvatures, thus forming Fresnel zone pattern. Hologram of two pinholes illuminated by a sodium lamp has been formed and reconstructed by HeNe laser [16]. But as the number of object points increase, contrast of the incoherent hologram decreases rapidly, because of the dc background. For an extended 2D object, the zone patterns from all the object points add incoherently. By using additional polarization and amplitude masks, several holograms are digitally combined to remove the dc and conjugate terms [17]. Two-dimensional test pattern is correctly reconstructed by digital holography. This is another example of digital holography making possible what is very difficult in conventional holography.

12.2 Optical Scanning Holography

12.2.1 Basic Principles of OSH

The optical scanning holography (OSH) is a unique method of hologram generation [18–20]. In standard holography methods, the interference of the plane reference wave and the spherical wavelets from each object point generates Fresnel zone pattern, which is recorded by an image sensor. The OSH turns the process around: a Fresnel zone pattern is projected on an object and the pattern is 2D scanned across the object, while a single point detector collects the light scattered by the whole object. The photo-current from the detector is filtered and processed to generate a pattern equivalent to the ordinary hologram, as described below. At the cost of some complexity of the system and the requirement of mechanical scanning, the method has unique capabilities and imaging characteristics.

For a basic OSH system (Fig. 12.9) the illumination is provided by an interference between a plane wave and a spherical wave, with a frequency offset between them. The spherical wave on an xy-plane a distance z from the center of curvature at $(x_0, y_0, 0)$ is in the form, with paraxial approximation,

$$E_1 = \exp\left\{\frac{ik}{2z}\left[(x - x_0)^2 + (y - y_0)^2\right] - i\omega t\right\}. \tag{12.12}$$

The plane wave is incident normally on the plane and so its phase is uniform but oscillates in time

$$E_2 = \exp\{-i(\omega + \Omega)t\}, \tag{12.13}$$

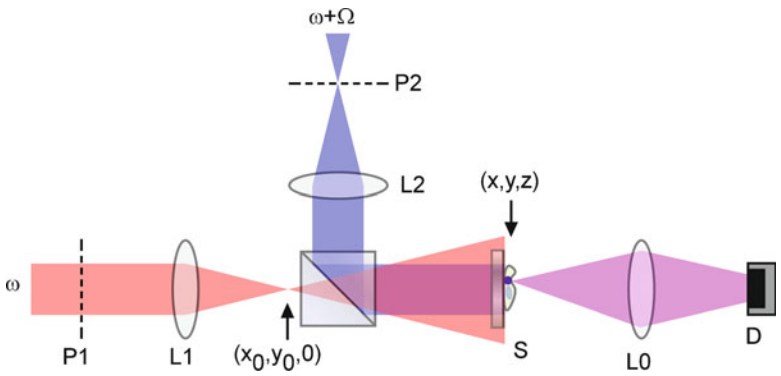

Fig. 12.9 Basic OSH system optical setup. P_1 *and* P_2 pupil planes, L_0, L_1, *and* L_2 lenses, *BS* beam combiner, *S* sample object, *D* detector

where Ω is the frequency offset between the two waves. For simplicity, we set the amplitudes equal to one. The intensity distribution is then given by

$$I(x,y,z;t) = |E_1 + E_2|^2 = 2 + 2\cos\left\{\frac{k}{2z}\left[(x-x_0)^2 + (y-y_0)^2\right] + \Omega t\right\}, \quad (12.14)$$

which is a Fresnel zone pattern (FZP) that appears to diverge from or converge toward the center at (x_0, y_0) because of the frequency offset Ω. Now suppose a point object is located at (x, y, z), and it reflects or scatters in proportion to the incident field. A lens collects some portion of the reflected/scattered light and focuses on a detector. The detector is a single point detector but collects light from an aperture of finite area. The electrical signal from the detector is then proportional to $I(x, y, z; t)$, which is processed through a lock-in detector. That is, the signal is multiplied with $\sin\Omega t$ and $\cos\Omega t$ followed by low-pass filtering, to generate the two phase-quadrature signals:

$$\begin{aligned} S_c &= \langle I(t)\cos\Omega t\rangle = \cos\left\{\frac{k}{2z}\left[\left(x-x_0{}^2\right) + \left(y-y_0{}^2\right)\right]\right\}, \\ S_s &= \langle I(t)\sin\Omega t\rangle = -\sin\left\{\frac{k}{2z}\left[\left(x-x_0{}^2\right) + \left(y-y_0{}^2\right)\right]\right\}. \end{aligned} \quad (12.15)$$

These signals can now be digitized and combined as

$$S = S_c - iS_s = \exp\left\{\frac{ik}{2z}\left[\left(x-x_0{}^2\right) + \left(y-y_0{}^2\right)\right]\right\}. \quad (12.16)$$

The process is repeated as the center (x_0, y_0) of the projected FZP is scanned in 2D, and the resulting 2D array of complex numbers $S(x_0, y_0)$ is equivalent to the spherical wavefront centered at (x, y, z). Once this complex hologram, which contains no zero-order or twin-image terms [21], is acquired, the numerical diffraction can be applied to reconstruct the image of the object point at any distance. Extension of the description to an extended object consisting of a set of object points is straightforward, because all the relevant terms are linear with respect to E_1.

12.2.2 Imaging Characteristics of OSH

With the OSH, it is possible to control the degree of spatial coherence of the image. As described above, when a detector with a narrow aperture is used at the focal plane of the collection lens L_0, it only collects plane waves propagating from the object along the optical axis. The imaging characteristics is similar to

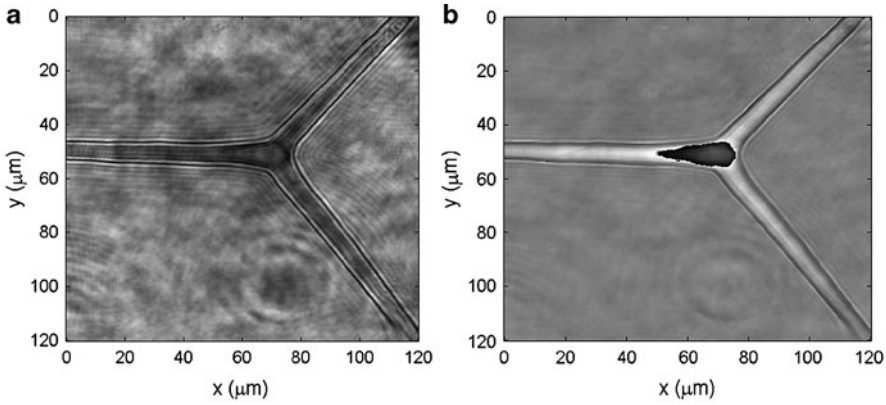

Fig. 12.10 Reconstruction of a hologram recorded in coherent mode. The object is a siliceous three-pronged spongilla spicule. (**a**) Absolute value of the reconstruction amplitude and (**b**) wrapped phase map of the optical thickness of the object relative to the mounting medium. (Reprinted from [22], under OpenAccess)

illumination of the object with a collimated laser in a conventional microscope. For example, the phase modulation of the plane wavefront by the presence of a phase object, such as a cell, allows quantitative phase microscopy, as in the conventional digital holography [22] (Fig. 12.10). On the other hand, if the detector aperture is enlarged, then it collects a large range of spatial modes, analogous to the illumination of the object with a broad source in a conventional microscope. In conventional microscopy, the spatial coherence of the image is controlled by the aperture of the illumination, whereas in OSH it is controlled by the aperture of the detector. The ability of OSH to record in an incoherent mode is one of its most significant attributes. The incoherent imaging mode has the characteristics of the low-coherence DH described in the previous section, such as the reduction of speckle noise and reduction of spurious interference noise from out-of-focus planes. Furthermore, the incoherent mode OSH allows holographic imaging of fluorescence [23, 24].

The frequency offset may be set up using a pair of AOMs as in heterodyne DH. It is simplest but least efficient to 2D-scan the FZP by translation of the object. Scanning by galvo-mounted mirrors and telecentric optics, as in confocal microscopy, would provide much improved scanning. In the basic OSH description above, the illumination is provided by the interference between a plane wave and a spherical wave. Other combinations are also possible. For example, by placing an annular aperture at the pupil plane P_1, an edge detection effect may be obtained [25]. It has been shown that if the plane wave is replaced with another spherical wave but with opposite curvature from the other, then the resulting PSF has improved lateral resolution by a factor of 2 and the depth of focus increases by an order of magnitude for extended focus imaging [26, 27].

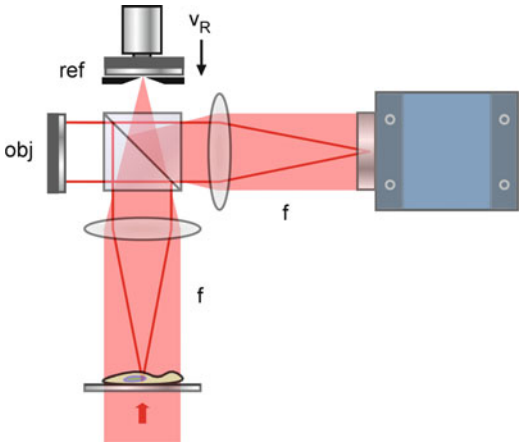

Fig. 12.11 Spatio-temporal holography. The object and the camera are at focal distance from the respective lenses, as well as the object and reference mirrors. The object mirror forms an image of the object at the camera, whereas the pinhole aperture on the reference mirror performs a spatial filtering. The reference mirror is *z*-scanned at a constant speed. (Adapted from [28])

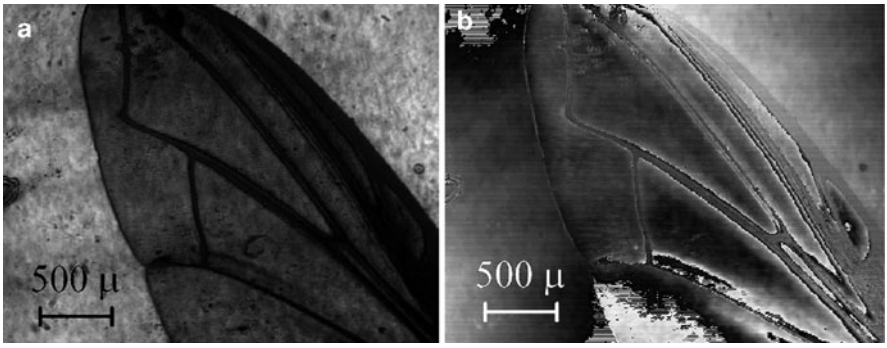

Fig. 12.12 Reconstructed wave front of a fly wing recorded behind a diffuser. (**a**) amplitude and (**b**) phase. (Reprinted from [29] by permission of OSA)

12.2.3 Related Techniques and Applications

The concept of two-pupil optical processing is found in a few different techniques, as well as in OSH. For example, in the system referred to as spatio-temporal digital holography (STDH) [28, 29], the optical field from the object is split into two parts. One is used to form an image of the object, while the other is spatial-filtered to transmit the zero-order component (Fig. 12.11). The two parts combine and interfere, while the reference is scanned axially at a constant speed to introduce a Doppler frequency. From the series of interferograms recorded by the camera, the time series of each pixel is demodulated to generate complex holograms. Both amplitude and phase-contrast images of an object behind diffusing medium are obtained (Fig. 12.12).

Similar strategy of interfering two copies of the same field is found in a number of low-coherence and common-path techniques. For example, the FINCH

technique that we described in the previous section has similarity with STDH, and some differences. The STDH involves spatial filtering and pixelwise heterodyne detection, while the FINCH uses pixelwise Fresnel zone pattern formation and temporal phase shifting. The Fourier phase microscopy and diffraction phase microscopy of Sect. 11.7 also have the similar concept of interference of the object field with the reference field, the latter obtained by spatial filtering of the former.

12.3 Optical Coherence Tomography

Optical coherence tomography (OCT), a scanning low-coherence interferometry technique, was introduced around 1990 by J. Fujimoto [30, 31] and A.F. Fercher [32]. Since then it has developed into a robust, mature biomedical imaging tool. We highlight some of the main techniques and newer developments of OCT. There are a number of books and review articles [33] one can consult.

12.3.1 Time-Domain OCT

For a Michelson interferometer illuminated with a monochromatic source, the detected signal $S(z)$ is proportional to

$$S(z) = S_0 + S_1 \cos 2k(z - z_R) \tag{12.17}$$

where S_0 and S_1 are constants, z and z_R are the object point and reference mirror distances, respectively, and $k = 2\pi/\lambda$. If the source has short coherence, either because it is a short pulse or because it has broad spectrum, the interference signal is modulated by an envelope of a width equal to the coherence length, with the center of the envelope at $z = z_R$. Therefore, the low coherence interferometry can be used to measure the axial distance of the object point. In the original time-domain OCT (TDOCT) (Fig. 12.13), the reference mirror is scanned at a constant speed $z_R = v_R t$, so that the interference signal is time-dependent

$$S(t) = S_0 + S_1 \cos 2k(z - v_R t) = S_0 + S_1 \cos 2(kz - \Omega t). \tag{12.18}$$

That is, the object field is heterodyned at the Doppler frequency $\Omega = \omega v_R/c$, where ω is the frequency of the light. Low-pass filtering of the heterodyne signal then yields the envelope function. Thus, the z-scan of the reference mirror provides the Doppler shift for heterodyne signal generation, as well as the scan across the depth of the object for tomographic imaging. In analogy with ultrasound imaging system, the z-scan is also referred to as the A-scan. In a typical OCT system, the object beam is also scanned in a lateral direction, for example, x-direction, to produce x–z tomographic section image – this is called the B-scan.

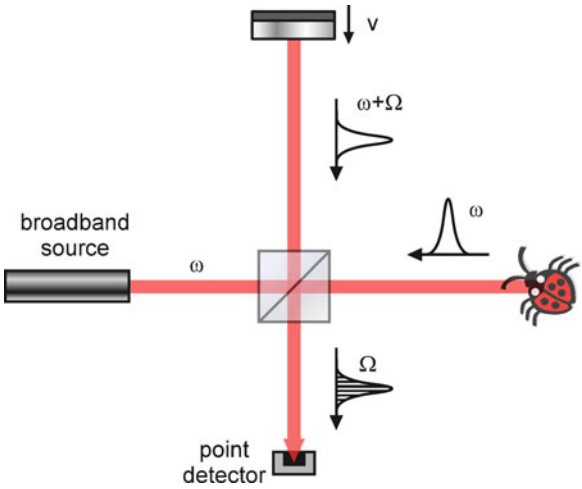

Fig. 12.13 Time-domain OCT

The interferometric and heterodyne signals from OCT are compatible with efficient electronic processing and lead to high dynamic range and sensitivity, exceeding 100 dB. Imaging of weakly scattering structures even in a scattering environment is possible, enabling noninvasive, in situ, and in vivo optical biopsy. Another advantage of OCT is the decoupling of the lateral and axial resolutions, the former determined by the NA of the imaging system, while the latter is determined by the coherence length of the light source. In practice, the NA is kept relatively low, in order to maintain uniform focus along the depth of the object. A main limitation of TDOCT is the mechanical z-scan of the reference mirror.

12.3.2 Fourier-Domain OCT

The interference term in (12.17) is sinusoidal with respect to the distance $(z - z_R)$ with a period equal to the wavelength $2\pi/k$. But it is also sinusoidal with respect to k with a period $2\pi/(z - z_R)$. If one uses a broadband source and a spectrometer is placed in the detection arm while the reference mirror is kept stationary, then the detected spectrum as a function of k is the Fourier transform of the object reflectance as a function of the axial distance. A 1D CCD array can be used to image the spectrum, and computation of its Fourier transform yields the A-scan. There is no mechanical motion for the A-scan, while the lateral scan can proceed as in TDOCT, thus providing much faster overall scan speed. This is called spectral domain OCT (SDOCT) (Fig. 12.14a). Instead of the broadband source and the spectrometer, a similar effect can also be achieved by using a wavelength-tunable light source and a single detector. The system is then referred to as the wavelength-scanning or swept-source OCT (SSOCT) [34] (Fig. 12.14b). For wavelength scanning, a tunable laser can be used, or an acousto-optical tunable filter is used on a white light source.

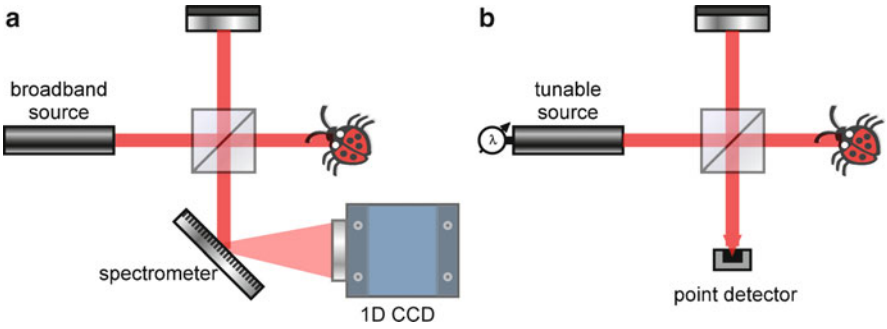

Fig. 12.14 (**a**) Spectral domain OCT (SDOCT) and (**b**) Swept source OCT (SSOCT)

The SDOCT and SSOCT together are sometimes referred to as Fourier-Domain (or frequency-domain) OCT (FDOCT).

The imaging characteristics of SDOCT are similar to TDOCT, but there are some differences. The axial scan range and the axial resolution in TDOCT are given by the mechanical scan range of the reference mirror and the coherence length of the light, respectively. In SDOCT, on the other hand, the axial range is proportional to $\lambda^2/\delta\lambda$, where $\delta\lambda$ is the wavelength resolution of the spectrometer. Similarly, the axial resolution is $\lambda^2/\Delta\lambda$, where $\Delta\lambda$ is the full wavelength range of the spectrometer, assuming that the spectrum of the light source covers that range. More significantly, it is shown that the SNR of SDOCT is better than TDOCT by a factor $\sqrt{N}$, where $N = \Delta\lambda/\delta\lambda$ is the number of detector elements on the spectrometer [35].

12.3.3 Doppler OCT

If a scatterer within the object volume is in motion, then its reflection generates Doppler shift in addition to that of the moving reference mirror [36]. This shows up as a phase change between two consecutive A-scans, and can be the basis of high-speed, high-sensitivity velocity measurement. Blood flow in human skin has been imaged with sensitivity of 10 μm/s [37].

12.3.4 Optical Coherence Microscopy

In order to improve the lateral resolution, one may use a large NA objective and the object 2D-scanned laterally, called the C-scan. The system is then referred to as optical coherence microscopy (OCM). For example, the lateral resolution of OCT in retinal imaging is typically 10–30 μm, which is insufficient to resolve the retinal cone mosaic. Retinal cone mosaic imaging was demonstrated by using a larger NA beam, performing C-scans, and imaging the periphery of the fovea, where the

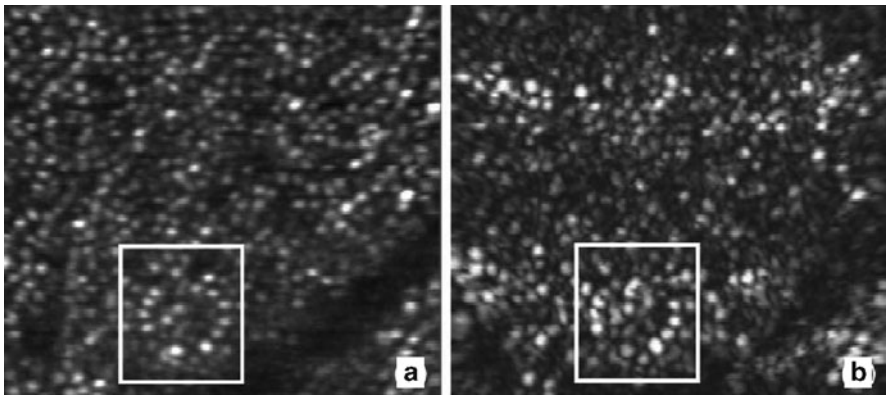

Fig. 12.15 Transverse images of human retina centered at ~4° nasal. (**a**) SLO (scanning laser ophthalmoscope) and (**b**) OCM images. The image size is 200 × 225 μm. (Reprinted from [38] by permission of OSA)

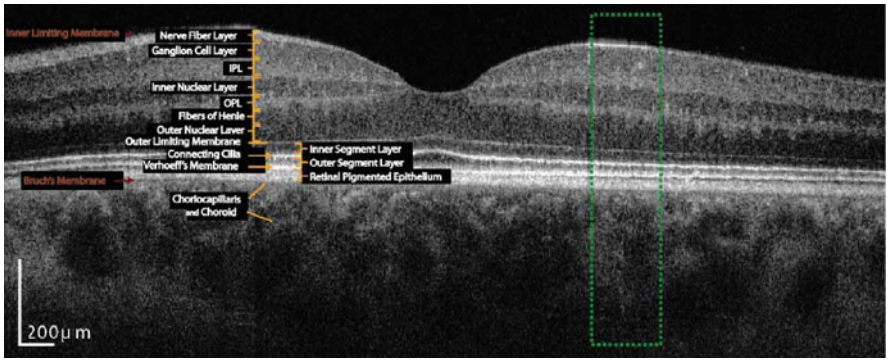

Fig. 12.16 High-resolution B-scan of retinal structures acquired with adaptive optics OCT instrument scanning 6 mm lateral range (4,000 A-scans). The following retinal layers are identified: Nerve fiber layer (NFL), Ganglion cell layer (GCL), Inner plexiform layer (IPL), Inner nuclear layer (INL), Outer plexiform layer (OPL), Fibers of henle with outer nuclear layer (ONL), Inner segment layer (ISL), Outer segment layer (OSL), Retinal pigment epithelium (RPE), Choriocapillaris and Choroid. The Outer Limiting Membrane (sometimes called External Limiting Membrane), Connecting Cilia and Verhoeff's Membrane may also be seen. (Reprinted from [39] by permission of OSA)

retinal cell spacing is somewhat larger [38] (Fig. 12.15). In ophthalmic imaging, however, higher-NA illumination for tighter focusing can aggravate the ocular aberration. Application of adaptive optics in ophthalmic OCT imaging has been demonstrated to reduce the aberration and improve the lateral resolution [39] (Fig. 12.16).

12.3.5 Phase-Sensitive OCT

In addition to the interference envelope, one can interrogate the phase of the interference signal for phase-sensitive OCT. This may be accomplished by phase-shifting techniques [40] or by Hilbert transform [41]. Then it is possible to probe subwavelength optical path-length variations within the coherence thickness of the object volume. Interpretation of the phase variation, however, may not be straightforward, except for simpler cases, for example, due to surface profile behind uniform index material.

12.3.6 Differential Phase-Contrast OCT

Differential phase-contrast (DPC) OCT uses two transversally separated beams of orthogonal polarizations [42]. Alternatively, two overlapping object beams with orthogonal polarizations are used with slightly different focal spot sizes [43]. The two interference signals are detected and processed separately to obtain phase signals, difference of which constitutes the DPC signal. Phase differences between the two sample beam components can be caused by transverse refractive-index variations within the medium in front of the back-reflecting interface. Also, depth variations of the back-reflecting interface or variations of the phase change on back-reflection, for example, at different metallic surfaces, can give rise to phase differences. The sample beam with the larger focal spot can be regarded as a reference for the other beam and provides the path length of the light that traverses the surrounding area of the small spot. Hence the path-length difference between the small spot beam and its surrounding is measured and imaged. DPC image of human microvascular endothelial cells showed clear DIC-like phase contrast (Fig. 12.17). Phase steps below scattering medium was also detected by DPC-OCT.

12.3.7 Phase-Dispersion Microscopy

Phase-dispersion microscopy (PDM) is a scanning microscopy technique, based on measuring the phase dispersion between the fundamental and the second-harmonic light [44]. The Michelson interferometer is illuminated with overlapping fundamental and second-harmonic output from a low-coherence Ti:sapphire laser. A constant motion of the reference mirror creates heterodyne signals for both wavelengths, which are detected separately. Bandpass filtering and Hilbert transform then yields the phase difference between the object and reference arms for each of the wavelengths. Because of the exact double frequency of the second harmonic, the two phase values can be combined to eliminate all noise that is due to optical path-length fluctuations. PDM was used to measure the refractive-index dispersion (10^{-4}) of very dilute DNA-water solutions (1%) and to generate clear contrast between the white matter and gray matter of a brain tissue microtome section.

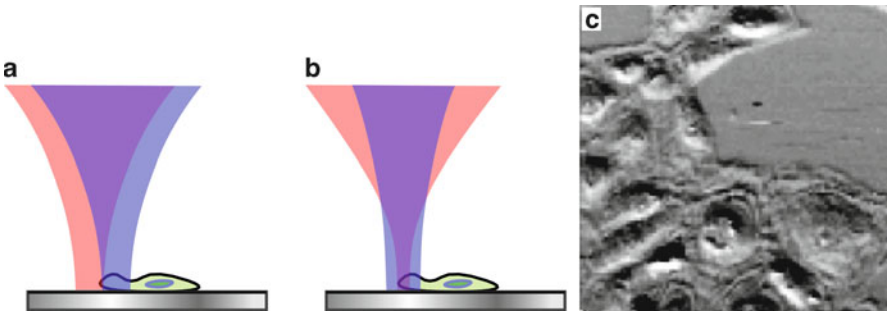

Fig. 12.17 Differential phase contrast by two orthogonal polarization components (**a**) with lateral shift or (**b**) with different focus. (**c**) DPC-OCT image of human microvascular endothelial cells. (Reprinted from [43] by permission of OSA)

In phase-dispersion optical tomography (PDOT), the principle of PDM is applied to OCT configuration with axial scan of the object [45]. PDOT is capable of detecting phase shift that is due to reflection at an interface or dispersion of a bulk material, even when the target is below the surface.

12.3.8 Phase-Referenced Interferometry

Detection of submicron motion is important for the study of subcellular dynamics, such as actin-based transport of organelles, ruffling of cell membranes, and motility of metastatic cells. In phase-referenced interferometry (PRI) in [46], an OCT interferometer is simultaneously illuminated with a laser of 775 nm and a SLD of 1,550 nm. The laser sets up interference of reference and the top surface of a cover glass, while, by way of the short coherence, the SLD has interference only with the sample specimen below the cover slip. The reference mirror is dithered and the heterodyne signals for the two wavelengths are detected separately. If the SLD wavelength is exactly twice the laser wavelength, the two signals can be combined so that any interferometer drift or fluctuations of the relative distance between the object and reference arms exactly cancel, as long as the specimen-to-cover slip distance remain constant. The system allowed measurement of axial motion with ~1 nm/s sensitivity, stable over many minutes.

12.4 Full-Field Optical Coherence Tomography

12.4.1 Principles of FFOCT

In full-field (or wide-field) optical coherence tomography (FFOCT), the process of coherence detection is carried out in parallel of all the pixels. A basic configuration in Fig. 12.18 is a Michelson interferometer using a low-coherence light source and

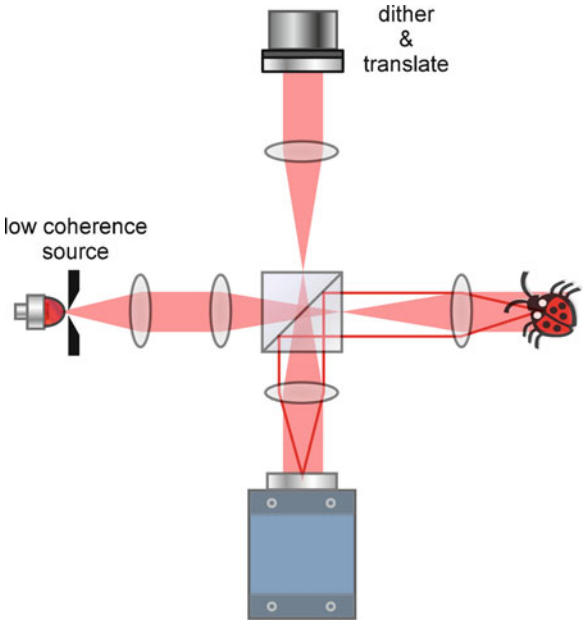

Fig. 12.18 Full-field OCT optical setup

phase-shifting interference technique. The interference signal is generated from points within the volume of the object that lie within the coherence length of the light source relative to the reference mirror surface. The interference signal can be extracted and the background suppressed by using the phase-shifting method, which allows tomographic imaging within scattering media. Microscope objective is added to the object arm for magnification and a matching objective is required in the reference arm for precise matching of the optical path lengths, so that one obtains the Linnik interferometer configuration. The phase shifting can be achieved by dithering of the reference mirror. In the original FFOCT experiment by Boccara et al., use of Michelson objective precluded piezo dithering; instead they used polarization modulation using photoelastic modulator [47].

Compared to the pointwise detection OCT, the camera-based FFOCT cannot acquire signals fast enough for conventional lock-in detection. Instead of synchronous detection of conventional lock-in amplifier, a technique of synchronous illumination is developed that collects and integrates time-varying parts of the image into phase-quadrature components. The synchronous illumination can be achieved by piezo-modulation of reference mirror while the light source is pulsed during appropriate quarter period of the modulation [48, 49] (Fig. 12.19).

Using a thermal light source (a tungsten halogen lamp) in [50], 3D tomographic images of a tadpole eye is obtained, with 3 μm lateral and 1 μm axial resolution (Fig. 12.20). A camera running at 200 fps and four frame captures per phase-shifting cycle results in 50 tomographic image acquisition per second. Averaging over 1 s for each section resulted in close to 80 dB SNR. Use of polarization components also allows tomography of birefringence in muscle tissues [51].

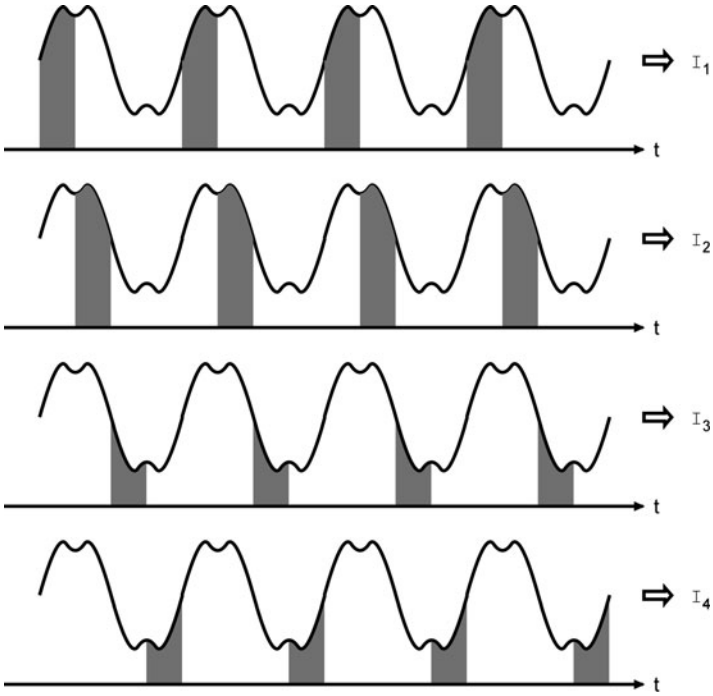

Fig. 12.19 Synchronous illumination detection. The *shaded areas* represent the periods when the illumination is on and the graphs plot the intensity variation of a pixel as the reference mirror dithers sinusoidally. The intensity of the shaded areas is accumulated during a camera exposure and stored as one of the four phase-quadrature images. (Adapted from [49])

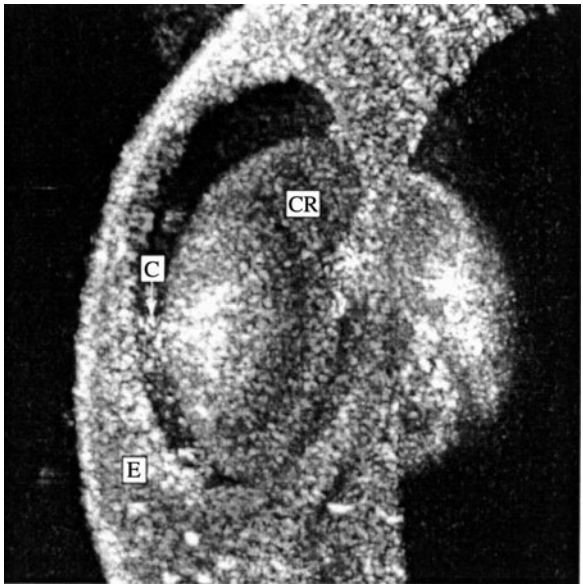

Fig. 12.20 3D reconstruction of a Xenopus laevis tadpole eye by means of 300 tomographic images. The volume is 360 × 360 × 200 μm^3. *E* exterior of the eye, *C* cornea, *CR* crystalline lens. (Reprinted from [50] by permission of OSA)

12.4.2 Techniques and Applications of FFOCT

Various light sources have been used for FFOCT, including LEDs [47, 52], femtosecond lasers [53], tungsten lamp [50, 54], and SLDs [55]. The technique of rotating ground glass has been used along with heterodyne generation of phase shift using two AOMs in [56].

Salathe et al. constructed a smart pixel array for 58 × 58 pixel parallel heterodyne detection [57]. Three-dimensional images are obtained at a sensitivity of 258 dB and a rate of 6 Hz. The method is effective for imaging through a turbid medium (intralipid solution) as well [58]. In [59], they have achieved 25 Hz video rate imaging of 210 × 210 × 80 μm^3 volume with 58 × 58 × 58 voxels. The resolution was 9 μm lateral and 3 μm axial and the sensitivity 76 dB.

Phase shifting is also achieved by a two camera system with liquid crystal shutters and a dithering reference mirror [55]. In [52], four phase-quadrature images are generated using quarter-wave plates, which are imaged on the four quadrants of a single camera, allowing video rate acquisition of the complete phase-shift image sets, but at the expense of resolution. An achromatic phase modulator operating on the geometric phase uses a pair of ferro-electric liquid crystal devices in [60].

In [61], a set of three FFOCT images of a colored object is generated using red, green, and blue LEDs, which are numerically combined and rendered to produce natural color 3D tomography (Fig. 12.21). That is, three sets – red, green, and blue – of image volumes are obtained by FFOCT, as displayed in the first three columns. These are then numerically combined into RGB images as shown in the fourth column. The first two rows show example cross-sections and the bottom row shows flat view, that is, accumulation of all the cross-sections. On the lower right corner is the picture of the painted surface of a coin being imaged.

A swept-source version of FFOCT has been demonstrated in [62] using a common-path interferometer, where the first air–glass interface serves as the reference reflection, and the specimen mounted on the other side of the coverslip provides the object reflection. A SLD transmitted through a tunable fiber Fabry–Perot filter provides the swept source. As the wave number k sweeps over a range, the axial distance of each object point is coded as the interference signal as a function of k. The Fourier transform over k then produces the signal strength as a function of distance. The phase profile of a coherence-sectioned plane then yields the optical thickness variations at the plane, such as due to presence of cells and other materials (Fig. 12.22).

In [63], the object is line-illuminated along x-direction with a cylindrical lens and the reference arm has a grating in Littrow configuration for retro-reflection with a time delay across y-direction (Fig. 12.23). In a manner analogous to light-in-flight holography, the high-speed CMOS then has x vs. time delay interference signal on its face, which, together with phase shifting by a dither of the grating, produces a B-scan tomographic image. Scan of the line-illumination across the object surface then yields a 3D volumetric tomogram. The system is used to image

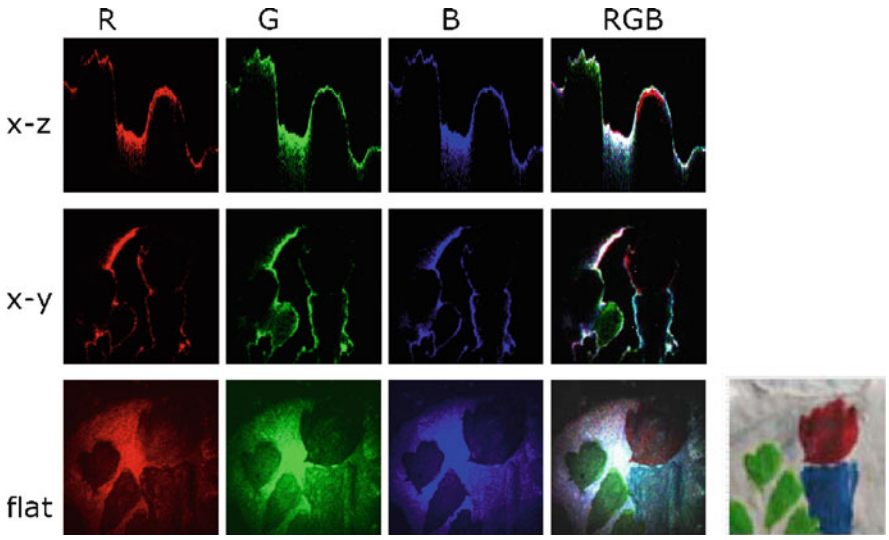

Fig. 12.21 Full-color full-field OCT of a painted coin surface [61]

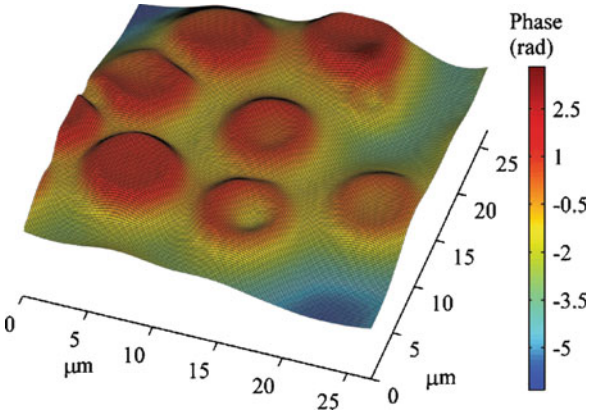

Fig. 12.22 Swept-source FFOCT of red blood cells. (Reprinted from [62] by permission of OSA)

a human finger pad in vivo at six volume images per second with 76 dB sensitivity (Fig. 12.24).

High-resolution subcellular-level imaging of human donor corneas is obtained using thermal light source and piezo-driven phase-shift method in a Linnik interferometer [64]. A lateral resolution of 2.4 μm and axial resolution of 2.0 μm were achieved. In [65], a method for automatic synchronization of the pulsed illumination and the Doppler frequency of the z-scanning reference mirror is proposed, which allowed ~800 μm/s scan speed. The synchronization was achieved by an auxiliary interferometer whose reference moves in tandem with the OCT interferometer and is illuminated with a cw LD of a similar wavelength.

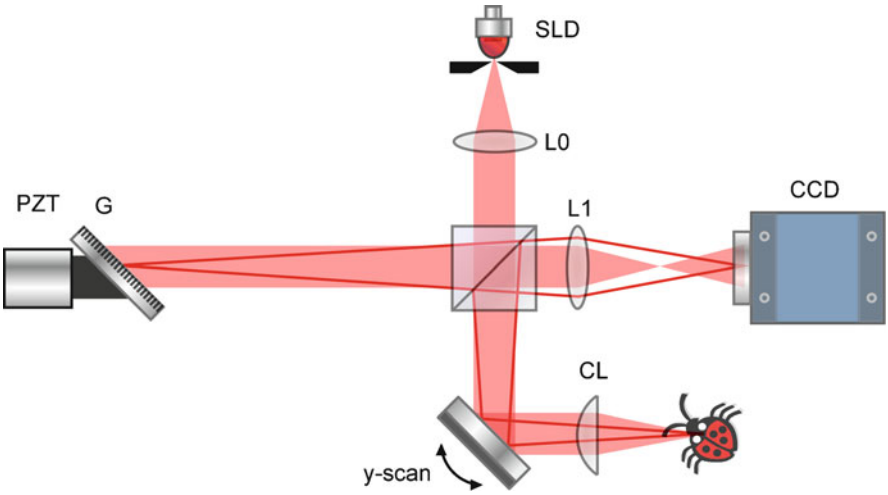

Fig. 12.23 3D axial-lateral, parallel time-domain OCT. *SLD* superluminescent diode, L_0 collimating lens, *G* Littrow grating mounted on PZT, *CL* cylindrical lens. The *solid lines* are the imaging rays. (Adapted from [63])

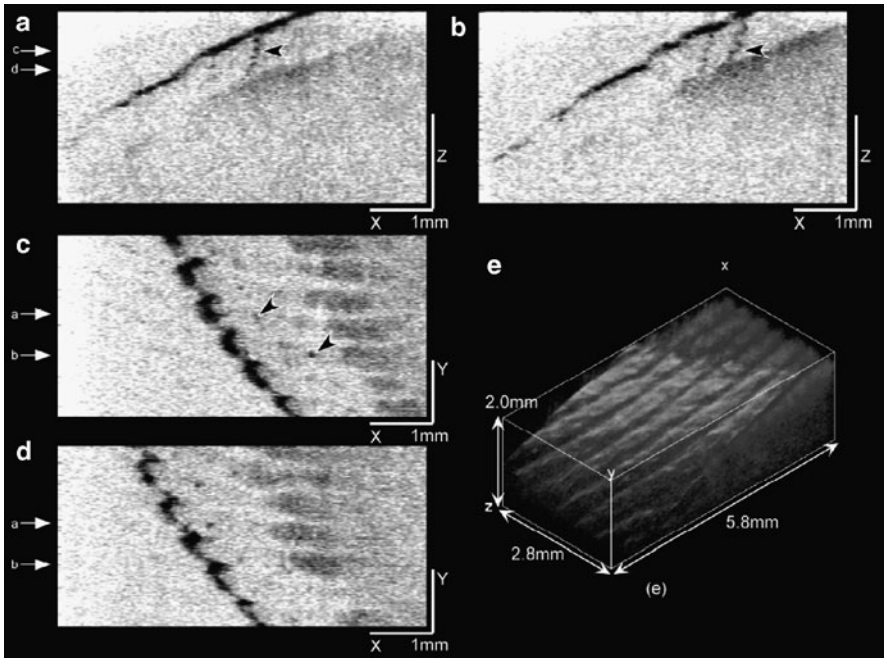

Fig. 12.24 3D OCT images of a human finger pad in vivo: (**a**, **b**) longitudinal OCT images in the *X*–*Z* plane, (**c**, **d**) transverse OCT images. The *white arrows* indicate the cross-sectional positions. (**e**) Volume-rendered image. The volume size was 5.8 × 2.8 × 2.0 mm^3. (Reprinted from [63] by permission of OSA)

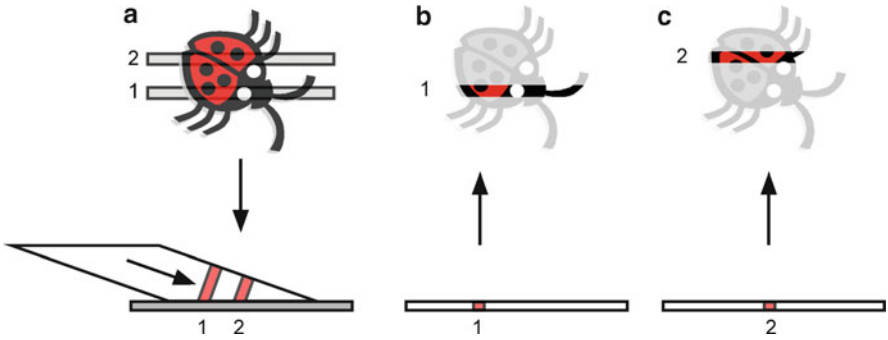

Fig. 12.25 Light-in-flight holography. (**a**) When the reference arrives at the positions 1 or 2 on the hologram, the object field from the slice 1 or 2, respectively, also arrives at the hologram. (**b**) Reconstruction using the strip 1 or 2 of the hologram results in the image of slice 1 or 2, respectively, of the object

12.4.3 Light-in-Flight Digital Holography

Light-in-flight holography (LIF) [66, 67] uses short coherence light and oblique incidence reference beam. Various parts of the reference beam arrives on the hologram plane at different times, and interferes with the various parts of the object beam arriving at the hologram that happen to be coincident within the coherence length. In Fig. 12.25, the delay between the object and reference is such that when the reference arrives at the positions 1 or 2 on the hologram, the object field from the slice 1 or 2, respectively, also arrives at the hologram. The entire 3D object volume is holographically stored to form varying contour or cross-sectional images of an object on various parts of a single hologram. When the strip at position 1 or 2 is used to reconstruct, holographic image of the slice 1 or 2 is formed, respectively. A DH analog of LIF was demonstrated in [68]. Because of the low resolution of CCD array, it is not possible to use an oblique reference. Instead, a blazed grating for Littrow reflection can be used for the reference, so as to achieve linearly varying time delay across the reference beam diameter [69] (Fig. 12.26). Various contours of a lightbulb reconstructed from different parts of a single CCD-acquired hologram is shown in Fig. 12.27 [70].

12.5 Digital Interference Holography

12.5.1 Principles of DIH

Figure 12.28 illustrates the general principle of digital interference holography (DIH) [71]. Suppose an object is illuminated by a laser beam of wavelength λ. A point P (at $\mathbf{r}_P$) on the object scatters the illumination beam into a Huygens

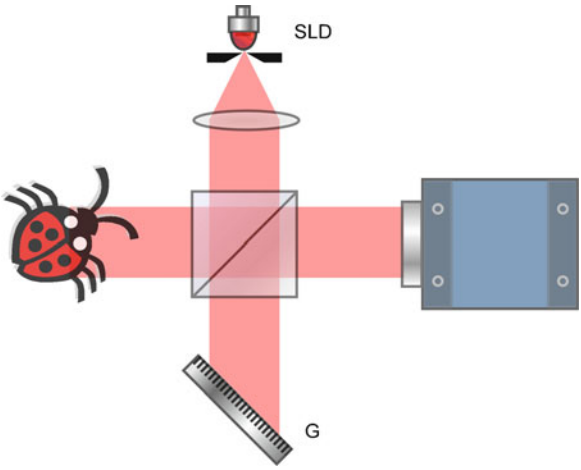

Fig. 12.26 Optical configuration for DH LIF using Littrow grating

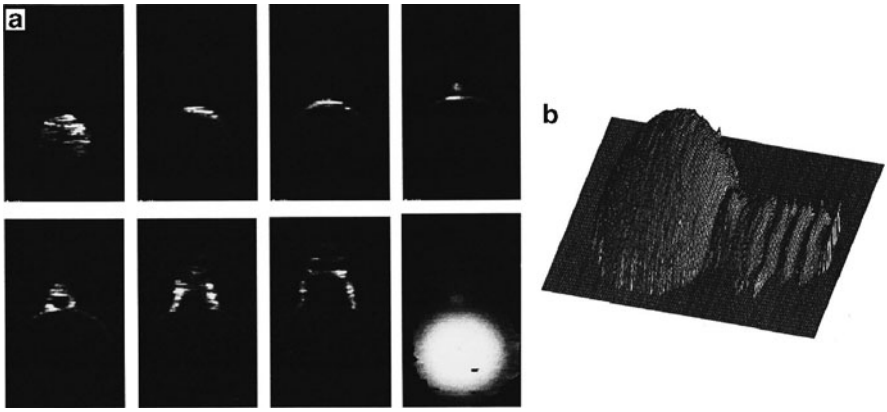

Fig. 12.27 (**a**) Digital LIF recording of a lightbulb, showing object contours reconstructed from different parts of the CCD, representing different depths. In the *lower right* corner, a gray-scale-coded depth map is shown. (**b**) Evaluated 3D shape of a lightbulb. (Reprinted from [70] by permission of SPIE)

wavelet, $A(\mathbf{r}_\mathrm{P})\exp(ik|\mathbf{r}-\mathbf{r}_\mathrm{P}|)$, where $A(\mathbf{r}_\mathrm{P})$is proportional to the amplitude and phase of the scattered wavelet. For an extended object, the field at $\mathbf{r}$ is

$$E(\mathbf{r}) \sim \int A(\mathbf{r}_\mathrm{P})\exp(ik|\mathbf{r}-\mathbf{r}_\mathrm{P}|)\mathrm{d}^3\mathbf{r}_\mathrm{P}, \tag{12.19}$$

where the integral is over the object volume. The amplitude and phase of this field at the hologram plane $z = 0$ is recorded by the hologram. If the holographic process

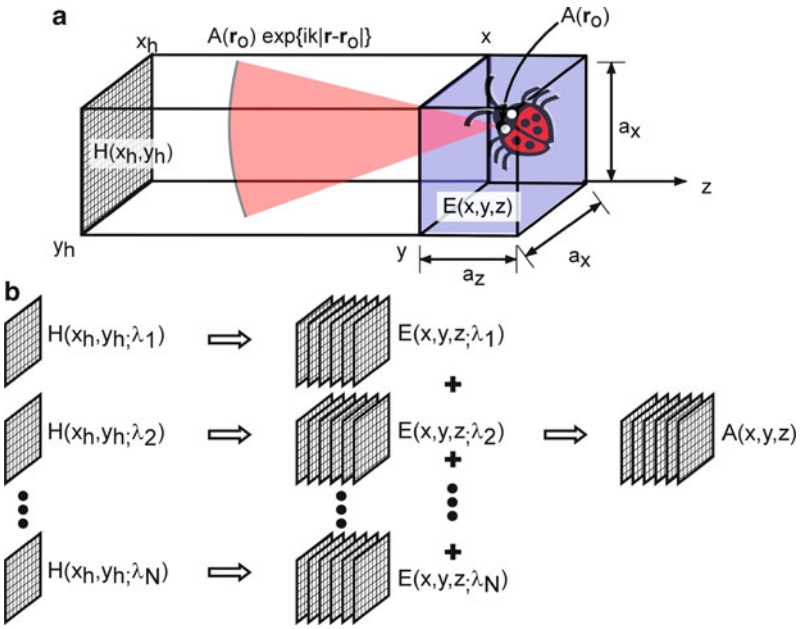

Fig. 12.28 (**a**) Geometry and (**b**) process of DIH. *H* hologram, *E* optical field in the object volume, *A* object function. See text for details

is repeated using N different wavelengths, and the reconstructed fields are all superposed together, then the resultant field is

$$E(\mathbf{r}) \sim \sum_k \int A(\mathbf{r}_\mathrm{P}) \exp(ik|\mathbf{r}-\mathbf{r}_\mathrm{P}|)\mathrm{d}^3\mathbf{r}_\mathrm{P} \sim \int A(\mathbf{r}_\mathrm{P})\delta(\mathbf{r}-\mathbf{r}_\mathrm{P})\mathrm{d}^3\mathbf{r}_\mathrm{P}$$
$$\sim A(\mathbf{r}). \tag{12.20}$$

That is, for a large enough number of wavelengths, the resultant field is proportional to the field at the object and is nonzero only at the object points. In practice, if one uses a finite number N of wavelengths at regular intervals of $\Delta(1/\lambda)$, then the object image $A(\mathbf{r})$ repeats itself (other than the diffraction/defocusing effect of propagation) at a beat wavelength $\Lambda = [\Delta(1/\lambda)]^{-1}$, with axial resolution $\delta = \Lambda/N$. By use of appropriate values of $\Delta(1/\lambda)$ and N, the beat wavelength Λ can be matched to the axial extent of the object, and δ to the desired level of axial resolution.

In a DIH experiment, the wavelength of a dye laser is scanned in the range of 575.0–605.0 nm in 20 steps, taking the exposure of a hologram at each step [72]. The optical field of a volume around the image location is calculated by numerical diffraction from each hologram. At this point, the field patterns in the individual 3D arrays show little variation along a few millimeters of z-direction. Now the 20 3D arrays are numerically superposed together, by adding the arrays elementwise, resulting in the accumulated field array of the same size. This new array then has

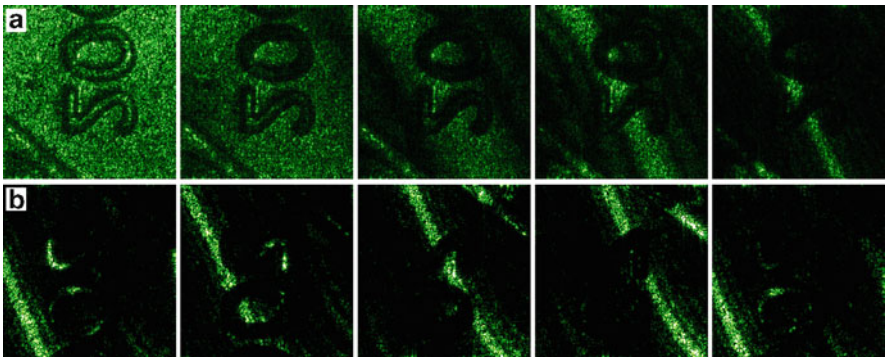

Fig. 12.29 (**a**) Buildup of axial resolution by superposition of holographic images with 1, 2, 4, 8, and 20 wavelengths. (**b**) Several contour images of the coin at 60 μm axial distance intervals [72]

field distribution that represents the three-dimensional object structure, with axial range of $\Lambda = 220$ μm and axial resolution of $\delta = 11$ μm, as described above. Figure 12.29a illustrates the building up of axial resolution as a series of holographic images are superposed using a range of wavelengths. The five frames shown are with 1, 2, 4, 8, and 20 wavelengths superposed, and one notices the narrowing of the contour widths as the synthesized coherence length shortens. Figure 12.29b shows a few contour images at 60 μm axial distance intervals.

We may note that the angular spectrum method is particularly advantageous in DIH calculation, because the field size depends neither on the distance nor the wavelength [72]. We have also demonstrated variable tomographic imaging of DIH by reconstruction on a plane with arbitrary tilt angle with respect to the optical axis, using an algorithm based on angular spectrum method [73]. This allows focusing on a tissue structure that may be oriented at an arbitrary angle within a 3D image volume.

Figure 12.30a shows the flat and stereoscopic views of the numeral 2 on the 2000 mintage mark of a penny [74]. A standard technique for viewing a stereo pair is to start with your eyes very close to the page. As you pull away, you would see two pairs of images: try to merge these into three images and try to focus on the center image. At a certain comfortable distance, the 3D perception will occur. Figure 12.30b shows the flat and stereoscopic views of the compound eye of a fire ant. The size of the individual lenses in the compound eye is measured to be about 25 μm, which is very well resolved by these images.

The DIH technique is applied to 3D ophthalmic imaging [75, 76]. The index of refraction of the retinal layer in an excised tissue is measured from the change in the apparent depth of the choroidal surface due to the presence of the retinal layer. Excised human eye tissue optic nerve disk region is reconstructed in Fig. 12.31. One can quantify the cup depth h being 355.11 μm, and the cup slope s of about 47°.

DIH is also applied to 3D biometry of finger prints [77]. For example in Fig. 12.32, an en face cross-sectional view (C-scan) of a plastic print is shown. The cross-sectional views in Fig. 12.32b, c clearly depict the crests and valleys of

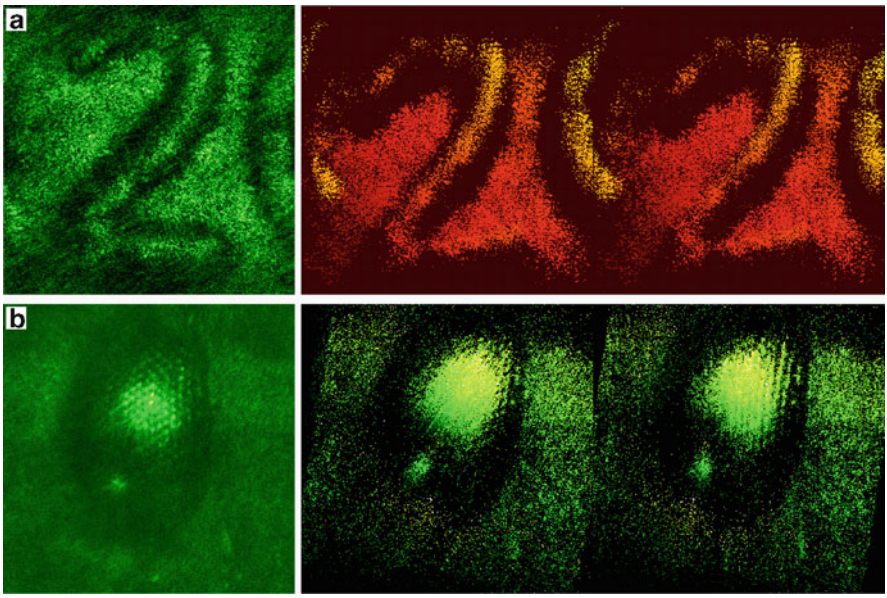

Fig. 12.30 (**a**) Flat and stereoscopic images of a numeral 2 in the 2000 mintage mark of a penny. (**b**) Flat and stereoscopic images of a fire ant's compound eye. The area of each image is 1×1 mm^2 [74]

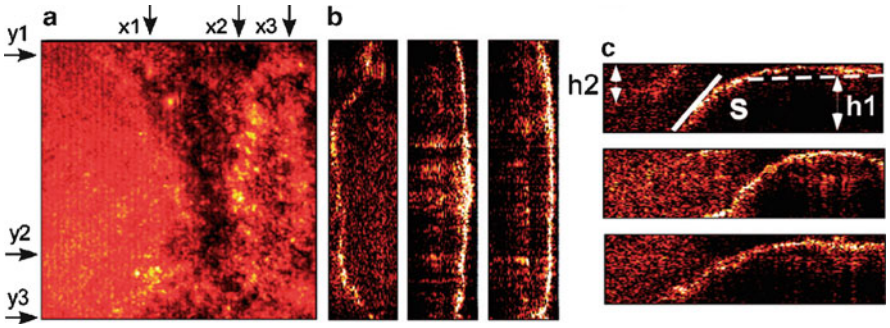

Fig. 12.31 The reconstructed volume of an excised human optic nerve disk sample. The image volume is $1{,}100 \times 1{,}100 \times 280$ μm^3. (**a**) x–y flat view, (**b**) y–z cross-sections at various x values, and (**c**) x–z cross-sections at various y values [76]

the friction ridges, with about 750 μm ridge periodicity and about 50 μm depth of grooves. These are plastic prints of clay material, so the subsurface structure is of no real interest, but there are clear evidence of signals from subsurface scattering points. This indicates feasibility of tomography of subsurface tissue and vein structures in live fingers, which can also be a basis of biometry.

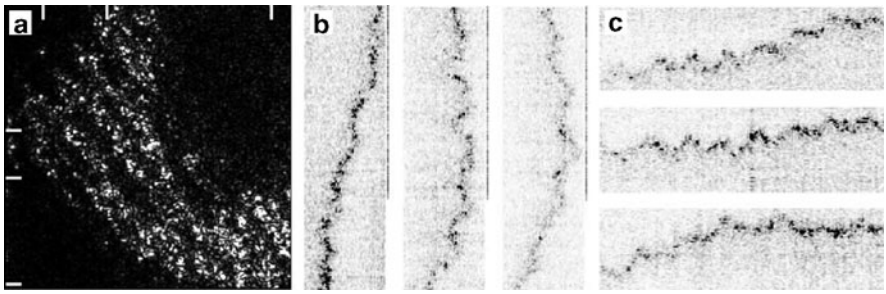

Fig. 12.32 Tomographic images of a plastic fingerprint by DIH. (**a**) A z-section of the three-dimensional volume image, (**b**) x-sections along three vertical lines indicated by the ticks in (**a**), and (**c**) y-sections along three horizontal lines indicated by ticks in (**a**). The image volume is $5.02 \times 5.02 \times 0.211$ mm^3 [77]

12.5.2 Related Techniques and Applications of DIH

Use of a large number of wavelengths or frequencies for determination of axial distance has been known in interferometry. The laser radar, described by Marron et al. acquires many-wavelength holograms, and a 3D Fourier transform of the accumulated holograms results in topographic profile of the object [78–80], such as automotive parts [81]. Leith et al. described a spectral holography system, also based on similar multiwavelength holography concept, and demonstrated it for a one-dimensional object, but its implementation in 3D imaging may be difficult [82]. Instead of direct summation of the multiwavelength holograms, a digital spectral shaping technique is shown to be effective in reducing the sidelobes of the amplitude modulation function, at the expense of some resolution [83]. Instead of a tunable laser, a combination of a superluminescent diode as a broadband source and an acousto-optic tunable filter is used to sweep the frequency, obtaining 200 μm range and 6.5 μm axial resolution [84].

In [85], a SDOCT system is used to acquire a 2D x–y scan of $I(x, y; k)$ data, Fourier transform of which from k to z domain produces the ordinary OCT A-scan. However, the lateral resolution is not uniform along the entire axial depth due to the finite focal depth. Instead, take the 2D data $I(x, y; k)$ for each value of k as a hologram for the corresponding wavelength, and proceed to compute the 3D volumes of optical field followed by superposition of all the computed volumes, as in the basic DIH. The technique can be very fast compared to the standard DIH, because it does not involve wavelength scanning.

Using 20 wavelengths covering the 480–700 nm range, Depeursinge et al. has demonstrated topographic imaging of calibrated microstructures with submicrometer axial resolution [86]. They have also successfully imaged the membrane profile of a single red blood cell [87] (Fig. 12.33).

Holographic contour generation is possible not only with multiwavelength interference, but also by changing the illumination angle. An illumination angle-scanning DIH system is introduced by Hong et al. [88, 89]. For example, by laterally shifting

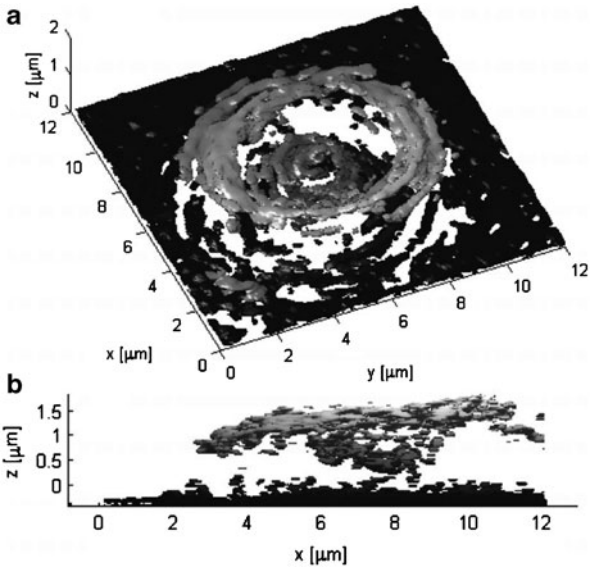

Fig. 12.33 (**a**) 3D representation of the tomography of a red blood cell and (**b**) lateral view of (**a**). (Reprinted from [87] by permission of OSA)

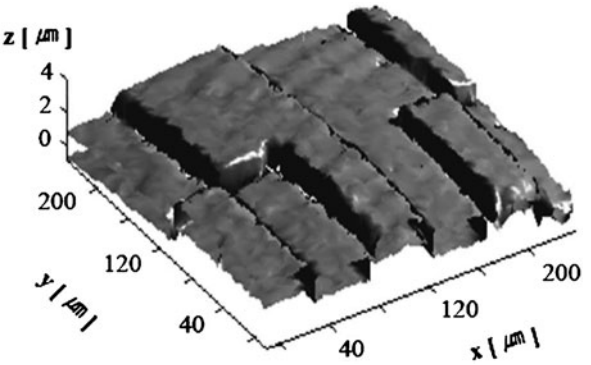

Fig. 12.34 Three-dimensional rendering of a step height standard imaged by angle-scanning DIH. (Reprinted from [89] by permission of OSA)

the illumination lens of the Michelson interferometer, the incident angle is scanned over a range of 14° at 0.26° steps, to obtain optical sectioned images of microstructures with axial resolution of 10 μm (Fig. 12.34).

12.6 Tomography

12.6.1 Optical Projection Tomography

Algorithms such as used in X-ray CAT can be applied to tomographic reconstruction from optical projections, and has been applied to imaging of foams [90] and fluorescent and nonfluorescent biological tissues [91]. Compared to other

3D microscopy techniques, the optical projection tomography (OPT) can image larger volumes, tens of millimeters, but is still limited by the requirement of high transparency and homogeneity of refractive index, as well as higher computational load.

12.6.2 Optical Diffraction Tomography

In the optical diffraction tomography (ODT), or other similarly named methods, a multitude of projections are acquired from many directions, but unlike the simple shadow projection of OPT, one accounts for the diffraction effect and obtains phase information of the object. Phase-shifting interferometry can be used but digital holographic method has the advantage of single exposure from each direction. In [92, 93], quantitative phase profiles obtained by DHM from a regularly spaced angular positions over a 180° range are combined by inverse Radon transform (Fig. 12.35). A tomographic volume image of the refractive-index distribution of a cell is obtained, with accuracy of index 0.01 and spatial resolution 1 μm in all three directions. For coverage of the illumination angles, a rotating sample chamber or a patch clamp micropipette were used. Instead of rotating the sample, the illumination beam can be scanned using a galvo-mounted mirror, [94–96]. As well as tomography of biological cells, ODT has been applied to holographic particle image velocimetry [97] and imaging of optical fiber profiles [98–100]. In [101], phase profile is calculated by using the noninterferometric phase retrieval method of Sect. 10.2, to obtain 3D tomographic profile of optical fiber splice. Fukutake and Milster [102] propose 3D phase-contrast microscopy by acquiring many

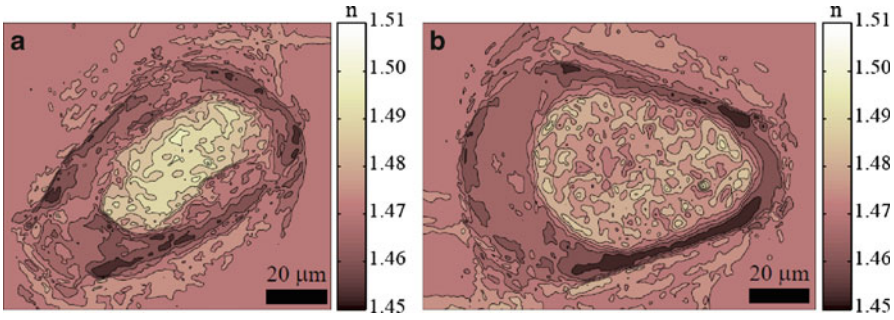

Fig. 12.35 Cuts in the tomographic reconstructions of two different *Hyalosphenia papilio*. Discrete values of the measured refractive index n are coded in false colors, the color-coding scales being displayed on the right part of each corresponding cut. (Reprinted from [93] by permission of OSA)

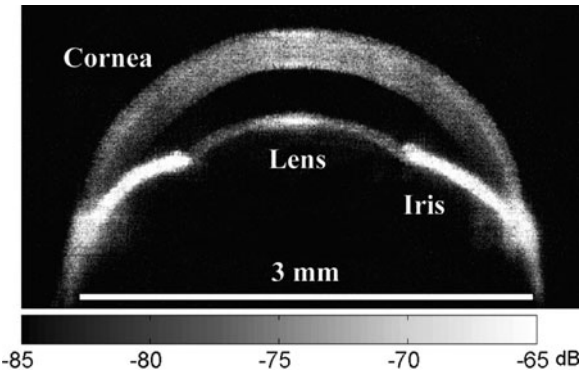

Fig. 12.36 Mouse eye in vitro mosaic section of the anterior segment extracted from ten flythroughs. (Reprinted from [104] by permission of OSA)

holograms while scanning the illumination angle and utilizing 4π configuration of a pair of objectives. A tutorial review of tomographic diffractive microscopy is given in [103].

12.6.3 Holographic Optical Coherence Imaging

The holographic optical coherence imaging (HOCI) is a low-coherence digital holography technique, where a tomographic image stack is obtained by using a femtosecond laser and varying the delay of reference light. In [104], the CCD placed at the Fourier plane of the system is used for Fourier-domain DH, and coherence-gated section image is obtained by Fourier transform of the hologram. Sensitivity of 86 dB was achieved and tomographic images of tumor spheroid and mouse eye are obtained (Fig. 12.36). In [105], a series of holograms are acquired at 1–2 fps and the speckle intensity variance of each pixel defines a motility metric that becomes a novel imaging contrast agent. Viable tumor cells within a tissue display large motility signals, whereas a cancer-drug-treated tissue has much reduced motility signals (Fig. 12.37). The method combines the nanometer sensitivity of interferometry with the large field of view of imaging.

12.6.4 Turbid Imaging

The ability of holography to image through a scattering medium has long been recognized. One typically uses time gating with short-pulse lasers or coherence gating with cw broadband source to suppress unwanted scattered light. The Fourier synthesis holography [106] collects a series of 1D holograms using a range of discrete wavelengths, to form a 2D array of space-wavelength dimensions. Its Fourier transform yields a 2D array of spatial frequency-time delay dimensions. This is used to image the first arriving light through a scattering medium.

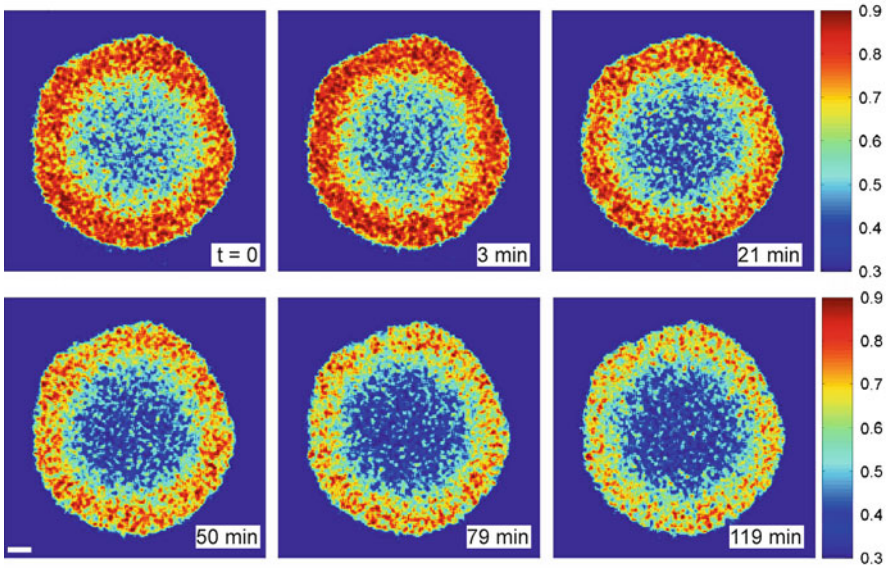

Fig. 12.37 Motility maps showing the response of an 820-μm-diameter tumor (at a fixed depth of 350 μm from the tumor top) to 10 μg/ml nocodazole as a function of time (from healthy to 120 min later). Motility in the viable shell decreases with time, showing how nocodazole suppresses the activity of viable tumor cells. Bar, 100 μm. (Reprinted from [105] by permission of OSA)

Advantages of this method compared to short-pulse interference technique [107] are the high fringe contrast of individual holograms and the flexibility of gating, at the cost of substantial computational load. Equivalence of short pulse and broad spectrum in holographic coherence gating was also demonstrated in [108].

In [109], transmission of a ~450 fs laser pulse through 1.3 cm of chicken meat hiding 1.25 mm crossed wires leads to stretching of the pulse to ~100 ps due to multiple scattering. The first arriving light is gated by the reference pulse, but the holographic interference is overwhelmed by the background. Difference of two hologram exposures substantially reduces fixed noise, and allowed imaging of the silhouette of the wires.

In [110], thousands of holograms are acquired of an object behind scattering surfaces illuminated by a laser. Phase images are unwrapped, which display severe corruption by speckle noise. But averaging the phase profiles over many holograms produced usable complex valued hologram, which, when numerically back-propagated, produced image of the object with resolution substantially improved compared to average of magnitude alone. The simulation and experiments were with 1D holograms.

Phase-shifting digital holography using a SLD with coherence length of 23 μm demonstrated the capability of LCDH to produce accurate amplitude and phase images of a structured surface hidden in up to OD 3.0 of scattering

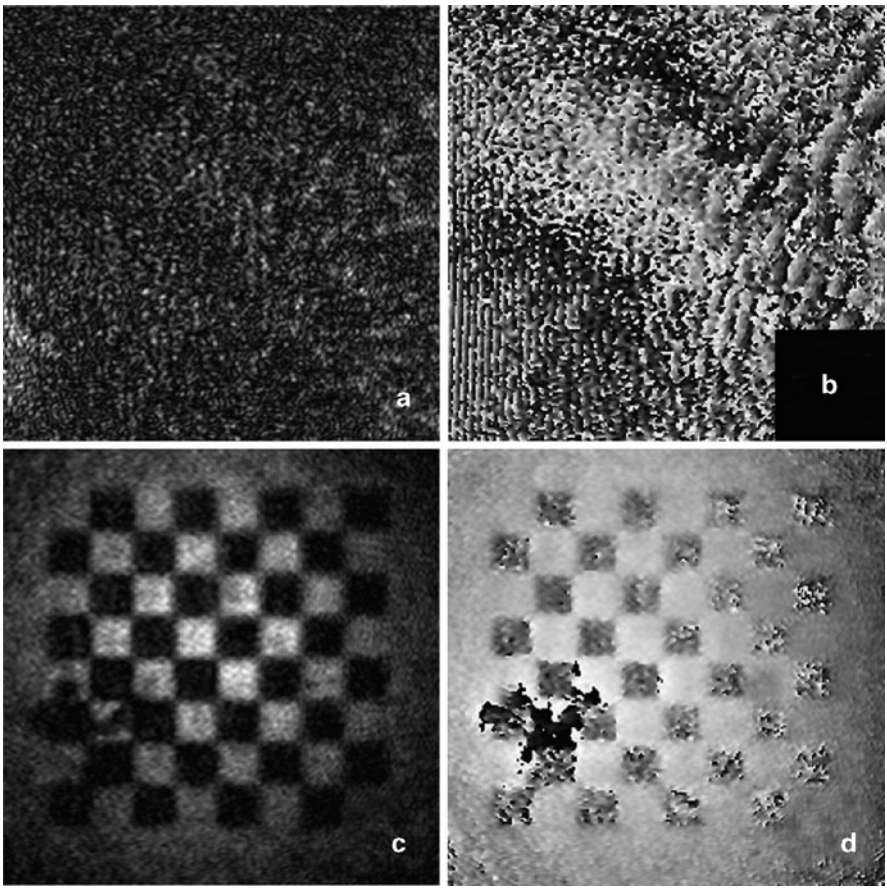

Fig. 12.38 (**a**) Amplitude and (**b**) phase distributions of the reconstructed image from a hologram recorded with the LD. (**c**) Amplitude and (**d**) phase distributions of the reconstructed image from a hologram recorded with the SLD. (Reprinted from [111] by permission of OSA)

medium – diluted milk [111]. On the other hand, when a LD, of unspecified but presumed much longer coherence length, is used in the same setup, multiply scattered light is also reconstructed, obliterating image of the hidden structure (Fig. 12.38).

References

1. F. Dubois, L. Joannes, and J. C. Legros, "Improved three-dimensional imaging with a digital holography microscope with a source of partial spatial coherence," Applied Optics **38**, 7085–7094 (1999).
2. G. Pedrini, and H. J. Tiziani, "Short-coherence digital microscopy by use of a lensless holographic imaging system," Applied Optics **41**, 4489–4496 (2002).

3. L. Martinez-Leon, G. Pedrini, and W. Osten, "Applications of short-coherence digital holography in microscopy," Applied Optics **44**, 3977–3984 (2005).
4. P. Massatsch, F. Charriere, E. Cuche, P. Marquet, and C. D. Depeursinge, "Time-domain optical coherence tomography with digital holographic microscopy," Applied Optics **44**, 1806–1812 (2005).
5. L. Repetto, E. Piano, and C. Pontiggia, "Lensless digital holographic microscope with light-emitting diode illumination," Optics Letters **29**, 1132–1134 (2004).
6. B. Kemper, S. Sturwald, C. Remmersmann, P. Langehanenberg, and G. von Bally, "Characterisation of light emitting diodes (LEDs) for application in digital holographic microscopy for inspection of micro and nanostructured surfaces," Optics and Lasers in Engineering **46**, 499–507 (2008).
7. J. Garcia-Sucerquia, J. H. Ramirez, and R. Castaneda, "Incoherent recovering of the spatial resolution in digital holography," Optics Communications **260**, 62–67 (2006).
8. F. Dubois, M. L. N. Requena, C. Minetti, O. Monnom, and E. Istasse, "Partial spatial coherence effects in digital holographic microscopy with a laser source," Applied Optics **43**, 1131–1139 (2004).
9. F. Dubois, N. Callens, C. Yourassowsky, M. Hoyos, P. Kurowski, and O. Monnom, "Digital holographic microscopy with reduced spatial coherence for three-dimensional particle flow analysis," Applied Optics **45**, 864–871 (2006).
10. J. Rosen, and G. Brooker, "Digital spatially incoherent Fresnel holography," Optics Letters **32**, 912–914 (2007).
11. J. Rosen, and G. Brooker, "Fluorescence incoherent color holography," Optics Express **15**, 2244–2250 (2007).
12. J. Rosen, and G. Brooker, "Non-scanning motionless fluorescence three-dimensional holographic microscopy," Nat. Photonics **2**, 190–195 (2008).
13. E. N. Leith, and Upatniek.J, "Holography with Achromatic-Fringe Systems," Journal of the Optical Society of America **57**, 975–& (1967).
14. G. Cochran, "New method of making Fresnel transforms with incoherent light," Journal of the Optical Society of America **56**, 1513–& (1966).
15. S. G. Kim, B. Lee, and E. S. Kim, "Removal of bias and the conjugate image in incoherent on-axis triangular holography and real-time reconstruction of the complex hologram," Applied Optics **36**, 4784–4791 (1997).
16. G. Sirat, and D. Psaltis, "Conoscopic Holography," Optics Letters **10**, 4–6 (1985).
17. L. M. Mugnier, G. Y. Sirat, and D. Charlot, "Conoscopic holography: two-dimensional numerical reconstructions," Opt. Lett. **18**, 66–68 (1993).
18. T. C. Poon, "Scanning Holography and Two-Dimensional Image-Processing by Acoustooptic 2-Pupil Synthesis," Journal of the Optical Society of America a-Optics Image Science and Vision **2**, 521–527 (1985).
19. T. C. Poon, "Optical Scanning Holography – A Review of Recent Progress," J. Opt. Soc. Korea. **13**, 406–415 (2009).
20. T.-C. Poon, "Three-dimensional image processing and optical scanning holography," Adv. Imaging & Electron Phys. **126**, 329–350 (2003).
21. T. C. Poon, T. Kim, G. Indebetouw, B. W. Schilling, M. H. Wu, K. Shinoda, and Y. Suzuki, "Twin-image elimination experiments for three-dimensional images in optical scanning holography," Optics Letters **25**, 215–217 (2000).
22. G. Indebetouw, Y. Tada, and J. Leacock, "Quantitative phase imaging with scanning holographic microscopy: an experimental assessment," Biomed. Eng. Online **5**, 63 (2006).
23. B. W. Schilling, T. C. Poon, G. Indebetouw, B. Storrie, K. Shinoda, Y. Suzuki, and M. H. Wu, "Three-dimensional holographic fluorescence microscopy," Optics Letters **22**, 1506–1508 (1997).
24. G. Indebetouw, and W. Zhong, "Scanning holographic microscopy of three-dimensional fluorescent specimens," J. Opt. Soc. Am. A **23**, 1699–1707 (2006).

25. T.-C. Poon, M. H. Wu, K. Shinoda, and T. Suzuki, "Optical scanning holography," Proc. IEEE **84**, 753–764 (1996).
26. G. Indebetouw, "Properties of a scanning holographic microscope: improved resolution, extended depth-of-focus, and/or optical sectioning," J. Mod. Opt. **49**, 1479–1500 (2002).
27. G. Indebetouw, Y. Tada, J. Rosen, and G. Brooker, "Scanning holographic microscopy with resolution exceeding the Rayleigh limit of the objective by superposition of off-axis holograms," Applied Optics **46**, 993–1000 (2007).
28. G. Indebetouw, and P. Klysubun, "Space-time digital holography: A three-dimensional microscopic imaging scheme with an arbitrary degree of spatial coherence," Applied Physics Letters **75**, 2017–2019 (1999).
29. G. Indebetouw, and P. Klysubun, "Imaging through scattering media with depth resolution by use of low-coherence gating in spatiotemporal digital holography," Optics Letters **25**, 212–214 (2000).
30. D. Huang, E. A. Swanson, C. P. Lin, J. S. Schuman, W. G. Stinson, W. Chang, M. R. Hee, T. Flotte, K. Gregory, C. A. Puliafito, and J. G. Fujimoto, "Optical coherence tomography," Science **254**, 1178–1181 (1991).
31. J. G. Fujimoto, M. E. Brezinski, G. J. Tearney, S. A. Boppart, B. E. Bouma, M. R. Hee, J. F. Southern, and E. A. Swanson, "Optical biopsy and imaging using optical coherence tomography," Nature Med. **1**, 970–972 (1995).
32. A. F. Fercher, K. Mengedoht, and W. Werner, "Eye-length measurement by interferometry with partially coherent light," Optics Letters **13**, 186–188 (1988).
33. A. F. Fercher, W. Drexler, C. K. Hitzenberger, and T. Lasser, "Optical coherence tomography - principles and applications," Rep. Prog. Phys. **66**, 239–303 (2003).
34. S. R. Chinn, E. A. Swanson, and J. G. Fujimoto, "Optical coherence tomography using a frequency-tunable optical source," Opt. Lett. **22**, 340–342 (1997).
35. M. A. Choma, M. V. Sarunic, C. Yang, and J. A. Izatt, "Sensitivity advantage of swept source and Fourier domain optical coherence tomography," Opt. Express **11**, 2183–2189 (2003).
36. M. D. Kulkarni, T. G. v. Leeuwen, S. Yazdanfar, and J. A. Izatt, "Velocity-estimation accuracy and frame-rate limitations in color Doppler optical coherence tomography," Opt. Lett. **23**, 1057–1059 (1998).
37. Y. Zhao, Z. Chen, C. Saxer, S. Xiang, J. F. d. Boer, and J. S. Nelson, "Phase-resolved optical coherence tomography and optical Doppler tomography for imaging blood flow in human skin with fast scanning speed and high velocity sensitivity," Opt. Lett. **25**, 114–116 (2000).
38. M. Pircher, B. Baumann, E. Gotzinger, and C. K. Hitzenberger, "Retinal cone mosaic imaged with transverse scanning optical coherence tomography," Optics Letters **31**, 1821–1823 (2006).
39. R. J. Zawadzki, S. M. Jones, S. S. Olivier, M. T. Zhao, B. A. Bower, J. A. Izatt, S. Choi, S. Laut, and J. S. Werner, "Adaptive-optics optical coherence tomography for high-resolution and high-speed 3D retinal in vivo imaging," Optics Express **13**, 8532–8546 (2005).
40. A. B. Vakhtin, K. A. Peterson, W. R. Wood, and D. J. Kane, "Differential spectral interferometry:an imaging technique for biomedical applications," Opt. Lett. **28**, 1332–1334 (2003).
41. J. Zhang, B. Rao, L. F. Yu, and Z. P. Chen, "High-dynamic-range quantitative phase imaging with spectral domain phase microscopy," Optics Letters **34**, 3442–3444 (2009).
42. M. Sticker, C. K. Hitzenberger, R. Leitgeb, and A. F. Fercher, "Quantitative differential phase measurement and imaging in transparent and turbid media by optical coherence tomography," Opt. Lett. **26**, 518–520 (2001).
43. M. Sticker, M. Pircher, E. Gtzinger, H. Sattmann, A. F. Fercher, and C. K. Hitzenberger, "En face imaging of single cell layers by differential phase-contrast optical coherence microscopy," Opt. Lett. **27**, 1126–1128 (2002).
44. C. Yang, A. Wax, I. Georgakoudi, E. B. Hanlon, K. Badizadegan, R. R. Dasari, and M. S. Feld, "Interferometric phase-dispersion microscopy," Opt. Lett. **25**, 1526–1528 (2000).

45. C. Yang, A. Wax, R. R. Dasari, and M. S. Feld, "Phase-dispersion optical tomography," Opt. Lett. **26**, 686 (2001).
46. C. Yang, A. Wax, M. S. Hahn, K. Badizadegan, R. R. Dasari, and M. S. Feld, "Phase-referenced interferometer with subwavelength and subhertz sensitivity applied to the study of cell membrane dynamics," Optics Letters **26**, 1271–1273 (2001).
47. E. Beaurepaire, A. C. Boccara, M. Lebec, L. Blanchot, and H. Saint-Jalmes, "Full-field optical coherence microscopy," Opt. Lett. **23**, 244–246 (1998).
48. A. Dubois, "Phase-map measurements by interferometry with sinusoidal phase modulation and four integrating buckets," J. Opt. Soc. Am. A **18**, 1972–1979 (2001).
49. A. Dubois, L. Vabre, A. C. Boccara, and E. Beaurepaire, "High-resolution full-field optical coherence tomography with Linnik microscope," Appl. Opt. **41**, 805–812 (2002).
50. L. Vabre, A. Dubois, and A. C. Boccara, "Thermal-light full-field optical coherence tomography," Opt. Lett. **27**, 530–532 (2002).
51. G. Moneron, A. L. Boccara, and A. Dubois, "Polarization-sensitive full-field optical coherence tomography," Optics Letters **32**, 2058–2060 (2007).
52. C. W. Dunsby, Y. Gu, and P. M. W. French, "Single-shot phase-stepped wide-field coherence-gated imaging," Opt. Express **11**, 105–115 (2003).
53. E. Bordenave, E. Abraham, G. Jonusauskas, N. Tsurumachi, J. Oberl, C. Rlliere, P. Minot, M. Lassegues, and J. Bazeille, "Wide-field optical coherence tomography: imaging of biological tissues," Appl. Opt. **41**, 2059–2064 (2002).
54. B. Laude, A. De Martino, B. Drevillon, L. Benattar, and L. Schwartz, "Full-field optical coherence tomography with thermal light," Appl. Opt. **41**, 6637–6645 (2002).
55. M. Akiba, K. P. Chan, and N. Tanno, "Full-field optical coherence tomography by two-dimensional heterodyne detection with a pair of CCD cameras," Opt. Lett. **28**, 816–818 (2003).
56. M. C. Pitter, C. W. See, and M. G. Somekh, "Full-field heterodyne interference microscope with spatially incoherent illumination," Opt. Lett. **29**, 1200–1202 (2004).
57. S. Bourquin, P. Seitz, and R. P. Salath, "Optical coherence topography based on a two-dimensional smart detector array," Opt. Lett. **26**, 512–514 (2001).
58. M. Ducros, M. Laubscher, B. Karamata, S. Bouquin, T. Lasser, and R. P. Salathe, "Parallel optical coherence tomography in scattering samples using a two-dimensional smart-pixel detector array," Opt. Comm. **202**, 29–35 (2002).
59. M. Laubscher, M. Ducros, B. Karamata, and R. P. Salathe, "Video-rate three-dimensional optical coherence tomography," Opt. Express **10**, 429–435 (2002).
60. M. Roy, G. Cox, and P. Hariharan, "Low-coherence interference microscopy with an improved switchable achromatic phase-shifter," Opt. Express **13**, 9125–9130 (2005).
61. L. F. Yu, and M. K. Kim, "Full-color three-dimensional microscopy by wide-field optical coherence tomography," Optics Express **12**, 6632–6641 (2004).
62. M. V. Sarunic, S. Weinberg, and J. A. Izatt, "Full-field swept-source phase microscopy," Optics Letters **31**, 1462–1464 (2006).
63. Y. Watanabe, K. Yamada, and M. Sato, "Three-dimensional imaging by ultrahigh-speed axial-lateral parallel time domain optical coherence tomography," Optics Express **14**, 5201–5209 (2006).
64. M. Akiba, N. Maeda, K. Yumikake, T. Soma, K. Nishida, Y. Tano, and K. P. Chan, "Ultrahigh-resolution imaging of human donor cornea using full-field optical coherence tomography," J. Biomed. Opt. **12**, 041202 (2007).
65. W. J. Choi, J. Na, H. Y. Choi, J. Eom, and B. H. Lee, "Active feedback wide-field optical low-coherence interferometry for ultrahigh-speed three-dimensional morphometry," Measurement Science & Technology **21**, 045503 (2010).
66. N. Abramson, "Light-in-Flight Recording by Holography," Optics Letters **3**, 121–123 (1979).
67. T. Kubota, and Y. Awatsuji, "Observation of light propagation by holography with a picosecond pulsed laser," Opt. Lett. **27**, 815 (2002).

68. J. Pomarico, U. Schnars, H. J. Hartmann, and W. Juptner, "Digital Recording and Numerical Reconstruction of Holograms - a New Method for Displaying Light in-Flight," Applied Optics **34**, 8095–8099 (1995).
69. B. Nilsson, and T. E. Carlsson, "Direct three-dimensional shape measurement by digital light-in-flight holography," Applied Optics **37**, 7954–7959 (1998).
70. T. E. Carlsson, B. Nilsson, and J. Gustafsson, "System for acquisition of three-dimensional shape and movement using digital Light-in-Flight holography," Optical Engineering **40**, 67–75 (2001).
71. M. K. Kim, "Wavelength scanning digital interference holography for optical section imaging," Opt. Lett. **24**, 1693–1695 (1999).
72. L. F. Yu, and M. K. Kim, "Wavelength-scanning digital interference holography for tomographic three-dimensional imaging by use of the angular spectrum method," Optics Letters **30**, 2092–2094 (2005).
73. L. F. Yu, and M. K. Kim, "Wavelength scanning digital interference holography for variable tomographic scanning," Optics Express **13**, 5621–5627 (2005).
74. A. Dakoff, J. Gass, and M. K. Kim, "Microscopic three-dimensional imaging by digital interference holography," J. Electron. Imaging **12**, 643–647 (2003).
75. M. C. Potcoava, and M. K. Kim, "Optical tomography for biomedical applications by digital interference holography," Measurement Science & Technology **19**, 074010 (2008).
76. M. C. Potcoava, C. N. Kay, M. K. Kim, and D. W. Richards, "In vitro imaging of ophthalmic tissue by digital interference holography," Journal of Modern Optics **57**, 115–123 (2010).
77. M. C. Potcoava, and M. K. Kim, "Fingerprint biometry applications of digital holography and low-coherence interferography," Applied Optics **48**, H9-H15 (2009).
78. J. C. Marron, and K. S. Schroeder, "3-Dimensional Lensless Imaging Using Laser Frequency Diversity," Applied Optics **31**, 255–262 (1992).
79. J. C. Marron, and T. J. Schulz, "3-Dimensional, Fine-Resolution Imaging Using Laser Frequency Diversity," Optics Letters **17**, 285–287 (1992).
80. J. C. Marron, and K. S. Schroeder, "Holographic laser radar," Opt. Lett. **18**, 385–387 (1993).
81. J. C. Marron, and K. Gleichman, "Three-dimensional imaging using a tunable laser source," Opt. Engg. **39**, 47–51 (2000).
82. M. P. Shih, H. S. Chen, and E. N. Leith, "Spectral holography for coherence-gated imaging," Opt. Lett. **24**, 52–54 (1999).
83. L. F. Yu, and Z. P. Chen, "Improved tomographic imaging of wavelength scanning digital holographic microscopy by use of digital spectral shaping," Optics Express **15**, 878–886 (2007).
84. G. Sheoran, S. Dubey, A. Anand, D. S. Mehta, and C. Shakher, "Swept-source digital holography to reconstruct tomographic images," Optics Letters **34**, 1879–1881 (2009).
85. L. F. Yu, and Z. P. Chen, "Digital holographic tomography based on spectral interferometry," Optics Letters **32**, 3005–3007 (2007).
86. F. Montfort, T. Colomb, F. Charriere, J. Kuhn, P. Marquet, E. Cuche, S. Herminjard, and C. Depeursinge, "Submicrometer optical tomography by multiple-wavelength digital holographic microscopy," Applied Optics **45**, 8209–8217 (2006).
87. J. Kuhn, F. Montfort, T. Colomb, B. Rappaz, C. Moratal, N. Pavillon, P. Marquet, and C. Depeursinge, "Submicrometer tomography of cells by multiple-wavelength digital holographic microscopy in reflection," Optics Letters **34**, 653–655 (2009).
88. S. J. Jeong, and C. K. Hong, "Illumination-angle-scanning digital interference holography for optical section imaging," Optics Letters **33**, 2392–2394 (2008).
89. Y. Jeon, and C. K. Hong, "Optical section imaging of the tilted planes by illumination-angle-scanning digital interference holography," Applied Optics **49**, 5110–5116 (2010).
90. M. R. Fetterman, E. Tan, L. Ying, R. A. Stack, D. L. Marks, S. Feller, E. Cull, J. M. Sullivan, D. C. Munson, S. Thoroddsen, and D. J. Brady, "Tomographic imaging of foam," Opt. Express **7**, 186–197 (2000).

91. J. Sharpe, U. Ahlgren, P. Perry, B. Hill, A. Ross, J. Hecksher-Serensen, R. Baldock, and D. Davidson, "Optical projection tomography as a tool for 3D microscopy and gene expression studies," Science **296**, 541–545 (2002).
92. F. Charriere, A. Marian, F. Montfort, J. Kuehn, T. Colomb, E. Cuche, P. Marquet, and C. Depeursinge, "Cell refractive index tomography by digital holographic microscopy," Optics Letters **31**, 178–180 (2006).
93. F. Charriere, N. Pavillon, T. Colomb, C. Depeursinge, T. J. Heger, E. A. D. Mitchell, P. Marquet, and B. Rappaz, "Living specimen tomography by digital holographic microscopy: morphometry of testate amoeba," Optics Express **14**, 7005–7013 (2006).
94. W. Choi, C. Fang-Yen, K. Badizadegan, S. Oh, N. Lue, R. R. Dasari, and M. S. Feld, "Tomographic phase microscopy," Nature Methods **4**, 717–719 (2007).
95. W. S. Choi, C. Fang-Yen, K. Badizadegan, R. R. Dasari, and M. S. Feld, "Extended depth of focus in tomographic phase microscopy using a propagation algorithm," Optics Letters **33**, 171–173 (2008).
96. M. Debailleul, B. Simon, V. Georges, O. Haeberle, and V. Lauer, "Holographic microscopy and diffractive microtomography of transparent samples," Measurement Science & Technology **19**, 074009 (2008).
97. J. Lobera, and J. M. Coupland, "Optical diffraction tomography in fluid velocimetry: the use of a priori information," Measurement Science & Technology **19**, 074013 (2008).
98. A. Devaney, and J. Cheng, "Optical diffraction tomography in an inhomogeneous background medium," Measurement Science & Technology **19**, 085505 (2008).
99. Y. Jeon, and C. K. Hong, "Rotation error correction by numerical focus adjustment in tomographic phase microscopy," Optical Engineering **48**, 105801 (2009).
100. T. Kozacki, R. Krajewski, and M. Kujawinska, "Reconstruction of refractive-index distribution in off-axis digital holography optical diffraction tomographic system," Optics Express **17**, 13758–13767 (2009).
101. N. M. Dragomir, X. M. Goh, and A. Roberts, "Three-dimensional refractive index reconstruction with quantitative phase tomography," Microscopy Research and Technique **71**, 5-10 (2008).
102. N. Fukutake, and T. D. Milster, "Proposal of three-dimensional phase contrast holographic microscopy," Optics Express **15**, 12662–12679 (2007).
103. O. Haeberle, K. Belkebir, H. Giovaninni, and A. Sentenac, "Tomographic diffractive microscopy: basics, techniques and perspectives," Journal of Modern Optics **57**, 686–699 (2010).
104. K. Jeong, J. J. Turek, and D. D. Nolte, "Fourier-domain digital holographic optical coherence imaging of living tissue," Applied Optics **46**, 4999–5008 (2007).
105. K. Jeong, J. J. Turek, and D. D. Nolte, "Volumetric motility-contrast imaging of tissue response to cytoskeletal anti-cancer drugs," Optics Express **15**, 14057–14064 (2007).
106. E. Arons, D. Dilworth, M. Shih, and P. C. Sun, "Use of Fourier synthesis holography to image through inhomogeneities," Opt. Lett. **18**, 1852–1854 (1993).
107. H. Chen, Y. Chen, D. Dilworth, E. Leith, J. Lopez, and J. Valdmanis, "2-Dimensional Imaging through Diffusing Media Using 150-Fs Gated Electronic Holography Techniques," Optics Letters **16**, 487–489 (1991).
108. E. Leith, C. Chen, H. Chen, Y. Chen, D. Dilworth, J. Lopez, J. Rudd, P. C. Sun, J. Valdmanis, and G. Vossler, "Imaging through Scattering Media with Holography," Journal of the Optical Society of America a-Optics Image Science and Vision **9**, 1148–1153 (1992).
109. P. Naulleau, and D. Dilworth, "Holographic first-arriving-light signal-to-noise ratio enhancement by differential holography," Opt. Lett. **20**, 2354–2356 (1995).
110. E. Leith, P. Naulleau, and D. Dilworth, "Ensemble-averaged imaging through highly scattering media," Opt. Lett. **21**, 1691–1693 (1996).
111. S. Tamano, Y. Hayasaki, and N. Nishida, "Phase-shifting digital holography with a low-coherence light source for reconstruction of a digital relief object hidden behind a light-scattering medium," Applied Optics **45**, 953–959 (2006).

Index

A
Aberration compensation, 2, 122–123, 163
Achromatic fringe system, 197–198
Achromatic phase shift, 101, 139, 187
Acousto-optical tunable filter, 205, 220
Acousto-optic modulator (AOM), 101–103, 105, 202, 212
Adaptive optics, 207
Adhesion, 172, 174, 175, 177
AH. *See* Analog holography
Airy disk, 15, 22
Aliasing, 49, 66, 67
Amplitude hologram, 37–38
Analog holography (AH), 1–5, 88, 166–168
Anamorphism, 123
Angle-scanning DIH, 220–221
Angular
  aperture, 151
  magnification, 36, 63
  multiplexing, 117, 130, 140, 141
  spectrum, 22–24, 43, 50–52, 55, 82, 88, 89, 91–93, 102, 112, 117, 119, 123, 136, 140, 163, 164, 177, 218
  spectrum filtering, 90–92, 102
Angular spectrum method (ASM), 24, 43, 50–53, 55, 92, 93, 112, 114, 218
AOM. *See* Acousto-optic modulator
Apodize, 93, 155
ASM. *See* Angular spectrum method
Asynchronous digital holography, 103
Auto-correlation, 17, 75–77
Auto-focusing, 109, 111
Awatsuji, Y., 103
Axial
  magnification, 36
  resolution, 73, 152, 205, 206, 210, 211, 213, 217, 218, 220, 221

B
Band-limited, 44, 45
Bandpass filter, 165, 208
Banerjee, P., 8
Barbastathis, G., 8
Beaurepaire, E., 210
Benton, S., 4
Bevilacqua, F., 169
Biometry, 218–220
Birefringence, 141, 157, 162, 210
Blanchot, L., 210
Boccara, A.C., 210
Boppart, S.A., 204
Bouma, B.E., 204
Bourquin, S., 212
Boyer, K., 5
Bragg diffraction, 4, 39
Bragg, W.L., 2
Bredebusch, I., 172
Brezinski, M.E., 204
Bright field, 153, 154, 177

C
Cai, L.Z., 99
Carl, D., 172
CGH. *See* Computer-generated hologram; Computer-generated holography
Chen, H.S., 220
Chirp function, 21, 37, 73
Chromatic aberration, 118, 123, 139, 152, 168
Coherence length, 63, 160, 185, 191, 192, 195, 204–206, 210, 215, 218, 224, 225
Color digital holography, 139–141
Comb function, 12, 43, 44, 71
Common-path configuration, 101, 157, 180, 181
Computer-generated hologram (CGH), 8

M.K. Kim, *Digital Holographic Microscopy: Principles, Techniques, and Applications*, Springer Series in Optical Sciences 162,
DOI 10.1007/978-1-4419-7793-9, © Springer Science+Business Media, LLC 2011

Computer-generated holography (CGH), 30
Condenser, 149–152, 154–155, 193
Confocal scanning microscopy, 158
Conoscopic holography, 199
Conventional holography, 1, 7, 29, 30, 39, 129, 141, 191, 197, 199
Convolution, 16–18, 20, 22, 24, 43, 49–50, 52, 75–77, 82, 112, 131, 132, 139, 178, 184, 193
Correlation, 16–18, 111, 129, 195–197
Cross-correlation, 16–18
Cuche, E., 169
Cullen, D., 5

D
Dark field, 154, 163, 177–179
Delta function, 12, 16, 18, 33, 71, 74, 193
Denisyuk, Y.N., 3
Depeursinge, C., 5, 7, 169
DGH. *See* Digital Gabor holography
DH. *See* Digital holography
DHM. *See* Digital holographic microscopy
DIC. *See* Differential interference contrast
Differential interference contrast (DIC), 150, 155–156, 177, 178, 180, 181, 183–184, 208
Differential phase-contrast (DPC), 180, 181, 208, 209
Diffraction, 1, 11, 29, 43, 55, 71, 90, 95, 109, 130, 149, 193
  diagram, 2
  microscopy, 3
  theory, 1, 5, 11, 19, 30, 71, 73, 96, 119
Diffraction phase microscopy (DPM), 182–183, 204
Diffractive optical element (DOE), 137, 195–197
Digital Fourier holography, 64–66, 142
Digital Fresnel holography, 66–68
Digital Gabor holography (DGH), 7, 60–61
Digital holographic microscopy (DHM), 63, 117, 137–139, 149–186, 191–199, 222
Digital holography (DH), 1, 30, 55, 71, 88, 95, 109, 129, 149, 191
Digital image plane holography, 63–64
Digital in-line holography, 61–62, 141
Digital interference holography (DIH), 119, 215–221
DIH. *See* Digital interference holography
Discrete Fourier transform, 43–47
DOE. *See* Diffractive optical element
Domschke, W., 172
Doppler frequency, 203, 204, 213
Doppler OCT, 206
Double exposure holography, 4
DPC. *See* Differential phase-contrast
DPM. *See* Diffraction phase microscopy
Dubois, F., 192, 193
Dynamic system, 103, 135–137

E
Electronic speckle pattern interferometry (ESPI), 4, 7
Electron microscope, 1
Epi-illumination, 149, 150, 157
Erythrocyte, 172
ESPI. *See* Electronic speckle pattern interferometry
Ewald sphere, 121
Extended focus, 111–112, 202
Eyepiece, 149–152

F
Fast Fourier transform (FFT), 5, 7, 45–48, 122
FDOCT. *See* Fourier-domain (or frequency-domain) optical coherence tomography
Fercher, A.F., 204
FFOCT. *See* Full-field optical coherence tomography
FFT. *See* Fast Fourier transform
FFTSHIFT, 46, 47
Field curvature, 152
Field diaphragm, 149–150
Field of view (FOV), 165–167, 177
FINCH. *See* Fresnel incoherent correlation holography
Finite optical system, 150
First arriving light, 223, 224
Fluorescence, 157–159, 163, 174, 191, 197, 202
Fluorescence microscopy, 157–159, 163, 174
Fourier
  optics, 8, 11–28, 154
  synthesis holography, 223
  theorem, 11–12
  transform, 5, 11–18, 21–24, 27, 28, 41, 43–50, 64–66, 74–80, 82, 86, 91, 105, 121, 132, 133, 135, 165, 181–184, 193–194, 205, 212, 223
Fourier–Bessel transform, 15
Fourier-domain (or frequency-domain) optical coherence tomography (FDOCT), 205–206

Fourier phase microscope (FPM), 181, 182
Four-wave mixing, 4, 40
FOV. *See* Field of view
FPM. *See* Fourier phase microscope
Fractional-order Fourier transform (FRFT), 78–80, 135
Fractional Talbot effect, 103–104
Fraunhofer diffraction, 22, 33, 38, 78, 80
Frequency shifting, 102, 103
Fresnel
  approximation, 21, 34, 47, 51, 131
  images, 104
  number, 77
  PSF, 21, 47, 49
  transform, 21, 24, 25, 43, 47–49, 66, 68, 112, 118, 139
Fresnel incoherent correlation holography (FINCH), 195–198, 203–204
Fresnel–Kirchoff diffraction formula, 19
Fresnel transform method (FTM), 47–49, 51, 52, 66, 112–114
Fresnel zone pattern (FZP), 34, 37, 198–202, 204
FRFT. *See* Fractional-order Fourier transform
Fringe projection, 82, 97
FTM. *See* Fresnel transform method
Fujii, A., 103
Fujimoto, J.G., 204
Fukutake, N., 222
Full-field optical coherence tomography (FFOCT), 209–215
FZP. *See* Fresnel zone pattern

G
Gabor, D., 1–3, 97
Gabor holography, 7, 60–61, 161, 181
Gabor wavelet, 80, 81
Gaussian function, 12
Gaussian integrals, 18
Geometric phase modulator (GPM), 187
Gerchberg–Saxton–Fienup algorithm, 134
Goldfish retinal rod cells, 173
Goodman, J., 5, 6, 8
Goss, W.P., 97
GPM. *See* Geometric phase modulator
Grating, 32, 33, 38–41, 103–104, 123, 130, 138, 182–184, 197–198, 212, 214–216

H
Haddad, W.S., 5
Hariharan, P., 8
Harmonic holography, 138
HCM. *See* Huygens convolution method
Hee, M.R., 204
Hepatocytes, 172
Heterodyne, 4, 101–103, 105, 179, 202, 204, 205, 208, 209, 212
Heterodyne digital holography, 101–103, 105
Hexagonal grating, 130
Hilbert phase microscopy (HPM), 181–182
Hilbert transform, 103, 182, 183, 208
HOCI. *See* Holographic optical coherence imaging
Hoink, A., 172
Hologram plane, 29, 31, 32, 34, 35, 39, 55–57, 60, 63, 64, 66, 68, 77, 78, 90, 95, 96, 165, 174, 215, 216
Holographic interferometry, 4, 8, 141, 168
Holographic optical coherence imaging (HOCI), 223
Holographic particle image velocimetry, 222
Holographic terms, 31–32, 56, 57, 194
Hong, C.K., 220
HPM. *See* Hilbert phase microscopy
Huygens convolution method (HCM), 49–53, 112
Huygens principle, 19, 24
Huygens PSF, 20, 49
Hypotonic shock, 169, 171

I
Infinity configuration, 149–151
Infrared, 3, 141, 159
Inside detector, 142
Inside source, 142
Interference microscopy, 5, 152, 156–157, 185–187
Interference reflection microscopy (IRM), 174
Interferometry, 4, 7, 8, 15, 82, 95, 96, 141, 162, 168, 181, 191, 204, 209, 220, 222, 223
Inverted microscope, 150, 162
IRM. *See* Interference reflection microscopy
Istasse, E., 193

J
Jeong, S.J., 220
Jeon, Y., 220
Joannes, L., 192
Jones vector, 141
Jueptner, W., 5, 6, 8
Juptner, W.P.O., 8

K
Kaneko, A., 103
Kemper, B., 172
Kim, M.K., 8, 172
Koehler illumination, 149
Koyama, T., 103
Kreis, T., 8
Kubota, T., 103
Kukhtarev, N., 8

L
Laser diode (LD), 3, 118, 160, 192, 213, 225
Laser microsurgery, 172–173
Laser radar, 220
Lateral resolution, 73, 151, 172, 202, 206, 207, 213, 220
Lawrence, R.W., 5
LCDH. *See* Low-coherence digital holography
LD. *See* Laser diode
Lead zirconate titanate (PZT), 96, 101, 102, 139, 214
Lebec, M., 210
LED. *See* Light emitting diode
Lee, B., 8
Legros, J.C., 192
Leith, E.N., 3, 220
LIF. *See* Light-in-flight holography
Light emitting diode (LED), 118, 160, 192, 212
Light-in-flight holography (LIF), 215, 216
Linnik microscope, 156, 157, 160, 161
Littrow reflection, 215
Liu, Q., 99
Lock-in detector, 201
Lo, C.M., 172
Lohmann, A.W., 8
Longworth, J.W., 5
Low-coherence digital holography (LCDH), 192, 223, 224
Low-coherence interference microscopy, 185–187
Low-pass filtering, 23, 195, 201, 204

M
Mach–Zehnder interferometer, 160, 161, 175, 179, 181, 194
Magnification, 4–5, 27, 29
Mann, C.J., 172
Marron, J.C., 220
Matoba, O., 103
Maximum distance, 43, 52
McPherson, A., 5
Mengedoht, K., 204
Michelson interferometer, 96, 156, 160, 204, 208–210, 221
Microscopy, 3, 50, 63, 73, 109, 134, 149, 191,
Microwave holography, 141
Millimeter wave, 141
Milster, T.D., 222
Minetti, C., 193
Minimum distance, 49, 73, 114
Mirau objective, 157
Monnom, O., 193
Mouth epithelial cell, 169, 170
Multiwavelength interferometry, 4, 141

N
Nanoparticle, 138, 163, 179
Neurons, 169–172
Newton's ring, 34
Nipkow disk, 159
Nishio, K., 103
NLO. *See* Nonlinear optics
Noise, 5, 7, 101, 102, 105, 116, 117, 137, 153, 160, 163, 165, 172, 173, 181, 183, 185, 192, 202, 208, 224
Nonlinear optics (NLO), 4, 37, 137–139, 159
Nonlinear spatial filtering, 93
Numerical
  aperture, 66, 73, 129, 150, 151
  diffraction, 1, 43–53, 55, 91, 95, 96, 109, 112, 118, 121, 137, 163, 167, 175, 201, 217
  focusing, 5, 109–112, 163, 166, 197
  parametric lens, 123
  shearing, 184
Nyquist frequency, 46, 51, 66

O
Objective, 63, 73, 123, 149–152, 154–157, 160, 162, 179, 184, 206, 210, 223
OCM. *See* Optical coherence microscopy
OCT. *See* Optical coherence tomography
ODT. *See* Optical diffraction tomography
Ophthalmic imaging, 207, 218
OPT. *See* Optical projection tomography
Optical coherence microscopy (OCM), 206–207
Optical coherence tomography (OCT), 204–210, 212–214
Optical diffraction tomography (ODT), 131, 222–223
Optical fiber, 102, 141, 222
Optical phase unwrapping (OPU), 7, 114–119, 163, 172, 178

Optical projection tomography (OPT), 221–222
Optical scanning holography (OSH), 200–204
Optical sectioning, 156, 183, 191
OPU. *See* Optical phase unwrapping
Orthoscopic image, 31
OSH. *See* Optical scanning holography
Osten, W., 8

P
Pancreatic cancer cell, 172
Parallax, 3, 31, 131, 167
Parallel
  heterodyne detection, 212
  phase-shifting, 103, 104
Paramecium, 166, 167, 172
Paraxial approximation, 24, 25, 73, 79, 200
Paris, D.P., 8
Parseval's theorem, 16, 46
Particle velocimetry, 63
PDM. *See* Phase-dispersion microscopy
PDOT. *See* Phase-dispersion optical tomography
Pedrini, G., 66
Phase
  conjugation, 40, 138–139
  hologram, 8, 37–38
  modulation, 102–103, 175, 202
  mosaic, 103–104
  problem, 131
  retrieval, 131–135, 222
Phase-dispersion microscopy (PDM), 208–209
Phase-dispersion optical tomography (PDOT), 209
Phase-referenced interferometry (PRI), 209
Phase-sensitive OCT, 208
Phase-shifting digital holography (PSDH), 7, 95–105, 139, 224
Phase-shifting Gabor holography, 181
Phase-shifting interferometry (PSI), 4, 95–97, 105, 181, 222
Photorefractive, 1, 4, 40, 137, 138
Piezoelectric transducer, 101
Pixel resolution control, 49, 112–114
Plane wave, 22–24, 29, 32–34, 37, 39–41, 51, 53, 55–57, 60, 63, 64, 66, 67, 74, 75, 77, 78, 86, 95, 104, 105, 119, 123, 160, 193, 195, 200–202
Plane-wave decomposition, 22
Point diffraction interferometer, 181
Point source, 16, 19, 24, 29, 32, 34–37, 41, 64, 66, 71, 73–77, 139, 142, 180, 192–194, 198, 199
Point spread function (PSF), 17, 20, 21, 47, 49, 73, 202
Polarization, 101, 141, 155, 157, 162, 175, 176, 183, 184, 199, 208–211
Poon, T.C., 8
PRI. *See* Phase-referenced interferometry
PSDH. *See* Phase-shifting digital holography
Pseudoscopic image, 31
PSF. *See* Point spread function
PSI. *See* Phase-shifting interferometry

Q
QPM. *See* Quantitative phase microscopy
Quadratic phase, 25, 27, 64, 73–77, 195–197
Quantitative DIC, 183–184
Quantitative phase microscopy (QPM), 5–7, 112, 117, 136, 168–170, 174, 181–187, 202
Quarter-wave plates, 101, 187, 212

R
Rat kangaroo kidney epithelial cell, 172–173
Rayleigh-Sommerfeld theory, 19, 24
RCH. *See* Reference calibrated hologram
Red blood cells, 169, 170, 172, 173, 177, 178, 183, 213, 220, 221
Reference calibrated hologram (RCH), 137
Reflection hologram, 38
Refractive index, 39, 40, 137, 138, 170, 182, 187, 208, 221–222
Requena, M.L.N., 193
Retinal cone mosaic, 206–207
RGG. *See* Rotating ground glass
Rhodes, C.K., 5
Ridge of the wavelet, 81, 82
Ronchi grating, 183, 184
Rosen, J., 8
Rotating ground glass (RGG), 193–195, 212

S
Saint-Jalmes, H., 210
Salath, R.P., 212
Sampling function, 71, 72
SAR. *See* Synthetic aperture radar
Sasada, M., 103
SBP. *See* Space-bandwidth product
Schafer, M., 172
Schnars, U., 6, 8
Schnekenburger, J., 172

Schroeder, K.S., 220
Schulz, T.J., 220
SDOCT. *See* Spectral domain OCT
Second harmonic generation (SHG), 138, 139
Seitz, P., 212
Sharpness metric, 109
SHG. *See* Second harmonic generation
Shift theorem, 15
Shih, M.P., 220
Signal-to noise ratio (SNR), 206, 210
Similarity property, 15
Sinusoid fitting method, 104–105
SKOV3 ovarian cancer cells, 168, 169
SLD. *See* Superluminescent diode
SLM. *See* Spatial light modulator
Smart pixel array, 212
SNR. *See* Signal-to noise ratio
Solem, J.C., 5
Southern, J.F., 204
Space-bandwidth product (SBP), 77–78
Space-limited, 45
Spatial filtering, 91, 93, 154, 183, 192, 203, 204
Spatial frequencies, 11, 21, 23, 32, 38, 47–48, 68, 74, 77, 121, 123, 129, 140, 167, 177, 193–194, 223
Spatial light modulator (SLM), 30, 101, 139, 181, 182, 195–196
Spatial phase shifting, 104–105
Spatio-temporal digital holography (STDH), 203–204
Speckle, 4, 29, 89–91, 105, 137, 160, 173, 192, 196, 202, 223, 224
  interferometry, 4, 82
Spectral domain OCT (SDOCT), 205, 206, 220
Spectral hole burning, 4, 40–41
Spectrometer, 205, 206
Spherical aberration, 123, 152
Spherical wave, 19–21, 24, 29, 32, 34, 36, 37, 57, 75, 165, 179, 195–196, 198–200, 202
Spiral
  phase contrast, 184–185
  phase plate, 101, 184–185
SSOCT. *See* Swept-source OCT
STDH. *See* Spatio-temporal digital holography
Stimulated photon echo, 41–42
Superluminescent diode (SLD), 185, 192, 209, 212, 214, 220, 224–225
Swanson, E.A., 204
Swept-source OCT (SSOCT), 205, 206
Synchronous
  detection, 210
  illumination, 210, 211
Synthetic
  aperture, 129–131
  wavelength, 116
Synthetic aperture radar (SAR), 129–130

T
Tadpole eye, 210, 211
Tahara, T., 103
Talbot distance, 103–104
TDOCT. *See* Time-domain OCT
Tearney, G.J., 204
Temporal phase shifting, 103, 192, 204
Terahertz (THz), 141
Thick hologram, 38–40
Thin hologram, 38–39
THz. *See* Terahertz
Tilted planes, 53, 56, 67, 112, 119–123, 175, 193
Time average holography, 4
Time-domain OCT (TDOCT), 204–206, 214
TIR. *See* Total internal reflection
TIRFM. *See* Total internal reflection fluorescence microscopy
TIRHM. *See* Total internal reflection holographic microscopy
Tiziani, H.J., 66
Total internal reflection (TIR), 174–176, 179
Total internal reflection fluorescence microscopy (TIRFM), 174
Total internal reflection holographic microscopy (TIRHM), 174–177
Transmission hologram, 37–38
Transport of intensity equation, 135
Triangular interferometer, 198–199
Tube lens, 149–151
Turbid imaging, 223–225
Turbid medium, 139, 212
Twin image problem, 3, 85, 131
Twin image terms, 31, 33–35, 56, 57, 61–62, 67, 85–93, 96, 102, 122, 177, 201

U
Uncertainty relation, 15
Upatnieks, J., 3
Ura, S., 103

V
von Bally, G., 172

W
Watson microscope, 156, 157
Wavelength mismatch, 34, 57, 58, 139
Wavelet, 19, 20, 80–82, 119, 139, 200, 215–216
Wave-vector matching, 39, 40
WDF. *See* Wigner distribution function
Werner, W., 204
Wigner distribution function (WDF), 74–78, 135
Wollaston prism, 103, 155, 177, 183

X
X-ray microscope, 2, 3, 134

Y
Yamaguchi, I., 95
Yang, X.L., 99
Yaroslavsky, L., 8
Yatagai, T., 8
Yeast cell, 172
Yoshikawa, H., 8
Yu, L.F., 172

Z
Zernike phase contrast (ZPC), 154–155, 177, 178
Zernike polynomials, 123
Zero-background, 157
Zero-order terms, 31, 33, 56, 57, 86, 88, 93, 164
Zero-padding method, 112–113
Zou, Y.L., 66
ZPC. *See* Zernike phase contrast